Gravitational-wave Astronomy

Aspects of the Theory of Binary Sources and Interferometric Detectors

Thesis by

Scott Alexander Hughes

In Partial Fulfillment of the Requirements

for the Degree of

Doctor of Philosophy

California Institute of Technology

Pasadena, California

1998

(Submitted May 11, 1998)

Unearned knowledge is perilous. Only by the seeking and the gaining of it may its uses be understood, its true worth measured.

—Stephen R. Donaldson, "White Gold Wielder"

Acknowledgements

When I was an undergraduate at Cornell University, I would sometimes pull away from my computer terminal and sit in the reading room of the Space Sciences building, flipping through the Ph.D. theses of former students, wondering if I would have the tenacity to eventually produce one myself. One thesis in particular caught my attention because of the author's very broad-minded attitude towards scientific research. This thesis, by Christopher Chyba (a student of Carl Sagan), taught me what I've come to think of as Chyba's Maxim: "**Never let your ignorance of any scientific field prevent you from publishing research papers in it.**" It has been my incredibly good fortune to a have a Ph.D. adviser who encourages his students to follow this maxim. I never thought when I arrived at Caltech that I would work on subjects as diverse as data analysis, seismology, and instrumental noise, besides astrophysical general relativity. Kip Thorne has been a paragon of what an adviser should be — always supportive and encouraging of my work, and allowing me a great deal of freedom to pursue ideas. I will always be grateful and glad for the opportunity I have had to work with him.

As though I weren't fortunate enough to have Kip as an adviser, my lucky streak continued with the two other people with whom I closely collaborated on projects in this thesis, Éanna Flanagan and Patrick Brady. Both showed incredible patience and good-naturedness in working with a somewhat overeager and naive student, and I thank them for that. Éanna in particular suffered quite a bit as we worked for nearly 3 years on the binary black hole projects — I'd especially like to thank him for his tolerance, and apologize for hounding him so much while he was at University of Chicago. As I look over the email exchanges Éanna and I had over those 3 years, I'm amazed that he never got badly annoyed at my nearly perpetual nagging.

One of the best things about Caltech, and the TAPIR (**T**heoretical **A**stro**P**hysics **I**ncluding **R**elativity) group in particular, are the students, postdocs, faculty, and visitors one meets and works with here. Most of what I've learned as a grad student, I've probably learned while chatting with them. For great conversations, fun, and much food, beer, and whiskey, I'd like to thank Alan Wiseman, Pat Brady, Eric Poisson, Nahum Arav, Nir and Hilla Shaviv, Andrew Melatos, Jolien and Jean Creighton, Daniel Kennefick, Yuri Levin, Teviet Creighton, Glenn Soberman, David Hogg, Ruben Krasnopolsky, Sterl Phinney, Roger Blandford, Tom Prince, Bruce Allen, Sam Finn, Sathyaprakash,

and Lee Lindblom. I especially need to thank my fellow members of the Order of the *Μαλακες*: Josh Bliss, Rick Jenet, Ben Owen, and Jim Mason, along with the others who entered Caltech in my class. You guys made the first tortuous few years bearable, and all the following years a lot of fun. I'd also like to thank Cobalt, who spent hours keeping me company while I finished writing this document.

Although Caltech is remarkably free of bureaucracy for a major research institute, there's enough present to make life difficult from time to time. For steering me through those difficult moments, and for always being willing to chat and procrastinate when I swing by, I thank Donna Driscoll, Shirley Hampton, and Kate Finnegan.

When I came to Caltech, I was assigned to live in the Mosher-Jorgensen Graduate Residence — a rather shabby, barracks-like building that happened to house some of the most fun people I've met at Caltech. I managed to keep my sanity during my first two years at Caltech by periodically losing it with Joe "Shifo" Sivo, Rajesh Kedia, Lakshman "Lucky" Benedict, Aseem Mehta, Ryan MacKay, Ralf Höchemer, Matt Werner, and Rahul Pathak.

My career in physics was launched at Cornell University. I would never have become so enthusiastic about this field if it hadn't been for the support and encouragement of Stu Shapiro, Saul Teukolsky, David Cassel, Jim Alexander and Martha Haynes. Many of my friends from Cornell — особенно мои друзья от Дома Иностранных Языков — provided a lifeline that helped remind me that there's life after graduate school. For the visits, phonecalls, and email, I thank Dan Gil, Svetlana Kogan, Frank Jary, Aparna Venkatesan, Paul Walker, Jen Wheary, Chuck Keeton, David Cohen, Neal Stern, and John Vibert. Marc Gallagher, from *way* back in my past, also kept in touch and helped me stay sane.

I would never have achieved what I have achieved without the love and support I have received from my family. Since childhood, my parents Joe and Rocky have never questioned why I was interested in the obtuse things that kept me occupied. Thanks for your support, for allowing me to destroy untold appliances and toys in a quest to find out how they worked, and for not getting too mad when I dug up the yard and garden looking for dinosaur bones. It was often my poor sister Sarah's toys and other stuff that suffered most strongly my nascent scientific curiosity; thanks for not telling on me as often as you could have.

Finally, I am infinitely grateful for the love and support I have gotten from my wife Amy. I warned her that living with a late-stage physics graduate student could get ugly, and I know that the final weeks putting this thesis together were not easy. Thank you for remaining an oasis of

tranquility for me and for us.

The research presented in this thesis was supported by NSF Grants PHY–9220644, PHY–9408378, PHY–9424337, PHY–9514726, and AST–9417371; and also by NASA Grants NAGW–4628 and NAGW–2897. I gratefully acknowledge the support of the National Science Foundation Graduate Program, and of a Caltech PMA division fellowship during my first year, as well as Teaching Assistantships during my second and third years. Chapter 4 relies in part on data generated by Joan Centrella and her research group at Drexel University; I thank them for providing it to me. Chapter 6 relies in part on seismic motion data taken by Alan Rohay of the Pacific Northwest National Laboratory. I thank him from providing me this data, and also Albert Lazzarini of LIGO for facilitating my access to it.

Abstract

This thesis presents a study of several problems and issues in the nascent field of gravitational-wave astronomy. Multi-kilometer baseline interferometers are being built in the United States [the LIGO (**L**aser **I**nterferometer **G**ravitational-wave **O**bservatory) project] and similar projects are underway in Europe (the VIRGO and GEO600 projects) and Japan (the TAMA300 project). LIGO will begin operations very soon (the first science run is scheduled for 2002), and detectors in other countries will begin soon as well. We are thus about 5 years from using gravitational waves as a new window to probe astrophysical processes in the universe.

Chapters 2, 3, and 4 of this thesis study gravitational waves from coalescences of compact binaries. Chapters 2 and 3 are a detailed examination, in collaboration with Éanna É. Flanagan, of binary black hole (BBH) coalescences. The birth rate of BBH systems in the universe is highly uncertain, so it is not immediately apparent how relevant they are to gravitational-wave astronomy. If such systems do in fact exist, we find that they will be visible to extremely large distances, far greater than the distances to which binary neutron star systems, for example, will be visible. This heightened visibility may compensate for the possible dearth of such binaries, making them an extremely important and interesting source. We suggest ways in which numerical modeling of BBHs may aid gravitational-wave data analysis, and techniques that can be used in BBH event searches and waveform analysis. Chapter 4 analyzes the measurement of gravitational waves from the final merger of binary neutron star systems. Such waves depend on details of the composition of neutron stars, such as their equation of state, and may be driven by hydrodynamic and nuclear processes that occur in the final merger. Unfortunately, these waves are emitted at high frequencies where LIGO-type detectors have poor sensitivity. Measuring such waves will require specialty "narrow-band" detectors. In this chapter, I present an algorithm for optimally configuring a network of multiple LIGO-type and narrow-band detectors to measure these merger waves. I find that improved theoretical modeling of the final merger will play an important role in designing such networks and in the analysis of their data. In Chapter 5, in collaboration with Patrick R. Brady, I analyze the stability of binary neutron star systems as they coalesce. Some rather controversial numerical calculations have found that neutron stars in binary systems are rendered unstable by their companion, and may collapse into black holes long before their final merger. This would have a huge impact on the

gravitational waves such systems emit. The claimed effect is first-order in a particular expansion. Motivated by this claim, Brady and I perform a first-order expansion of the fluid and field equations of general relativity, in the limit in which one star is much smaller than the other. We find that no such effect can exist. Finally, Chapter 6 is an analysis, in collaboration with Kip S. Thorne, of seismic gravity-gradient noise, a noise source that may be of concern to future detector designs. This noise source arises from fluctuations in the density of the earth near and below a LIGO-type interferometer's test masses. It is gravitational in origin, and thus cannot be shielded. By carefully studying the geological structures in the earth near the two LIGO sites, considering the propagation of elastodynamic waves in such structures, and computing the gravitational fluctuations such waves cause, we find seismic gravity-gradient noise is likely to become unavoidable at frequencies below roughly 5 Hertz. This has strong implications on plans to improve the low frequency sensitivity of the LIGO detectors.

Contents

List of Figures

List of Tables

Chapter 1

Introduction and overview

1.1 Motivation

As mentioned in the Abstract, the first detectors in a network of sensitive gravitational-wave antennae are scheduled to begin operations in a mere four years: it is planned that the first two-year science run of both LIGO interferometers will begin in the year 2002 [1]. Assuming that the European VIRGO and GEO600 projects finish construction and begin operations on the same time-table, there will soon exist a world-wide network of broad-band gravitational-wave detectors with sensitivity to wave strains of roughly 10^{-21}. The era of gravitational-wave astronomy is about to begin.

In many ways, the astrophysical information that is carried by gravitational waves can be thought of as "orthogonal" to the various forms of electromagnetic waves that astronomers have studied for millennia. Consider the following differences: electromagnetic waves typically come from the incoherent superposition of radiation, arising due to the motion of charged particles in an astrophysical environment. Quite often, they provide information about the thermodynamic state of that environment. Gravitational waves are coherent superpositions of radiation that arise from the bulk motion of the source. They provide information about the overall dynamics of the emitting system. The wavelengths of electromagnetic waves are typically rather smaller than the size of the emitting source. They can thus be used to form an image of the source; electromagnetic astronomy is analogous to vision. By contrast, the wavelengths of gravitational waves are of order or greater than the size of the emitting source. Such waves *cannot* be used to form an image of the source, and are more similar to sound. Gravitational-wave astronomy is thus akin to audition, and one may regard gravitational-wave detectors as "ears" listening for violent astrophysical events. Electromagnetic waves interact rather strongly with matter, whereas gravitational waves interact very weakly. This means that gravitational waves can propagate practically unhindered[1] from their source to detectors on the earth. (Unfortunately, this also means that the waves interact very weakly with these detectors. Because of

[1] Gravitational waves *are* gravitationally lensed by large mass distributions, exactly as electromagnetic waves are.

this, the detection of gravitational waves is an arduous process.) Finally, the frequency band of relevance to gravitational-wave astronomy is far different from the band of relevance to electromagnetic astronomy: $10^{-18}\,\mathrm{Hz} \lesssim f_{\mathrm{GW}} \lesssim 10^{4}\,\mathrm{Hz}$, whereas $10^{7}\,\mathrm{Hz} \lesssim f_{\mathrm{EM}} \lesssim 10^{24}\,\mathrm{Hz}$. Because the processes that generate gravitational waves are so different from the processes that generate electromagnetic waves, the information that they carry will be quite different. The era of gravitational-wave astronomy is likely to be exciting and full of many surprises.

As mentioned parenthetically in the above paragraph, the detection and measurement of gravitational waves is an arduous task. The experimental effort that has gone into the design and building of the LIGO facilities is almost overwhelming: thousands of cubic meters of vacuum produced by enormous vacuum pumps; extremely long period pendular suspensions for the test masses, which are themselves of extreme purity; high-stability lasers; isolation from myriad possible noise sources; and so on, seemingly *ad infinitum*.

Despite the incredible achievements of the experimentalists who have designed and constructed modern gravitational-wave observatories, it is not a foregone conclusion that gravitational waves are about to be detected. Much remains unknown about event rates and event distributions for well-understood sources, about data analysis for unknown sources or known sources with poorly understood waveforms, and even about certain classes of detector noise. Theorists can do much to shed light onto issues such as these. Indeed, considering how much effort experimentalists have put into developing instruments that are capable of measuring astrophysical gravitational waves, one could argue that theorists have a *duty* to contribute in such a way. Gravitational-wave astronomy has the potential to revolutionize gravitation theory, and theorists should participate in this revolution in all ways possible. At a recent open forum of gravitation theorists at the University of Oregon, Jimmy York put it quite succinctly (if a little undiplomatically) when he told the audience that it's time to "put up or shut up" [2].

This thesis consists of one theorist's efforts[2] to contribute to the development of gravitational-wave astronomy. In it, I present studies of gravitational waves from binary black hole systems, measurement of gravitational waves from the final hydrodynamic merger of binary neutron stars, the stability of neutron stars in binary systems, and seismic gravity-gradient noise in interferometric detectors. This Introduction is intended to be a summary of the complete contents of this thesis, and so it describes in moderate detail the motivations, methods, and results of each chapter. I note here that four of the five chapters in this thesis describe research results that I produced in collaboration

[2]More accurately, the efforts of one theorist who often worked in collaboration with wiser heads.

with others: Chapters 2 and 3 represent work done with Éanna É. Flanagan of Cornell University; Chapter 5 represents work done with Patrick R. Brady of Caltech; and Chapter 6 represents work done with Kip S. Thorne of Caltech. In all of these chapters, however, there is only one significant result to which I did not contribute substantially. (This particular result is the noise-monitoring search technique, described briefly in Chapter 2.) I contributed at least equally to all the remaining work discussed in this thesis.

1.2 Gravitational waves from compact binaries

Compact binary systems have been known to be a very promising astrophysical source of gravitational waves for quite a long time; see Thorne's review article in [3] for a brief history of the subject, or Kennefick's Ph.D thesis [4] for a rather less brief history. Indeed, compact binaries are so promising and in some sense so well-understood that it is not uncommon to see research papers whose introductions state, somewhat misleadingly, that "compact binaries systems are the most promising sources of gravitational waves for detectors such as LIGO." More accurately, they are the most *well-understood* sources of gravitational waves, at least over an important fraction of their evolutionary history.

The evolutionary history of a compact binary system may be divided into three more or less distinct epochs. First, there is the *inspiral.* In this epoch, the bodies are widely separated, and the system's evolution is adiabatic — the time scale $\tau_{\rm RR}$ on which radiation reaction changes the binary's orbit is greater than the orbital period. Thus, the binary spends many orbital cycles near some particular point in its evolutionary phase space. Theoretical analyses do a rather good job describing the inspiral. The reason is that when the bodies in the binary are widely separated, their interaction fields are relatively weak. This is a happy circumstance, for it means that one does not need to use the full mathematical machinery of general relativity, which is very hard, but instead one can use general relativity's *post-Newtonian* expansion [5]. Consider, for example, the equations of motion of one body in a compact binary. In the post-Newtonian expansion, these equations of motion heuristically have the form

$$m\ddot{\mathbf{r}} = \mathbf{F}_0 + \epsilon\mathbf{F}_1 + \epsilon^2\mathbf{F}_2 + \epsilon^{5/2}\mathbf{F}_{5/2} + \ldots \tag{1.1}$$

Here, ϵ is of order $(v/c)^2 \sim M_{\rm tot}/r$, where v is the orbital speed of the bodies in the binary, c is

the speed of light, $M_{\rm tot}$ is the total mass of the binary, and r is the bodies' separation. The force $\mathbf{F}_0$ is the zeroth post-Newtonian term, *i.e.*, the contribution to the acceleration of the body that would come from Newtonian gravity alone. The force $\mathbf{F}_1$ is the first post-Newtonian correction that one finds from an expansion of Einstein's field equations; this correction scales with $(v/c)^2$. The other $\mathbf{F}_n$ terms are the n-th post-Newtonian corrections that one can find in a similar manner. [Notice that there are no $n = 1/2$ or $n = 3/2$ terms, *i.e.*, no terms that scales with v/c or $(v/c)^3$. The reason for this is that odd powers of v/c (fractional powers of n) correspond to dissipative, time-asymmetric radiation-reaction forces, and the lowest such term is the quadrupole-order gravitational radiation reaction force, for which $n = 5/2$. If the lowest order gravitational radiation were dipolar rather than quadrupolar, there could be an $n = 3/2$ term; and if there were scalar gravitational radiation, there could be an $n = 1/2$ term.] From such equations of motion, one can calculate the gravitational waveforms that binary systems emit. These waveforms play an important role in planned schemes to analyze the data from LIGO and other observatories: they will be used to make a bank of *matched filters* against which the data will be cross-correlated. These matched filters will be described in greater detail below.

As the bodies in the binary spiral close together, the radiation reaction timescale gets progressively smaller, decreasing at a rate faster than the orbital period. Eventually the radiation reaction timescale becomes roughly equal to the orbital period, and the evolution of the system cannot be described in an adiabatic manner. At roughly the same time, the orbit of the binary system may become dynamically unstable, so that the compact bodies will violently plunge and collide, eventually settling down to some quiescent final state. This violent plunge and collision is the *merger*. Theoretical analysis of the merger cannot be done using any kind of approximations; the fully nonlinear mathematical machinery of general relativity must be used instead. Researchers in numerical relativity are attempting to model both binary neutron star and binary black hole mergers using supercomputers. For binary neutron stars, such models are especially complicated: not only must the gravitational dynamics be treated using the full apparatus of general relativity, but an accurate description of the hydrodynamics and microphysics of the neutron star material must be included as well. Binary black holes are thus in some sense simpler to treat (although there are also a host of technical problems in their case as well).

If the final state of the system contains a single black hole, then the tail end of the merger epoch will be dominated by *ringdown* waves. This will certainly be the case in the merger of binary black holes, and it is quite likely to be the case in the merger of binary neutron stars as well. By the no-hair

and uniqueness theorems [6], the final state of any coalescence that generates a black hole must be given by the Kerr solution. As described in the above paragraph, the spacetime must pass through a regime of complicated and violent dynamics en route to the formation of this Kerr black hole. When most — but not all — of the complicated deviations from the Kerr solution have radiated away, the spacetime geometry of the coalescing system will be describable as a perturbed black hole. These final perturbations will radiate away in a simple, well-understood fashion, described as *quasi-normal modes* of the black hole. These modes emit damped sinusoidal gravitational waves, rather similar to the sound waves that a bell emits when it is struck. This mental picture is quite apt, as the quasi-normal modes of a black hole can be thought of as arising from a bell-like ringing of the spacetime curvature near the black hole. It is for this reason that these waves are called the ringdown[3].

Thus, for compact binary systems, the inspiral and ringdown are fairly well-understood, and the merger is poorly understood. This has strong consequences for certain planned data analysis schemes, which, as mentioned above, rely on the technique of matched filtering. A digression to describe matched filtering in greater detail is in order at this point.

Suppose that one has a set of model gravitational waveforms ("templates") for the inspiral (computed with the post-Newtonian expansion) or for the ringdown (computed from the quasi-normal modes of Kerr black holes). Suppose further we construct N of these templates in such a way that they span in what we believe is a reasonable manner the parameter space of systems we expect to observe [8]. Let this set of templates be $h_j(t)$, $j \in (1, \ldots, N)$. Let

$$\tilde{h}_j(f) = \int_{-\infty}^{\infty} h_j(t)\, e^{2\pi i f t}\, dt \tag{1.2}$$

be the Fourier transform of $h_j(t)$. Let $S_h(f)$ be the one-sided spectral density of strain noise in one's detector, *i.e.*, the strain noise power spectrum (modulo some more or less unimportant factors). Then, the set of functions

$$\tilde{K}_j(f) = \frac{\tilde{h}_j(f)}{S_h(f)} \tag{1.3}$$

is the bank of matched filters that will be used in gravitational-wave data analysis. In the frequency domain, each filter is just a template inversely weighted by the expected noise power — noisy frequency intervals contribute less to the filter than do quiet intervals.

[3]It is worth noting, however, that the quality factor of the black hole is extremely poor compared to a bell: for a black hole, $Q \sim 10 - 20$, whereas a bell has $Q \sim 10^3 - 10^5$. A useful aphorism to describe this is due to Sam Finn: "Black holes don't ring; they thud" [7].

In the data analysis process, the observer simply cross-correlates the filters $K_j(t)$ [obtained by inverse Fourier transforming $\tilde{K}_j(f)$] with the data stream $s(t)$; detection occurs if the maximum value of this cross-correlation exceeds some threshold. More quantitatively,

$$\rho \equiv \max_{\tau} \int K(t+\tau)\, s(t)\, dt \geq \rho_{\text{threshold}} \Longrightarrow \text{Detection}. \tag{1.4}$$

To summarize, systems whose gravitational waveforms are well-known can be analyzed and searched for in a straightforward manner: simply construct a large bank of templates and their associated filters, and cross-correlate the data stream with this bank. Detection occurs when one of the cross-correlations exceeds some threshold (one of the filters "rings" strongly). For compact binary systems, this straightforward scheme should be possible (and not particularly difficult) to implement for the inspiral and ringdown. For the merger, however, waveforms do not yet exist, and may not exist for use as templates by the time that LIGO and other gravitational-wave observatories begin operations.

1.3 Gravitational waves from binary black holes

In light of the discussion in the above paragraph, it is clear that a detailed examination of gravitational waves from compact binary sources is worthwhile. It turns out that, for binary neutron stars, the inspiral waveform is by far the most relevant epoch of the coalescence for observatories such as LIGO. The reason is that the adiabatic description of the evolution of binary neutron star systems doesn't begin to break down until the emitted gravitational-wave frequency is of order 1 kilohertz. At these frequencies, the detectors' sensitivity is degraded due to photon shot noise. LIGO's best sensitivity lies close to 100 Hz, where gravitational waves from binary neutron stars are well-described by the inspiral waveform.

As a binary system is made more massive, features in its waveform are shifted to lower frequencies. Thus, the merger and ringdown are likely to be important in systems which are more massive than binary neutron star systems (whose total masses are expected to lie rather close to $2.8\,M_{\odot}$). Binary black hole (BBH) systems are exactly such systems. In Chapters 2 and 3 of this thesis, I present research performed in collaboration with Éanna É. Flanagan of gravitational waves from BBHs, discussing in particular: models of the gravitational wave strain; the signal-to-noise ratios that can be expected when such waves are measured; data analysis techniques that can be used to

measure the (currently poorly understood) merger waves; information that numerical simulations can provide to aid observations; and accuracy requirements that numerical simulations will need to satisfy in order that their waveform predictions may be usable as data analysis templates. In the remainder of this Section of the Introduction, I summarize these two chapters.

BBH systems are usefully categorized by their total mass, M, a parameter that has a very important influence on the signal's visibility to a variety of gravitational-wave detectors. Flanagan and I consider three different mass classes of BBH systems:

First, *solar mass* binaries — binaries that are formed from massive main-sequence progenitors (field binaries) or binaries formed from capture processes in stellar clusters or galactic centers (capture binaries). For these binaries, the mass $M \lesssim 50\, M_\odot$. The merger rate of solar mass binaries is not well-known. Sigurdsson and Hernquist argue [9] that there should be at least one BBH coalescence per core-collapsed stellar cluster, and thereby claim that the merger rate of capture binaries is likely to be about 3 per year out to a distance of 600 Mpc. There may be some problems with their calculation, however, and it is not clear how useful a guide it is [10]; also, there are large uncertainties in the number of stellar clusters in galaxies. The merger rate of field binaries is perhaps even more uncertain. The literature on binary evolution theory currently contains estimates of the merger rate which range from about $10^{-8} - 10^{-6}$ per year per galaxy [11] (which is roughly comparable to the expected rates for binary neutron star mergers) to zero [12]. (Zero is the most recent estimate of Zwart and Yungelson, who argue that binary black holes will form with too large a separation to merge in a Hubble time.)

Second, we consider *supermassive* binaries — binaries in which the total mass is $10^4\, M_\odot$ to $10^8\, M_\odot$. Individual black holes with such masses almost certainly exist in the cores of many galaxies; binaries of this type could be formed when galaxies collide and merge. There is some observational evidence for these systems: wiggles in the radio jet of QSO 1928+738 have been attributed to the orbital motion of a supermassive BBH [13], as have variations in quasar luminosities [14] and in emission line redshifts [15]. Even more recently, it has been shown that variations in the x-ray spectrum of the Seyfert galaxy IRAS18325-5926 are not inconsistent with the presence of a binary black hole at that galaxy's center [16]. If this is the case (which the authors of [16] caution is quite unlikely), then the binary is expected to merge late in April 1998, just in time to make the present author look foolish before his Ph.D examination committee.

Finally, there is a broad range of masses between solar mass and supermassive binaries — *intermediate* mass binaries. At present, there is no particularly compelling reason to believe in their

existence. Solar mass BBHs are formed naturally in the evolution of massive star systems; although it is a very real question whether such systems will coalescence quickly enough to be of interest to gravitational-wave detectors, there is little question that they *can* form. Likewise, supermassive BBHs are naturally formed in the collision and merger of galaxies. By contrast, there are no compelling mechanisms known to explain the existence of BBHs with $50\,M_\odot \lesssim M \lesssim 10^4 M_\odot$. Quinlan and Shapiro [17] suggest one mechanism whereby such binaries could be produced en route to the formation of a $10^3\,M_\odot$ black hole in the evolution of a dense cluster of main sequence stars, but such a scenario must be considered speculative. Nonetheless, we consider intermediate mass systems since it is simple to do so once the machinery for considering solar mass and supermassive binaries is in place; and, we wish to work in the spirit that gravitational-wave astronomy is likely to produce surprises, and observation of the merger of intermediate mass BBHs may turn out to be one of those surprises.

Regardless of their mass, all BBH systems will evolve in a similar manner, as described in the previous section: a slow, adiabatic and relatively well-understood inspiral, followed by a violent, dynamical, poorly understood merger, which ends in the well-understood ringdown. We characterize these three epochs by the energy spectrum of gravitational waves emitted in each. Consider first the inspiral and the ringdown. The energy spectrum of inspiral waves is given approximately by a power law, $dE/df \propto f^{-1/3}$, down to the point that the binary's orbit becomes dynamically unstable and inspiral ends. We denote the frequency at which this occurs $f_{\rm merge}$, and estimate its value in Chapter 2:

$$f_{\rm merge} = 200\,{\rm Hz}\left(\frac{20\,M_\odot}{M}\right). \tag{1.5}$$

The energy spectrum of ringdown waves have a peaked resonance form, as one would expect for a damped sinusoid. The peak is centered at the quasi-normal ringing frequency, $f_{\rm qnr}$, and has a width $1/\tau_{\rm qnr}$ given by the quality factor $Q \equiv \pi f_{\rm qnr}\tau_{\rm qnr}$. The ringing frequency and quality factor can be calculated using perturbation theory on the Kerr spacetime [18]; they turn out to depend on the mass of the final black hole, M, and its dimensionless spin, $a \equiv |\vec{S}|/M^2$. For black holes, $0 \leq a \leq 1$. Assuming that the final spin is $a = 0.98$, [19]

$$\begin{aligned} f_{\rm qnr} &= 1400\,{\rm Hz}\left(\frac{20\,M_\odot}{M}\right), \\ Q &= 12. \end{aligned} \tag{1.6}$$

Note that we have no particularly good reason for choosing $a = 0.98$. We expect that the final merged black hole will be rapidly rotating since the binary has a lot of angular momentum, but any value of $a \geq 0.9$ (say) seems reasonable. Likely, this issue cannot be settled until simulations (or observations) tell us what the final spin of merged black holes is. In the range $0.9 \leq a \leq 1$, $f_{\rm qnr}$ changes by a relatively small amount (about 20%) from the value given above, but Q changes by quite a bit, diverging in the limit $a \to 1$.

The merger waves then consist of all gravitational waves and associated power radiated in the frequency band $f_{\rm merge} \leq f \leq f_{\rm qnr}$. At the present time, we have very little guidance regarding the shape and magnitude of the merger energy spectrum, at least for coalescing binaries. Extensive calculations have been done of head-on collisions of black holes; however, such systems have no angular momentum. We believe that gravitational radiation during mergers will be driven by the need to shed enough angular momentum to allow the system to form a coalesced Kerr black hole, so the head-on collisions are not particularly relevant. The shape of the energy spectrum will have to be determined by future numerical calculations; for now, we simply use a flat spectrum in which a fraction ϵ of the system's total mass is radiated over the merger band:

$$\frac{dE}{df} = \frac{\epsilon M}{f_{\rm qnr} - f_{\rm merge}}. \tag{1.7}$$

To estimate the value of ϵ, we consider the merger of two rapidly spinning black holes whose spin angular momenta are parallel to one another and to the system's orbital angular momentum. From initial data sets produced by Cook [20], we know that the orbital angular momentum at $f_{\rm merge}$ is $|\vec{L}|/M^2 \simeq 0.9$. We (rather crudely) assume that the spins of two maximally spinning Kerr black holes can be added to this [$|\vec{S}| = (M/2)^2$ for each hole]. Then, the total angular momentum of the system at the beginning of merger is $1.4\,M^2$, too large by $0.4\,M^2$ to form a Kerr black hole. This excess angular momentum must be shed via gravitational radiation during the merger. Assuming that most of the radiation is quadrupolar, so that $E_{\rm rad} = \pi f_{\rm rad} J_{\rm rad}$, we find that about 10% of the system's mass can be radiated in the merger, so $\epsilon \simeq 0.1$. As should be clear from the above discussion, there are quite a large number of uncertainties in this estimate; among other things, it is not clear how many systems will in fact have large, parallel spins. The figure 10% should be taken as indicative of what kinds of radiation efficiencies are reasonable for strongly radiating mergers; we use it as fiducial value for our calculations.

Now that we have built models of the three epochs of binary black hole coalescence, it is a

simple matter to combine them with descriptions of detector noise and compute signal-to-noise ratios (SNRs). The SNRs one calculates using these energy spectra are the matched filtering SNRs, rms averaged over all sky positions and orientations of the binary. These SNRs should thus be thought of as the signal-to-noise ratios that *could be* achieved when templates are available. They are realistic estimates of the SNRs for the inspiral and ringdown, and are a rough upper limit on the SNRs that can be measured for the merger. If merger templates are not available, alternative data analysis techniques will be needed. Such techniques will not be able to achieve SNRs as high as those that matched filtering achieves.

We calculate these angle-averaged SNRs for three classes of gravitational-wave detector: initial LIGO interferometers, advanced LIGO interferometers, and LISA interferometers. LISA is a proposed space-based gravitational-wave detector that would have 5×10^6 kilometer arms and orbit the sun. It would have sensitivity in a band from roughly 10^{-4} Hz to 0.1 Hz. Our most important results are as follows:

- It is quite possible that coalescing solar mass black holes will be the first astrophysical sources detected by the LIGO/VIRGO network of ground-based detectors. Binary neutron stars have been regarded as the canonical "bread-and-butter" source for such systems; however, BBHs are detectable to a far greater distance in the universe (roughly 250 Mpc, versus 30 Mpc for the first LIGO interferometers). This factor of 8 in distance means that BBHs probe a volume of the universe roughly 500 times larger than do binary neutron stars. Provided that the birth rate of solar mass BBH systems is not *too* small, this factor of 500 may mean that BBHs will be more plentiful in the detectors' data than binary neutron stars.

- For total system mass $M \lesssim 20\,M_\odot - 30\,M_\odot$, BBHs can be found by searching for the well-understood inspiral waveform. For larger masses, however, observers will need to search for the ringdown waveform, or for the poorly understood merger waveform. In particular, in the mass range $30\,M_\odot \lesssim M \lesssim 400\,M_\odot$ the merger is potentially the strongest epoch of BBH coalescence for LIGO.

Clearly, if templates for the merger are available for use in data analysis, they could have a very large impact on gravitational-wave astronomy. However, what if they are not available? To get some idea of how badly off observers would be without merger templates, we considered using simple band-pass filters in data analysis — filters which excise all signal power except that which lies in a band $f_{\rm low} \leq f \leq f_{\rm high}$. We show that the merger SNR which one achieves using such

filters is degraded, relative to matched filters, by a factor of $1/\sqrt{\mathcal{N}_{\rm bins}}$, where $\mathcal{N}_{\rm bins}$ is the number of Fourier coefficients (number of frequency bins) needed to describe the merger waveform. The number of bins is related to the bandwidth Δf and the duration T of the waveform by $\mathcal{N}_{\rm bins} = 2T\Delta f$. Although we have a fairly good understanding of the waveform's bandwidth, its duration is very poorly understood. We expect that it will depend rather strongly on the binary's parameters, especially the spins of the binary's constituent black holes: as argued above, if the spins are large and aligned, the system must shed a great deal of angular momentum in the merger. This could cause it to centrifugally hang-up, and the merger may last a long time. On the other hand, if the spins are not large, the system may not need to shed much angular momentum at all — the merger could be quick and relatively uninteresting. At any rate, we argue in Chapter 2 that very likely $\sqrt{\mathcal{N}_{\rm bins}} \simeq 5$ for merger events with the greatest duration. Thus, if templates are not available by the time that BBH events are detected, the measured SNR may be reduced by a factor of 5 relative to the maximum that they could be.

This factor of 5 is large enough that it significantly changes the conclusions discussed above regarding the importance of the merger signal: if the merger SNR is in fact that badly degraded, searches for the merger probably won't be particularly effective, and observers should just search for the inspiral or ringdown. This could mean quite a loss for BBH signal searches — the factor 5 loss in SNR could potentially mean an event rate reduction of $5^3 \sim 100$. Because such a large fraction of the system's mass could be radiated in merger waves, we advocate searching for those waves as effectively as possible; band-pass filters clearly are not very effective.

Improving the effectiveness of merger searches will require input from theoretical modeling. If theoretical modeling can help observers to understand what durations are reasonable for the merger, a technique called *noise monitoring*, suggested by Flanagan [21], might be useful. A brief description of noise monitoring is given in Chapter 2. Very briefly, the method works as follows. First, band-pass filter the data so that only power in the frequency band $f_{\rm merge} \leq f \leq f_{\rm qnr}$ remains. Further subdivide this band into $\mathcal{N}_{\rm bins}$ smaller pieces of width $\delta f = 1/2T$. Then, incoherently add these pieces. The resulting quantity is a measure of the rms power in the band from $f_{\rm merge}$ to $f_{\rm qnr}$. If only Gaussian noise is present, then this power will have a well-understood statistical behavior. Statistically significant deviations from the expected behavior are indicative of the presence of an interesting signal. This technique is conceptually and mathematically quite similar to two techniques used in radio astronomy. In one technique, the radio astronomer incoherently adds power at some frequency and its harmonics. This is less computationally intensive then coherently adding

the power. A second technique is used to analyze segments of data that are too long to Fourier transform. Rather than deal with the full data set, observers break the set into N shorter segments, and then incoherently add the power spectra of these segments. The primary differences between noise-monitoring and these two techniques are that noise-monitoring is a suggested tool for the analysis of broad-band, rather than narrow-band, signals; and, noise-monitoring is suggested as a means to deal with our ignorance of the signal's form, rather than as a means of reducing computational burden.

On paper, the noise-monitoring technique appears to be a promising tool that greatly improves the effectiveness of merger wave searches. Using fairly pessimistic parameters, we find that noise-monitoring searches for the merger are likely to bring the measured event rate back to within a factor of roughly 4 of the event rate that could be achieved with matched filtering. It should be emphasized, however, that this is based on the statistics of Gaussian noise. The noise-monitoring technique has not yet been tested on realistic signals in realistic noise; it remains to be seen whether it remains effective in the presence of non-Gaussian noise events [22].

The noise-monitoring search technique gives some indication of how, as prior knowledge of the merger waveform improves, data analysis techniques to search for the merger can be made more sophisticated and effective. In Chapter 3, Flanagan and I consider more generically how information from theoretical modeling of the merger might be used to aid data analysis, and suggest specific ways that numerical relativity can help gravitational-wave astronomy. In particular, we are interested in ways in which numerical relativity can aid data analysis efforts short of simply calculating a complete bank of waveforms — it seems quite unlikely that numerical relativity will be able to compute a complete catalog of BBH merger waveforms by 2002, when gravitational-wave observatories begin observations.

To begin this discussion, we consider the possible states in which theoretical modeling is likely to be at the time that gravitational-wave observations begin. At the risk of being overly pedantic, we describe theoretical modeling with four categories:

- *No information*: numerical modeling fails to provide any input about the characteristics of BBH merger waves. If this is the case, very likely all that will be definitely known about the merger is its approximate bandwidth and location in the time domain, since it must lie between the inspiral and the ringdown.

- *Information limited in principle*: numerical modeling can provide some information about BBH mergers, but modeling of arbitrary mergers is not possible. For example, supercomputer

codes may exist that can only model some special classes of BBH mergers such as equal mass binaries, or binaries in which the constituent holes have zero spin. It seems likely that numerical relativity will exist in this state for quite a while once it gets beyond the "No information" state — each time numericists try to make the system more complicated, there will probably be serious technical problems that must be overcome.

- *Information limited in practice*: numerical modeling can evolve and study arbitrary BBH mergers, but practical considerations prevent numericists from being able to assemble a "full" bank of filters that completely spans [8] the relevant parameter space. This may be the case if it turns out that generating a single template takes, say, several hundred hours of CPU time.

- *Full information*: numerical modeling can generate an arbitrary number of arbitrary BBH merger waveforms, more or less at will. Our cartoon for this is that one will simply press the "BBH Merger" icon on one's laptop, and the computer will then generate the waveform. Obviously, this possibility is highly unlikely, although it is the end state to which numerical relativity strives.

Concomitant to these four states are three possible scenarios for analysis of waves from the merger epoch. Consider first the possibility that no useful information from numerical simulations is available. In this case, it will not be possible to learn anything interesting about the astrophysics and strong field general relativistic dynamics of binary black hole mergers; the best one can hope to do is to reconstruct the waveform as well as possible from the noisy data stream, and then to try to interpret it as theoretical understanding of the merger improves. In the absence of any useful input about the merger, reconstructing the waveform boils down to band-pass filtering the data stream to remove all power outside of the relevant frequency band, and then hoping that the signal is strong enough that it stands above the noise in the remaining (filtered) output. For the sake of pedagogy, we call a merger signal that is in fact strong enough to stand above the noise in such a fashion "visible." As we show in Chapter 3, some BBH systems, *detected* via their well-understood inspiral waves, will have visible merger signals (modulo the many uncertainties regarding the merger waveform that we have modeled away with the merger wave spectrum described above). For initial LIGO interferometers, a signal whose inspiral SNR is at the detection threshold will likely have a merger signal that is barely visible above the noise. Signals that are not so close to threshold will of course be more visible. Rather counterintuitively, signals that are at threshold for advanced LIGO interferometers will have merger signals that are even less visible — because advanced LIGO can

coherently measure the inspiral over many more cycles than initial LIGO, it wil be able, via the well-understood inspiral, to detect systems whose merger signals are very weak.

To summarize the above paragraph, without some prior information about the merger waves from numerical simulations, gravitational-wave astronomy will only be able to measure the merger waveform rather crudely — a simple reconstruction without any associated understanding of the underlying astrophysics and strong field general relativistic dynamics. And, the ability to perform this reconstruction will be very limited, since only a small portion of signals will be "visible," *i.e.*, strong enough that they can be usefully reconstructed from the noisy data stream. This is a clear impetus for numerical relativists to press on and develop codes that are capable of accurately modeling the BBH merger.

This brings us naturally to the second scenario in which data analysis might operate in analyzing BBH merger waves: some information, and perhaps even a few waveform templates, are available, but by no means is it possible to produce a complete set of templates that spans the entire BBH merger parameter space. [This corresponds to the second ("Information limited in principle") and perhaps the third ("Information limited in practice") categories of theoretical information availability.] First of all, in this circumstance it may be possible to search for the merger directly, rather than searching for the inspiral or ringdown and then attempting to analyze the merger afterwards. As described above, the noise-monitoring technique may be practical if simulations provide an understanding of the merger waveform's duration; and improvements or more sophisticated variants of noise-monitoring might be constructed to incorporate other relevant bits of information. What can be learned once the merger has been located is rather more interesting in this case. We again advocate reconstructing the waveform from the noisy data stream; however, since in this scenario there is more known about the astrophysics of merger wave generation, it will be possible to use this reconstructed waveform to learn something about the BBH source. For instance, suppose that simulations demonstrate that there is a strong correlation between the spins of the binary's constituent black holes and the duration of the merger. Then, a measurement of the merger duration tells us something about the spins of the source.

In this second scenario, reconstructing the waveform can be done in a rather more sophisticated manner than the rather simple band-pass filter method described in the context of the first data analysis scenario (no information). Data analysts should be able to use the (possibly sketchy) knowledge that exists of the merger waveform to choose a family of basis functions that is appropriate for the merger. For instance, if simulations indicate that the instantaneous gravitational-wave

frequency $f_{\rm GW}(t)$ of the merger has some easily understood behavior (perhaps it "chirps" from the low frequency $f_{\rm merge}$ to the high frequency $f_{\rm qnr}$; perhaps, if rapidly spinning black holes tend to become centrifugally hung-up in the merger, it spends several cycles hung up at some frequency $f_{\rm hang-up}$; ...), it may be possible to choose a family of wavelets or other appropriate basis functions that encapsulates this behavior. We present in Chapter 3 an algorithm for projecting the data stream onto this family of basis functions. In a rough sense, this algorithm can be thought of as a generalization of band-pass filtering. It reduces to band-pass filtering in the limit that one's basis is simply a Fourier basis (*i.e.*, sines and cosines) and in which one chooses whether to keep or reject a component of the data based solely on its frequency band. The generalized algorithm can use arbitrary basis functions, and allows one to keep or reject a component of the data based on a broader set of criteria than simply its frequency.

The third possible merger data analysis scenario is that eventually enough templates will be available that matched filtering will become practical. This will certainly and obviously be the case if theoretical understanding of BBH mergers reaches "Full information," but should also be practical to some extent in the case of "Information limited in practice." In this second case, we imagine that theorists and observers will work closely together in order to fit the results of numerical simulations to observed data. For instance, a first rough cut at measuring the merger will likely give some indication which parameters (masses, spins, *etc.*) characterizes the measured merger. This rough cut will be enough for numerical relativists to fire up their codes and produce a set of a dozen or so waveforms that are consistent with that measurement. This can be iterated until the theoretical waveform matches the data as well as possible. In this kind of scenario, relativity theorists will work in a manner akin to theorists in fields such as particle physics in which high-quality experimental data has been available for years — their calculations and motivations will be driven very strongly by experimental data. It should be a salubrious experience, and is an example of how LIGO and other such gravitational-wave observatories could have a strong effect on the development of theoretical gravitation.

In this scenario, the templates produced by numerical relativity will need to meet certain accuracy requirements — since they will be produced by numerical computation, they will of necessity contain some amount of systematic numerical error. In Chapter 3, we set guidelines regarding the tolerable limit of this numerical error in two different ways. First, note that errors in one's templates will cause a degradation in signal-to-noise ratio. This is an unavoidable consequence of template error. If such templates were used to perform a signal search, this degradation would cause one to

not detect some fraction of BBH merger events. We demand that the loss in SNR due to systematic numerical error be kept small enough one does not miss a "significant" number of events. Observers or numerical relativists can define "significant" as they like; for concreteness, we've defined a loss of 3% of events to be significant. Second, note that errors in one's templates will interfere with one's ability to "extract information" from a merger measurement. That is, template error will impede the process of recasting the measured data in terms of the astrophysical characteristics of the source, thereby impeding one's ability to learn about the astrophysics and characteristics of strong field gravitational dynamics from BBH mergers. Template error thus causes a loss in information about the BBH source. We quantify this loss using the mathematical machinery of information theory. In the language of information theory, a measurement yields a certain number of bits of information, I. In the context of BBH mergers, this means that the measurement could have distinguished between $N_{\text{dist.}} = 2^I$ different BBH sources. When the templates contain error, some portion δI of that information is lost, and the measurement cannot distinguish between as many BBH sources: the new number of distinguishable sources, $N'_{\text{dist.}} = 2^{I-\delta I} = N_{\text{dist}}/2^{\delta I}$. By demanding that δI be kept less than, say, 1 bit, we derive a condition on the allowable amount of error in numerical templates. This condition turns out to be roughly the same as the condition one derives by demanding that one does not lose a significant number of BBH events.

1.4 Measuring gravitational waves from the final merger of binary neutron stars

In contrast to the BBHs discussed in the previous section, the merger waveform of binary neutron stars does not lie in a region of frequency space in which LIGO is especially sensitive. The merger of binary neutron stars occurs at frequencies of order 1 kHz, where the sensitivity of laser interferometers is severely degraded by photon shot noise. In other words, laser interferometers have good sensitivity to binary neutron star inspiral, but poor sensitivity to the merger.

The insensitivity of laser interferometers to the binary neutron star merger waveform is unfortunate, since what can be learned from merger observations is quite different from what can be learned from inspiral observations. The inspiral waveform depends on "clean," simple parameters — for example, the masses of the individual neutron stars, their spins, and the binary's eccentricity. Measurement of the inspiral waveform is therefore a measurement of these parameters. Depending on the signal-to-noise ratio, the accuracy with which these parameters can be mea-

sured is in some cases quite good. For example, the so-called "chirp mass" of detected binaries, $\mathcal{M} \equiv m_1^{3/5} m_2^{3/5}/(m_1+m_2)^{1/5}$, will be measurable in advanced LIGO interferometers with a fractional accuracy of approximately 0.1%. (Even initial LIGO interferometers will be able to measure this parameter in detected binaries with a fractional accuracy of about 1%.) The merger waveform, by contrast, depends on "messy" details of the stars' internal constitution and processes that occur during the stars' merger — the neutron star equation of state and details of the hydrodynamic evolution of the merger detritus. A measurement of the merger might teach us quite a bit about these messy astrophysical details. A few numerical calculations of binary neutron star merger have been performed to date [23]; although they must be considered preliminary, they probably indicate some of the features that will be present in the true astrophysical merger waveform. These calculations indicate that the merger waveform may cut off rather sharply at some frequency of order a few $\times\ 10^3$ Hz. They also indicate that a transient bar-like structure might form in the merged fluid configuration. This transient bar may radiate very strongly for several cycles, producing a distinctive peak in the gravitational-wave energy spectrum.

The peak associated with this bar and the waveform cutoff are two features that one might hope to look for with gravitational-wave measurements — accurate measurement of such features might provide a useful handle that, with information from theoretical calculations, could be used to gain insight into the structure of neutron stars and the processes that occur during merger. Such measurement will require detector technology that improves the sensitivity of instruments to gravitational waves in the vicinity of a kilohertz. It is probably not possible to improve broad-band sensitivity at such frequencies (that is, sensitivity over a frequency bandwidth Δf comparable to the frequency itself), but it should definitely be possible to improve *narrow-band* gravitational-wave sensitivity. Acoustic gravitational-wave detectors and certain interferometer configurations permit gravitational-wave observations at kilohertz frequencies with a fractional bandwidth $\Delta f/f \lesssim 0.01 - 0.05$. A narrow-band instrument with sensitivity at some frequency $f_{\rm NB}$ answers the simple "yes-no" question "Is there significant gravitational-wave power at $f_{\rm NB}$?"

As such, a "xylophone" of narrow-band instruments should be a very useful tool for probing gross, "obvious" features of the merger waveform, such as the sharp cutoff and transient bar peak discussed above. Clearly, one will want to combine narrow-band instruments with broad-band detectors such as LIGO — the broad-band detectors will be able to measure the inspiral waveform and alert the narrow-band detectors that the merger waveform is present in their data.

The question of interest then becomes: What is the optimal detector network for measuring

the merger? Finding an answer to this question is particularly important given that the number of narrow-band detectors in the network will be limited by expense and other practical considerations. (For instance, narrow-banded laser interferometers will have to operate in the same vacuum system as the broad-band instruments. Because of limited space, it won't be possible to have more than a few such interferometers running at each site.) Observers will need to configure their narrow-band detectors in such a way as to get as much information about the merger waveform as possible.

The question may be more usefully phrased as follows. Suppose that the merger waveform depends in some important way upon a parameter λ. For instance, λ might represent the frequency at which there is a sharp cutoff in the waves' spectrum, or the frequency at which a transient bar radiates for several cycles. What, then, is the network that measures λ with as little error as possible?

In Chapter 4, I present an algorithm to be used for designing such an optimal detector network. It works by defining an error measure for λ, and then minimizing that error with respect to all adjustable parameters that describe the network. For example, the central frequency of a dual-recycled laser interferometer is a tunable parameter. Consider a detector network that consists of broad-band LIGO interferometers plus several dual-recycled laser interferometers. (Dual-recycling is one of several methods by which laser interferometers may be made to operate in a narrow-band configuration. Further discussion, as well as references to technical articles about it, is given in Chapter 4.) The algorithm I present would design the optimal detector network by finding the set of central frequencies for the dual-recycled interferometers that minimize the measured error in λ.

Three probability distributions play a crucial role in this algorithm. Two of them have been discussed by Finn [24] and have been used extensively in the gravitational-wave data analysis literature. Denote the binary neutron star gravitational waveform h_λ. Then, the two distributions discussed by Finn are the *prior* distribution, which I shall write $p_0(\lambda)$, and the *posterior* distribution, $P_{\rm post}(\lambda|\hat{\lambda})$. The prior distribution is a function that summarizes all of our prejudices and prior knowledge of λ before measurement is made. For example, if nothing is known about λ except that it must lie between an upper bound $\lambda_{\rm HIGH}$ and a lower bound $\lambda_{\rm LOW}$, then one should choose $p_0(\lambda) = 1/(\lambda_{\rm HIGH} - \lambda_{\rm LOW})$ inside that range, $p_0(\lambda) = 0$ outside it. The posterior distribution summarizes what is known about the distribution of λ after measurement is made. It depends upon the detector network's characteristics, and also upon the measured datastream. Because the datastream contains the *true* gravitational waveform, $h_{\hat{\lambda}}$, the posterior distribution depends implicitly upon the unknown, true value $\hat{\lambda}$ of the parameter λ.

The posterior distribution can be used to calculate the error in one's estimate of λ after measure-

ment is made. This posterior error is given by

$$\sigma^2_{\rm post} = \int (\lambda - \bar{\lambda}_{\rm post})^2 \, P_{\rm post}(\lambda|\hat{\lambda}) \, d\lambda, \tag{1.8}$$

where

$$\bar{\lambda}_{\rm post} = \int \lambda \, P_{\rm post}(\lambda|\hat{\lambda}) \, d\lambda. \tag{1.9}$$

Unfortunately, the posterior error is not a useful quantity to consider for designing a detector network. It describes the error in λ after measurement is made, and — obviously! — one needs to design the detector network before measurement. What is needed is a quantity that describes the error that we *anticipate* in our measurement of λ.

To that end, I introduce one additional probability distribution: the *anticipated* distribution of λ. It is simply given by integrating the implicit $\hat{\lambda}$ dependence out of the posterior distribution, weighting the integral according to our best knowledge of $\hat{\lambda}$'s distribution: $P_{\rm ant}(\lambda) = \int p_0(\hat{\lambda}) \, P_{\rm post}(\lambda|\hat{\lambda}) \, d\hat{\lambda}$. This function describes the distribution of λ that we anticipate we will measure, given our ignorance of the true value $\hat{\lambda}$. Because it is constructed from the posterior distribution, it depends upon the characteristics of the detector network. From it, we can construct an anticipated error:

$$\sigma^2_{\rm ant} = \int (\lambda - \bar{\lambda}_{\rm ant})^2 \, P_{\rm ant}(\lambda) \, d\lambda, \tag{1.10}$$

where

$$\bar{\lambda}_{\rm ant} = \int \lambda \, P_{\rm ant}(\lambda) \, d\lambda. \tag{1.11}$$

The error measure $\sigma^2_{\rm ant}$ is the central quantity in the network design algorithm described in Chapter 4 — the optimal detector network is the network which minimizes $\sigma^2_{\rm ant}$.

Notice that the prior distribution p_0 plays a very important role in designing the detector network: the network is optimal *given our best prior knowledge of λ's distribution.* This provides the algorithm with a natural, Bayesian way to update and improve the network as our understanding of λ improves. Consider the following sequence. Before any binary neutron star mergers are measured, the best prior distribution is likely to be a flat distribution between some extremes $\lambda_{\rm HIGH}$ and $\lambda_{\rm LOW}$, as described above. After a measurement has been made, however, one can construct from the data the posterior distribution for λ. This posterior distribution can then be used as the prior distribution for the next measurement. In other words, the prior distribution for measurement i is the posterior distribution constructed after measurement $i-1$.

In Chapter 4, I test this "Minimal $\sigma^2_{\rm ant}$" algorithm using a simple, idealized detector network, and using two models of the binary neutron star merger waveform. The detector network I use consists of a single broad-band detector with "advanced LIGO interferometer" noise characteristics [25], plus some fixed number $N_{\rm DR}$ of narrow-band dual-recycled laser interferometers. The first waveform model (which I call the "toy" model) is one in which the gravitational waves are sharply cutoff at frequency $f = \lambda \times 1000$ Hz: in the frequency domain, the waveform is given by the Newtonian, quadrupole waveform for $f < \lambda \times 1000$ Hz, and is zero above that frequency. This models the cutoff behavior seen in some numerical models. The second model (which I call the "ZCM" model) uses the numerical waveforms that were produced by the Newtonian, quadrupole-order[4] numerical computations of Zhuge, Centrella, and McMillan [23]. The gravitational-wave energy spectrum dE/df produced by their simulation is shown in Figure 4.12. Of primary interest in this figure are the sharp drop-off in the spectrum near 2500 Hz, followed by a peak at 3200 Hz. The drop-off in the spectrum is produced very soon after the stars come into contact; the peak at 3200 Hz appears to be associated with the formation of a bar-like structure that radiates for several cycles. In this second model, I assume that the gross features seen in the ZCM computations are correct, but that they might lie at different frequencies in the true astrophysical waveform. Let the raw ZCM waveform, in the frequency domain, be $\tilde{h}_{\rm ZCM}(f)$. Then, to encode this proposed waveform model, I write $\tilde{h}_\lambda(f) = \tilde{h}_{\rm ZCM}(\lambda f)$. In other words, features that appear at frequency f in the ZCM waveform appear at f/λ in this model.

In the tests I performed, I imagined that there were repeated binary neutron star events occurring approximately 300 Mpc from earth (for which the inspiral signal-to-noise ratio in advanced LIGO interferometers is 50), and examined how many measurements it took before the probability distribution for λ became strongly peaked. The results of these measurement sequences for the toy model are summarized in Figures 4.8–4.11. It turns out that measurements of the toy model converge rather quickly — depending on the actual value $\hat{\lambda}$ present in the data and on the number of dual-recycled interferometers used, measurements converged to a very peaked probability distribution after 4 to about 15 binary neutron star merger measurements. This is because the toy merger waveform has only one extremely sharp feature: it is easy for narrow-band measurements to pick out this feature. (Recall that in this measurement scheme each narrow-band detector simply indicates whether there

[4]Here, "Newtonian" means that the system's gravitational dynamics are calculated using Newtonian gravity; "quadrupole-order" means that the gravitational-wave generation is calculated using the quadrupole formula (see, for example [29]). The quadrupole formula describes the lowest order radiation-reaction corrections to the motion of gravitating systems.

is significant power at its central frequency. This is clearly sufficient when the waveform has a very sharp cutoff, as the toy model does.) By contrast, measurements of the ZCM waveform do not converge nearly so quickly. It takes roughly 50 measurements before the distribution becomes effectively peaked at all, and even then the degree of peakedness is not as great as it is with the toy model; *cf.* Figures 4.13–4.16. This is because the ZCM waveform has a larger number of features which are close together and not so sharply defined. It is more difficult for narrow-band measurements to distinguish between these multiple features, and so many measurements are needed to be sure the features in the spectrum are indeed being measured correctly.

These tests indicate that the efficacy of binary neutron star merger measurements will depend rather strongly on our prior knowledge of the merger waveform — this prior knowledge will play a crucial role in knowing how to configure detector networks for measuring the binary neutron star inspiral effectively. This provides a strong motivation to encourage (and cajole) the numerical relativity community to produce codes that can accurately model the final merger of binary neutron stars. It is unreasonable to expect that numerical relativity will be able to provide perfectly accurate waveform templates for binary neutron star merger — because neutron star structure and merger interactions are complicated and messy, waveforms that are produced in binary neutron star merger simulations will not be accurate enough to act as data analysis filters. However, numerical relativity should be able to provide robust information about features that are likely to be present in the merger waveform, and how such features behave as the stars' parameters (their spins, their equation of state) are varied. This information will be needed when gravitational-wave astronomy is mature enough that measurement of the binary neutron star merger is possible.

1.5 The stability of neutron star binaries

From the previous section, it is clear that there is strong motivation to accurately model neutron star coalescence. Modeling such coalescence in general relativity is a difficult task, since one needs to properly model both gravitational dynamics in a fully strong field, highly relativistic regime *and* model the hydrodynamics of the dense nuclear fluid that composes neutron stars[5]. These two tasks are not independent, either: the neutron star material acts as a source for the gravitational dynamics, and the gravitational dynamics governs the evolution and dynamics of the neutron star material. A useful approximation scheme would be helpful, especially for the development of the first numerical

[5]Eventually, simulations will have to go beyond purely fluid neutron stars and incorporate factors such as neutron-star crusts and magnetic field interactions.

merger codes.

A potentially useful approximation scheme for evolving the late inspiral of binary neutron stars was introduced in 1995 by Wilson and Mathews [26], and was investigated by Wilson, Mathews, and Marronetti [27] (WMM). The idea behind their scheme is to note that at this stage in its evolution the system is in *quasi-equilibrium*. If gravitational radiation were not causing the system to slowly inspiral, it would be in strict equilibrium. As long as the radiation is "small" then the system will be nearly in equilibrium, and its dynamics driven by non-radiative gravitational fields. The expectation, and one of the key assumptions in Wilson and Mathew's scheme, is that even when the system is very far from equilibrium it is the non-radiative part of the gravitational field that dominates the system's evolution.

In a system that is strictly in equilibrium, one can choose a coordinate system in which the first and second time derivatives of the spacetime metric are zero. In quasi-equilibrium, these derivatives are non-zero, but should be small. One should be able to exploit this smallness through an approximate scheme of solving the Einstein field equations of general relativity.

The Einstein equations can be divided into two classes: *constraint* equations, which contain no time derivatives higher than first order, and *evolution* equations, which contain second time derivatives. The constraint equations are conditions that the gravitational fields must satisfy at any moment, but say nothing about the dynamical evolution — that is, they do not say how to evolve from one moment to another. The evolution equations, by contrast, do specify how to evolve from moment to moment. This split of the Einstein equations into constraint and evolution equations has a parallel in Maxwell's equations: the constraint equations are analogous to $\vec{\nabla}\cdot\vec{E} = 4\pi\rho$, $\vec{\nabla}\cdot\vec{B} = 0$, and the evolution equations are analogous to $\vec{\nabla}\times\vec{B} = 4\pi\vec{J} + \partial\vec{E}/\partial t$, $\vec{\nabla}\times\vec{E} = -\partial\vec{B}/\partial t$.

Wilson and Mathew's approximation is to ignore the evolution equations for the *gravitational* dynamics, evolving only the *fluid* dynamics of their stars. Schematically, the Wilson and Mathews evolution scheme works as follows:

1. Pick an initial neutron star matter configuration.

2. Self-consistently solve the constraint equations and the hydrodynamic fluid equations. This solution represents the quasi-equilibrium solution at some moment of time.

3. Perturb the neutron star matter into a new configuration.

4. Go to 2.

This is an interesting and promising way to make progress in the numerical study of binary neutron star systems. However, the first announcement by WMM of the results of this analysis [27] stunned much of the relativity community: they claim a striking instability as the stars spiral towards one another. They find that the central density of each star gradually *increases*. If the gravitational coupling between the two stars were purely tidal, one would expect that the central density would instead decrease [28]. The WMM density increase must be occurring at an order lower than tidal.

The reason that this result is so shocking is that it has dramatic consequence for the evolution of binary neutron star systems. In particular, if the neutron stars that constitute the binary are close to the maximum mass, so that in isolation they would be marginally stable, WMM's results indicate that they would be destabilized as they spiral in, being "crushed" into black holes. If this is the case, there may be *no* binary neutron star mergers, only binary black hole mergers!

WMM claimed that this effect was caused by a *first-order* enhancement of each star's gravitational potential due to the presence of the companion. Consider a binary system in which star-A has mass M_A and star-B has mass M_B. In isolation, let the gravitational potential of each star be Φ_A and Φ_B respectively. WMM claimed that in the binary system, these potentials are modified in the following manner: $\Phi'_A = \Phi_A(1 + \alpha M_B/R)$, $\Phi'_B = \Phi_B(1 + \alpha M_A/R)$, where R is the distance between the stars and α is of order 1. This potential increase causes the central densities of the stars to be likewise augmented by terms that scale as M/R.

When this result was first announced, there was speculation that it might have been caused by the particular functional choice that WMM make for their spacetime metric. Consider a constant time "slice" of spacetime, and choose spherical-like coordinates r, θ, ϕ on that 3 dimensional slice. The general form of the differential line element on the resulting spatial surface can be written $ds^2 = g_{rr}dr^2 + g_{\theta\theta}d\theta^2 + g_{\phi\phi}d\phi^2$, where in general the functions g_{rr}, $g_{\theta\theta}$ and $g_{\phi\phi}$ have no particular relation to one another[6]. If spacetime is flat — that is, there is no gravitating object or gravitational waves around — the line element is $ds^2_{\rm flat} = dr^2 + r^2(d\theta^2 + \sin^2\theta d\phi^2)$, the familiar Euclidean line element in spherical coordinates. WMM choose a "conformally flat" metric, meaning that the line element is equal to the flat space metric at each point in space, times some function: $ds^2_{\rm CF} = \Psi(r,\theta,\phi)^4\left[dr^2 + r^2(d\theta^2 + \sin^2\theta d\phi^2)\right]$. This approximation reduces the three independent functions g_{rr}, $g_{\theta\theta}$, and $g_{\phi\phi}$ to a single function $\Psi(r,\theta,\phi)$ — a reduction that is known not to be possible in the full theory of general relativity. This greatly reduces the computational complexity of

[6]One might expect there to be off-diagonal terms, $g_{r\theta}drd\theta$, *etc.* In fact, one can perform a gauge transformation (which in general relativity is equivalent to a coordinate transformation) on that slice to eliminates such terms.

the problem, but one might worry that it also so severely and incorrectly constrains the gravitational dynamics that it induces spurious effects, such as WMM's neutron star crusher.

Recall, however, that WMM initially claimed that the crushing effect scaled proportional to M/R. This is exactly the form that one would expect if such a crusher were evident within the first post-Newtonian approximation to general relativity. It turns out that the metric that describes a binary star system in the first post-Newtonian approximation actually *is* conformally flat. A first order crushing effect is therefore *independent* of the assumption of conformal flatness.

The question of interest is then: *Is* there in fact such a first-order crushing effect in general relativity? Chapter 5 presents the approach that Patrick Brady and I took to answering this question. Because the effect is first order in the stars' mass, it should also be evident in a perturbation limit in which star-A has a mass $M_A \equiv M$ appropriate to a neutron star, and star-B is shrunk to a point particle of mass $\mu \ll M$. In this limit, it is possible to solve the combined Einstein-fluid equations *exactly* to first order in μ. If the crushing effect does exist in general relativity, it should be evident in this calculation.

Consider first star-A in isolation. We demand that star-A's fluid configuration be a solution of the Oppenheimer-Volkoff (OV) equations [29], which describe a spherical, non-rotating, gravitating ball of perfect fluid. Solutions to the Oppenheimer-Volkoff equations are uniquely determined by the equation of state $P(\rho)$ (which relates the star's pressure P to its energy density ρ), and by the central energy density ρ_c (or equivalently the central baryon density n_c)[7]. With the equation of state fixed, solutions of the OV equations are effectively a one parameter family of functions: the central density determines all physically relevant quantities of the star — its total mass, its radius, and its internal fluid configuration. Likewise, if one chooses a particular value of the mass or radius, then the internal fluid configuration and central density are fully determined.

Next, place the "star" of mass μ in orbit around star-A. The presence of this star will perturb the background spacetime of star-A and modify its fluid configuration. When one writes out the perturbed Einstein-fluid equations, it very quickly becomes clear that all perturbations can be broken down into a multipole decomposition: any physically relevant quantity ψ may be written $\psi(r,\theta,\phi,t) = \psi^0(r) + \sum_{l,m,\omega} \delta\psi_{l,m,\omega}(r) Y_{lm}(\theta,\phi) e^{i\omega t}$. Here, $\psi^0(r)$ is the value of the quantity when the perturbation is not present, and Y_{lm} is a spherical harmonic. That such a decomposition is possible is not too surprising — the unperturbed star and spacetime are spherically symmetric, so

[7] One must also demand regularity at the origin: the total mass-energy inside a sphere of radius r, $m(r)$, must be 0 at $r = 0$. This is less trivial than one might think — black holes are solutions in which $m(0) \neq 0$.

we are just doing perturbations on a spherical background.

In particular, the density of the star can be expanded in this fashion: $\rho(r,\theta,\phi,t) = \rho^0(r) + \sum_{l,m,\omega}\delta\rho_{l,m,\omega}(r)Y_{lm}(\theta,\phi)e^{i\omega t}$. From this, one can see immediately that $\delta\rho_{l,m,\omega}(0) = 0$ for all multiple orders $l \geq 1$. If this change were nonzero, the star's central density would be multivalued at the origin[8]. Thus, only the spherically symmetric monopole piece of the perturbation can possibly affect the central density at linear order in μ.

A spherically symmetric perturbation can, at most, only move the star from one spherically symmetric solution of the OV equations to another such solution. Is it possible, then, for the perturbation to move the star to a solution of the OV equations in which the central density is larger? The answer is a resounding **no**: as shown in Chapter 5, the perturbation does not change the mass of the star. If one chooses a value of the star's mass, the central density is fully determined. Thus, if the mass does not change, the central density of the star cannot change. *To linear order in μ, there is no neutron star crusher in general relativity.*

Before Brady and I realized that our entire analysis could be done analytically, we numerically experimented with the perturbed Einstein-fluid equations and discovered something interesting: incorrectly setting the boundary conditions on the system's gravitational mass *can* lead to a crushing effect. Consider a quasi-equilibrium sequence parameterized by the radius R of the particle's orbit. As R changes, the total *baryon* mass — the integrated baryon density of the system — must remain constant. There is no way for the orbiting particle to create or destroy baryons in the star. However, the gravitational mass — the mass that one measures with Keplerian orbits — is *not* constant. The gravitational mass of star plus particle decreases because of gravitational radiation. Heuristically, if $E_{\rm rad}$ is the total gravitational-wave energy in the spacetime at a given instant, then the sum $M_A + \mu + E_{\rm rad}$ is constant. We were reminded of this when (rather stupidly) we required as a boundary condition that the sum $M_{\rm star} + \mu$ be constant, and found that the central density ρ_c of star-A increased. Roughly speaking, our erroneous boundary condition took the mass-energy that should have been in gravitational waves and forced it back into the system. This silly error is a stark reminder that failure to satisfy boundary conditions on important quantities such as the system's gravitational mass can cause unphysical effects, such as a neutron star crusher. Because of the simplicity of the OV-star plus perturbation system, it is easy to see where Brady and I went wrong. It

[8] In actual fact, the center of the star cannot be at the coordinate origin, since the orbiting point particle will shift it to some other point in the orbital plane. However, the magnitude of that shift must be of the same order as the perturbation itself. From this, it is simple to convince oneself with a Taylor expansion that any change in the central density from $l \geq 1$ pieces of the perturbation must occur at greater than linear order in μ, which we do not include in this analysis.

is far more difficult in a complicated system consisting of two realistic stars. We speculate that a similar boundary condition error might be the cause of WMM's crushing effect.

At the time that Brady and I performed this calculation, Alan Wiseman performed a similar calculation using the post-Newtonian expansion of general relativity [30]. Wiseman also found that, to first order, there is no crushing effect in general relativity. However, there *can* be such effects in other theories of gravity — in particular, gravity theories that do not respect the strong equivalence principle[9]. The violation of the strong equivalence principle in this instance can be thought of as arising from a modification of the gravitational constant at star-A due to the gravitational potential of star-B: $G_{\rm local} = G_{\rm Newtonian}(1 + \varepsilon\Phi_B)$, where ε is a number whose value happens to be zero in general relativity.

Other work done since the first papers by Brady, myself, and Wiseman indicates that in general relativity such a destabilization is unlikely at any order. In particular Flanagan [32] has shown that there is no coupling between the stars' orbital motion and internal structure at any order lower than tidal squared; and Thorne [33] has shown that such an effect at tidal order squared will be *stabilizing* rather than destabilizing — that is, it *decreases* the central density, rather than increases it. Also compelling is numerical work by Baumgarte *et al.* [34]. This work finds a quasi-equilibrium solution for the late stages of binary neutron star inspiral in a manner than is extremely close to the technique used by WMM. In particular, they also use a conformally flat spatial metric, and ignore the evolution pieces of the Einstein field equations. They, however, find *no* crushing effect; instead, they actually find that the stars are stabilized, exactly as shown in the analytic analysis by Thorne.

Putting this work together seems to indicate that there must be a problem buried somewhere in WMM's code. In their defense, there is one significant way in which their code differs from all other analyses performed to date. This last untested area of parameter space has to do with the motion of fluid inside the neutron stars. The work by Baumgarte *et al.* assumes that the stars are rigidly corotating — that is, the spin periods of the individual stars matches the orbital periods, so that the stars are locked together. Thorne's analysis assumes the spin is rigid, but not necessarily corotating. (The work presented in Chapter 5 and the work by Wiseman ignores spin altogether since any effect it could induce would occur at a higher order than linear in the masses.) Indeed, WMM have since recanted their original claim that the crushing effect occurs at linear order in the masses, and now claim that it is quadratic in the mass[10]. In particular, they claim it is due to a velocity dependent

[9]The strong equivalence principle tells us that any body, even one that generates a gravitational field, follows a trajectory in spacetime independent of its internal structure [31].

[10]This, however, opens another can of worms: a crushing effect that is quadratic in the masses can be ascribed to an

compression force which is absent when the stars are rigidly corotating [36]; indeed, when they impose rigid corotation on their stars [37], their results are in accord with those of Baumgarte *et al.* (Note, though, that WMM have not yet wiggled free of the constraints imposed by Thorne's paper — they have not shown that their effect vanishes under rigid but non-corotating motion.)

Therefore, this rather exciting and dynamic field must still be regarded as in a state of flux. In this author's opinion, it is unlikely that a crushing effect exists in reality: as discussed in footnote 10, we again need to question whether the conformal flatness assumption is valid, and one must wonder if the boundary conditions are being imposed correctly. One very positive aspect of this controversy is that many groups are now interested in numerical modeling of binary neutron star coalescence; with so many people working on the problem now, I am hopeful that significant progress will be made towards a relativistic description of binary neutron star systems.

1.6 Seismic gravity-gradient noise

The final chapter of this thesis is something of a diversion from the previous four chapters. It presents work, done in collaboration with Kip Thorne, of a particular noise source that may have a strong impact on future high-sensitivity ground-based laser interferometers. As the title of this section indicates, this source is *seismic gravity-gradient noise.*

Seismic gravity-gradient noise is present in any detector that is located on the earth's surface. In the ground at any time is a stochastic background of propagating elastodynamic seismic waves. These waves entail a density change, squeezing and stretching the ground as they propagate. This density change causes a stochastically fluctuating gravitational force on the test masses of ground-based interferometers. This force is a source of noise which can mask or mimic an astrophysical gravitational-wave signal.

Gravity gradients were first recognized as a potential noise source for laser interferometers by Rai Weiss in 1972 [38]. Thorough quantitative analyses of gravity gradients were performed in the 1980s by Peter Saulson [39] and Robert Spero [40]. Recently, Saulson updated his 1983 analysis [41], concluding that seismic gravity gradients were likely to constitute the most important source of gravity-gradient noise. Indeed, Saulson noted that his 1983 estimates underestimated seismic gravity-gradient noise because he relied on data taken at underground seismic stations. Motion

effect that should be evident in the *second order* post-Newtonian expansion of general relativity. However, it is known [35] that the spatial metric in the second post-Newtonian expansion is *not* spatially conformally flat! Thus, we are brought back to the question of whether the assumption of spatial conformal flatness is causing the crushing effect.

at the surface is quite a bit larger (by a factor of about 20) due to effects such as human cultural activity, wind blowing against trees and buildings, rain, *etc.* When more reliable ground motion measurements are folded into his 1983 analysis, the resultant gravity-gradient noise appears to be a significant low frequency ($3\,\mathrm{Hz} \lesssim f \lesssim 30\,\mathrm{Hz}$) noise source, sticking above the vibrational seismic noise of advanced LIGO interferometers in the vicinity of 10 Hz [25, 41]. However, the model of the seismic waves that Saulson used in his analysis was rather simplistic — he idealized the motion as due to an incoherent superposition of purely compressional seismic modes. Given the degree to which seismic gravity-gradient noise appears, in this model, to degrade low frequency sensitivity of laser interferometers, a more thorough and careful analysis was clearly warranted.

Thus, we set out to construct a more reliable and sophisticated model of the stochastic seismic background at the LIGO sites than was used by Saulson. The seismic background in the frequency band of greatest concern to us ($3\,\mathrm{Hz} \lesssim f \lesssim 30\,\mathrm{Hz}$) are composed of *surface waves*: waves that are confined to within a few kilometers of the earth's surface. Surface waves fall into two categories: *Love* waves and *Rayleigh* waves.

Love waves are horizontally polarized shear waves ("S-waves") that resonate in near surface geological strata. Because they are purely shear, they entail no density fluctuations as they propagate, and hence do not cause gravity gradients. Rayleigh waves, by contrast, are a mixture of vertically polarized shear waves and compressional, or pressure, waves ("P-waves"). The P-component of Rayleigh waves changes the ground's density as it propagates, and so Rayleigh waves cause gravity gradients. The P- and S-components of Rayleigh waves are coupled to one another by boundary conditions at the surface (the elastodynamic stress of the wave [42] must match the atmosphere at the surface) and at any geological interface (elastodynamic stress must be continuous across the interface, and particle displacement must be likewise continuous). Layered media, such as the ground at both the Hanford, Washington and Livingston, Louisiana LIGO sites can support multiple modes of Rayleigh waves; I will elaborate on this below.

An important constraint on modes that are present at a site is their *anisotropy ratio*, $\mathcal{A} \equiv \tilde{Z}(f)/\tilde{X}(f)$ (that is, the ratio of their vertical ground motion to their horizontal ground motion). Because Love waves entail purely horizontal motions, $\mathcal{A}_{\mathrm{Love}} = 0$. Rayleigh waves, by contrast, typically entail a moderately large amount of vertical motion. The anisotropy ratio for the various Rayleigh modes can differ by quite a bit; but, for example, the so-called "fundamental" Rayleigh mode RF has $\mathcal{A}_{\mathrm{RF}} \simeq 2$. All of the various modes that are present must add in a way such that their combined anisotropy ratio is consistent with the anisotropy ratio that is actually observed.

We embody the results of our analysis in a transfer function $T(f)$ that takes the ground motion spectrum $\tilde{W}(f)$ (rms averaged over all horizontal and vertical directions) to a spectrum of test-mass motion $\tilde{x}(f)$: $\tilde{x}(f) = T(f)\tilde{W}(f)$. Further, we express $T(f)$ in terms of a dimensionless correction $\beta(f)$ to a formula originally derived by Saulson [[39], his Eq. (12)] for the transfer function:

$$T(f) = \frac{4\pi G\rho}{\sqrt{(\omega^2 - \omega_0^2)^2 + \omega^2/\tau^2}}\,\beta(f) \simeq \frac{4\pi G\rho}{(2\pi f)^2}\,\beta(f). \tag{1.12}$$

(Here, $\omega_0 \simeq 1\,\mathrm{rad/sec}$ and $\tau \simeq 10^7\,\mathrm{sec}$ are the resonant frequency and damping times, respectively, of the test masses' pendular suspensions.) We call $\beta(f)$ the *reduced* transfer function, and shall present all of our gravity-gradient results in terms of it. As a point of comparison, Saulson's calculation predicts $\beta = 1/\sqrt{3} \simeq 0.58$.

As mentioned above, layered sites can support multiple Rayleigh modes. They are distinguished by (among other characteristics) their dispersion relation $c_H(f)$ (*i.e.*, the horizontal phase speed as a function of frequency). The mode with the lowest phase speed at all frequencies is the fundamental Rayleigh mode, RF. This mode exists even at sites that are not layered (indeed, it is the only Rayleigh mode that can exist in a perfectly uniform layer). The fundamental mode is usually evanescent in all layers: the amplitudes of its S- and P-wave components decay with increasing depth z as e^{-skz} and e^{-qkz} respectively (where $s \sim 0.3$, $q \sim 0.9$ have a well-understood form discussed in Chapter 6). The horizontal phase speeds of higher order modes are rather faster; these modes are typically not evanescent in several of the layers[11]. Some of these modes consist predominantly of S-waves, and we denote them RSn (where n is the number of nodal points one encounters in these modes as one traverses the vertical axis). Likewise, other modes consist predominantly of P-waves, and are denoted RPn.

For simplicity, consider for a moment the fundamental Rayleigh mode alone. The anisotropy ratio one obtains for this mode is roughly 2. Measurements show [43] that, at quiet times, the anisotropy ratios actually present at the two LIGO sites in the frequency band $3\,\mathrm{Hz} \lesssim f \lesssim 30\,\mathrm{Hz}$ are rather lower than this ($\mathcal{A}_{\mathrm{Hanford}} \simeq 1.0$, $\mathcal{A}_{\mathrm{Livingston}} \simeq 0.6$), so the fundamental Rayleigh mode alone cannot be responsible for all seismic motions at the sites. Consider, then, mixing Love waves in with the RF mode. Recall that the anisotropy ratio for Love waves is exactly zero, since Love waves entail only horizontal motions. By adjusting the amount of Love waves present, relative to

[11] Although the modes *must* be evanescent in the lowest layer, else the amplitude would not go to zero as $z \to \infty$, and their energy content would be infinite.

the RF mode, we can rather easily bring the anisotropy ratio of the entire Love + RF mixture down to the levels that are observed at the two LIGO sites.

Unfortunately, it is not clear from the LIGO-site data currently available to us whether the ambient seismic motions are, indeed, predominantly RF and Love waves. However, a moderately extensive review of seismic measurements made at other sites [44] indicates that such a Love + RF mixture is likely, rather generically, to describe surface motion at quiet times. We therefore conclude that, at quiet times when there are no unusually noisy or violent seismic motions at the LIGO sites, the *most likely* form of the stochastic seismic background is the fundamental Rayleigh mode, plus enough Love waves to bring the anisotropy ratio down to the levels observed at the two sites. We suggest, in the conclusion of Chapter 6 measurements that can — and should — be performed to test the robustness of this conclusion and to determine more accurately the true seismic wave mixture. At any rate, when we examine mixtures that are consistent with the anisotropy ratios that are measured at the two sites, we find that the reduced transfer function lies in the following range:

$$\begin{aligned} \beta_{\text{net, quiet times}} &\simeq 0.35 - 0.45 \text{ at Livingston} \\ &\simeq 0.35 - 0.6 \text{ at Hanford.} \end{aligned} \tag{1.13}$$

In Figure 6.2 (dark gray band) we present the seismic gravity-gradient noise this transfer function implies when it is folded into a seismic noise spectrum appropriate for the LIGO sites, at quiet times (the "standard LIGO seismic spectrum"), compared to the projected noise spectrum for advanced LIGO interferometers. This noise is agrees rather well with the noise given by Saulson [41]. It is everywhere lower than advanced LIGO noise, but not by a large amount — and, it is just barely smaller in the vicinity of 10 Hz.

At noisier times, it does not appear to be appropriate to treat the seismic background as RF + Love. During these times, measurements indicate [45] that there is probably a mixture of higher order Rayleigh modes present, both RS and RP. The RP modes in particular are "dangerous," in that they consist to a large extent of P-waves and thus create copious gravity gradients. The most pessimistic estimates we can obtain are given by considering a mixture of Love waves, RF waves, and some number of RPn modes, and requiring that the mixture be consistent with the observed anisotropies (which, as mentioned in note [45], tended to fluctuate rather wildly from about 0.2 to 5 at the noisiest times). The reduced transfer function we obtain in these pessimistic cases allows us

to set what we believe is an upper limit on the reduced transfer function at the LIGO sites:

$$\beta_{\text{net, noisy times}} \lesssim 1.4 \ . \tag{1.14}$$

This is about twice as large as Saulson's value, and sticks up quite strongly into the advanced LIGO curve. The region delineated by this upper limit is shown in Figure 6.2 as the light gray band.

Because seismic gravity gradients, by definition, couple gravitationally to the test masses of LIGO-type interferometers, it is unlikely that there will ever exist effective means of isolating the interferometers from them[12]. (In reference to this, Saulson [41] calls gravity gradients a "Short Circuit Around Vibrational Isolation.") If this is indeed the case, then the most important aspect of seismic gravity gradients will be to set limits on the frequency to which experimenters should strive to achieve effective seismic isolation. Consider again Figure 6.2. In that plot, the advanced LIGO noise curve is shown with seismic isolation at 10 Hz. Imagine now moving the line to lower and lower frequencies. As this is done, one simply picks up more and more of the light gray region. In other words, improved seismic isolation — achieved through painstaking experimental effort — only allows us to observe the local seismic activity via gravitational coupling! It is not worth the effort or expense to greatly improve seismic isolation in this case. Although the analysis Thorne and I present should be revisited when improved measurements of the seismic background at the LIGO sites gives us a more detailed understanding of the local seismic background, it seems likely that it simply is not worthwhile to improve vibrational isolation below about 5 Hz. This may strongly impact future R&D for ground-based interferometric gravitational-wave detectors.

[12]It may be possible to exclude some fraction of seismic modes from the vicinity of the test masses by digging deep ($z \simeq 5$ m) "moats" around the test masses. These moats would simply prevent RF modes from propagating near the interferometers' corner and end stations. However, they would not be effective in preventing modes that penetrate deeper than 5 m (as the RS and RP modes do); and, they may even make the noise *worse* by acting as a resonant chamber. It may also be possible to remove seismic gravity-gradient noise "in software": if observers can measure, using a three-dimensional network of seismic instruments, the seismic background to good accuracy, they could then calculate the gravity gradient noise being produced and remove it from the data stream. If gravity gradients turn out to be a serious noise source in the future, seemingly suggestions such as these will have to be carefully investigated.

Bibliography

[1] Information regarding the early plan of operation for LIGO is available at the URL

http://www.ligo.caltech.edu/LIGO_web/Collaboration/collab3.html

[2] J. W. York, statement made during the open discussion period on directions in gravitation theory (chaired by J. B. Hartle) at the 14th Pacific Coast Gravity Meeting, University of Oregon, Eugene, Oregon, 21 March 1998.

[3] K. S. Thorne, in *300 years of Gravitation*, edited by S. W. Hawking and W. Israel (Cambridge University Press, Cambridge, England, 1987), pp. 330–458.

[4] D. Kennefick, unpublished Ph.D thesis, California Institute of Technology, 1996; particularly *Part II: Controversies in the History of the Radiation Reaction Problem in General Relativity*.

[5] In actual fact, the post-Newtonian expansion becomes unsuitable to describe the inspiral several orbits (~ 10, or ~ 100 radians of gravitational-wave phase) before an adiabatic description of the system breaks down. Numerical methods which exploit the adiabaticity of this regime are currently being developed at Caltech and the University of Utah.

[6] Some rather remarkable theorems by Carter and Robinson establish that the Kerr solution is the only possible stationary, axisymmetric black hole. The results of Price indicate that all "hair" other than mass and angular momentum is carried off by radiation during gravitational collapse. These results indicate that the generic endpoint of any collapse that forms a black hole is the Kerr solution. The relevant references are: B. Carter, Phys. Rev. Lett. **26**, 331 (1971); D. C. Robinson, Phys. Rev. Lett. **34**, 905 (1975); R. H. Price, Phys. Rev. D **5**, 2419 (1972); R. H. Price, Phys. Rev. D **5**, 2439 (1972). The work by Carter and Robinson generalizes earlier work by Israel, which demonstrated that the Schwarzschild solution was the only zero-angular momentum black hole solution: W. Israel, Phys. Rev. **164**, 1776 (1967). (Note that I am ignoring here the possibility of charged black holes, which are not astrophysically relevant.)

[7] L. S. Finn, private communication.

[8] "Spanning the parameter space" in this instance means that the templates cover the expected range of parameters densely enough that discretization of the (nominally continuous) function space does not induce a significant loss of signal-to-noise ratio in measurement. For further discussion, see B. J. Owen, Phys. Rev. D **53**, 6749 (1996).

[9] S. Sigurdsson and L. Hernquist, Nature (London) **364**, 423 (1993).

[10] T. Prince and D. Bass, private communication.

[11] A. V. Tutukov and L. R. Yungelson, Mon. Not. R. Astron. Soc. **260**, 675 (1993); V. M Lipunov, K. A. Postnov, and M. E. Prokhorov, New Astron. **2** (1997); V. M. Lipunov, K. A. Postnov, and M. E. Prokhorov, Astron. Lett. **24**, 492 (1997).

[12] S. F. P. Zwart and L. R. Yungelson, "Formation and evolution of binary neutron stars", Astron. Astrophys. (to be published); also astro-ph/9710347.

[13] N. Roos, J. S. Kaastra, and C. A. Hummel, Astrophys. J. **409**, 130 (1993).

[14] A. Sillanpaa *et al.*, Astrophys. J. **325**, 628 (1988).

[15] C. M. Gaskell, Astrophys. J. **464**, L107 (1996); in *Jets from Stars and Galaxies*, edited by W. Kundt (Springer, Berlin, 1996), pp. 165–196.

[16] A. C. Fabian *et al*, Mon. Not. R. Astron. Soc., in press; astro-ph/9803075.

[17] G. D. Quinlan and S. L. Shapiro, Astrophys. J. **343**, 725 (1989) (especially Fig. 12); **356**, 483 (1990).

[18] E. W. Leaver, Proc. R. Soc. London **A402**, 285 (1985).

[19] F. Echeverria, Phys. Rev. D **40**, 3194 (1989).

[20] G. B. Cook, Phys. Rev. D **50**, 5025 (1994). See in particular Fig. 3.

[21] É. É. Flanagan, in preparation.

[22] W. Anderson *et al*, in preparation.

[23] X. Zhuge, J. M. Centrella, and S. L. W. McMillan, Phys. Rev. D **50**, 6247 (1994).

[24] L. S. Finn, Phys. Rev. D **46**, 5236 (1992).

[25] A. Abramovici *et al.*, Science **256**, 325 (1992).

[26] J. R. Wilson and G. J. Mathews, Phys. Rev. Lett. **75**, 4161 (1995).

[27] J. R. Wilson, G. J. Mathews, and P. Marronetti, Phys. Rev. D **54**, 1317 (1996); G. J. Mathews and J. R. Wilson, Astrophys. J **482**, 929 (1997).

[28] D. Lai, Phys. Rev. Lett. **76**, 4878 (1996).

[29] C. W. Misner, K. S. Thorne, and J. A. Wheeler, *Gravitation* (Freeman, New York, 1973).

[30] A. G. Wiseman, Phys. Rev. Lett. **79**, 1189 (1997).

[31] C. M. Will, *Theory and Experiment in Gravitational Physics* (Cambridge University Press, Cambridge, England, 1981).

[32] É. É. Flanagan, "Gravitational coupling between orbital motion and internal degrees of freedom for inspiraling binary neutron stars", submitted to Phys. Rev. D; gr-qc/9706045.

[33] K. S. Thorne, "Tidal Stabilization of Rigidly Rotating, Fully Relativistic Neutron Stars", Phys. Rev. D, in press; gr-qc/9706057.

[34] T. W. Baumgarte *et al.*, Phys. Rev. Lett. **79**, 1182 (1997).

[35] C. M. Will and A. G. Wiseman, Phys. Rev. D **54**, 4813 (1996).

[36] G. J. Mathews, P. Marronetti and J. R. Wilson, "Relativistic hydrodynamics in close binary systems: analysis of neutron-star collapse", unpublished preprint; G. J. Mathews, private communication.

[37] P. Marronetti, G. J. Mathews, and J. R. Wilson, "Binary Neutron-Star Systems: From the Newtonian Regime to the Last Stable Orbit", gr-qc/9803093.

[38] R. Weiss, "Quarterly Progress Report of the Research Laboratory of the Massachusetts Institute of Technology," Volume 105, p. 54 (1972).

[39] P. R. Saulson, Phys. Rev. D **30**, 732 (1983).

[40] R. Spero, in *Science Underground*, Proceedings of the Los Alamos Conference, 1982, edited by M. M. Nieto *et al.* (AIP, New York, 1983).

[41] P. R. Saulson, *Fundamentals of Interferometric Gravitational Wave Detectors* (World Scientific, Singapore, 1994).

[42] L. D. Landau and E. M. Lifschitz, *Theory of Elasticity* (Pergamon Press, Oxford, 1986), Chapter 24.

[43] These numbers are based on extensive calculations of the anisotropy ratios that the present author performed using data obtained by Alan Rohay of the Pacific Northwest National Laboratory. Rohay's data are presented in two LIGO reports: A. Rohay, "Ambient Ground Vibration Measurements at the Livingston, Louisiana LIGO Site", LIGO Document LIGO–C961022–A–O1; A. Rohay, "Ambient Ground Vibration Measurements at the Hanford, Washington LIGO Site", LIGO Document LIGO–C950572–02–O1.

[44] M. W. Asten, Bull. Seis. Soc. Am. **68**, 1623 (1978); A. C. Liaw and T. V. McEvilly, Geophys. **44**, 1097 (1979); E. J. Douze and S. J. Laster, Geophys. **44**, 1570 (1979); S. E. Hough *et al.*, Bull. Seis. Soc. Am. **82**, 1186 (1992); C. A. Powell, Bull. Seis. Soc. Am. **82**, 1889 (1992); G. Milana *et al.*, Bull. Seis. Soc. Am. **86**, 320 (1996).

[45] In a private communication, Alan Rohay, who carried out the LIGO ambient seismic surveys at both sites, noted that he observed modes that traveled with P-wave velocities; however, these modes were at frequencies far lower than those that are of concern to us ($f \simeq 1/8$ Hz). They are indicative, however, of the fact that RP modes are present at the sites. In addition, Rohay's data (cited in [43]) for noisy times demonstrate anisotropy ratios that fluctuate from about 0.2 to 5, indicating that a large number of RP and RS modes might be present.

Chapter 2

Measuring gravitational waves from binary black hole coalescences: I. Signal to noise for inspiral, merger, and ringdown

Coauthored with Éanna É. Flanagan; published in *Physical Review D* [Phys. Rev. D **57**, 4535 (1998)].

Abstract

We estimate the expected signal-to-noise ratios (SNRs) from the three phases (inspiral, merger, and ringdown) of coalescing binary black holes (BBHs) for initial and advanced ground-based interferometers (LIGO/VIRGO), and for the space-based interferometer LISA. Ground-based interferometers can do moderate SNR (a few tens), moderate accuracy studies of BBH coalescences in the mass range of a few to about 2000 solar masses; LISA can do high SNR (of order 10000) high accuracy studies in the mass range of about 10^5 to 10^8 solar masses. BBHs might well be the first sources detected by LIGO/VIRGO: they are visible to much larger distances — up to 500 Mpc by initial interferometers — than coalescing neutron star binaries (heretofore regarded as the "bread and butter" workhorse source for LIGO/VIRGO, visible to about 30 Mpc by initial interferometers). Low-mass BBHs (up to 50 $M_\odot$ for initial LIGO interferometers; 100 $M_\odot$ for advanced; 10^6 $M_\odot$ for LISA) are best searched for via their well-understood inspiral waves; higher mass BBHs must be searched for via their poorly understood merger waves and/or their well-understood ringdown waves. A matched filtering search for massive BBHs based on ringdown waves should be capable of finding BBHs in the mass range of about 100 $M_\odot$ to 700 $M_\odot$ out to about 200 Mpc for initial LIGO interferometers, and in the mass range of roughly 200 $M_\odot$ to 3000 $M_\odot$ out to about $z \sim 1$ for advanced interferometers. The required number of templates is of order 6000 or less. Searches based on merger waves could increase the number of detected massive BBHs by a factor of order 10 over those found from inspiral and ringdown waves, without detailed knowledge of the waveform shapes, using a noise monitoring search algorithm which we describe. A full set of merger templates from numerical relativity simulations could further increase the number of detected BBHs by an additional factor of roughly 4.

2.1 Introduction and Summary

2.1.1 Coalescences of black hole binaries

It has long been recognized that coalescences of binary black hole (BBH) systems could be an important source of gravitational waves [1, 2], both for the ground based interferometric detectors LIGO [3] and VIRGO [4] currently under construction, and also for the possible future space-based interferometer LISA [5, 6, 7]. The orbits of BBHs gradually decay from energy and angular momentum loss to gravitational radiation. Eventually, they merge to form a single black hole.

The process of coalescence can be divided into three more or less distinct phases:

- An adiabatic *inspiral*, during which the gravitational radiation reaction timescale is much longer than the orbital period. The inspiral ends when the binary orbit becomes relativistically dynamically unstable at an orbital separation of $r \sim 6M$ (in units where $G = c = 1$) [8, 9]. The gravitational waves from the inspiral carry encoded within them the masses and spins of the two black holes, some of the binary's orbital elements, and the distance to the binary [1, 10].
- Towards the end of inspiral, the black holes encounter a dynamical instability and make a gradual transition from a radiation-reaction driven inspiral to a freely-falling plunge [8, 11, 12]. After the plunge, the black holes would still merge even if radiation reaction could be turned off. We will call the subsequent plunge and violent collision the *merger* phase. Gravitational waves from the merger could be rich with information about the dynamics of relativistic gravity in a highly nonlinear, highly dynamic regime which is poorly understood today.
- As the system settles down to a stationary Kerr state, the nonlinear dynamics of the merger gradually become more and more describable as oscillations of the final black hole's quasinormal modes [13, 14]. The corresponding gravitational waves consist of a superposition of exponentially damped sinusoids. We will call the phase of the coalescence for which the gravitational waves are dominated by the strongest $l = m = 2$ quasinormal mode the *ringdown*. The ringdown waves carry information about the mass and spin of the final black hole [15, 16]. (For want of a better terminology, we will always use *coalescence* to refer to the entire process of inspiral, merger and ringdown, and reserve the word merger for the phase intermediate between inspiral and ringdown.)

In this chapter, we focus primarily on BBHs in which the masses of the two black holes are

approximately the same, although we do also consider sources with one black hole much smaller than the other. We consider three different classes of BBHs:

(i) *Solar mass* black hole binaries: these are binaries that are formed either from massive main-sequence progenitor binary stellar systems (field binaries) or from capture processes in globular clusters or Galactic centers (capture binaries). Field binaries are expected to have total masses in the range $10M_\odot \lesssim M \lesssim 50M_\odot$, but not much larger than this, while capture binaries could have somewhat larger masses [17]. The event rate of solar-mass BBH coalescences is not well known. For globular cluster capture binaries, Sigurdsson and Hernquist argue that generically at least one BBH coalescence should occur per core-collapsed globular cluster [18], yielding $\sim 3\,\mathrm{yr}^{-1}$ in a distance of 600 Mpc using the extrapolation method of Sec. 3.1 of Ref. [19]. This rate is one or two orders of magnitude smaller than the expected event rate for what has traditionally been regarded as the most promising source for ground based interferometers, coalescences of neutron star—neutron star (NS-NS) binaries [3, 10] (about $10^{-5}\,\mathrm{yr}^{-1}$ in our Galaxy, or several per year in a distance of 200 Mpc [20, 19, 21, 22, 23]). However, BBH systems can be seen to much greater distances than NS-NS systems, so it is possible that BBH coalescences will be seen before NS-NS coalescences. For field binaries, estimates of the coalescence rate by experts in binary evolution theory range from $\sim 10^{-8}\,\mathrm{yr}^{-1}$ to $\sim 10^{-6}\,\mathrm{yr}^{-1}$ in our Galaxy [22, 24], to completely negligible [25]. There are large uncertainties associated with these theoretical estimates of the coalescence rates [26].

(ii) *Intermediate mass* black hole binaries: these are binaries with total masses in the range $50M_\odot \lesssim M \lesssim (\text{a few}) \times 10^3 M_\odot$. In contrast to the cases of solar mass black holes and supermassive black holes (discussed below), there is little direct observational evidence for the existence of black holes in this mass range [27]. Despite the lack of evidence, it is plausible that black holes in this mass range are formed in the cores of globular clusters, or in galactic nuclei in the process of formation of a supermassive black hole [30]. Simulations by Quinlan and Shapiro suggest that black holes with $M \sim 100M_\odot - 1000M_\odot$ could be formed in the evolution of dense stellar clusters of main sequence stars in galactic nuclei [17], and that coalescences of binaries of such black holes could be possible en route to the formation of a supermassive black hole. Even if the coalescence rate of intermediate mass BBHs is only 10^{-4} that of NS-NS binaries, they are visible to such great distances that they would still be seen more often than NS-NS binaries by initial and advanced LIGO interferometers, and thus could be the first detected type of source. (See Sec. 2.1.5 for further details.)

(iii) *Supermassive* black hole binaries: there is a variety of strong circumstantial evidence that

supermassive black holes (SMBHs) in the mass range $10^6 M_\odot - 10^9 M_\odot$ are present in quasars and active galactic nuclei, and that a large fraction of nearby massive spiral and elliptical galaxies harbor quiescent SMBHs [7, 31, 30]. One of the main goals of the LISA project is to detect and monitor various processes involving SMBHs, such as the capture of compact stars [2, 7, 10, 32, 33], and their formation [2, 7]. In particular, the coalescences of SMBH binaries that are formed in galaxy mergers, in which the individual SMBHs are driven together by dynamical friction and gas accretion until gravitational radiation reaction takes over [34], have often been suggested as a promising source for space-based interferometers [1, 2, 7, 10, 35, 36]. Such coalescences would be detectable throughout the observable universe with large signal to noise ratios [7, 10]. There is some observational evidence for SMBH binaries: wiggles in the radio jet of QSO 1928+738 have been attributed to the orbital motion of a SMBH binary [37], as have time variations in quasar luminosities [38] and in emission line redshifts [39]. The overall event rate is uncertain, but could be large ($\gtrsim 1/\mathrm{yr}$), especially if the hierarchical scenario for structure formation is correct [36].

2.1.2 Status of theoretical calculations of the gravitational-wave signal

Detailed theoretical understanding and predictions of the gravitational waveforms $h_+(t)$ and $h_\times(t)$ produced in BBH coalescences will facilitate both the detection of the gravitational-wave signal, and the extraction of its information. In situations where a complete family of theoretical template waveforms is available, it will be possible to use Wiener optimal filtering ("matched filtering") to search the interferometer data streams and to detect the signal [1, 40]. The resulting signal-to-noise ratios (SNRs) can be larger than those obtainable without theoretical templates by a substantial factor; see Sec. 2.2. Thus, while it is possible to detect the various phases of BBH coalescences without theoretical templates, such templates can greatly increase the effective range of the interferometers and the event detection rate. Such theoretical template waveforms are available for the inspiral and ringdown phases of the coalescence, but not yet for the merger phase, as we now discuss.

For the inspiral, the gravitational waves and orbital evolution can be described reasonably well using the post-Newtonian approximation to general relativity. To date, inspiral waveforms have been calculated to post-2.5-Newtonian order [41], and the prospects look good for obtaining waveforms up to post-3.5-Newtonian order [42, 43]. Post-Newtonian templates will be fairly accurate over most of the inspiral, the most important error being a cumulative phase lag [44, 45]. This cumulative phase lag will not be important for searches for inspiral waves; template phasing error will be largely compensated for by systematic errors in best-fit values of the binary's parameters, and the signals

will still be found [44, 46, 47, 48]. By contrast, template inaccuracies will be significant when one attempts to extract from the data the binary's parameters. In particular, post-Newtonian templates' errors start to become very significant around an orbital separation of $r \sim 12M$ [49], well before the end of the inspiral at the dynamical orbital instability ($r \sim 6M$). Templates for the phase of the inspiral between roughly $12M$ and $6M$ will most likely have to be calculated using methods other than the post-Newtonian approximation. The methods of full blown numerical relativity cannot be applied to this "Intermediate Binary Black Hole" (IBBH) phase, since the total time taken to evolve from $12M$ to $6M$ is about $1500M$, too long for supercomputer simulations to evolve. Analytical and numerical methods for calculating IBBH waveforms based on the adiabatic approximation are under development [50]; it is likely they will be successfully implemented before gravitational-wave interferometers begin measurements [51].

Waveforms from the dynamic, complicated merger can only be obtained from numerical relativity. Unlike mergers of neutron star binaries, BBH mergers are particularly clean in the sense that there is no microphysics or hydrodynamics to complicate simulations of the evolution, and external perturbations are negligible: the entire merger can be described as a solution to the vacuum Einstein equation [53]. Finding that solution is not a particularly easy task: a major computational effort to evolve the vacuum Einstein equation for BBH mergers using massive computational resources is currently underway, funded by the National Science Foundation's Grand Challenge program [54, 55].

The ringdown phase of the coalescence can be accurately described using perturbation theory on the Kerr spacetime background [56]. The gravitational waveforms from this phase are well understood, being just exponentially damped sinusoids. Thus, matched filtering is feasible for searches for ringdown waves.

2.1.3 Purpose of this chapter

The principal purpose of this chapter is to estimate, in more detail than has been done previously, the prospects for measuring gravitational waves from the three different phases of coalescence events, for various different detectors, and for a wide range of BBH masses. We estimate in each case the distances to which the different types of source can be seen by calculating expected SNRs. In particular, we determine for each BBH mass and each detector whether a coalescence event is most effectively detected by searching for the inspiral, or the merger, or the ringdown. We also determine how much the availability of theoretical templates for the merger could increase the event

detection rate. Previous estimates of SNRs for ground-based interferometers have focused on the inspiral [1, 44] and ringdown [15, 16], and also focused on solar-mass BBHs. For space-based interferometers, previous estimates of SNRs from the merger [7, 10] were restricted to specific masses and did not consider the ringdown.

In the following chapter, we discuss in detail the useful information carried by the three phases of the gravitational-wave signal, and methods and prospects for extracting this information both with and without templates for the merger phase [57].

2.1.4 Estimating the signal-to-noise ratios: method and assumptions

We calculate SNRs for three different types of interferometer: initial and advanced ground-based interferometers (LIGO/VIRGO), and the proposed space-based interferometer LISA. The noise spectra of the initial and advanced ground-based interferometers we took from Ref. [3], and that for LISA from Ref. [7]. Our approximate versions of these noise spectra are given in Eqs. (2.74)–(2.77), and are illustrated in Figs. 2.1–2.3 in Sec. 2.5.1.

We consider the following three different signal-detection methods:

(i) *Matched filtering searches:* For those phases of the coalescence for which a complete set of theoretical templates will be available (the inspiral, the ringdown, and possibly the merger), matched filtering can be used to search for the waves [1, 40, 58, 59, 60]. For any source of waves, the SNR ρ obtained from matched filtering is related to the gravitational waveform $h(t)$ measured by the interferometer and to the spectral density $S_h(f)$ of the strain noise in the interferometer via [61]

$$\rho^2 = 4\int_0^\infty \frac{|\tilde{h}(f)|^2}{S_h(f)} df, \tag{2.1}$$

where $\tilde{h}(f)$ is the Fourier transform of $h(t)$ defined by Eq. (2.9). The SNR (2.1) depends, through the waveform $h(t)$, on the orientation and position of the source relative to the interferometer. In Sec. 2.2.3 we show that if we perform an rms average over source orientations and positions (at a fixed distance), the rms SNR thus obtained depends only on the energy spectrum dE/df of the emitted gravitational waves. The resulting relationship between the waves' energy spectrum and the rms angle-averaged SNR forms the basis for most of our calculations. It is given by [*cf.* Eq. (2.36)]

$$\langle \rho^2 \rangle = \frac{2(1+z)^2}{5\pi^2 D(z)^2} \int_0^\infty df \, \frac{1}{f^2 S_h(f)} \frac{dE}{df}[(1+z)f], \tag{2.2}$$

where z is the source's cosmological redshift and $D(z)$ its luminosity distance. In order for a signal to be detected, the waves' measured SNR must be larger than a certain threshold which we discuss in Sec. 2.2.3 [*cf.* Eq. (2.15]].

(ii) *Band-pass filtering searches:* For the merger phase, a complete set of theoretical templates may not be available, and so methods other than matched filtering will need to be used. Band-pass filtering, followed by setting a detection threshold in the time domain, is a simple method of searching an interferometer data stream for bursts of unknown form [40]. In Sec. 2.2.1 we derive an approximate relation between the SNR obtainable from band-pass filtering, and the SNR (2.1) obtainable from matched filtering, for any burst of waves:

$$\left(\frac{S}{N}\right)_{\rm band-pass} \approx \frac{1}{\sqrt{2T\Delta f}} \left(\frac{S}{N}\right)_{\rm matched}. \tag{2.3}$$

Here T is the duration of the burst and Δf is the bandwidth of the band-pass filter [*cf.* Eq. (2.21)]. The quantity $2T\Delta f$ is the dimension of the linear space of signals being searched for, and is roughly the same as the "number of cycles" of the gravitational waveform. In Sec. 2.6.2, we use the formula (2.3) to estimate the SNRs from band-pass filter searches for merger waves, by inserting on the right hand side the rms angle-averaged matched-filter SNR (2.2), and by making estimates of T and Δf.

(iii) *Noise-monitoring, nonlinear filtering searches:* The traditional view has been that the SNR (2.3) is about the best that can be achieved in the absence of templates, that is, that the gain in SNR obtainable from matched filtering is approximately the square root of the number of cycles in the gravitational wave signal [Eq. (2.21) below]. This view is based on the assumption that the search method used in the absence of templates is band-pass filtering or something very similar. However, we suggest in Sec. 2.2.2 an alternative search method, motivated by Bayesian analyses and incorporating nonlinear filtering, which performs much better than band-pass filtering and in some cases almost as well as matched filtering. In essence, one monitors the noise level in the data stream in a certain frequency band, over short timescales, and looks for statistically significant changes. The noise level is estimated by calculating the quantity

$$\frac{1}{T}\int_{-T/2}^{T/2} d\tau\, s(t+\tau)^2, \tag{2.4}$$

where T is the maximum expected duration of the signal, and $s(t)$ is a suitably pre-filtered version of the data stream.

The efficiency of this noise-monitoring search method cannot usefully be described in terms of an SNR, since the detection statistic is non-Gaussian. Instead, its efficiency can be described in the following way. Let ρ denote the SNR that would be obtained if matched filtering were possible [Eq. (2.1)]. We use ρ as a convenient parameterization of the signal strength; as such, it is meaningful even in situations where matched filtering cannot be carried out. A signal will be detected with high confidence using the noise-monitoring technique whenever ρ is larger than a threshold ρ_* given by Eq. (2.35) below. In practice, ρ_* is slightly larger than the threshold for matched filtering but not greatly larger.

The relation (2.2) forms the basis of our SNR calculations. We use the thresholds (2.15) and (2.35) to deduce from the SNR values the detectability of the various parts of the gravitational wave signal. To calculate the SNRs, we also need to specify the waves' energy spectra for the three different phases of the coalescence. As we now outline, the waves' energy spectrum is essentially known for the inspiral and ringdown phases, and we make an educated guess for the merger. Sec. 2.3 gives more details.

Inspiral energy spectrum: We use the leading order expression for dE/df obtained using Newtonian gravity supplemented by the quadrupole formula [62] [Eq. (2.61)]. Strictly speaking, this spectrum describes the SNR that would be achieved by searching for Newtonian, quadrupole waves using Newtonian, quadrupole templates. The actual SNR obtained when searching for a real, general-relativistic inspiral using post-Newtonian templates should deviate from this by only a few tens of percent [63]. We terminate the spectrum at the frequency $f_{\rm merge} = 0.02/M$ which is (roughly) the frequency of quadrupole waves emitted at the orbital dynamical instability at $r \sim 6M$ [8]. For LISA, we assume that the measurement process lasts at most one year, and choose the frequency at which the spectrum starts accordingly.

Ringdown energy spectrum: The spectrum that we use [Eq. (2.65)] is determined, up to its overall amplitude, by the properties of the $l = m = 2$ quasi-normal ringing (QNR) mode of the final Kerr black hole. This mode is the most slowly damped of all QNR modes, so we expect it to dominate the last stages of gravitational-wave emission. The QNR spectrum depends on three parameters: the modes' frequency $f_{\rm qnr}$, damping time τ, and initial amplitude of excitation, which in turn depend on the mass M and dimensionless spin parameter a of the final black hole, and on the total energy radiated in the ringdown. The spectrum is peaked at $f = f_{\rm qnr}$ with width $\Delta f \sim 1/\tau$.

We (somewhat arbitrarily) assume $a = 0.98$. It seems likely that in many coalescences the spin

of the final black hole will be close to maximal, since the total angular momentum of the binary at the end of the inspiral is $\sim 0.9M^2$ when the individual black holes are non-spinning [65], and can be larger when they are spinning. Exactly how close to extremal the final black hole will be is a matter that probably will not be decided until supercomputer simulations—or observations—settle the issue. In any case, the ringdown SNR values that we obtain depend only weakly on our assumed value of a [*cf.* Eq. (2.124)], for fixed total energy radiated in the ringdown.

The overall amplitude of the ringdown signal depends upon one's delineation of where "merger" ends and "ringdown" begins, which is somewhat arbitrary. For equal-mass BBHs, we assume a value of the overall amplitude that corresponds to a total radiated energy in the ringdown of $0.03M$, *i.e.*, a 3% radiation efficiency. This number is based on a quadrupole-formula-based estimate of the QNR amplitude when the distortion of the horizon of the black hole is of order unity (*cf.* Sec. 2.3.4). Although this radiation efficiency may seem rather high, there have been numerical evolutions of distorted, spinning black holes in which the ringdown waves carry away $\gtrsim 3\%$ of the black hole's total mass [66].

For non equal-mass black holes, we assume that the total energy radiated in the ringdown is $F(\mu/M)\,0.03M$, where

$$F(\mu/M) = (4\mu/M)^2 \tag{2.5}$$

and μ is the reduced mass of the binary. The reduction factor (2.5) gives the correct results for equal masses and also gives the correct scaling law in the regime $\mu \ll M$. For general mass ratios, it is probably a good approximation.

Merger energy spectrum: Realistic merger energy spectra will vary substantially from event to event (depending on the initial BH spins). Currently, we have very little concrete information about such spectra, pending supercomputer simulations. We adopt the following crude model for equal-mass BBHs [Eq. (2.60) below]: a flat spectrum $dE/df = \text{const}$ extending from the frequency $f_{\rm merge} = 0.02/M$ of quadrupole waves at the end of inspiral to the quasinormal ringing frequency $f_{\rm qnr} = 0.13/M$, with amplitude such that the total radiated energy in the merger is 10% of the total mass energy of the spacetime. In Sec. 2.3.2 we describe various circumstantial pieces of evidence, culled from the literature, which motivated this choice of energy spectrum. In particular, we outline two different "handwaving" arguments which suggest that in favorable cases the merger radiation efficiency may be as high as our assumed value of $\sim 10\%$. One of these arguments, due originally to Smarr [67] and explored by Detweiler [68], is based on extrapolation of perturbation theory results;

the other argument is based on angular momentum conservation.

Our assumed radiation efficiencies of 3% and 10% for the ringdown and merger phases should be interpreted as reasonable upper bounds that could be achieved in favorable cases, rather than as best-guess estimates. We note that numerical simulations that have been performed to date (which are restricted to axisymmetric situations) generally yield lower radiation efficiencies than we have assumed [69]; moreover, these axisymmetric simulations generally find that ringdown waves carry most of the radiated energy. In Sec. 2.3.2 we argue that the radiated energy in the merger phase could be boosted by the lack of symmetry in generic black hole mergers, and especially by the individual black holes' spins (if these spins are large).

For non-equal mass BBHs, we again reduce the energy spectrum by the factor (2.5), while the upper and lower frequencies $f_{\rm merge}$ and $f_{\rm qnr}$ are taken to be independent of μ.

2.1.5 Signal-to-noise ratios: results and implications

By inserting our assumed energy spectra (2.61), (2.60) and (2.65) into Eq. (2.2), we obtain matched-filtering SNRs for the three different phases of BBH coalescences as a function of the redshifted total mass $(1+z)M$ of the binary. The results are summarized in Appendix B, and graphed in Figs. 2.4, 2.5 and 2.6. In Sec. 2.3.5 we estimate that the number of independent frequency bins $\mathcal{N}_{\rm bins} \equiv 2T\Delta f$ characterizing the merger falls in the range $10 \lesssim \mathcal{N}_{\rm bins} \lesssim 30$; a conservative upper-bound is ~ 60. We use this upper bound in Sec. 2.6.2 to estimate the SNR threshold (2.35) for merger waves using noise-monitoring searches when templates are unavailable. We discuss the implications of these SNRs and SNR thresholds in Sec. 2.6; here we summarize our main conclusions:

- Ground-based interferometers can study black-hole mergers in the mass range (a few)$M_\odot$ to $\sim 2000 M_\odot$; LISA can study mergers in the mass range $10^5 M_\odot \lesssim (1+z)M \lesssim 10^8 M_\odot$.
- Ground-based interferometers can do moderate SNR (a few tens), moderate accuracy studies of the dynamics of merging black holes. LISA, by contrast, can do high SNR (a few $\times 10^4$), high-accuracy studies.
- Coalescing black holes may well be the first sources detected by LIGO/VIRGO: because of their larger masses, they can be seen to much greater distances than coalescing neutron star binaries. (With the initial LIGO interferometers, BBHs with $M \lesssim 50 M_\odot$ can be seen to $\sim$ 250 Mpc, whereas binary neutron stars can be seen to $\sim$ 25 Mpc [70]). The distance gain for BBHs could easily compensate for their smaller birth rate discussed above.

- Low-mass BBHs [$M \lesssim 30 M_\odot$ for initial LIGO interferometers; $M \lesssim 80 M_\odot$ for advanced; $(1+z)M \lesssim 3 \times 10^6 M_\odot$ for LISA] are best searched for via their well-understood inspiral waves; more massive BBHs must be searched for via their poorly understood merger waves and/or their well-understood ringdown waves.

- A search for massive BBHs based on the ringdown waves can be performed using matched filtering. We show in Sec. 2.6.1 that the number of templates needed for such a search is about 6000 or less, assuming that one wants the event rate reduction due to discreteness of the template family to be no more than 10%. Such a search with the first LIGO interferometers should be capable of finding equal-mass BBHs in the mass range $100 M_\odot$ to $700 M_\odot$ out to about 200 Mpc. With advanced LIGO interferometers, BBHs with $200 M_\odot \lesssim M(1+z) \lesssim 3000 M_\odot$ should be detectable out to $z \sim 1$; and with LISA, BBHs with $10^6 M_\odot \lesssim (1+z)M \lesssim 3 \times 10^8 M_\odot$ should be visible out to $z \gtrsim 100$. These distances are reduced by a factor of $\sim (4\mu/M)$ for non-equal-mass BBHs.

- The effectiveness of a search based on the merger waves will depend on how much one has learned about the waves from numerical relativity. With only knowledge of the merger waves' range of frequency bands and range of temporal durations, a search can be performed using the noise-monitoring search algorithm discussed above. Such a search could increase the number of discovered BBHs by a factor ~ 10 over those found from the inspiral and ringdown waves. A full set of merger templates based on numerical relativity simulations could further increase the event rate by an additional factor of up to ~ 4.

2.1.6 Organization of this chapter

In Sec. 2.2 we discuss the three methods of searching for gravitational wave signals referred to above. In Sec. 2.3 we discuss our assumptions about the BBH gravitational-wave signal: the splitting into three epochs, details of the emitted gravitational-wave energy spectrum during each epoch, and reasonable estimates of the duration and bandwidth of the dynamical merger. In Sec. 2.4 we devise a simple piece-wise power-law analytic fit [Eq. (2.74)] to the noise spectra of an initial LIGO interferometer, an advanced LIGO interferometer, and a space-based LISA interferometer. This single formula, by adjustment of its parameters, can describe all three interferometer types.

In Sec. 2.5 we insert these noise spectra models and the gravitational-wave energy spectra into the general SNR formula (2.2) to produce the matched filtering SNR for each type of interferometer,

and for each phase of BBH coalescence. Detailed SNR results are given in Appendix B. We give intuitive insight into these SNRs in Sec. 2.5.1 by re-expressing the power SNR for a source as

$$\rho^2 = \int d(\ln f)[h_{\rm char}(f)/h_n(f)]^2, \tag{2.6}$$

where $h_{\rm char}(f)$ is the source's "characteristic amplitude" as a function of frequency, and $h_n(f)$ is the detector's rms noise in a bandwidth equal to frequency for sources with random orientations. We give plots of $h_{\rm char}(f)$ and $h_n(f)$ for five specific examples of binaries with widely varying masses and distances. In Sec. 2.5.2, we plot and discuss the SNRs as functions of source mass [Figs. 2.4, 2.5, and 2.6]. These plots are the foundation for our conclusions, summarized above, about what features of which binaries should be observable with which interferometers. A detailed discussion of these conclusions is given in Sec. 2.6. In Sec. 2.6.1, we estimate the number of templates required for a search for ringdown waves based on matched filtering, estimate the SNR detection thresholds, and hence the range of the various interferometers for ringdown waves. In Sec. 2.6.2 we examine the prospects for searches for BBHs via their merger waves, both with and without templates.

2.2 Derivation of general formulae for signal-to-noise ratios and detection threshholds

In this section we discuss the various signal-search methods which were briefly described in the introduction of this chapter. In Sec. 2.2.1 we derive the approximate relation (2.3) between the SNR achievable using matched filtering searches for signals and the SNR obtainable via band-pass filtering searches. In Sec. 2.2.2 we describe our proposed noise-monitoring search method, and derive the detection threshold (2.35) discussed in Sec. 2.1.5. Finally, in Sec. 2.2.3 we derive the general formula (2.2) discussed in the introduction for the angle-averaged, matched-filtering SNR for a gravitational-wave source.

2.2.1 Searches for gravitational-wave bursts: band-pass filtering and matched filtering

Suppose that some arbitrary gravitational-wave burst $h(t)$ is present in the data stream $s(t)$, so that

$$s(t) = h(t) + n(t), \tag{2.7}$$

where $n(t)$ is noise. Suppose one integrates a filter $K(t)$ against $s(t)$ to produce a number, $Y = \int K(t)s(t)\,dt$. The standard definition of the SNR is then [61]

$$\begin{aligned}\frac{S}{N} &= \frac{\text{expected value of } Y \text{ when signal present}}{\text{rms value of } Y \text{ when no signal present}} \\ &= \frac{\langle Y\rangle}{\sqrt{\langle Y^2\rangle_{s=0}}} \\ &= \frac{4\int_0^\infty df\,\Re\left[\tilde{h}(f)^*\tilde{K}(f)\right]}{\sqrt{4\int_0^\infty df\,\left|\tilde{K}(f)\right|^2 S_h(f)}};\end{aligned} \tag{2.8}$$

see, *e.g.*, Refs. [58, 59]. Here tildes denote Fourier transforms according to the convention

$$\tilde{h}(f) = \int_{-\infty}^{\infty} e^{2\pi i f t}\,h(t)\,dt, \tag{2.9}$$

and $S_h(f)$ is the power spectral density of strain noise in the detector [61].

Now consider searching for a signal $h(t)$ when the only information one has about it is its approximate bandwidth in the frequency domain. Perhaps the simplest search algorithm one could use to search for $h(t)$ is to choose for $K(t)$ the following band-pass filter:

$$\tilde{K}(f) = e^{2\pi i f t_{\rm start}}\Theta(\Delta f/2 - |f - f_{\rm char}|). \tag{2.10}$$

Here Θ is the step function and $t_{\rm start}$ is the starting time of the filter. This filter chops out all the data in the frequency domain except that in a bandwidth Δf about a characteristic central frequency $f_{\rm char}$ [71]. Suppose that the frequency interval has been chosen wisely, so that the signal $h(t)$ has negligible power outside the interval. Then $\tilde{h}(f)$ can be taken to vanish outside the chosen bandwidth, and Eqs. (2.8) and (2.10) yield

$$\left(\frac{S}{N}\right)_{\rm band-pass} = \frac{h(t_{\rm start})}{\sqrt{\int_{\Delta f} df\,S_h(f)}} \approx \sqrt{\frac{f_{\rm char}}{\Delta f}}\,\frac{h(t_{\rm start})}{h_{\rm rms}(f_{\rm char})}, \tag{2.11}$$

where $h_{\rm rms}(f) \equiv \sqrt{f S_h(f)}$ is the rms fluctuation in the noise at frequency f in a bandwidth equal to f. The starting time of the filter $t_{\rm start}$ is then varied to give the maximum filter output Y, which is achieved at some value $t_{\rm best}$ of $t_{\rm start}$. At this maximum overlap time, the SNR is given by Eq. (2.11) with $t_{\rm start}$ replaced by $t_{\rm best}$. In particular, for broadband signals for which $\Delta f \sim f_{\rm char}$, Eq.

(2.11) simplifies to the standard result [40]

$$\left(\frac{S}{N}\right)_{\rm band-pass} \approx \frac{h(t_{\rm best})}{h_{\rm rms}(f_{\rm char})}. \tag{2.12}$$

By contrast, if the shape of the signal is known one can use the well known optimal or matched filter $\tilde{K}(f) = \tilde{h}(f)/S_h(f)$ [58, 59, 61]:

$$\rho^2 = \left(\frac{S}{N}\right)^2_{\rm matched} = 4\int_0^\infty \frac{|\tilde{h}(f)|^2}{S_h(f)} df. \tag{2.13}$$

A crucial element of both matched filtering searches and most especially band-pass filtering searches with ground-based interferometers is the use of coincidencing between different interferometers to circumvent the effects of non-Gaussian noise bursts [40]. Coincidencing between the 4 interferometers in the LIGO/VIRGO network (the Hanford 2 km, Hanford 4 km, Livingston 4 km and Pisa 3 km interferometers) should be sufficient to achieve this. To be conservative, our assumed detection thresholds for the SNR values are based on combining just the two LIGO 4 km interferometers, albeit with assumed Gaussian statistics.

In order for a signal to be detected with matched filtering, the waves' measured SNR must be larger than the detection threshold $\rho_{\rm threshold}$ given by

$${\rm erfc}(\rho_{\rm threshold}/\sqrt{2}) = \frac{\epsilon}{\mathcal{N}_{\rm start-times}\,\mathcal{N}_{\rm shapes}} \tag{2.14}$$

see, for example, Ref. [44]. Here ϵ is the false alarm probability, which we will assume below to be 10^{-3}, corresponding to a false alarm rate of once per thousand years if the length of the data set is one year. The quantity $\mathcal{N}_{\rm start-times}$ is the number of independent starting times of the gravitational wave signal that are searched for in the data set, determined by the total duration of the data set (of order one year) and the sampling time. The quantity $\mathcal{N}_{\rm shapes} = \mathcal{N}_{\rm shapes}(\rho_{\rm threshold})$ is the number of statistically independent waveforms with SNR $\leq \rho_{\rm threshold}$ in the set of signals to be searched for [72]; Eq. (2.14) must be solved self-consistently to determine $\rho_{\rm threshold}$. To a good approximation, Eq. (2.14) reduces to

$$\rho_{\rm threshold} \approx \sqrt{2\ln(\mathcal{N}_{\rm start-times}/\epsilon) + 2\ln(\mathcal{N}_{\rm shapes})}. \tag{2.15}$$

Typical values of these parameters are $\epsilon = 10^{-3}$, a sampling time of 0.01 s and a data set of one

year's duration; for these values $\mathcal{N}_{\rm shapes}/\epsilon \sim 3 \times 10^{12}$ and thus the value of the threshold (2.15) depends only weakly on $\mathcal{N}_{\rm shapes}$ since $\mathcal{N}_{\rm shapes} \ll 10^{12}$.

There is a standard lore that the matched-filtering SNR (2.13) is larger than the band-pass filtering SNR (2.12) by approximately the square root of the number of cycles in the waveform [1, 40]. This relation is strictly speaking only applicable to waveforms that are almost monochromatic, *i.e.*, of the form $h(t) = h_{\rm amp}(t)\cos\left[\Phi(t)\right]$, where the amplitude $h_{\rm amp}(t)$ and instantaneous frequency [given by $2\pi f(t) = d\Phi/dt$] are slowly evolving. The standard lore relation can be obtained by inserting the stationary phase approximation to the Fourier transform of $h(t)$ into Eq. (2.13), which yields

$$\rho^2 = \int d(\ln f)\, n_{\rm cyc}(f)\, \frac{h_{\rm amp}\left[t(f)\right]^2}{h_{\rm rms}(f)^2}, \tag{2.16}$$

where $n_{\rm cyc}(f) \equiv f^2/\dot{f}$ is the number of cycles spent within a bandwidth $\Delta f \sim f$ centered on f, and $t(f)$ is the time at which the gravitational-wave frequency is f. Comparing Eqs. (2.12) and (2.16), we see that $n_{\rm cyc}(f)$ is the gain factor in SNR squared for matched filtering over band-pass filtering, per logarithmic interval in frequency [1].

This analysis does not apply to signals which are not quasi-monochromatic. We can, however, derive an approximate formula for the SNR (2.12) for general signals. Approximating $S_h(f)$ to be constant in Eq. (2.13) gives [40]

$$\begin{aligned}\left(\frac{S}{N}\right)^2_{\rm matched} &\approx \frac{2}{S_h(f_{\rm char})}\int_{-\infty}^{\infty} dt\left[h(t)\right]^2 \\ &\approx 2 f_{\rm char} T\,\frac{\bar{h}^2}{h_{\rm rms}(f_{\rm char})^2}\end{aligned} \tag{2.17}$$

where $\bar{h}$ is an rms average of $h(t)$ and T is the effective duration of the signal. Comparing Eqs. (2.17) and (2.11) we find that

$$\frac{(S/N)_{\rm band-pass}}{(S/N)_{\rm matched}} \approx \frac{h(t_{\rm best})}{\bar{h}}\,\frac{1}{\sqrt{\mathcal{N}_{\rm bins}}}, \tag{2.18}$$

where

$$\mathcal{N}_{\rm bins} = 2T\Delta f. \tag{2.19}$$

The quantity $\mathcal{N}_{\rm bins}$ can be interpreted as the "number of *a priori* frequency bins," since when one searches for a signal of duration $\leq T$ and bandwidth $\leq \Delta f$, the relevant data is described by $\mathcal{N}_{\rm bins}$ real Fourier coefficients or, equivalently, frequency bins.

This notion of number of *a priori* frequency bins is closely related to the notion of number of cycles in the waveform: the number of waveform cycles, $\mathcal{N}_{\rm cyc} \approx T\, f_{\rm char}$ is roughly equal to $\mathcal{N}_{\rm bins}$ for a broadband burst with $f_{\rm char} \sim \Delta f$. An important distinction, however, is that $\mathcal{N}_{\rm cyc}$ is intrinsic to the signal, whereas $\mathcal{N}_{\rm bins}$ depends upon the characteristics of our band-pass filter. The number of frequency bins thus characterizes in part our *a priori* assumptions about the signal.

The first factor on the right hand side of Eq. (2.18) is the ratio between the peak strain amplitude $h(t_{\rm best})$ in the time domain and an rms value $\bar{h}$ of this strain amplitude. By defining the effective duration T of the signal to be given by

$$\int dt\, [h(t)]^2 = T\, h(t_{\rm best})^2, \tag{2.20}$$

this factor reduces to unity. With this interpretation of T in Eq. (2.19), Eq. (2.18) reduces to

$$\frac{(S/N)_{\rm band-pass}}{(S/N)_{\rm matched}} \approx \frac{1}{\sqrt{\mathcal{N}_{\rm bins}}}, \tag{2.21}$$

as discussed in the ntroduction to this chapter. We use this result in Sec. 2.6.2.

2.2.2 Searches for gravitational-wave bursts: noise monitoring

In this section we describe a "noise-monitoring" method to search for gravitational wave bursts of unknown form; more details can be found in Ref. [73]. A variant of the method was first suggested by Schutz [40] (there called an autocorrelation method); here we modify slightly Schutz's suggestion and also calculate detection thresholds. In essence, the method consists of monitoring the total rms noise in the detector output in the frequency band in which the signal is expected, rms averaged over timescales of the expected signal duration, and waiting for statistically significant changes in one's estimate of the noise power.

Suppose that the maximum expected signal duration is T, and that the interferometer output is $s(t)$. Focus attention on the data stream $s(\tau)$ in the time interval $t - T/2 \leq \tau \leq t + T/2$. Since the data stream is discrete, this data can be represented by the numbers

$$s_j = s(t - T/2 + j\Delta t) \tag{2.22}$$

for $0 \leq j \leq N_{\rm total} = T/\Delta t$, where Δt is the sampling time. From Eq. (2.7) we have

$$s_j = h_j + n_j, \tag{2.23}$$

where h_j is the gravitational-wave signal and n_j is the noise. Now because the interferometer noise is colored, the noise matrix

$$\Sigma_{ij} \equiv \langle n_i n_j \rangle \tag{2.24}$$

will not be diagonal. Here, angle brackets denote ensemble averaging over realizations of the noise. If one performs an FFT just of this finite stretch of data, the noise matrix on the new basis will not be diagonal either because of aliasing effects. However, it is possible to change to a basis which diagonalizes the matrix (2.24). We will denote this new basis by capital Roman letters I, J, K. The data points s_I on this new basis can be chosen to correspond approximately to frequencies $f_I = I/T, I = 1, -1, 2, -2, \ldots$ [73]. Equation (2.24) can now be replaced by

$$\langle n_I \, n_J \rangle = \delta_{IJ} \, \sigma_I^2. \tag{2.25}$$

The data s_I extend up to some high frequency (of order several kHz) determined by the sampling time. We next discard all data above some upper cutoff frequency; thus, we have effectively band-pass filtered the data, since the restriction to a segment of length T in the time domain removes frequency components at $f \lesssim 1/T$. The total number of data points remaining will be approximately $\mathcal{N}_{\rm bins} = 2T\Delta f$, where Δf is the bandwidth of our effective band-pass filter.

In terms of this new basis, matched filtering consists of calculating, for each trial waveform shape h_J, the quantity

$$\frac{\sum_J s_J h_J/\sigma_J^2}{\sqrt{\sum_J h_J^2/\sigma_J^2}}. \tag{2.26}$$

(We are assuming here that all the trial waveform shapes have duration less than T and most of their power within the bandwidth Δf.) We introduce the notation $\rho_I = h_I/\sigma_I$; then, the matched filtering SNR (2.1) becomes

$$\rho^2 = \sum_I \rho_I^2 = \sum_I \frac{h_I^2}{\sigma_I^2}. \tag{2.27}$$

Thus, the quantity ρ_I^2 is the matched filtering SNR-squared per data bin. Throughout this subsection, we use ρ as a convenient parameterization of the signal strength, which is meaningful even in situations where templates are not available and where matched filtering cannot be carried out.

In this language, band-pass filtering (of a pre-whitened data stream) approximately corresponds to calculating the statistic

$$\hat{\rho}_{\rm BP} \equiv \max_J \frac{s_J}{\sigma_J}. \tag{2.28}$$

This will have an expected value of $\sim \rho/\sqrt{\mathcal{N}_{\rm bins}}$ [*cf.* Eq. (2.21)] if the signal is spread out over the bandwidth Δf rather than peaked at some frequency.

In the noise-monitoring technique, the detection statistic is

$$Q(t) = -\mathcal{N}_{\rm bins} + \sum_{J=-\mathcal{N}_{\rm bins}/2}^{J=\mathcal{N}_{\rm bins}/2} \frac{s_J^2}{\sigma_J^2}. \tag{2.29}$$

Up to an additive constant, $Q(t)$ is an estimate of the noise power in the given bandwidth over the given time interval. That constant, $-\mathcal{N}_{\rm bins}$, is chosen so that when no signal is present, $\langle Q(t)\rangle = 0$ and so $Q(t)$ fluctuates between positive and negative values. On the other hand, when a signal is present, $Q(t)$ will with high probability be large and positive. One monitors $Q(t)$ as a function of time, setting a threshold that it has very low probability of exceeding in the absence of a signal. This search method constitutes a type of nonlinear filtering.

Noise-monitoring is closely related to two commonly used techniques in radio astronomy. In the first such technique, observers sum the power from frequency bins which are expected to contain harmonics of the signal they are trying to detect. This procedure is not as effective as coherently combining the signal from all the frequency bins, but is computationally much easier. The second technique [74] is applicable when one is looking for periodic signals in a data train that is too long to Fourier transform. One splits the data into shorter segments, takes the FFT of each segment, and adds the FFTs incoherently (*i.e.*, adds the individual power spectra). This is not the optimal search method, but is often useful given finite computational resources. Although noise-monitoring and the radio astronomy techniques have different motivations (in radio astronomy, one adds frequency bins incoherently to save computational cost; in noise-monitoring, one performs such addition because the phase relationships are unknown), they are operationally quite similar.

We now turn to a derivation of the efficiency and performance of the method. From Eq. (2.29), when a signal is present,

$$\begin{aligned} \langle Q(t)\rangle &= \rho^2, \\ \left\langle [Q(t) - \langle Q(t)\rangle]^2 \right\rangle &= 4\rho^2 + 2\mathcal{N}_{\rm bins}. \end{aligned} \tag{2.30}$$

With no signal present, Eqs. (2.30) continue to hold with $\rho = 0$. These equations show that a signal should be detectable in the regime

$$\mathcal{N}_{\rm bins}^{1/4} \ll \rho \lesssim \mathcal{N}_{\rm bins}^{1/2}, \tag{2.31}$$

as well as at larger ρ: in the regime (2.31) the expected value (2.30) of Q is large compared to its rms value in the absence of a signal. By contrast, a signal is detectable using band-pass filtering only in the regime $\rho \gtrsim \mathcal{N}_{\rm bins}^{1/2}$ [Eq. (2.28) above and associated discussion].

The approximate SNR threshold predicted by Eqs. (2.30) is correct in order of magnitude, but to obtain an accurate SNR threshold one needs to calculate the full probability distribution for the statistic Q. This probability distribution is given by, from Eqs. (2.23), (2.25) and (2.29),

$$P[Q(t) \geq Q_0] = \frac{\Gamma[\mathcal{N}_{\rm bins}/2, (Q_0 + \mathcal{N}_{\rm bins})/2]}{\Gamma(\mathcal{N}_{\rm bins}/2)} \tag{2.32}$$

where $\Gamma(\cdots,\cdots)$ is the incomplete Gamma function and $\Gamma(\cdots)$ is the usual Gamma function. Suppose that we examine $\mathcal{N}_{\rm start-times}$ starting times t. We wish to find the number Q_0 such that the probability (2.32) of $Q(t)$ exceeding Q_0 for any t, in the absence of a signal, is some small number ϵ (below we will take $\epsilon = 10^{-3}$). This threshold Q_0 is obtained by solving

$$\frac{\Gamma[\mathcal{N}_{\rm bins}/2, (Q_0 + \mathcal{N}_{\rm bins})/2]}{\Gamma(\mathcal{N}_{\rm bins}/2)} = \frac{\epsilon}{\mathcal{N}_{\rm start-times}}. \tag{2.33}$$

From Eqs. (2.30), this threshold will be exceeded by a signal whenever the signal strength (2.27) satisfies

$$\rho \geq \rho_* = \sqrt{Q_0}. \tag{2.34}$$

Eqs. (2.33) and (2.34) determine the threshold ρ_* as a function of the parameters ϵ, $\mathcal{N}_{\rm start-times}$, and $\mathcal{N}_{\rm bins}$; we use these formulae in Sec. 2.6.2. For $\mathcal{N}_{\rm bins} \gg 1$, ρ_* is approximately given by solving the equation

$$\rho_*^2 = 2\ln(\mathcal{N}_{\rm start-times}/\epsilon) + \mathcal{N}_{\rm bins} \ln\left(1 + \rho_*^2/\mathcal{N}_{\rm bins}\right). \tag{2.35}$$

The above derivation is based on frequentist statistics. In Ref. [73] a Bayesian analysis is outlined of the detection of gravitational wave signals of unknown form which automatically identifies the statistic $Q(t)$ as optimal, and which also approximately reproduces the detection threshold ρ_*.

In practice, this search method would be combined with coincidencing between interferometers to achieve high detection reliability and to reduce the effects of non-Gaussian noise, as is the case

with band-pass and matched filtering discussed above. Matched filtering could be more efficient than the noise-monitoring method at combating non-Gaussian noise via coincidencing: when coincidencing with templates, one can demand that the SNR in each interferometer be above the appropriate threshold, *and* that the signal-parameter values deduced in each interferometer be consistent with each other. For the noise-monitoring searches, one can only demand that the SNR in each interferometer be above the appropriate threshold. Hence, matched filtering has more discriminating power against situations in which all the interferometers have moderately large non-Gaussian noise spikes somewhere in the relevant time window. Non-Gaussian noise may therefore make the less-discriminating noise-monitoring search perform somewhat worse in practice, relative to matched filtering searches, than is indicated by the threshold (2.35).

2.2.3 Signal-to-noise ratio for matched filtering in terms of waves' energy spectrum

In this section we derive the relation (2.36) between the expected value of the matched-filtering SNR (2.13), and the energy spectrum of emitted gravitational waves. In general, the SNR (2.13) for a burst of waves depends on the details of the gravitational waveform, on the orientation of the source with respect to the interferometer, and on the direction to the source. By contrast, the quantity $\langle \rho^2 \rangle$, the average of the squared SNR over all orientations of and directions to the source, depends only on the total energy per unit frequency dE/df carried off from the source by the waves. Consider a gravitational-wave source located at a cosmological redshift z and corresponding luminosity distance $D(z)$. Let the locally measured frequency of the waves near the source be f_e, related to the frequency f measured at the interferometer by $f = f_e/(1+z)$. Let the locally measured energy spectrum of the waves be $dE_e/df_e(f_e)$. Then the orientation-averaged SNR squared is given by

$$\langle \rho^2 \rangle = \frac{2(1+z)^2}{5\pi^2 D(z)^2} \int_0^\infty df \, \frac{1}{f^2 S_h(f)} \, \frac{dE_e}{df_e}[(1+z)f]. \tag{2.36}$$

Note that the relation (2.36) refers to an angle-averaged SNR obtained from an *rms average* of signal amplitudes over different possible orientations of the source and interferometer. This averaging convention differs from that adopted in Refs. [1, 10], where the angle-averaged SNR is taken to be a cube root of an average of cubed signal amplitudes. That "cube root of a mean cube" method is appropriate for calculating the expected event detection rate [1]. As a result, the SNR formulae used in Refs. [1, 10] are a factor of $\sqrt{3/2}$ larger than those used in this paper, the factor of $\sqrt{3/2}$ being an approximation to the effect of the different angle-averaging methods.

Turn now to the derivation of Eq. (2.36). First, consider a source close enough that cosmological effects can be neglected. Let the source be at a distance r from the detector and at a location (θ, φ) on the sky. Let (ι, β) denote the direction towards the detector (spherical polar angles) with respect to a set of Cartesian axes centered at and determined by the source. Let the two independent polarizations of the strain amplitude at the interferometer be $h_+(t, r, \iota, \beta)$ and $h_\times(t, r, \iota, \beta)$, and let the polarization angle be ψ. Then the response of the interferometer will be $h(t) + n(t)$, where $n(t)$ is the noise, and

$$h(t) = F_+(\theta, \varphi, \psi)h_+(t, r, \iota, \beta) + F_\times(\theta, \varphi, \psi)h_\times(t, r, \iota, \beta). \tag{2.37}$$

Here F_+ and $F_\times$ are the interferometer beam pattern functions, given in, *e.g.*, Ref. [1]. The dependence of the Fourier transformed waveform $\tilde{h}_+$ on r is of the form

$$\tilde{h}_+(f, r, \iota, \beta) = H_+(f, \iota, \beta)/r \tag{2.38}$$

for some function H_+; we define $H_\times(f, \iota, \beta)$ similarly. Combining Eqs. (2.13), (2.37) and (2.38) gives

$$\rho^2(r, \theta, \varphi, \psi, \iota, \beta) = \frac{4}{r^2}\int_0^\infty \frac{|F_+H_+ + F_\times H_\times|^2}{S_h(f)}df. \tag{2.39}$$

We now average over the angles $\theta, \varphi, \psi, \iota$ and β. The average over polarizations and over the sky location gives $\langle F_+^2\rangle = \langle F_\times^2\rangle = 1/5$, $\langle F_+F_\times\rangle = 0$ [1], where the meaning of the angular brackets is given by, for example,

$$\langle F_+^2\rangle \equiv \frac{1}{4\pi}\int d\Omega_{\theta,\varphi}\int_0^\pi \frac{d\psi}{\pi}\, F_+(\theta, \varphi, \psi)^2. \tag{2.40}$$

From Eq. (2.39) this gives

$$\langle\rho^2\rangle = \frac{4}{5r^2}\int_0^\infty \frac{H(f)^2}{S_h(f)}df, \tag{2.41}$$

where

$$H(f)^2 \equiv \frac{1}{4\pi}\int d\Omega_{\iota,\beta}\left(|H_+(\iota, \beta)|^2 + |H_\times(\iota, \beta)|^2\right). \tag{2.42}$$

We now express the energy spectrum dE/df of the waves in terms of the quantity $H(f)^2$. The local energy flux is

$$\frac{dE}{dA\,dt} = \frac{1}{16\pi}\overline{\left[\left(\frac{\partial h_+}{\partial t}\right)^2 + \left(\frac{\partial h_\times}{\partial t}\right)^2\right]}, \tag{2.43}$$

where the overbar means an average over several cycles of the wave. Switching to the frequency domain using Parseval's theorem, inserting a factor of two to account for the folding of negative frequencies into positive, and using $|\tilde{h}_{+,\times}(f)|^2 dA = |\tilde{H}_{+,\times}(f)|^2 d\Omega$ gives

$$\frac{dE}{d\Omega df} = \frac{\pi f^2}{2}\left(|\tilde{H}_+(\iota,\beta)|^2 + |\tilde{H}_\times(\iota,\beta)|^2\right). \tag{2.44}$$

Combining Eqs. (2.41), (2.42) and (2.44) now yields

$$\left\langle \rho^2 \right\rangle = \frac{2}{5\pi^2 r^2}\int_0^\infty df \int d\Omega \, \frac{1}{f^2 S_h(f)} \frac{dE}{d\Omega df}(f). \tag{2.45}$$

This is Eq. (2.36) with $z = 0$ and $D(z) = r$, the limiting form that applies when cosmological effects are neglected.

Consider now sources at cosmological distances. First, observe that Eq. (2.45) is valid for arbitrary bursts of gravitational waves provided that we interpret the quantity

$$\frac{1}{r^2}\frac{dE}{d\Omega df}$$

as the locally measured energy flux $dE/dA\,df$. Next, note that the number of gravitons per unit solid angle per unit frequency is conserved for propagation in a Friedmann-Robertson-Walker background in the geometric optics limit:

$$\frac{dE}{d\Omega df}(f) = \frac{dE_e}{d\Omega df_e}[(1+z)f]. \tag{2.46}$$

Here f_e is the frequency at the source and $f = f_e/(1+z)$ is the frequency at the detector. Finally, the conversion factor at the detector from energy per unit solid angle to energy per unit area is $(1+z)^2/D(z)^2$, where $D(z)$ is the luminosity distance [75]. Hence

$$\frac{dE}{dAdf}(f) = \frac{(1+z)^2}{D(z)^2}\frac{dE_e}{d\Omega df_e}[(1+z)f]. \tag{2.47}$$

Combining this with Eq. (2.45) yields Eq. (2.36).

2.3 The gravitational-wave signal from coalescing black holes

In this section we describe our assumptions concerning the gravitational-wave signal from BBH mergers, and the evidence that underlies those assumptions.

2.3.1 The three phases of the gravitational-wave signal

As discussed in this chapter's introduction, the coalescence and its associated gravitational-wave signal can be divided into three successive epochs in the time domain: inspiral, merger, and ringdown. The inspiral consists of the coalescence epoch in which the black holes are separated bodies that gradually lose energy and angular momentum, slowly spiraling towards one another. The merger is the epoch in which the dynamics are highly nonlinear and must be treated by numerical relativity. With this in mind, it is useful to define the end of inspiral as the time and frequency at which numerically generated templates become needed [76]. Up to this time, post-Newtonian templates, possibly supplemented with IBBH templates, will be used (*cf.* Sec. 2.1.2).

After merger, the system will gradually settle down to a Kerr black hole; the last gravitational waves we expect to see are those produced by the quasinormal modes of this merged black hole. It is clear that there will be a smooth transition in the gravitational waveform from the merger portion to the ringdown portion, as the effects of nonlinearities become less and less important with time. As this happens, the signal should become increasingly well approximated by a linear combination of exponentially decaying sine waves. This is the behavior that has been seen in numerical simulations of, for example, head-on collisions [77, 78]. At late times, the $l = m = 2$ mode will probably dominate over other quasi-normal modes, for two reasons which are of comparable importance: (i) The $l = m = 2$ mode is the most slowly damped of all the QNR modes [14], and (ii) during coalescence, the binary will have a rotating shape roughly corresponding to spheroidal harmonic indices $l = m = 2$, so this mode will be preferentially excited [79]. We define the ringdown as beginning when the waveform becomes dominated by the $l = m = 2$ QNR mode; the merger thus contains those portions of the waveform where other modes and/or non-linear mode-mode couplings are important. Clearly there is some arbitrariness in the exact time at which the ringdown starts, related to the accuracy we require of the fit of the waveform to the ringdown signal.

By definition, the three phases of the signal are disjoint in the time domain. It does not follow that they should be disjoint in frequency: their energy spectra might overlap. However, it is at least approximately true that the inspiral and merger are disjoint in both time and frequency. The

adiabatic approximation is only just beginning to break down at the end of inspiral; thus, there is a well-defined frequency as a function of time $f(t)$ over almost the entire inspiral. Because the inspiral chirps upward monotonically in frequency, almost all energy emitted before the merger lies at frequencies less than $f_{\rm merge}$, the gravitational-wave frequency at the end of inspiral. We discuss below estimates of $f_{\rm merge}$. We shall assume that the merger waves' spectrum is confined to the frequency regime $f > f_{\rm merge}$. One particular component of the gravitational-wave signal, the Christodoulou memory [80], *will* violate this assumption. This component has most of its power below $f_{\rm merge}$ in the frequency domain, but accumulates gradually during the inspiral, merger and ringdown in the time domain. It will probably not be detectable with ground based interferometers, but very probably will be detectable with LISA [81]. We will neglect the memory component of the waves in our analysis, since it will not be as easy to detect as the components we do discuss.

2.3.2 Energy spectrum of the radiation from the merger phase

The total amount of energy radiated in BBH mergers, and its distribution in frequency, is highly uncertain because detailed numerical calculations of these mergers have not yet been made. In this subsection, we discuss what little evidence there is about the energy radiated, and describe our crude model of the spectrum.

The total amount of energy radiated during a BBH coalescence will be some fraction ϵ of the total mass $M = m_1 + m_2$ of the system: $E_{\rm radiated} = \epsilon M$. The fraction ϵ will depend only on the mass ratio m_1/m_2, on the initial spins $\mathbf{S}_1$ and $\mathbf{S}_2$ of the two black holes, and on the initial direction $\hat{\mathbf{L}}$ of the orbital angular momentum [82]:

$$\epsilon = \epsilon\left(\frac{m_1}{m_2}, \frac{\mathbf{S}_1}{M^2}, \frac{\mathbf{S}_2}{M^2}, \hat{\mathbf{L}}\right). \tag{2.48}$$

We can very roughly divide up this fraction as

$$\epsilon = \epsilon_{\rm inspiral} + \epsilon_{\rm merger} + \epsilon_{\rm ringdown}, \tag{2.49}$$

according to the amounts of energy radiated in the three different epochs of the waveform. We emphasize that there is some arbitrariness in this division, related to the choice of frequency at the end of inspiral, and the time at the beginning of ringdown.

We now discuss estimates of the frequency $f_{\rm merge}$. From a data-analysis oriented viewpoint,

$f_{\rm merge}$ should represent the frequency at which post-Newtonian templates cease to be useful and numerical templates will be needed. On the other hand, $f_{\rm merge}$ could be chosen at the supposed point of transition from a radiation-reaction driven inspiral to a freely-falling plunge [8, 11, 12]. These two viewpoints turn out to give roughly the same value for $f_{\rm merge}$.

To estimate the frequency where numerical templates are likely to be needed, we examined numerical initial data sets of black holes binaries generated by Cook [9]. Comparing the predictions of second post-Newtonian order calculations to his initial data sets, Cook finds that the discrepancy in the binding energy between the two methods is $\sim 5\%$ at $f \approx 0.02/M$ (where M is the total system mass), and is $\sim 15\%$ at $f \approx 0.05/M$. Thus, numerical relativity's predictions begin to significantly deviate from post-Newtonian theory near $f = 0.02/M$.

The "innermost stable circular orbit" (ISCO) for black hole binaries only exists, strictly speaking, in the test particle limit $m_1 \ll m_2$, and it is not clear that it is well defined, even approximately, in the equal mass case. Nevertheless, various methods have been proposed to locate the supposed transition point from inspiral to plunge. Cook estimates the gravitational wave frequency at the ISCO to be $f_{\rm ISCO} \sim 0.055/M$ for equal mass black holes [9], by using his initial data sets together with the calculation of an "effective potential." In post-Newtonian theory, the ISCO can be defined by artificially turning off the radiation reaction terms in the equations of motion. Using this method, Kidder, Will and Wiseman estimate $f_{\rm ISCO} \sim 0.02/M$ [8]. This value varies by less than $\sim 20\%$ as the mass ratio is varied. Finally, earlier analyses by Blackburn and Detweiler used a variational principle together with the assumption of periodic solutions to Einstein's equations to obtain the approximate lower bound $f_{\rm ISCO} \gtrsim 0.06/M$ [83]. All of these estimates are for equal mass, non-spinning black holes; the value of the frequency $f_{\rm ISCO}$ can presumably also vary by factors $\gtrsim 2$ if the black holes are spinning and/or have different masses.

Given this uncertainty, we adopt the conservative value

$$f_{\rm merge} = \frac{0.02}{M} = 205\,{\rm Hz}\left(\frac{20M_\odot}{M}\right). \tag{2.50}$$

This (low) value of $f_{\rm merge}$ is conservative in the sense that we can be reasonably sure numerically generated templates will not be needed before $f = f_{\rm merge}$. On the other hand, it may overestimate the merger SNR by increasing the number of cycles in what we define as our merger waveform at the expense of the inspiral.

We next discuss our choice of upper frequency shutoff for the merger energy spectrum. As

discussed above, we define the end of merger to occur at a time $t_{\rm qnr}$ after which the waveform can be accurately fit by the $l = m = 2$ QNR signal. The merger and ringdown will therefore be disjoint in the time domain, but not necessarily in the frequency domain. It seems likely, however, that an approximate upper bound for the frequencies carrying appreciable power during the merger is the quasinormal ringing frequency itself. This conjecture is supported by calculations in the test particle limit (*cf.* Fig. 2 of Ref. [68]) and calculations of the head-on collision of two black holes [77, 78]. It is not clear how relevant these calculations are to the merger of comparable mass black holes, but there is no other guidance available at this time.

Therefore, we use the frequency $f_{\rm qnr}$ of the $l = m = 2$ quasinormal mode as our upper merger frequency. This frequency depends on the dimensionless spin parameter a of the final Kerr black hole; for concreteness, we use the value of $a = .98$, for which $f_{\rm qnr} \simeq 0.9/(2\pi M)$ [56, 15]:

$$f_{\rm qnr} = \frac{0.13}{M} = 1320\,{\rm Hz}\left(\frac{20M_\odot}{M}\right). \tag{2.51}$$

Our reasons for assuming a high value of a are discussed in Sec. 2.3.4 below.

Finally, consider the total amount of energy

$$E_{\rm rad} = (\epsilon_{\rm merger} + \epsilon_{\rm ringdown})M \tag{2.52}$$

radiated during the final merger and ringdown. We consider two methods of estimating this radiation efficiency, which yield consistent results. The first method, due to Smarr [67, 77], is an extrapolation from perturbation theory: the energy radiated in the test particle limit is of the form

$$E_{\rm rad} = k\mu^2/M, \tag{2.53}$$

where k is a dimensionless constant, μ is the mass of the particle, and M the total mass of the system. Replacing μ by the reduced mass of the system, one finds that the formula (2.53) reliably predicts (to within $\sim 20\%$) the energy radiated in the head-on collision of two black holes [68, 77, 78, 84]. Consider applying a similar extrapolation to an inspiral-preceded merger. Detweiler [68] examined the amount of energy radiated per orbit by a test particle on the final, marginally bound orbit of a Kerr black hole. He found that the energy radiated is of the form (2.53), with $0.65 \leq k \leq 2.8$ as the spin of the black hole varies from 0 to .95. Assuming that there will be $\gtrsim 1$ effective orbit during

the final plunge, Detweiler estimates [68]

$$0.03M\,F(\mu/M) \lesssim E_{\rm rad} \lesssim 0.2M\,F(\mu/M), \tag{2.54}$$

where $F(\mu/M)$ is given in Eq. (2.5).

A second method, based on angular momentum conservation, also suggests a lower bound on $E_{\rm rad}$ of about $0.1M$ for equal-mass BBHs in the most favorable cases. Roughly speaking, the system's angular momentum divides up as

$$\mathbf{S}_1 + \mathbf{S}_2 + \mathbf{L}_{\rm orb} = \mathbf{J}_{\rm rad} + \mathbf{S}_{\rm final}, \tag{2.55}$$

where $\mathbf{S}_1$ and $\mathbf{S}_2$ are the black hole spins just before the final plunge, $\mathbf{L}_{\rm orb}$ is the orbital angular momentum just before the plunge, $\mathbf{J}_{\rm rad}$ is the angular momentum radiated in the merger/ringdown waves, and $\mathbf{S}_{\rm final}$ is the spin of the final Kerr black hole. This splitting of the spacetime's total angular momentum is, strictly speaking, well defined only in a post-Newtonian type of limit; however, the effects of this ambiguity are presumably not important for the purposes of our crude estimate. Specialize now to the most favorable case where $\mathbf{S}_1$, $\mathbf{S}_2$ and $\mathbf{L}_{\rm orb}$ are all aligned. We assume $|\mathbf{L}_{\rm orb}| \approx 0.9M^2$, the value predicted by Cook's initial data sets at $f = .02/M$ [9]. We also assume that both black holes are rapidly spinning, so that $|\mathbf{S}_1| \approx |\mathbf{S}_2| \approx (M/2)^2$. Equation (2.55) then yields

$$|\mathbf{J}_{\rm rad}| \gtrsim 0.4M^2, \tag{2.56}$$

since $|\mathbf{S}_{\rm final}| \leq M^2$. Next, we use that fact that the energy $E_{\rm rad}$ and the angular momentum $J_{\rm rad}$ carried off by gravitons of frequency f and azimuthal multipole order m are related by [85]

$$E_{\rm rad} = 2\pi f J_{\rm rad}/m. \tag{2.57}$$

If we estimate $f \approx (f_{\rm merge} + f_{\rm qnr})/2$, and make the admittedly optimistic assumption that most of the radiation is quadrupolar, we obtain from Eqs. (2.56) and (2.57) the estimate [86]

$$E_{\rm rad} \gtrsim 0.1M. \tag{2.58}$$

This estimate includes both merger and ringdown radiation; we need to subtract the ringdown portion to obtain the energy radiated in the merger. Below we estimate $\sim 0.03M$ to be an approximate

upper bound for the ringdown energy. Hence most of the energy (2.58) should be radiated as merger waves.

There is an additional, separate argument one can make which indicates that most of the energy (2.58) should be radiated as merger waves and not as ringdown waves. As noted by Eardley and Hirschmann [87], any system with $J > M^2$ cannot evolve to $J < M^2$ by radiating quadrupolar waves at the ringing frequency $f_{\rm qnr} \sim 1/(2\pi M)$ of a near-extremal Kerr black hole. This is because at this high frequency, too much mass-energy is radiated per unit angular momentum radiated; Eq. (2.57) with $m = 2$ and with $f = f_{\rm qnr}$ yields $\Delta J = \Delta(M^2)$. Hence, since the final black hole must have $J < M^2$, a substantial amount of the radiation must be emitted at lower frequencies.

Based on the estimates (2.54) and (2.58), and on the estimated upper bound $\sim 0.03M$ which we derive below for the ringdown radiated energy, we take $0.1M$ as our radiated energy for the merger in the equal mass case. For non-equal-mass BBHs we assume that the radiated energy is reduced by the factor (2.5), so that

$$E_{\rm merger} = \epsilon_{\rm merger}\, F(\mu/M)\, M = 0.1 F(\mu/M) M. \tag{2.59}$$

This rather high radiation efficiency is probably most plausible in the context of rapidly spinning coalescing black holes. In particular, if the spins and the orbital angular momentum are somewhat misaligned, one would intuitively expect that such systems have more "settling down" to do to get to the final Kerr black hole, and that correspondingly the nonlinear, highly dynamical phase should last longer and/or produce more radiation. Also, the potential barrier that surrounds the final black hole (which normally tends to reflect back into the black hole the dominant waves of frequency $f \sim 1/$a few times M) presumably will effectively not be present during the violent phase of a merger in which the spins and orbital angular momentum are of comparable magnitude and are misaligned.

Coalescences which radiate as much energy as Eq. (2.59) may also radiate a substantial amount of linear momentum; the consequent recoil of the final black hole could correspond to a kick velocity that is a moderate fraction of the speed of light.

Finally, consider the shape of the energy spectrum dE/df between $f_{\rm merge}$ and $f_{\rm qnr}$. For simplicity, and for lack of evidence in favor of anything more specific, we choose a flat spectrum:

$$\frac{dE}{df} = \frac{\epsilon_m\, M\, F(\mu/M)}{f_{\rm qnr} - f_{\rm merge}}\, \Theta(f - f_{\rm merge})\Theta(f_{\rm qnr} - f)$$

$$= \quad 0.91 M^2 F(\mu/M)\ \Theta(f - f_{\rm merge})\Theta(f_{\rm qnr} - f), \tag{2.60}$$

where $\epsilon_m = \epsilon_{\rm merger} = 0.1$ and Θ is the step function.

2.3.3 Energy spectrum of the radiation from the inspiral phase

The standard quadrupole formula prediction for the inspiral energy spectrum is (see, *e.g.*, Ref. [88])

$$\frac{dE}{df} = \frac{1}{3}\pi^{2/3}\mu M^{2/3} f^{-1/3}. \tag{2.61}$$

This formula is adequate to estimate the SNR obtained from matched filtering of the inspiral waveform; it will be accurate to within a few tens of percent up to $f = f_{\rm merge}$ [63]. Using Eq. (2.61) to estimate the SNR assumes that both the gravitational-wave signal and the templates used to filter the data stream are given by the quadrupole approximation (2.61). The SNR we calculate using (2.61) will be approximately the same as that found by cross-correlating real signals against sufficiently accurate theoretical templates [which incorporate higher order corrections to Eq. (2.61)]. As outlined in Sec. 2.1.2, the required template accuracy should be achievable by post-Newtonian expansions [48, 89], perhaps supplemented with alternative techniques for the latter, high frequency part of the signal at $0.01/M \lesssim f \lesssim 0.02/M$ (the IBBH regime). We assume that the inspiral energy spectrum shuts off at $f = f_{\rm merge} = 0.02/M$, as discussed in Sec. 2.3.2 above.

2.3.4 Energy spectrum of the radiation from the ringdown phase

The ringdown of the gravitational-wave signal is that portion which can be fit fairly accurately by an exponentially decaying sinusoid corresponding to the $l = m = 2$ quasinormal mode of the final black hole. The shape of the corresponding energy spectrum is well understood: it is a resonance curve (although see Appendix B for discussion of a subtlety in the applicability of the concept of the waves' energy spectrum to calculating ringdown SNRs). The overall amplitude of the energy spectrum, however, is not well understood.

The QNR gravitational waveforms $h_+(t, \iota, \beta)$ and $h_\times(t, \iota, \beta)$ are given by [15]

$$h_+ - i h_\times = \frac{\mathcal{A} M}{r}\, {}_2S_2^2(\iota, \beta, a) e^{-2i\pi f_{\rm qnr} t - t/\tau + i\varphi_0}, \tag{2.62}$$

for $t > 0$. Here we have chosen $t = 0$ to be the start of the ringdown, M is the final black hole mass,

aM^2 is its spin, and φ_0 is a constant phase. The quantities ι and β are spherical polar coordinates centered on the black hole [*cf.* Sec. 2.2.3], ${}_2S_2^2(\iota,\beta,a)$ is a spin weighted spheroidal harmonic whose angle averaged rms value is

$$\left(\frac{1}{4\pi}\int d\Omega\,|{}_2S_2^2(\iota,\beta,a)|^2\right)^{1/2} = \frac{1}{\sqrt{4\pi}}, \tag{2.63}$$

and $\mathcal{A}$ is a dimensionless coefficient that describes the magnitude of the perturbation when the ringdown begins. The quantities $f_{\rm qnr}$ and τ are the frequency and damping time, respectively, of the $l=m=2$ QNR mode. The quality factor Q of the mode is given by $Q=\pi\tau f_{\rm qnr}$.

As mentioned in the Introduction, there is a mapping, explored by Leaver [90] and Echeverria [15], between the parameters (M,a) and $(f_{\rm qnr},\tau)$. Using the Teukolsky equation, Leaver produced catalogs of τ and $f_{\rm qnr}$ as functions of black hole mass M and dimensionless spin a [90]. From that data, Echeverria [15] produced the following analytic fits, which are good to about 5%:

$$\begin{aligned} f_{\rm qnr} &\approx \left[1-0.63(1-a)^{3/10}\right]\frac{1}{2\pi M} \\ &= \left[1-0.63(1-a)^{3/10}\right]\left(\frac{20\,M_\odot}{M}\right)1620\,{\rm Hz} \\ Q &\equiv \pi f_{\rm qnr}\tau \approx 2\,(1-a)^{-9/20}. \end{aligned} \tag{2.64}$$

The energy spectrum for the QNR waveform (2.62) is derived in Appendix A and is given by

$$\frac{dE}{df} = \frac{\mathcal{A}^2M^2f^2}{32\pi^3\tau^2}\left\{\frac{1}{[(f-f_{\rm qnr})^2+(2\pi\tau)^{-2}]^2}+\frac{1}{[(f+f_{\rm qnr})^2+(2\pi\tau)^{-2}]^2}\right\} \tag{2.65}$$

$$\approx \frac{1}{8}\mathcal{A}^2QM^2f_{\rm qnr}\,\delta(f-f_{\rm qnr})\,[1+O(1/Q)]\,. \tag{2.66}$$

Approximating the energy spectrum by a delta function as in Eq. (2.66) will often (but not always) provide a fairly good approximation to the SNR; see Appendix A for more details.

The value of the spin a of the final black hole and also of the amplitude $\mathcal{A}$ will depend on the initial parameters of the system, as in Eq. (2.48). This dependence is very poorly understood at present. We expect the final black hole to be rapidly spinning since, as explained in Sec. 2.3.2, the total angular momentum of the binary at the end of the inspiral is $\sim 0.9M^2$ when the individual black holes are non-spinning [65], and the individual black hole spins can augment this. Moreover, the individual black holes may typically have been spun up to near maximal rotation by an accretion disk [91]. For definiteness, we somewhat arbitrarily take $a=0.98$, which corresponds, from Eq.

(2.64), to $Q = 12$ and $f_{\rm qnr} = 0.13/M$. The final ringdown SNRs we obtain vary only weakly with our assumed value of a [*cf.* Eq. (2.124)], for fixed total energy radiated in the ringdown.

Although the value of the overall amplitude $\mathcal{A}$ is uncertain, we can estimate an upper bound on it for equal mass BBHs. Consider a Kerr black hole, distorted by an $l = m = 2$ perturbation such that the horizon's cross section is a rotating oval, rather than a circle. Quantify the distortion by computing the ratio of the polar circumference about the long axis of this oval to that about the short axis. Let $\mathcal{A}_2$ denote the perturbation amplitude such that this ratio of circumferences is $2:1$. Clearly, the validity of linear perturbation theory must break down for amplitudes $\mathcal{A} \gtrsim \mathcal{A}_2$ (due to nonlinear couplings between the $l = m = 2$ mode and other modes). At this $2:1$ distortion ratio, the signal will not be very well approximated by just the $l = m = 2$ mode. Therefore, $\mathcal{A}_2$ is a reasonable upper bound for the true amplitude $\mathcal{A}$.

In principle, we could calculate $\mathcal{A}_2$ by writing the spacetime metric as

$$g_{ab} = g_{ab}^{\rm KERR} + \mathcal{A}_2\, h_{ab}^{\rm QNR}$$

where $g_{ab}^{\rm KERR}$ is the Kerr metric and $h_{ab}^{\rm QNR}$ is the $l = m = 2$ quasinormal mode whose asymptotic form at large r is given by Eq. (2.62), and by calculating from this metric the ratio of circumferences [92]. For this paper, we used a much less sophisticated method to estimate $\mathcal{A}_2$. Using the quadrupole formula, we examined the radiation produced by a solid body that is distorted to this $2:1$ circumference ratio, and obtained the estimate $\mathcal{A}_2 \approx 0.4$ [93]. Setting our waveform amplitude $\mathcal{A}$ to this value yields an rms angle-averaged waveform $h = (0.4/\sqrt{4\pi})(M/r) = 0.1(M/r)$ at the beginning of ringdown. From Eq. (2.65), the corresponding radiated energy is

$$E_{\rm ringdown} \approx \frac{1}{8}\mathcal{A}^2 M^2 f_{\rm qnr} Q \approx 0.03M. \tag{2.67}$$

As mentioned in this chapter's introduction, comparable ringdown radiation efficiencies $\sim 3\%$ have been seen in numerical simulations of the evolution of distorted, spinning black holes [66].

To summarize, our assumed values for the black hole spin parameter a and for the amplitude $\mathcal{A}$ for equal-mass BBHs are

$$\begin{aligned} a &= 0.98 \\ \mathcal{A} &= 0.4. \end{aligned} \tag{2.68}$$

These imply the values

$$\begin{aligned} f_{\rm qnr} &= \frac{0.13}{M} = 1320\,{\rm Hz}\left(\frac{20M_\odot}{M}\right) \\ Q &= 12 \\ \epsilon_{\rm ringdown} &= E_{\rm ringdown}/M = 0.03. \end{aligned} \tag{2.69}$$

For non-equal-mass BBHs, we assume that $\epsilon_{\rm ringdown}$ is reduced by the factor (2.5).

2.3.5 Number of independent frequency bins for the merger phase

In Sec. 2.2.1 we showed that for any burst of gravitational waves, the band-pass filtering SNR is smaller than the matched filtering SNR by a factor of approximately

$$\sqrt{\mathcal{N}_{\rm bins}} = \sqrt{2T\Delta f} \tag{2.70}$$

[*cf.* Eq. (2.19) and associated discussion]. In this section, we estimate $\mathcal{N}_{\rm bins}$ for the merger gravitational waves, and hence determine the factor by which the SNR is degraded if band-pass filtering rather than matched filtering is used for merger wave searches.

First consider the bandwidth Δf. Our assumed bandwidth for the merger signal is $\Delta f = f_{\rm qnr} - f_{\rm merge} \approx f_{\rm qnr}$ [since $f_{\rm merge} \ll f_{\rm qnr}$; *cf.* Eqs. (2.50) and (2.51)]. We cannot, however, be completely confident that all signal power in the merger will lie at frequencies below $f_{\rm qnr}$, so a more appropriate choice might be $\Delta f \sim 2f_{\rm qnr}$. Also the quasinormal ringing frequency $f_{\rm qnr}$ depends on the dimensionless spin parameter a of the final black hole as given by Eq. (2.64). Choosing the highest possible value, $f_{\rm qnr} = 1/(2\pi M)$, yields

$$\Delta f \sim \frac{1}{\pi M}. \tag{2.71}$$

Turn, now, to the effective duration T of the merger, defined by Eq. (2.20). We expect that T will vary considerably from event to event, depending on the black hole parameters. To get a feeling for the range possible values of T, consider first the type of coalescence described in Sec. 2.3.2, with both black holes nearly maximally spinning with spins and orbital angular momentum aligned. In this favorable case, recall that the binary has to shed an excess angular momentum of about $0.4M$ during the merger in order to settle down its final Kerr state. Thus, the two black holes

might well be centrifugally hung-up, orbiting for many cycles before their event horizons merge, so that the duration of the merger might be quite long. By contrast, when two non-spinning black holes merge, there is probably no excess angular momentum that must be shed after the orbital dynamical instability, so the merger might be fairly quick. (In such a case, the ringdown waves might carry most of the emitted energy.)

To estimate T in the angular-momentum-excess scenario, assume that the luminosity dE/dt during the merger is about the same as the luminosity at the start of the ringdown, $2\epsilon_{\rm ringdown}M/\tau$. Since the total energy radiated in the merger is $\epsilon_{\rm merger}M$, we find

$$T \approx \frac{1}{2}\frac{\epsilon_{\rm merger}}{\epsilon_{\rm ringdown}}\tau. \tag{2.72}$$

Clearly this estimate will become invalid for high values of τ ($a \to 1$); in that limit, the high quality factor of the QNR mode causes a low QNR luminosity, whereas there is no reason for the merger luminosity to be comparably low. Nevertheless, we insert our assumed parameter values (2.59), (2.69), and (2.68) into Eqs. (2.64) and (2.72) and find $T \sim 50M$. Combining this with Eqs. (2.19) and (2.71) yields

$$\sqrt{\mathcal{N}_{\rm bins}} \sim \sqrt{30} \sim 5. \tag{2.73}$$

For inspiraling Schwarzschild black holes, on the other hand, T may not be much larger than a single QNR damping time: $T \approx \tau \approx 10M$ (assuming $a = 0.5$ say), yielding $\sqrt{\mathcal{N}_{\rm bins}} \approx \sqrt{6}$.

The factor $\sqrt{\mathcal{N}_{\rm bins}}$ is thus likely to lie in the range $2 \lesssim \sqrt{\mathcal{N}_{\rm bins}} \lesssim 5$. We adopt the estimate $\sqrt{\mathcal{N}_{\rm bins}} = 4$ in Sec. 2.6.2 to estimate the reduction in SNR resulting from using band-pass filtering instead of matched filtering. We use the conservatively large value $\mathcal{N}_{\rm bins} = 60$ in Sec. 2.6.2 to estimate detection thresholds for noise-monitoring searches for signals.

2.4 Interferometer noise curves

In this section we describe our piecewise power law, analytic approximation to the noise curves for initial LIGO interferometers, advanced LIGO interferometers, and the LISA interferometer. We express our model in terms of the dimensionless quantity $h_{\rm rms}(f) \equiv \sqrt{fS_h(f)}$, where $S_h(f)$ is the one sided power spectral density of the interferometer noise [61]. Our model for the noise spectrum

is

$$h_{\rm rms}(f) = \begin{cases} \infty & f < f_s, \\ h_m \left(\alpha f/f_m\right)^{-3/2} & f_s \leq f < f_m/\alpha \\ h_m & f_m/\alpha \leq f < \alpha f_m \\ h_m \left[f/(\alpha f_m)\right]^{3/2} & \alpha f_m < f. \end{cases} \tag{2.74}$$

The noise curve depends on four parameters: (i) A lower shutoff frequency f_s below which the noise rapidly becomes very large and can be taken to be infinite. For ground based interferometers, this low-frequency shutoff is due to seismic noise; for LISA, it is due to accelerometer noise (Ref. [7], p. 23). (ii) A frequency f_m, which is the location of the center of the flat portion of the spectrum. (iii) A dimensionless parameter h_m, which is the minimum value of $h_{\rm rms}(f)$. (iv) A dimensionless parameter α which determines the width of the flat portion of the noise curve. We approximate the noise curves by piecewise power laws in this way for calculational convenience.

For initial and advanced LIGO interferometers, we determined best-fit values of the parameters f_s, f_m, h_m and α by fitting to the noise curves given in Ref. [3]. (Note that Fig. 7 of Ref. [3] is a factor of 3 too small from $\sim$ 10 Hz to $\sim$ 70 Hz. This error does not appear in Fig. 10 of that reference [94].) The resulting parameter values are:

$$\left.\begin{array}{rcl} f_s &=& 40\,{\rm Hz} \\ f_m &=& 160\,{\rm Hz} \\ \alpha &=& 1.4 \\ h_m &=& 3.1 \times 10^{-22} \end{array}\right\} \quad \begin{array}{l} \text{INITIAL LIGO} \\ \text{INTERFEROMETER,} \end{array} \tag{2.75}$$

and

$$\left.\begin{array}{rcl} f_s &=& 10\,{\rm Hz} \\ f_m &=& 68\,{\rm Hz} \\ \alpha &=& 1.6 \\ h_m &=& 1.4 \times 10^{-23} \end{array}\right\} \quad \begin{array}{l} \text{ADVANCED LIGO} \\ \text{INTERFEROMETER.} \end{array} \tag{2.76}$$

For ground-based interferometers, the $f^{-3/2}$ portion of our approximate formula (2.74) models the thermal suspension noise and the $f^{3/2}$ portion models the laser shot noise [97].

For the space-based LISA interferometer, we determined best-fit values of the parameters f_m, h_m and α by fitting to the noise curve given in Ref. [10], and obtained the lower cutoff frequency

f_s from Ref. [7]. The resulting parameter values are:

$$\left.\begin{array}{rcl} f_s &=& 10^{-4}\,\mathrm{Hz} \\ f_m &=& 3.7\times 10^{-3}\,\mathrm{Hz} \\ \alpha &=& 5.5 \\ h_m &=& 5.8\times 10^{-22} \end{array}\right\} \begin{array}{l} \text{LISA} \\ \text{INTERFEROMETER.} \end{array} \tag{2.77}$$

Our piecewise power-law model is less accurate for LISA than for the LIGO interferometers, but it is still a fairly good approximation.

The sensitivity of LISA at the lower end of its frequency window may be degraded somewhat by a background of gravitational waves from white dwarf binaries [7]. We neglect this issue here as this white dwarf noise level is fairly uncertain (see Ref. [99] for a recent discussion).

2.5 Signal-to-noise ratios

In this section we calculate the angle-averaged SNRs for the three coalescence epochs (inspiral, merger, and ringdown) for initial LIGO interferometers, for advanced LIGO interferometers, and for LISA.

2.5.1 Specific examples

We start by rewriting the general formula (2.36) for the SNR in a more useful form. If we define the characteristic gravitational-wave amplitude

$$h_{\mathrm{char}}(f)^2 \equiv \frac{2(1+z)^2}{\pi^2 D(z)^2}\,\frac{dE}{df}[(1+z)f], \tag{2.78}$$

then from Sec. 2.2.3 the SNR squared (2.13) for an optimally oriented source can be written as

$$\rho^2_{\text{optimal orientation}} = \int d(\ln f)\,\frac{h_{\mathrm{char}}(f)^2}{h_{\mathrm{rms}}(f)^2}, \tag{2.79}$$

where $h_{\mathrm{rms}}(f) = \sqrt{f S_h(f)}$. From Eq. (2.36), the angle-averaged SNR squared is a factor of 5 smaller than the optimal value (2.79), so we can rewrite Eq. (2.36) as

$$\langle \rho^2 \rangle = \int d(\ln f)\,\frac{h_{\mathrm{char}}(f)^2}{h_n(f)^2}, \tag{2.80}$$

where $h_n(f) \equiv \sqrt{5} h_{\rm rms}(f)$ is the rms noise appropriate for waves from random directions with random orientations [100]. Plotting $h_{\rm char}(f)$ and $h_n(f)$ for various sources illustrates [from Eq. (2.80)] the possible SNR values and the distribution of SNR squared with frequency.

In Fig. 2.1, we show the rms noise amplitude $h_n(f)$ for our model (2.74) of the initial and advanced LIGO interferometer noise curves, together with the characteristic amplitude $h_{\rm char}(f)$ for two different BBH coalescences: a coalescence of total mass $20\,M_\odot$ at a distance of $D = 200\,{\rm Mpc}$, and a $30\,M_\odot$ coalescence at redshift $z = 1$. (We assume that the cosmological parameters are $\Omega_0 = 1$ and $H_0 = 75\,{\rm km\,s^{-1}\,Mpc^{-1}}$.) In each case, the sloped portion of the dashed $h_{\rm char}$ line is the inspiral signal, the flat portion is our crude model of the merger, and the separate dotted portion is the ringdown. Note that the ringdown and merger overlap in the frequency domain since (as we have defined them) they are disjoint in the time domain, while the inspiral and merger are approximately disjoint in both the frequency and time domains (Sec. 2.3.1 above).

In both cases, $20\,M_\odot$ and $30\,M_\odot$, the waves' characteristic amplitude $h_{\rm char}(f)$ is rather larger than $h_n(f)$ for most of the merger spectrum for the advanced interferometers, indicating the detectability of the merger waveform when matched filtering can be used. In particular, note that the waves should be quite visible to the advanced interferometers for the $30\,M_\odot$ binary even though it is at a cosmological distance. Even if such binaries are rare, they are visible to such great distances that they may be an important and interesting source. Cosmological binaries have an enhanced SNR in part because the cosmological redshift moves their frequency spectrum down closer to LIGO's optimal band.

Figure 2.1 also shows that, of these two example BBH coalescences, only the nearby one at a distance of $D = 200\,{\rm Mpc}$ would be detectable by the initial interferometers. As discussed in the Introduction, such coalescences may yield an interesting event rate for the initial interferometers.

A qualitatively different, possibly important type of source for the initial LIGO interferometers (and also for the advanced interferometers) is the coalescence of black hole binaries with masses of order $100\,{\rm M}_\odot$, as we have discussed in the Introduction. In Fig. 2.2 we show the characteristic amplitude $h_{\rm char}(f)$ for a hypothetical BBH coalescence of total mass $100\,M_\odot$ at redshift $z = 0.5$, corresponding to a luminosity distance of $D = 2.2\,{\rm Gpc}$. Note in particular that the initial LIGO interferometer noise curve has best sensitivity near 200 Hz just where the (redshifted) ringdown frequency is located. We discuss further in Sec. 2.6 the range of initial LIGO interferometers for this type of source.

Turn, now, to the detection of supermassive BBH signals by the space-based detector LISA

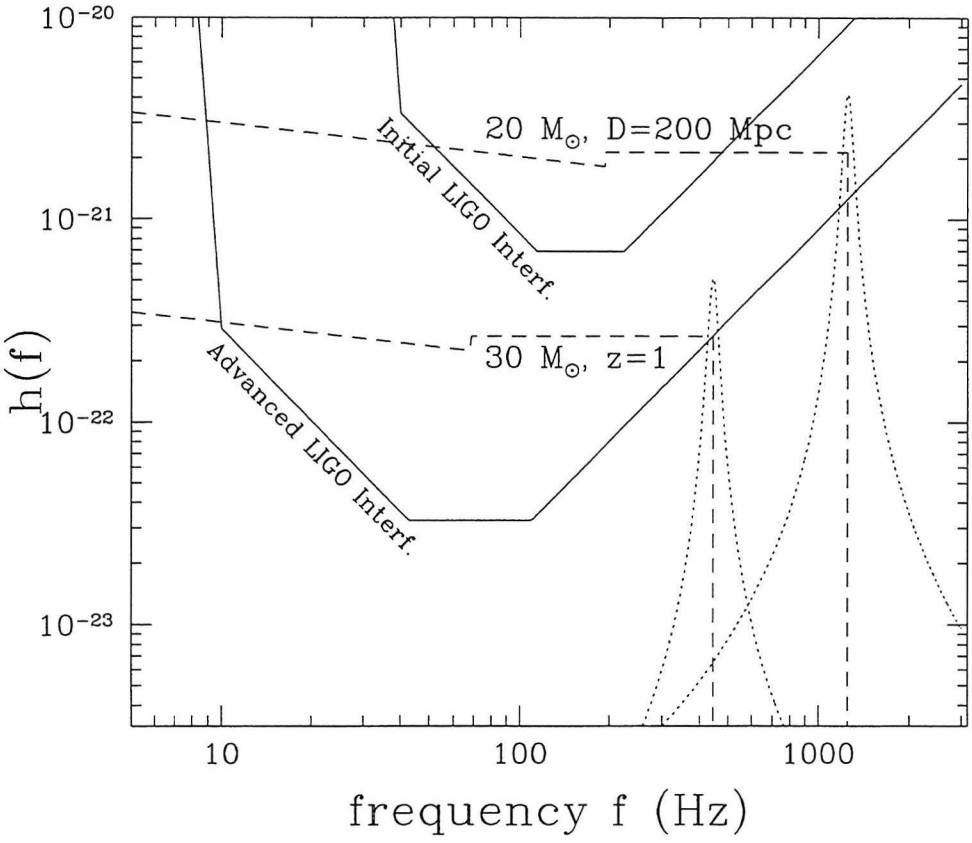

Figure 2.1: The relative magnitudes of our estimates of the *inspiral*, *merger* and *ringdown* energy spectra for two solar-mass BBH mergers.

The solid lines are the rms noise amplitudes $h_n(f) \equiv \sqrt{5fS_h(f)}$ for our assumed model (2.74) of the LIGO initial and advanced interferometer noise spectra. The dashed and dotted lines show the characteristic amplitude $h_{\rm char}(f) \propto \sqrt{dE/df}$ of the waves, defined by Eq. (2.78). The definition of $h_{\rm char}$ is such that the signal-to-noise ratio squared for a randomly oriented source is given by $(S/N)^2 = \int d(\ln f)\, [h_{\rm char}(f)/h_n(f)]^2$. The upper dashed and dotted lines correspond to a binary of two $10M_\odot$ black holes at a distance of $D = 200$ Mpc. The sloped portion of the dashed line is the inspiral, which gives an SNR for the initial (advanced) interferometer noise curve of 2.6 (84). The flat portion is our crude model of the merger, which gives an SNR of 2.1 (16). The dotted line is our estimate of the ringdown, which gives an SNR of 0.1 (0.86). The lower dashed and dotted lines correspond to a binary of two $15M_\odot$ black holes at redshift $z = 1$ (or at a luminosity distance of $D = 4.6$ Gpc; the cosmological parameters $\Omega_0 = 1$ and $H_0 = 75\,{\rm km\,s^{-1}Mpc^{-1}}$ were assumed). In this case the inspiral, merger and ringdown SNRs for the initial (advanced) interferometers are 0.08, 0.42, and 0.07 (6.6, 7.2 and 0.5) respectively. Black hole binaries with constituents this massive will be visible to great distances, making them a possibly important source, depending on the very uncertain event rate. The SNR from the merger is enhanced for these massive distant sources in part because the combination of cosmological redshift and lower intrinsic frequency brings the merger waves down to lower frequencies where the interferometer noise is smaller.

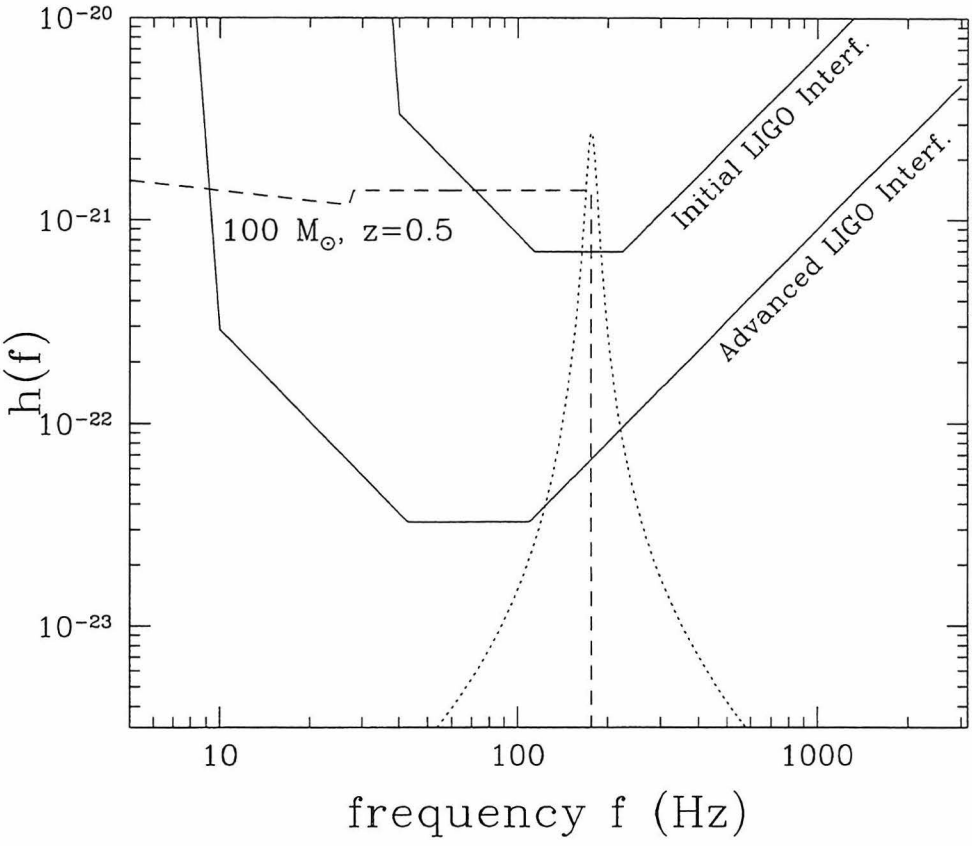

Figure 2.2: The relative magnitudes of our estimates of the energy spectra for an intermediate-mass BBH merger.

The gravitational-waves depicted here come from the merger of a binary consisting of two 50 $M_\odot$ black holes at redshift $z = 0.5$. They are plotted with the rms noise amplitudes $h_n(f)$ for both the initial and advanced interferometer noise curves for LIGO (see caption of Fig. 2.1). The SNRs for the inspiral, merger, and ringdown stages are about 0, 1.7 and 1.0 respectively for the initial interferometer noise level, and about 11, 52 and 11 respectively for advanced interferometers.

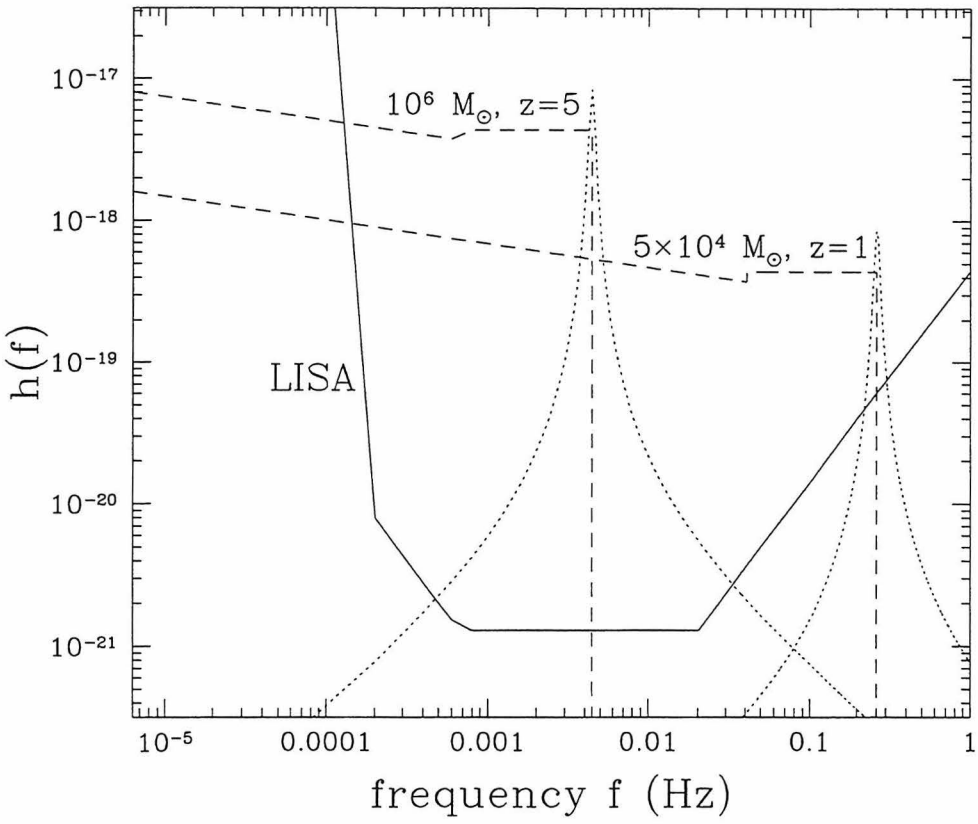

Figure 2.3: The relative magnitudes of our estimates of the energy spectra for two supermassive BBH mergers.

The noise spectrum $h_n(f)$ of the space-based detector LISA, together with the characteristic amplitudes $h_{\rm char}$ of two equal-mass BBH coalescences (see caption of Fig. 2.1). The first is a binary of total mass $10^6\,M_\odot$ at redshift $z = 5$. The inspiral signal of this binary enters the LISA waveband at $f \simeq 10^{-4}$ Hz about one week before the final merger; the SNRs from inspiral, merger and ringdown are about 1800, 4600 and 1700 respectively. The second is a binary of total mass $5 \times 10^4 M_\odot$ at redshift $z = 1$, which enters the LISA waveband about twenty years before the final merger. For this binary an SNR of approximately 900 would be obtained for the last year of inspiral (from $f \simeq 1.6 \times 10^{-4}$ Hz to $f \simeq 4 \times 10^{-2}$ Hz). The SNRs from the merger and ringdown would be about 70 and 4.

[5, 6]. LISA can study BBH mergers with far higher accuracy and resolution than the ground based interferometers, because the SNR values are typically much higher ($\gtrsim 10^3$). When calculating inspiral SNRs for LISA, it is necessary to restrict the integral over frequency in Eq. (2.36) to a domain that corresponds to, say, one year of observation—some binaries require hundreds of years to pass through LISA's band. See Appendix B for details.

Figure 2.3 shows our approximate model [Eqs. (2.74) and (2.77)] of LISA's projected noise spectrum, together with the gravitational-wave amplitude $h_{\rm char}(f)$ for the inspiral, merger and ringdown stages of two different BBH coalescences: a BBH of total mass $10^6 M_\odot$ at redshift $z = 5$, and a BBH of total mass $5 \times 10^4 M_\odot$ at redshift $z = 1$. The $10^6 M_\odot$ BBH enters the LISA waveband at $f = f_s \simeq 10^{-4}$ Hz roughly one week before the final merger. The SNRs obtained in this case from the inspiral, merger and ringdown signals are approximately 1800, 4600 and 1700 respectively. The $5 \times 10^4 M_\odot$ BBH enters the LISA waveband about twenty years before the final merger. The SNR obtained from the last year of the inspiral signal, from $f \simeq 1.6 \times 10^{-4}$ Hz to $f \simeq 4 \times 10^{-2}$ Hz is approximately 900, while the merger and ringdown SNRs are about 70 and 4 respectively.

2.5.2 The general signal-to-noise ratio results

We now turn from these specific examples to the dependence of the SNR values on the mass of and distance to the binary in general. In Appendix B we obtain analytic formulae for the SNR values for the three phases of BBH coalescences, and for the various interferometers. In this section we plot the results for equal-mass BBHs, which are shown in Figs. 2.4, 2.5 and 2.6. The inspiral and merger curves in these figures (except for the LISA inspiral curves; see Appendix B) are obtained from Eqs. (2.114) and (2.120) of Appendix B, while the ringdown curves are obtained by numerically integrating Eq. (2.65) in Eq. (2.36).

The SNR values for the initial LIGO interferometers are shown in Fig. 2.4. This figure shows that an important source for the initial LIGO interferometers may be the coalescences of binary black holes with total masses of order several hundred solar masses. These would be visible out to almost 1 Gpc. For such sources, the inspiral portion of the signal would not be detectable, and one would need to search for the ringdown or merger to detect the waves. See Sec. 2.6 for further discussion. The event rate for such high mass BBHs is very uncertain; see Ref. [17] for a possible formation scenario. Intermediate mass BBHs with $\mu \ll M$ (*e.g.*, $m_1 = 10\,M_\odot$, $m_2 = 500 M_\odot$) are presumably much more common than the intermediate mass BBHs with $\mu \sim M$ discussed above. The SNRs for such mixed binaries will be much lower, however. As seen in Appendix A, the merger

and ringdown SNR's scale as $(\mu/M)^2$, while the inspiral scales as μ/M. (The scaling difference arises because the inspiral duration scales as $1/\mu$, whereas the merger and ringdown durations are approximately independent of μ.)

Figure 2.4 also shows that the inspiral of BBH mergers with $M \lesssim 30M_\odot$ should be visible to about 200 Mpc (the SNR detection threshold is about 5 [44]). The ground-based interferometers will, over a period of years, gradually be improved from the initial sensitivity levels to the advanced sensitivity levels [3]. Roughly half way between the initial and advanced interferometers, the range of the detector system for $M \lesssim 30M_\odot$ BBHs will be $\sim$ 1 Gpc. If the BBH birthrate is as large as was discussed in this chapter's introduction, they should be detected early in the gradual process of interferometer improvement.

Figure 2.5 shows the SNR values for the advanced LIGO interferometers. It can be seen that for advanced LIGO interferometers, equal-mass BBH inspirals will be visible out to $z \sim 1/2$ for the entire range of masses $10M_\odot \lesssim (1+z)M \lesssim 300M_\odot$. Thus, there is likely to be an interesting event rate. Indeed, the SNRs will be high enough even for rather large distances that it should be possible to extract each binary's parameters with reasonable accuracy [10]. By contrast, the ringdown SNR is fairly small except for the largest mass systems. For very massive binaries or binaries that are closer than 1 Gpc, advanced interferometers may measure fairly large ringdown SNRs, which would allow fairly good estimates of the mass and spin of the final black hole [15, 16].

Figure 2.6 shows the SNR values obtainable from the three phases of BBH coalescences by LISA: the last year of inspiral, the merger and the ringdown. We also show the SNR value obtainable from one year of integration of the inspiral signal one hundred years before the merger, and a similar curve for one thousand years before the merger. This figure shows that LISA will be able to perform very high accuracy measurements of BBH mergers (SNR values $\gtrsim 10^3$) essentially throughout the observable Universe ($z \lesssim 10$) in the mass range $10^6\, M_\odot \lesssim M \lesssim 10^9\, M_\odot$. As discussed in this chapter's introduction, there is a good chance there will be an interesting event rate. The SNR curves in Fig. 2.6 for measurements one hundred and one thousand years before merger show that many inspiraling BBHs that are far from merger should be detectable by LISA as well. If the merger rate of SMBH binaries turns out to be about one per year throughout the observable Universe, then at any given time one would expect roughly one thousand SMBH binaries to be a thousand years or less away from merger. LISA will be able to monitor the inspiral of such binaries (if they are of sufficiently low mass) with moderate to large SNR [10].

Finally, it should be noted that the relative magnitude of the merger and ringdown SNR values

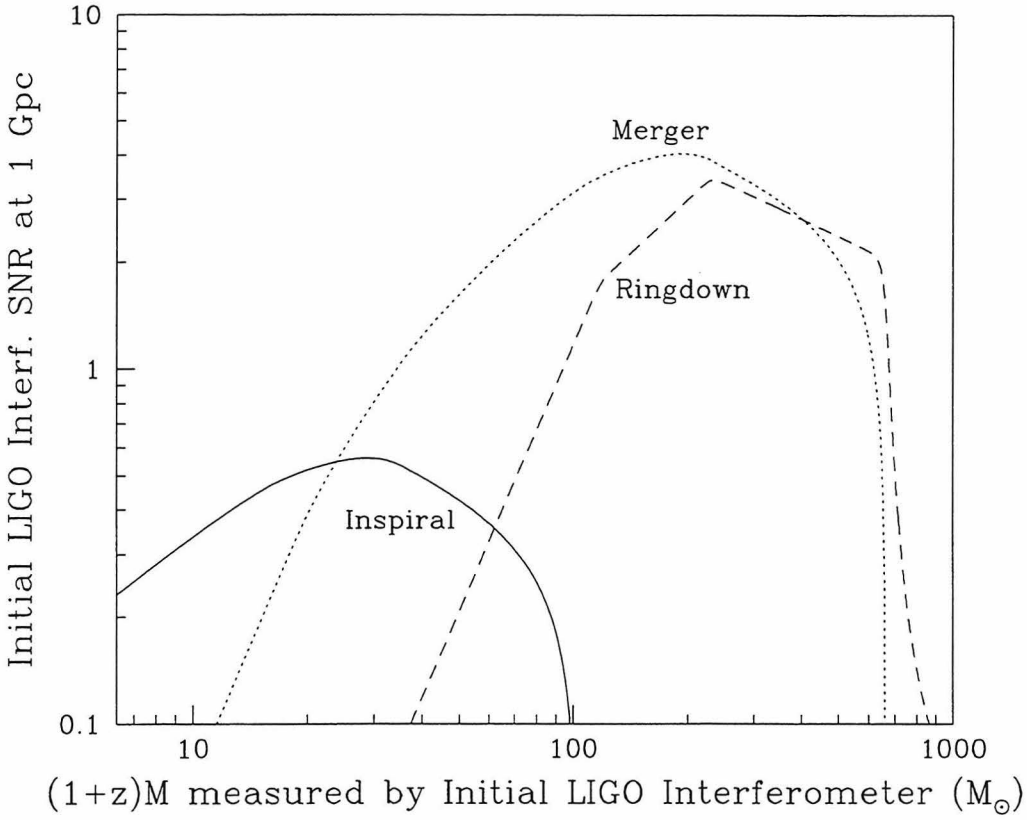

Figure 2.4: The SNR for equal-mass BBH coalescences detected by LIGO initial interferometers, assuming matched filtering.

The SNR is given as a function of the redshifted mass $(1+z)M$ of the final black hole, at a luminosity distance of $D = 1$ Gpc. For fixed redshifted mass, the SNR values are inversely proportional D. The solid, dotted, and dashed curves are the SNR values from the inspiral, merger and ringdown respectively. For non equal-mass binaries, the inspiral SNRs will be reduced by the factor $\sim \sqrt{4\mu/M}$, while the merger and ringdown SNRs will be reduced by $\sim 4\mu/M$; thus the inspiral will be enhanced relative to the merger and ringdown. This plot indicates that BBH coalescences of systems with masses of order several hundred solar masses may be an important source for the initial LIGO interferometers. These events would be visible to almost 1 Gpc. For such sources, the inspiral would not be detectable, and the waves would have to be detected using either the ringdown or the merger.

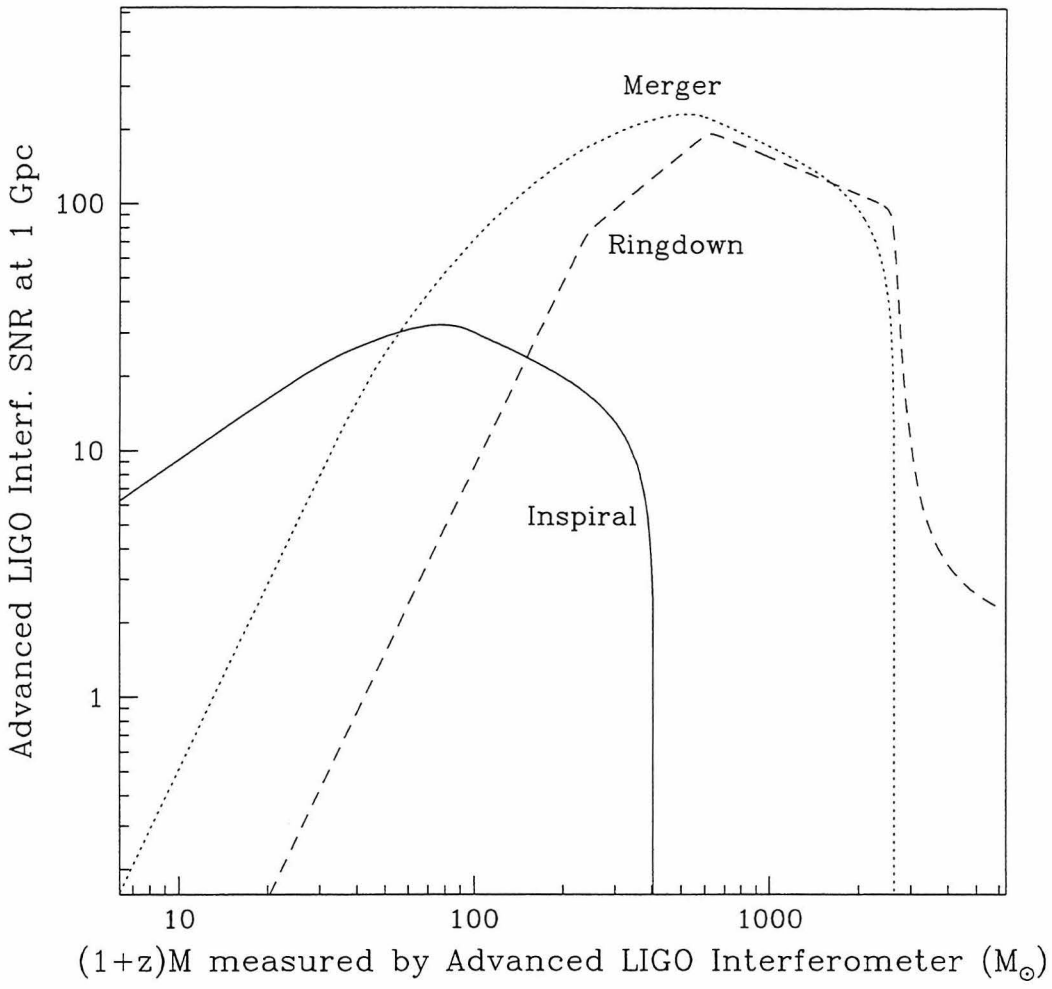

Figure 2.5: The SNR for equal-mass BBH coalescences detected by LIGO advanced interferometers, assuming matched filtering.

The SNR values are shown for the inspiral (solid line), merger (dotted line) and ringdown (dashed line) phases of equal-mass BBH coalescences at a luminosity distance of $D = 1\,\mathrm{Gpc}$; see the caption of Fig. 2.4. For values of the redshifted final mass lower than $\sim 60\,M_\odot$ the inspiral SNR is largest, while for larger BBH systems the merger and/or ringdown portions of the signal dominate.

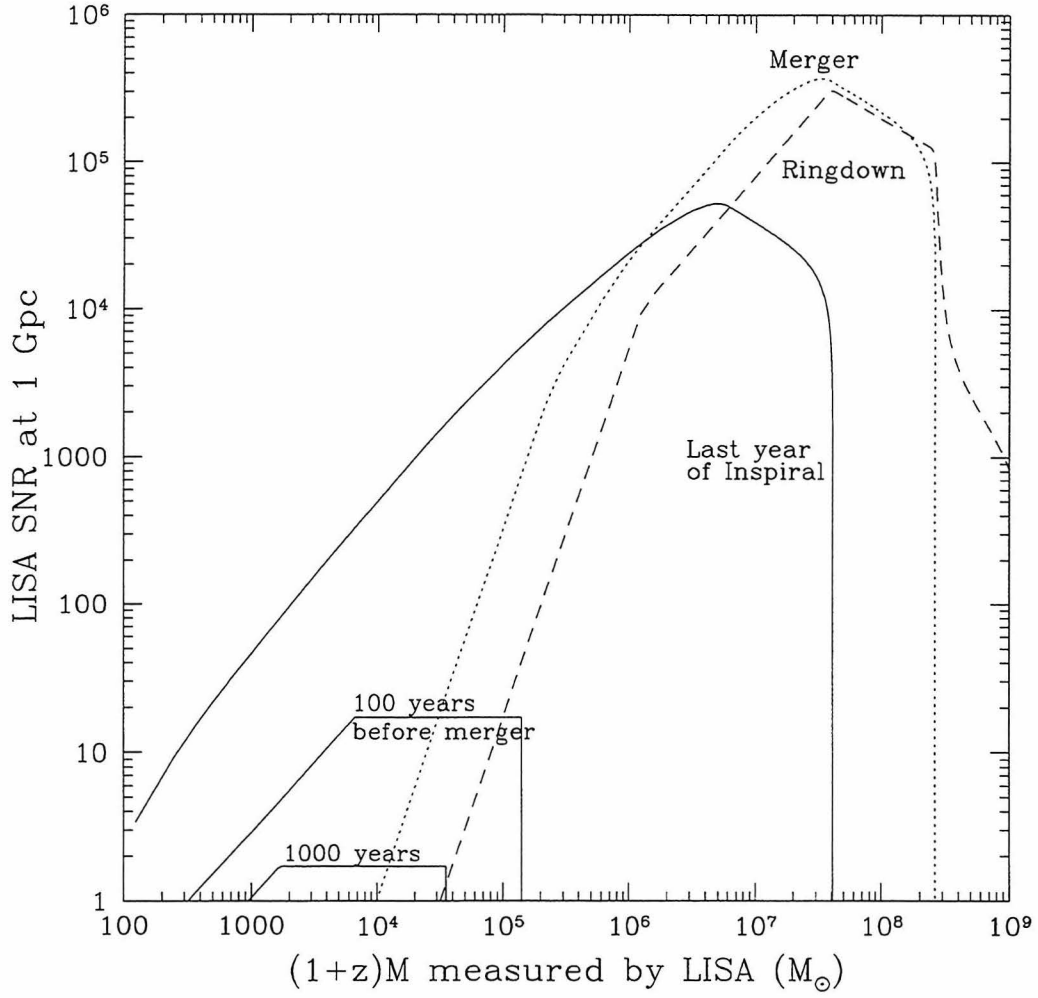

Figure 2.6: The SNR for equal-mass BBH coalescences detected by LISA, assuming matched filtering.

The SNR values are shown as a function of the redshifted mass $(1+z)M$ of the final black hole, at a luminosity distance of $D = 1\,\mathrm{Gpc}$. The dotted and dashed curves are the SNR values from the merger and ringdown, respectively. The upper solid curve is the SNR that would be obtained from measuring the last year of the inspiral. For $(1+z)M \lesssim 10^6\,M_\odot$, the last-year-inspiral SNR is largest; for larger BBH systems the merger and/or ringdown dominate. Also shown (lower solid curves) are the SNRs that would be obtained from one year of integration of the inspiral at one hundred and one thousand years before the final merger. If the rate of SMBH coalescences within $z \lesssim$ (a few) is roughly one per year, then one would expect roughly one thousand SMBH binaries to be a thousand years or less away from merger. This plot shows that LISA will be able to measure the inspiral of such binaries (provided they are of sufficiently low mass) with moderate to large SNR [10].

is somewhat uncertain. We have assumed a total radiated energy of $0.1M$ in the merger portion of the signal, and $0.03M$ in the ringdown portion, a ratio of $3:1$. It may turn out that in individual cases the ratio is as high as 10 or as low as $\lesssim 1$. It may even turn out to be the case that for many coalescences, the ringdown portion of the waveform carries most of the radiated energy of the combined merger/ringdown regime (depending possibly on the distribution of initial spins). Thus, the SNR values shown in Figs. 2.4, 2.5 and 2.6 should merely be taken as illustrative.

2.6 Implications for detectability of the gravitational-wave signal

One of the reasons that coalescences of compact objects are such good sources for gravitational-wave detectors is that the inspiral is very predictable, so that matched filtering may be used for signal searches [1]. As we have discussed, matched filtering enhances the achievable inspiral SNR values by a factor of roughly $\sqrt{\mathcal{N}_{\rm cyc}}$, where $\mathcal{N}_{\rm cyc}$ is the number of cycles of the waveform in the frequency band of the detectors. For neutron star-neutron star (NS-NS) coalescences, $\mathcal{N}_{\rm cyc}$ will be on the order of several thousand, while for low mass ($M \lesssim 50M_\odot$) BBH coalescences it will be on the order of several hundred [44]. Thus, for NS-NS coalescences and for low mass BBH coalescences, the inspiral will be used to *detect* the entire waveform. In these cases, it is not necessary to *search* for the merger and ringdown portions of the waveform, since it will be known roughly where in the interferometer data stream they are expected to lie.

For larger mass BBHs, however, our results show that the merger and ringdown SNRs can be larger than the inspiral SNRs. For equal-mass BBHs, this will occur whenever $(1+z)M \gtrsim 30M_\odot$ for the initial LIGO interferometers, and whenever $(1+z)M \gtrsim 60M_\odot$ for the advanced LIGO interferometers. Indeed, the inspiral SNR completely shuts off for large enough $(1+z)M$, as can be seen from Figs. 2.4 and 2.5. Admittedly, BBH binaries of total mass $\gg 20M_\odot$ may well be very much more rare than BBH binaries of $\sim 20M_\odot$; however, they will be visible to such great distances that there may be an interesting event rate. Moreover, for the initial LIGO interferometers, the mass scale $\sim 30M_\odot$ at which the inspiral SNR becomes much smaller than the merger/ringdown SNRs is not terribly high.

In such high mass cases for which the merger and inspiral SNRs exceed the inspiral SNR, it will be necessary to perform a search for the merger and/or ringdown portions of the signal, independently of any searches for inspiral signals, in order that all possible events be detected. If one seeks to detect the waves merely by optimal filtering for the inspiral waveform, some fraction

of the events will be missed which otherwise might have been detectable. In fact, it may very well turn out that merger signals from BBH coalescences could be the dominant source for the initial LIGO interferometers.

One might imagine that the gravitational waves would generally be easier to detect by searching for the merger signal than for the ringdown, since we have estimated that the SNR values for the merger phase are typically a factor of a few larger than those for the ringdown (*cf.* Figs. 2.4 and 2.5). There are several factors that complicate this conclusion, however. On the one hand, the ringdown's waveform shape is better understood, which makes it easier to produce search templates and hence easier to detect the signal. On the other hand, the ratio between the merger and ringdown SNRs is really quite uncertain, as discussed in Sec. 2.5.2, and so it is plausible that the merger SNR will be larger than we have indicated relative to the ringdown SNR. In any case, the ratio between merger and ringdown SNRs will presumably vary a lot from event to event. Thus, it would seem that searches will be necessary for *both* types of signal in the data stream, at least for the mass range in which the ringdown SNR is expected to exceed the inspiral SNR. [From Sec. 2.5 we estimate this mass range to be $(1+z)M \gtrsim 200\,M_\odot$ for the advanced interferometers, and $(1+z)M \gtrsim 60 M_\odot$ for the initial interferometers.]

We summarize the discussion of this subsection by displaying the optimum search strategies for various mass ranges for the three different interferometers. In each case below, the mass range marked merger refers to matched filtering searches for merger signals. If merger templates are available, then in the indicated mass ranges merger searches will probably be more successful than inspiral or ringdown searches; the question mark is a reminder that merger templates may not be available.

$$\left.\begin{array}{lcll} \text{INSPIRAL} & : & 1M_\odot \lesssim M \lesssim 60M_\odot & \\ \text{RINGDOWN} & : & 60M_\odot \lesssim M \lesssim 1000M_\odot & \text{INITIAL} \\ \text{MERGER (?)} & : & 30M_\odot \lesssim M \lesssim 1000M_\odot & \text{INTERF.} \end{array}\right\} \tag{2.81}$$

$$\left.\begin{array}{lcll} \text{INSPIRAL} & : & 1M_\odot \lesssim M \lesssim 200M_\odot & \\ \text{RINGDOWN} & : & 200M_\odot \lesssim M \lesssim 3000M_\odot & \text{ADVANCED} \\ \text{MERGER (?)} & : & 80M_\odot \lesssim M \lesssim 3000M_\odot & \text{INTERF.} \end{array}\right\} \tag{2.82}$$

$$\left.\begin{array}{lll} \text{INSPIRAL} & : & 10^3 M_\odot \lesssim M \lesssim 10^7 M_\odot \\ \text{RINGDOWN} & : & 10^7 M_\odot \lesssim M \lesssim 10^9 M_\odot \\ \text{MERGER (?)} & : & 2 \times 10^6 M_\odot \lesssim M \lesssim 10^9 M_\odot \end{array}\right\} \begin{array}{l} \text{LISA} \\ \\ \text{INTERF.} \end{array} \tag{2.83}$$

2.6.1 The detectability of high mass black-hole coalescences via the ringdown signal

Consider first the search for ringdown signals. In this case, since the shape of the signal is known up to several unknown parameters, it will be feasible to implement a matched filtering search. The number $\mathcal{N}_{\text{templates}}$ of required templates [72] can be estimated by combining the formalism developed by Owen [89] and the results of Echeverria and Finn on the expected measurement accuracy of the ringdown frequency and damping time [15, 16]. Using Eqs. (4.15) of Ref. [16] and Eqs. (2.23) and (2.28) of Ref. [89] we find that the metric defined by Owen on the space of parameters is given by [101]

$$ds^2 = \frac{1}{8Q^2} dQ^2 + \frac{Q^2}{2f_{\text{qnr}}^2} df_{\text{qnr}}^2, \tag{2.84}$$

where Q is the quality factor. The formula (2.84) for the Owen metric is valid only in the high Q limit; it has corrections of order $1/Q^2$. Moreover, the formula is also only valid when the noise spectrum $S_h(f)$ does not vary significantly within the resonance bandwidth $\Delta f \sim f_{\text{qnr}}/Q$. Therefore estimates obtained from Eq. (2.84) for the number of template shapes required for ringdown searches will only be accurate to within factors of order unity; this is adequate for our purposes.

Using Eq. (2.16) of Ref. [89] we find that that the number of required templates is approximately

$$\mathcal{N}_{\text{templates}} \approx \frac{1}{8} Q_{\max} (1 - MM)^{-1} \ln \left[\frac{M_{\max}}{M_{\min}} \right], \tag{2.85}$$

where $Q_{\max}$, $M_{\min}$ and $M_{\max}$ are the extremal values of the quality factor and of the black hole mass that define the range of signal searches. The quantity MM in the formula (2.85) is the *minimal match* parameter introduced by Owen. A lattice of templates with minimal match MM will have an event detection rate smaller than the ideal rate (achieved with an infinitely dense template grid) by the factor $(MM)^3$ [89]. We assume $MM = 0.97$ as in Ref. [89], corresponding to a 10% event rate loss, and take $Q_{\max} = 100$ [which by Eq. (2.64) corresponds to $1 - a \simeq 10^{-4}$]. For the initial and advanced LIGO interferometers, the mass range to be searched corresponds to roughly

$M_{\rm min} \simeq 1 M_\odot$ and $M_{\rm max} = 5000 M_\odot$, yielding

$$\mathcal{N}_{\rm templates} \lesssim 4000. \tag{2.86}$$

This is a rather small number of templates compared to the number expected to be necessary for inspiral searches [89], so a ringdown search should be fairly easy to implement. A similarly small number of required template shapes ($\mathcal{N}_{\rm templates} \lesssim 6000$) is obtained for LISA assuming $M_{\rm min} \sim 10^3 M_\odot$ and $M_{\rm max} \sim 10^9 M_\odot$.

We next discuss the distance to which BBH mergers should be detectable via their ringdown signals. As explained in Sec. 2.2.3, an estimate of the appropriate SNR threshold for detection using one interferometer is [102]

$$\rho_{\rm threshold} \approx \sqrt{2 \ln[\mathcal{N}_{\rm templates} T/(\epsilon \Delta t)]} \tag{2.87}$$

where T is the observation time, Δt is the sampling time and $\epsilon = 10^{-3}$ is as defined in Section 2.2.2. In fact coincidencing between the 4 different interferometers in the LIGO/VIRGO network will be carried out, in order to increase detection reliability and combat non-Gaussian noise (see Sec. 2.2.1). If the noise were exactly Gaussian, the appropriate detection criterion would be to demand that

$$\sum_j \rho_j^2 \geq \rho_{\rm threshold}^2, \tag{2.88}$$

where the sum is over the different SNRs obtained in each interferometer. In order to combat non-Gaussian noise, the detection criterion will be modified to require approximately equal SNRs in each interferometer:

$$\rho_j \geq \rho_{\rm threshold}/\sqrt{2} \ \text{ for all } j. \tag{2.89}$$

We have chosen a factor of $\sqrt{2}$ here to be conservative; it corresponds to combining the outputs of just two interferometers (say, the two LIGO 4km interferometers) instead of four interferometers.

Taking $T = 10^7$ s and $\Delta t = 1$ ms yields the estimate $\rho_{\rm threshold}/\sqrt{2} \approx 6.0$ for the initial and advanced LIGO interferometers. Therefore, from Fig. 2.4, we see that the initial LIGO interferometers should be able to see ringdowns from equal-mass BBHs in the mass range $100 M_\odot \lesssim M \lesssim 700 M_\odot$ out to about 200 Mpc, if the radiation efficiency $\epsilon_{\rm ringdown}$ is as large as we have estimated. The advanced LIGO interferometers, by contrast, should see ringdowns in the mass

range $200M_\odot \lesssim (1+z)M \lesssim 3000M_\odot$ out to $z \sim 1$ (from Fig. 2.5). For non equal-mass BBHs, these distances are reduced roughly by the factor $\sim (4\mu/M)$.

For LISA, the detection threshold is given by Eq. (2.87). Although LISA does incorporate several partially independent interferometers, we have used the noise spectrum (2.77) which is the effective noise spectrum that applies to the LISA detector as a whole [7]. Thus it is consistent to treat LISA as one interferometer. Taking $T = 10^7$ s and $\Delta t = 1$ s, and using the value $\mathcal{N}_{\rm shapes} = 6000$ estimated above yields $\rho_{\rm threshold} \approx 7.5$. Hence, from Fig. 2.6, LISA should see ringdowns in the mass range $10^6 M_\odot \lesssim (1+z)M \lesssim 3 \times 10^8 M_\odot$ out to $z \gtrsim 100$.

2.6.2 The detectability of high mass black-hole coalescences via the merger signal

We next discuss the feasibility of searches for the merger signal. As we have explained, this will be most necessary when the merger SNR is larger than both the inspiral and ringdown SNRs by factors of a few (since the fractional loss in event detection rate, if searches for the merger signal are not carried out, is the cube of the ratio of the SNR values).

Consider first the ideal situation in which theoretical template waveforms are available, so that matched filtering can be used in searches. From Figs. 2.4 and 2.5 it can be seen that the merger SNR values are larger than the inspiral/ringdown values by a factor of up to ~ 4, in the mass ranges $30M_\odot \lesssim M \lesssim 200M_\odot$ for initial LIGO interferometers and $100M_\odot \lesssim M \lesssim 400M_\odot$ for advanced LIGO interferometers. More precisely, in this mass range,

$$\frac{\left(\frac{S}{N}\right)_{\rm merger}}{\max\left[\left(\frac{S}{N}\right)_{\rm inspiral}, \left(\frac{S}{N}\right)_{\rm ringdown}\right]} \lesssim 4\sqrt{\frac{\epsilon_{\rm merger}/0.1}{\epsilon_{\rm ringdown}/0.03}}. \tag{2.90}$$

The detection threshold for merger searches should be approximately the same as that for inspiral and merger searches, if the number of template shapes $\mathcal{N}_{\rm shapes}$ is not too large (see further discussion below). Therefore, the gain in event rate over inspiral/ringdown searches should vary between 1 and about $4^3 = 64$, depending on the mass of the system, if our estimates of $\epsilon_{\rm merger}$ and $\epsilon_{\rm ringdown}$ are reasonable. The large possible gain in event rate clearly demonstrates the importance of merger searches [103].

Note however that it is not clear how feasible it will be to produce a set of numerically generated templates that is complete enough to be used to successfully implement an optimal filtering search. There may be a very large number of distinct waveform shapes, each of which will require extensive

numerical computations. If both black holes are spinning rapidly, the waveforms could depend in significant and nontrivial ways on 6 distinct angular parameters, suggesting that the number of distinct shapes could be very large.

Next, consider the situation in which merger templates are unavailable. Consider first band-pass filtering searches. From the estimate $\sqrt{\mathcal{N}_{\rm bins}} = 4$ of Sec. 2.3.5, combined with Eq. (2.21), we see that the merger SNR in a band-pass filtering search is reduced by a factor of 4 from the values presented in Appendix B and Figures 2.4, 2.5, and 2.6. By Eq. (2.90), the achievable band-pass filtering merger SNR is likely to be essentially no larger than the inspiral and ringdown SNRs.

Noise monitoring searches for the merger waveform will be more effective than band-pass filtering searches, approaching the effectiveness of matched filtering searches. [By contrast, noise-monitoring searches for inspiral waves would perform very badly , since $\mathcal{N}_{\rm bins}$ is much larger ($\gtrsim 1000$) for inspiral waves than it is for merger waves ($\lesssim 60$)]. The event-detection rate from noise-monitoring is a factor

$$\mathcal{R} = \left(\frac{\rho_*}{\rho_{\rm threshold}}\right)^3 \tag{2.91}$$

lower than the event rate from matched filtering. Here ρ_* is the noise-monitoring detection threshold, given by Eqs. (2.33) and (2.34) as a function of the parameters ϵ, $\mathcal{N}_{\rm start-times}$ and $\mathcal{N}_{\rm bins}$, and $\rho_{\rm threshold}$ is the matched filtering threshold, given by Eq. (2.14) as a function of the parameters $\mathcal{N}_{\rm shapes}$ and $\mathcal{N}_{\rm start-times}$. As discussed in Sec. 2.2.2, the calculation we have given of the threshold ρ_* assumes Gaussian noise behavior; the possible residual non-Gaussianity of real data even after coincidencing between detectors may degrade the effectiveness of noise-monitoring.

We now estimate the loss factor in event rate $\mathcal{R}$. To obtain the most pessimistic estimate, we use the following assumptions: (i) The number of template shapes in the matched filtering search is $\mathcal{N}_{\rm shapes} = 1$. A realistic larger number would yield a smaller $\mathcal{R}$. (ii) The number of frequency bins is $\mathcal{N}_{\rm bins} = 60$, twice the upper limit estimated in Sec. 2.3.5 [104]. (iii) The number of starting times in the data stream is $\mathcal{N}_{\rm start-times} = 10^8$, corresponding to a sampling time of 0.1 s in a data set of one third of a year. Such a large sampling time (and small $\mathcal{N}_{\rm start-times}$) would only be appropriate for the largest BBHs; more realistic sampling times will be smaller. Larger values of $\mathcal{N}_{\rm start-times}$ give smaller values of $\mathcal{R}$. (iv) The parameter ϵ in Eqs. (2.33) and (2.14) is $\epsilon = 10^{-3}$. With these assumptions we obtain $\rho_{\rm threshold} = 6.8$, $\rho_* = 10.3$; the resulting loss factor is

$$\mathcal{R} = 3.5.$$

Hence, noise-monitoring searches should only be a factor of at most ~ 4, and more typically ~ 2, worse than matched filtering searches.

The above discussion assumed that $\mathcal{N}_{\rm shapes}$ is small. As the number $\mathcal{N}_{\rm shapes}$ increases, the advantage of matched filtering searches decreases; at some number $\mathcal{N}_{\rm shapes,\,max}$, matched filtering and noise monitoring perform about equally well. In Ref. [73] we show that [105]

$$\ln(\mathcal{N}_{\rm shapes,max}) \approx \frac{1}{2}\mathcal{N}_{\rm bins} \ln\left(1+\rho^2/\mathcal{N}_{\rm bins}\right). \tag{2.92}$$

From Eqs. (2.92) and (2.33), the critical value of the number of shapes is $\sim 10^{13}$ for $\mathcal{N}_{\rm bins} = 60$, and $\sim 10^7$ for $\mathcal{N}_{\rm bins} = 20$, assuming $\mathcal{N}_{\rm start-times} = 10^8$.

The actual number of shapes $\mathcal{N}_{\rm shapes}$ will vary with the SNR level ρ. We can define an effective dimension N_d of the manifold of signals by the equation

$$\ln\left[\mathcal{N}_{\rm shapes}(\rho)\right] = \frac{1}{2}N_d(\rho)\,\ln\left[1+\rho^2/N_d(\rho)\right]; \tag{2.93}$$

the parameter $N_d(\rho)$ is the dimension of the equivalent (linear) space of signals that has the same number of distinguishable wave shapes with SNR $\leq \rho$ as the true, curved, manifold of merger signals [57]. In Fig. 2.7, we show the gain factor $\mathcal{R}$ as a function of $\mathcal{N}_{\rm bins}$ for the values $N_d = 0$, 5, and 10. The true value of N_d is quite uncertain; at high SNR levels it could conceivably be as large as ~ 10.

Combining the gain factor of 64 discussed above with the loss factor $\mathcal{R}$, it follows that noise-monitoring searches for merger waves could increase the event rate—and hence the number of discovered BBHs—by a factor up to about 10 over those found from inspiral and ringdown searches for ground based interferometers. (For LISA, the expected SNRs are so high that the availability of merger templates will likely have no impact on event detection rates.)

2.7 Conclusions

It seems quite likely that gravitational waves from merging BBH systems will be detected by the ground-based interferometers that are now under construction. Initial LIGO interferometers will be able to detect low mass ($\lesssim 30M_\odot$) coalescences of equal-mass BBHs to about 200 Mpc via their inspiral waves, and higher mass ($100M_\odot \lesssim M \lesssim 700M_\odot$) systems to about 200 Mpc via their ring-down waves. Advanced LIGO interferometers will be able to detect equal-mass BBH coalescences

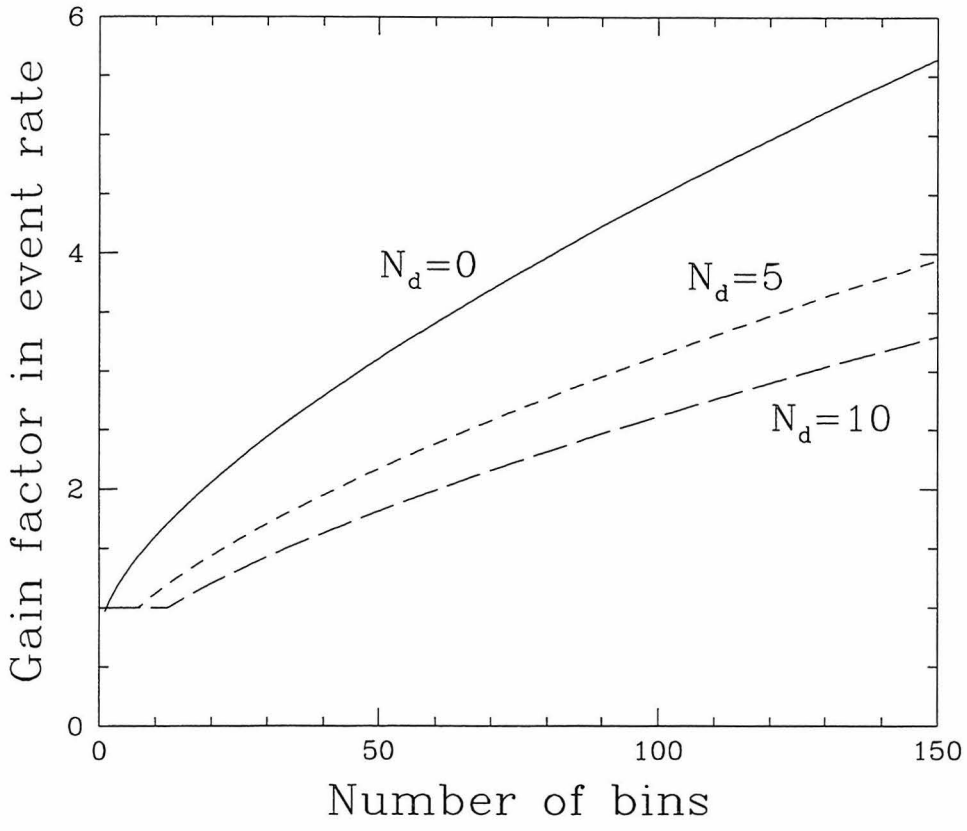

Figure 2.7: The factor by which the event detection rate is increased when one uses matched filters for the merger waves *vs.* using a noise monitoring search.

Plotted on the horizontal axis is the number $\mathcal{N}_{\rm bins} = 2T\Delta f$ of independent frequency bins characterizing the space of signals one searches for; T is the maximum expected signal duration and Δf is the frequency bandwidth. The vertical axis shows gain factor $\mathcal{R}$ in event rate. This gain factor depends on the number of statistically independent waveform shapes in the set of signals one is searching for, which is currently unknown. This number of waveform shapes can be characterized by the effective dimension $\mathcal{N}_d$ of the manifold of signals; *cf.* Eq. (2.93). The solid line shows the gain factor in the limit in which the number of waveform shapes is small ($\mathcal{N}_d = 0$); it is an upper limit on the gain factor obtainable from matched filtering. The lower two dashed lines show the gain factor when $\mathcal{N}_d = 5$ and $\mathcal{N}_d = 10$. Our best estimate of $\mathcal{N}_{\rm bins}$ is roughly 30, corresponding to $T = 50M$ and $\Delta f = 1/(\pi M)$; it is unlikely to be much larger than 100 (Sec. 2.3.5). This plot can be generated by combining Eqs. (2.33), (2.34), (2.14) and (2.93) of the text, with the parameter values $\mathcal{N}_{\rm start-times} = 10^8$ and $\epsilon = 10^{-3}$.

in the mass range $10M_\odot \lesssim M \lesssim 300M_\odot$ to $z \sim 1/2$ via their inspiral waves, and higher mass ($200M_\odot \lesssim M \lesssim 3000M_\odot$) systems to $z \sim 1$ via their ringdown waves. For non-equal mass BBHs, these distances will be reduced by a factor of about $\sqrt{4\mu/M}$ for inspiral signals and about $4\mu/M$ for ringdown signals.

Searches for massive BBHs ($M \gtrsim 50M_\odot$ for LIGO/VIRGO) based on merger waves could increase the range of the interferometers by a additional factor of ~ 2, without requiring detailed knowledge of the waveform shapes. It seems likely that BBH coalescences will be detected early in the gradual improvement towards advanced interferometers, and there is a strong possibility that they will be the first sources of gravitational radiation to be detected.

Theoretical template waveforms obtained from numerical relativity supercomputer simulations will be crucial for analyzing the measured merger waves. A match of the detected waveform with a predicted waveform would be a triumph for the theory of general relativity and an absolutely unambiguous signature of the existence of black holes. A complete set of such theoretical templates would also aid the search for BBHs, but not by a large amount.

The space-based interferometer LISA will be an extremely high precision instrument for studying the coalescences of supermassive BBHs. Coalescences with masses in the range $10^6 M_\odot \lesssim (1+z)M \lesssim 10^9 M_\odot$ should be detectable out to $z \sim 10$ with very large SNRs ($\gtrsim 10^3$), via their merger and ringdown waves. Additionally, systems in the mass range $10^4 M_\odot \lesssim (1+z)M \lesssim 3 \times 10^7 M_\odot$ should be detected to similar distances and with SNRs $\gtrsim 10^2$ via their inspiral waves.

Acknowledgments

We thank Kip Thorne for suggesting this project to us, for being a constant source of ideas and encouragement along the way, and for detailed comments on the paper's content and presentation. We also thank Patrick Brady and David Chernoff for some helpful conversations, and Tom Prince and Chip Sumner for locating a well-hidden typo in one of our equations. This research was supported by NSF Grants PHY–9220644, PHY–9408378, PHY–9424337, and PHY–9514726, and by NASA grant NAGW-4268. S.A.H. gratefully acknowledges the support of a National Science Foundation Graduate Fellowship, and É.F. likewise acknowledges the support of an Enrico Fermi fellowship.

Appendix A Energy spectrum for ringdown waves

There is a subtlety in calculating the SNR for the ringdown waves, related to the fact that the SNR squared does not accumulate locally in the time domain. In order to explain this subtlety, let us focus not on the angle-averaged SNR squared which was our main concern in the body of the paper, but rather on the SNR squared obtained in one interferometer from a specific source with specific relative angular orientations. In this case the waveform $h(t)$ seen in the interferometer, for $t > 0$, is of the form

$$h(t) = h_0 \cos(2\pi f_{\rm qnr} t + \psi_0) e^{-t/\tau} \tag{2.94}$$

for some constants h_0 and ψ_0, while $h(t)$ is the (unknown) merger waveform for $t < 0$.

Let us also focus first on the simple, idealized case of white noise, $S_h(f) = S_h = \text{const}$. Then, the SNR squared (2.13) accumulates locally in time:

$$\rho^2 = \frac{2}{S_h} \int_{-\infty}^{\infty} dt\, h(t)^2. \tag{2.95}$$

Hence, for white noise, the SNR squared from the ringdown is clearly unambiguously given by

$$\begin{aligned} \rho^2_{\rm ringdown} &= \frac{2}{S_n} \int_0^{\infty} h_0^2 \cos^2(2\pi f_{\rm qnr} t + \psi_0)^2 e^{-2t/\tau} \\ &= \frac{h_0^2 \tau}{2S_h} \left[1 + \frac{\cos(2\psi_0) - Q \sin(2\psi_0)}{1+Q^2} \right] \\ &\approx \frac{h_0^2 \tau}{2S_h} \left[1 + O(1/Q) \right], \end{aligned} \tag{2.96}$$

where $Q = \pi f_{\rm qnr} \tau$. Now consider the case when the noise is not exactly white. Naively, we expect that in the Fourier domain the energy spectrum of the ringdown signal will be a resonance curve that peaks at $f = f_{\rm qnr}$ with width $\sim f_{\rm qnr}/Q$. Thus, for large Q we would expect that most of the SNR squared will be accumulated near $f = f_{\rm qnr}$, unless the noise spectrum varies very strongly with frequency. Moreover, if the noise spectrum $S_h(f)$ does not vary much over the bandwidth $\sim f_{\rm qnr}/Q$ of the resonance peak, then we would expect the formula (2.96) to be valid to a good approximation, with S_h replaced by $S_h(f_{\rm qnr})$. We show below that this is indeed the case: under such circumstances, Eq. (2.96) is fairly accurate, and the resulting approximate ringdown SNR is embodied in our approximate delta-function energy spectrum (2.66) and in Eqs. (2.123)–(2.127) of Appendix B [106].

In many cases of interest, it will indeed be true that most of the SNR squared for ringdown waves will be accumulated in the vicinity of the resonance peak, so that the SNR will approximately be given by Eq. (2.96). However, this will not always be the case. For instance, suppose that we were lucky enough that two $10^5 M_\odot$ black holes were to merge at the center of our own galaxy. Would such an event be detectable by advanced LIGO interferometers? Clearly, most of the power in the ringdown waves in this case would be far below the LIGO/VIRGO waveband. However, given that the merger is only at $\sim 10\,\mathrm{kpc}$, one might hope to be able to detect the tail of the ringdown waves that extends upwards in frequency into the LIGO/VIRGO waveband. Or, consider the detectability of a ringdown of a nearby $10^3 M_\odot$ black hole by LISA. In this case most of the ringdown power is concentrated at frequencies above LISA's optimum waveband, and the detectability of the signal is determined by the amount of power in the low frequency tail of the ringdown. In such cases, it is clearly necessary to understand the power carried in the ringdown waves at frequencies far from the resonant frequency.

Normally, such an understanding is obtained simply by taking a Fourier transform of the waveform $h(t)$. In the case of ringdown waves from BBH mergers, however, the waveform for $t < 0$ is the unknown, merger waveform. In order to obtain the SNR squared from the ringdown signal alone, one might guess that the appropriate thing to do is to take $h(t) = 0$ for $t < 0$, and insert this together with Eq. (2.94) into the standard formula (2.13) for the signal to noise squared. However, the resulting energy spectrum has unrealistic high frequency behavior due to a discontinuity in $h(t)$ at $t = 0$ (or a discontinuity in $h'(t)$ at $t = 0$ in the case $\psi_0 = \pi/2$), and the resulting SNRs can in some cases differ from the correct values (see below) by factors $\gtrsim 10$. Other choices for $h(t)$ for $t < 0$ [for instance $h(t) = h(0)$] get around this problem but instead have unrealistic low frequency behavior. In any case, it is clear that these choices are somewhat *ad hoc* and that there should be some more fundamental, unique way to calculate the SNR.

We now explain the correct method to calculate the SNR. The question that effectively is being asked is: What is the probability that there is a ringdown waveform present in the data stream, starting at (say) $t = 0$? This probability is to be calculated given only the data from $t > 0$, without using the measured data from $t < 0$ which is contaminated by the unknown merger waveform. To do this one must effectively integrate over all possible realizations of the noise for $t < 0$. The necessity for such an integration is illustrated by the following simple analogy. Suppose that one is measuring two real variables, h_+ ("waveform for positive t") and h_- ("waveform for negative t"), and that the measured values of these variables are $\bar{h}_+$ and $\bar{h}_-$. Suppose that because of the noise in

the measurement process, the probability distribution for the true values of these parameters given their measured values is

$$p(h_+, h_-) = \frac{1}{2\pi\sigma^2} \exp\left\{ -\frac{1}{2\sigma^2}[(h_+ - \bar{h}_+)^2 + (h_- - \bar{h}_-)^2 + 2\varepsilon(h_+ - \bar{h}_+)(h_- - \bar{h}_-)]\right\}. \quad (2.97)$$

Thus, h_+ and h_- are Gaussian distributed about their means $\bar{h}_+$ and $\bar{h}_-$, and they are correlated. If we assume that $h_- = 0$ [analogous to assuming $h(t) = 0$ for $t < 0$], we obtain for the probability distribution for h_+

$$p(h_+|h_- = 0) = \frac{1}{\sqrt{2\pi}\sigma} e^{-(h_+ - \bar{h}'_+)^2/(2\sigma)^2}, \quad (2.98)$$

where $\bar{h}'_+ = \bar{h}_+ - \varepsilon\bar{h}_-$. By contrast, if we instead calculate the probability distribution for h_+ alone by integrating over h_- we find

$$p(h_+) = \frac{1}{\sqrt{2\pi}\sigma^*} e^{-(h_+ - \bar{h}_+)^2/(2\sigma^*)^2}, \quad (2.99)$$

where $\sigma^* = \sigma/\sqrt{1-\varepsilon^2}$. It is clear in this simple example that one should use the reduced distribution (2.99) rather than the distribution (2.98). Note also that the widths of the probability distributions (2.98) and (2.99) are different, and that the correct distribution (2.99) could not have been obtained from the joint distribution (2.97) for any assumed choice of h_-.

Turn now to the analogous situation for random processes. If $n(t)$ is the interferometer noise, let $C_n(\Delta t) \equiv \langle n(t)n(t+\Delta t)\rangle$ denote the autocorrelation function. Define the inner product

$$\langle h_1 | h_2 \rangle \equiv \int_0^\infty dt \int_0^\infty dt'\, K(t,t')\, h_1(t) h_2(t') \quad (2.100)$$

on the space of functions $h(t)$ for $t > 0$, where the kernel $K(t,t')$ is determined from

$$\int_0^\infty dt'' K(t,t'') C_n(t''-t') = \delta(t-t') \quad (2.101)$$

for $t, t' \geq 0$. The quantity $K(t,t')$ is analogous to the modified width σ^* in Eq. (2.99) above. Using the inner product (2.100), the usual theory of matched filtering [59, 60] can be applied to random processes on the half line $t > 0$. Thus, if $s(t)$ is the interferometer output and $h(t)$ is the waveform (2.94), the detection statistic is $Y = \langle s|h\rangle$, and the SNR squared for the measurement is

$$\rho^2 \equiv \frac{E[Y]^2}{E[Y^2] - E[Y]^2}$$

$$= \langle h|h\rangle$$
$$= \int_0^\infty dt \int_0^\infty dt' K(t,t')h(t)h(t'), \tag{2.102}$$

where $E[...]$ means expectation value. If we define

$$G(f,f') = \int_0^\infty dt \int_0^\infty dt'\, e^{2\pi i f t}\, e^{-2\pi i f' t'}\, K(t,t') \tag{2.103}$$

and

$$\tilde{h}(f) = \int_0^\infty e^{2\pi i f t}\, h(t)\, dt, \tag{2.104}$$

the SNR squared can be rewritten as

$$\rho^2 = \int_{-\infty}^\infty df \int_{-\infty}^\infty df'\, \tilde{h}(f)^*\, G(f,f')\tilde{h}(f'). \tag{2.105}$$

Note that the Fourier transform $G(f,f')$ of $K(t,t')$ is not proportional to $\delta(f-f')/S_h(f)$ but instead is in general *non-diagonal* in frequency.

The formula (2.105) resolves the ambiguities discussed above in the method of calculating the ringdown SNR; the result does not require a choice of the waveform $h(t)$ for $t<0$. Unfortunately, the final answer (2.105) is complicated in the sense that it cannot be expressed in the form (2.36) for any effective energy spectrum dE/df. This is somewhat inconvenient for the purposes of this paper: the wave's energy spectrum is a useful and key tool for visualizing and understanding the SNRs. Clearly, an approximate, effective energy spectrum (to the extent that one exists) would be very useful. We now turn to a derivation of such an approximate, effective energy spectrum, namely the spectrum (2.65) which is used throughout the body of this paper.

We start our derivation by describing an alternative method of calculating the exact ringdown SNR given by Eqs. (2.94) and (2.102). It is straightforward to show that the quantity (2.102) can be obtained by (i) choosing *any* waveform $h(t)$ for $t<0$, (ii) calculating the SNR from the usual formula (2.13), and (iii) minimizing over all choices of the function $h(t)$ on the negative real axis. We have experimented with several choices of $h(-t)$ for $t>0$, namely $h(-t)=0$, $h(-t)=h(0)$, $h(-t)=h(t)$. We found that the SNR obtained by minimizing over these choices is always (for the entire black hole mass ranges discussed in Sec. 2.5) within a few tens of percent of the SNR obtained from the following prescription: (i) Assume that $h(t)$ for negative t is identical to the waveform for

positive t except for the sign of t/τ; *i.e.*, that

$$h(t) = h_0 \cos(2\pi f_{\rm qnr} t + \psi_0) e^{-|t|/\tau} \tag{2.106}$$

for positive and negative t. (ii) Calculate the total SNR using the standard formula (2.13). (iii) Divide by a correction factor of $\sqrt{2}$ in amplitude to compensate for the doubling up. This prescription gives the correct, exact result (2.102) for white noise. For more realistic noise curves, the errors of a few tens of percent resulting from this prescription are unimportant compared to the uncertainty in the overall amplitude $\mathcal{A}$ of the ringdown signal. Moreover, the resulting SNR values multiplied by $\sqrt{2}$ are an upper bound for the true SNR (since if our *ad hoc* choice of $h(t)$ for $t < 0$ happened to be exactly right, then the prescription would underestimate the SNR by $\sqrt{2}$).

We now explain how to obtain the energy spectrum (2.65) from the above approximate prescription. From Eqs. (2.37) and (2.62) it can be seen that the waveform as seen in one interferometer, before angle averaging, is given by Eq. (2.94) with

$$h_0 e^{i\psi_0} = \frac{\mathcal{A}M}{r} \left[F_+(\theta,\varphi,\psi) + iF_\times(\theta,\varphi,\psi)\right] {}_2S_2^2(\iota,\beta,a) e^{i\varphi_0}. \tag{2.107}$$

Here the angles θ, φ, ψ, ι and β have the meanings explained in Sec. 2.2.3. Let us now insert the waveform (2.94) into the formula (2.102) for the exact SNR, and then average over the angles θ, φ, ψ, ι and β using Eqs. (2.40) and (2.63). This yields for the angle-averaged, exact SNR squared

$$\langle \rho_{\rm exact}[h(t)]^2 \rangle = \frac{1}{20\pi} \left[\rho_{\rm exact}[h_{+,0}(t)]^2 + \rho_{\rm exact}[h_{\times,0}(t)]^2 \right], \tag{2.108}$$

where $\rho_{\rm exact}[h(t)]$ denotes the exact SNR functional (2.102) and

$$\begin{aligned} h_{+,0}(t) &= \frac{\mathcal{A}M}{r} \cos(2\pi f_{\rm qnr} t)\, e^{-t/\tau}, \\ h_{\times,0}(t) &= \frac{\mathcal{A}M}{r} \sin(2\pi f_{\rm qnr} t)\, e^{-t/\tau}, \end{aligned} \tag{2.109}$$

for $t > 0$. Now, for each of the two terms on the right hand side of Eq. (2.108), we make the approximation discussed above consisting of using Eqs. (2.13) and (2.106) and dividing by 2. This yields

$$\langle \rho_{\rm exact}[h(t)]^2 \rangle \approx \frac{1}{10\pi} \int_0^\infty df\, \frac{\left[|\tilde{h}_{+,0}(f)|^2 + |\tilde{h}_{+,0}(f)|^2\right]}{S_h(f)}, \tag{2.110}$$

where it is understood that $h_{+,0}$ and $h_{\times,0}$ have been extended to negative t in the manner of Eq. (2.106). Finally, evaluating the Fourier transforms yields an angle averaged SNR squared of the form (2.36), with energy spectrum given by Eq. (2.65).

Appendix B Signal-to-noise ratio formulae

In this appendix, we give the details of our SNR calculations. Note that throughout this appendix we use "M$M_\odot$" (Mega solar-mass) as shorthand for $10^6\ M_\odot$.

Inspiral

To calculate the angle-averaged SNR squared for the inspiral, we insert the inspiral energy spectrum (2.61) and our parameterized model (2.74) of an interferometer's noise spectrum into Eq. (2.36), and integrate from $f = f_s$ to $f = f_{\rm merge}$. The result is

$$\langle\rho^2\rangle = \begin{cases} \mathcal{F}_i(M,z,D)\left[9\alpha^{1/3} - \frac{36}{5}\alpha^{-1/3} - \frac{4}{5}\alpha^{-1/3}v^{10/3} - \alpha^3\left(\frac{f_s}{f_m}\right)^{8/3}\right], & \\ & \alpha f_m \le f_{\rm merge}/(1+z); \\ \mathcal{F}_i(M,z,D)\left[9\alpha^{1/3} - 8\left(\frac{v}{\alpha}\right)^{1/3} - \alpha^3\left(\frac{f_s}{f_m}\right)^{8/3}\right], & \\ & f_m/\alpha \le f_{\rm merge}/(1+z) < \alpha f_m; \\ \mathcal{F}_i(M,z,D)\left[\alpha^{1/3}\left(\frac{\alpha^2}{v}\right)^{8/3} - \alpha^3\left(\frac{f_s}{f_m}\right)^{8/3}\right], & \\ & f_s \le f_{\rm merge}/(1+z) < f_m/\alpha; \\ 0 & f_{\rm merge}/(1+z) < f_s; \end{cases} \tag{2.111}$$

where

$$v \equiv \frac{(1+z)\alpha f_m}{f_{\rm merge}} \tag{2.112}$$

and

$$\mathcal{F}_i(M,z,D) = \frac{[(1+z)M]^{5/3}[4\mu/M]}{80\pi^{4/3}D(z)^2 h_m^2 f_m^{1/3}}. \tag{2.113}$$

Here $D(z)$ is the luminosity distance to the source, f_s, α, f_m and h_m are parameters characterizing the detector noise spectrum (2.74), and $f_{\rm merge}$ is given by Eq. (2.50).

Inserting the values of the noise spectrum parameters from Eq. (2.75) for initial LIGO interfer-

ometers, we obtain the following numerical values for the SNR in the equal-mass case $\mu = M/4$:

$$\left(\frac{S}{N}\right)_{\text{initial}} = \begin{cases} 2.8\left(\frac{200\,\text{Mpc}}{D(z)}\right)\left(\frac{(1+z)M}{18\,M_\odot}\right)^{5/6}\left[1-0.20\left(\frac{(1+z)M}{18\,M_\odot}\right)^{10/3}\right]^{1/2}, \\ \qquad\qquad (1+z)M \leq 18\,M_\odot; \\ 4.7\left(\frac{200\,\text{Mpc}}{D(z)}\right)\left(\frac{(1+z)M}{18\,M_\odot}\right)^{5/6}\left[1-0.71\left(\frac{(1+z)M}{18\,M_\odot}\right)^{1/3}\right]^{1/2}, \\ \qquad\qquad 18\,M_\odot < (1+z)M \leq 36\,M_\odot; \\ 2.7\left(\frac{200\,\text{Mpc}}{D(z)}\right)\left(\frac{(1+z)M}{36\,M_\odot}\right)^{-1/2}\left[1-0.06\left(\frac{(1+z)M}{36\,M_\odot}\right)^{8/3}\right]^{1/2}, \\ \qquad\qquad 36\,M_\odot < (1+z)M \leq 102\,M_\odot; \\ 0 \qquad\qquad 102\,M_\odot < (1+z)M. \end{cases} \tag{2.114}$$

For the noise curve parameters (2.76) appropriate for advanced LIGO interferometers we obtain

$$\left(\frac{S}{N}\right)_{\text{advanced}} = \begin{cases} 27\left(\frac{1\,\text{Gpc}}{D(z)}\right)\left(\frac{(1+z)M}{37\,M_\odot}\right)^{5/6}\left[1-0.16\left(\frac{(1+z)M}{37\,M_\odot}\right)^{10/3}\right]^{1/2}, \\ \qquad\qquad (1+z)M \leq 37\,M_\odot; \\ 43\left(\frac{1\,\text{Gpc}}{D(z)}\right)\left(\frac{(1+z)M}{37\,M_\odot}\right)^{5/6}\left[1-0.65\left(\frac{(1+z)M}{37\,M_\odot}\right)^{1/3}\right]^{1/2}, \\ \qquad\qquad 37\,M_\odot < (1+z)M \leq 95\,M_\odot; \\ 31\left(\frac{1\,\text{Gpc}}{D(z)}\right)\left(\frac{(1+z)M}{95\,M_\odot}\right)^{-1/2}\left[1-.021\left(\frac{(1+z)M}{95\,M_\odot}\right)^{8/3}\right]^{1/2}, \\ \qquad\qquad 95\,M_\odot < (1+z)M \leq 410\,M_\odot; \\ 0 \qquad\qquad 410\,M_\odot < (1+z)M. \end{cases} \tag{2.115}$$

As explained in Sec. 2.5.1, the calculation of the inspiral SNR for LISA differs from the other SNR calculations in the following way. If one were to integrate over the whole frequency domain in the interferometer waveband up to $f = f_{\text{merge}}$ (as is done for the initial and advanced interferometers in LIGO), in some cases one would obtain the SNR for a measurement of several hundred years duration, which is obviously irrelevant. Thus, it is necessary to restrict the integral over frequency in Eq. (2.36) to the domain that corresponds to, say, one year of observation when calculating inspiral LISA SNRs. Using the Newtonian relationship for the rate of frequency sweep, we obtain for the frequency at time T before merger in the equal-mass case

$$f_{\text{insp}}(T) = \left[f_{\text{merge}}^{-8/3} + \frac{64}{5}\pi^{8/3}M^{5/3}(1+z)^{5/3}T\right]^{-3/8}. \tag{2.116}$$

Binaries of redshifted total mass $(1+z)M$ larger than about $5 \times 10^5 M_\odot$ enter the LISA waveband at $f = f_s = 10^{-4}\,\mathrm{Hz}$ less than one year before merger, while binaries of smaller redshifted mass spend more than one year in the LISA waveband. To calculate the SNR, we insert Eq. (2.61) into Eq. (2.36) and integrate numerically from the larger of f_s and $f_{\rm insp}(1\,\mathrm{yr})$ to $f_{\rm merge}$. The resulting SNR values are shown in Fig. 2.6. We also show in Fig. 2.6 the SNR obtained from one year of observation one hundred years before the final merger, obtained by integrating from $f_{\rm insp}(100\,\mathrm{yr})$ to $f_{\rm insp}(99\,\mathrm{yr})$, as well as a similar curve for one thousand years prior to merger.

Eq. (2.111) applies to LISA only for $(1+z)M \gtrsim 5 \times 10^5 M_\odot$. By combining Eqs. (2.111) and (2.77) for $(1+z)M \gtrsim 5 \times 10^5 M_\odot$ together with an approximate fit to Fig. 2.6 in the regime $(1+z)M \lesssim 10^5 M_\odot$ we obtain the following SNRs in the equal-mass case for the last year of inspiral:

$$\left(\frac{S}{N}\right)_{\rm LISA} \approx \begin{cases} 1.5 \times 10^4 \left(\frac{1\,\mathrm{Gpc}}{D(z)}\right) \left(\frac{(1+z)M}{0.5\,\mathrm{M}M_\odot}\right), & \\ & 100 M_\odot \lesssim (1+z)M \lesssim 0.5\,\mathrm{M}M_\odot; \\ 1.9 \times 10^4 \left(\frac{1\,\mathrm{Gpc}}{D(z)}\right) \left(\frac{(1+z)M}{0.5\,\mathrm{M}M_\odot}\right)^{5/6} \left[1 - 0.38 \left(\frac{(1+z)M}{0.5\,\mathrm{M}M_\odot}\right)^{1/3}\right]^{1/2}, & \\ & 0.5\,\mathrm{M}M_\odot < (1+z)M \leq 6.0\,\mathrm{M}M_\odot; \\ 5.0 \times 10^4 \left(\frac{1\,\mathrm{Gpc}}{D(z)}\right) \left(\frac{(1+z)M}{6\,\mathrm{M}M_\odot}\right)^{-1/2} \left[1 - 0.006 \left(\frac{(1+z)M}{6\,\mathrm{M}M_\odot}\right)^{8/3}\right]^{1/2}, & \\ & 6.0\,\mathrm{M}M_\odot < (1+z)M \leq 41\mathrm{M}M_\odot; \\ 0 & 41\mathrm{M}M_\odot < (1+z)M. \end{cases} \tag{2.117}$$

Merger

To calculate the merger SNR we use the energy spectrum (2.60) and follow the same procedure as above. The result is

$$\langle\rho^2\rangle = \begin{cases} \mathcal{F}_m(\epsilon_m, M, z, D) v^3 \left[\frac{\kappa^3-1}{\kappa^3}\right], \\ \qquad\qquad f_{\rm merge}/(1+z) \geq \alpha f_m; \\ \mathcal{F}_m(\epsilon_m, M, z, D) \left[3\ln v - \frac{v^3-\kappa^3}{\kappa^3}\right], \\ \qquad\qquad f_m/\alpha \leq f_{\rm merge}/(1+z) < \alpha f_m \leq f_{\rm qnr}/(1+z); \\ {}^{\rm I,A}\mathcal{F}_m(\epsilon_m, M, z, D) \left[2 - \frac{\alpha^6}{v^3} - \frac{v^3}{\kappa^3} + 6\ln\alpha\right], \\ \qquad\qquad f_{\rm merge}/(1+z) \leq f_m/\alpha < \alpha f_m \leq f_{\rm qnr}/(1+z); \\ {}^{\rm L}\mathcal{F}_m(\epsilon_m, M, z, D) \left[3\ \ln\kappa\right], \\ \qquad\qquad f_m/\alpha \leq f_{\rm merge}/(1+z) < f_{\rm qnr}/(1+z) \leq \alpha f_m; \\ {}^{\rm I}\mathcal{F}_m(\epsilon_m, M, z, D) \left[2 - \left(\frac{\alpha f_s}{f_m}\right)^3 - \frac{v^3}{\kappa^3} + 6\ln\alpha\right], \\ \qquad\qquad f_{\rm merge}/(1+z) \leq f_s < f_m/\alpha < \alpha f_m \leq f_{\rm qnr}/(1+z); \\ {}^{\rm A,L}\mathcal{F}_m(\epsilon_m, M, z, D) \left[1 + 3\ln\left(\frac{\kappa\alpha^2}{v}\right) - \frac{\alpha^6}{v^3}\right], \\ \qquad\qquad f_s \leq f_{\rm merge}/(1+z) < f_m/\alpha \leq f_{\rm qnr}/(1+z); \\ {}^{\rm I,A}\mathcal{F}_m(\epsilon_m, M, z, D) \left[1 - \left(\frac{\alpha f_s}{f_m}\right)^3 + 3\ln\left(\frac{\kappa\alpha^2}{v}\right)\right], \\ \qquad\qquad f_{\rm merge}/(1+z) \leq f_s < f_m/\alpha \leq f_{\rm qnr}/(1+z); \\ {}^{\rm L}\mathcal{F}_m(\epsilon_m, M, z, D) \left[\alpha^6 v^{-3}(\kappa^3 - 1)\right], \\ \qquad\qquad f_s \leq f_{\rm merge}/(1+z) < f_{\rm qnr}/(1+z); \\ \mathcal{F}_m(\epsilon_m, M, z, D) \left[\left(\frac{\kappa\alpha^2}{v}\right)^3 - \left(\frac{\alpha f_s}{f_m}\right)^3\right], \\ \qquad\qquad f_{\rm merge}/(1+z) \leq f_s < f_{\rm qnr}/(1+z) \leq f_m/\alpha; \\ 0 \qquad\qquad f_{\rm qnr}/(1+z) < f_s. \end{cases} \tag{2.118}$$

Here v is given by Eq. (2.112), ϵ_m is the fraction of total mass energy radiated during the merger (which we have also denoted by $\epsilon_{\rm merger}$ in the body of the paper), $\kappa \equiv f_{\rm qnr}/f_{\rm merge}$, and

$$\mathcal{F}_m(\epsilon_m, M, z, D) = \frac{2\epsilon_m M(1+z)^2[4\mu/M]^2}{15\pi^2 D(z)^2 h_m^2 f_{\rm merge}(\kappa - 1)}. \tag{2.119}$$

Lines marked with the superscript "I" turn out to hold for the initial LIGO interferometer parameters; those with "A" hold for advanced LIGO interferometer parameters; and those with "L" hold for LISA.

Using the numerical values of the noise curve parameters (2.75) for initial LIGO interferometers, and Eqs. (2.50), (2.51), (2.112), and (2.118) we find for the initial LIGO interferometers in the equal-mass case

$$\left(\frac{S}{N}\right)_{\text{initial}} = \begin{cases} 1.5\left(\frac{\epsilon_m}{0.1}\right)^{1/2}\left(\frac{200\,\text{Mpc}}{D(z)}\right)\left(\frac{(1+z)M}{18\,M_\odot}\right)^{5/2}, \\ \qquad\qquad (1+z)M \leq 18\,M_\odot; \\ 1.5\left(\frac{\epsilon_m}{0.1}\right)^{1/2}\left(\frac{200\,\text{Mpc}}{D(z)}\right)\left(\frac{(1+z)M}{18\,M_\odot}\right) \\ \quad \times\left[1+3\ln\left(\frac{(1+z)M}{18\,M_\odot}\right)-3.6\times10^{-3}\left(\frac{(1+z)M}{18\,M_\odot}\right)^3\right]^{1/2}, \\ \qquad\qquad 18\,M_\odot < (1+z)M \leq 36\,M_\odot; \\ 6.1\left(\frac{\epsilon_m}{0.1}\right)^{1/2}\left(\frac{200\,\text{Mpc}}{D(z)}\right)\left(\frac{(1+z)M}{36\,M_\odot}\right) \\ \quad \times\left[1+.23\left(\frac{(1+z)M}{36\,M_\odot}\right)^{-3}-0.007\left(\frac{(1+z)M}{36\,M_\odot}\right)^3\right]^{1/2}, \\ \qquad\qquad 36\,M_\odot < (1+z)M \leq 102\,M_\odot; \\ 17.3\left(\frac{\epsilon_m}{0.1}\right)^{1/2}\left(\frac{200\,\text{Mpc}}{D(z)}\right)\left(\frac{(1+z)M}{102\,M_\odot}\right)\left[1-.17\left(\frac{(1+z)M}{102\,M_\odot}\right)^3\right]^{1/2}, \\ \qquad\qquad 102\,M_\odot < (1+z)M \leq 118\,M_\odot; \\ 9.9\left(\frac{\epsilon_m}{0.1}\right)^{1/2}\left(\frac{200\,\text{Mpc}}{D(z)}\right)\left(\frac{(1+z)M}{118\,M_\odot}\right)\left[1-3.1\ln\left(\frac{(1+z)M}{230\,M_\odot}\right)\right]^{1/2}, \\ \qquad\qquad 118\,M_\odot < (1+z)M \leq 230\,M_\odot; \\ 20\left(\frac{\epsilon_m}{0.1}\right)^{1/2}\left(\frac{200\,\text{Mpc}}{D(z)}\right)\left(\frac{(1+z)M}{230\,M_\odot}\right)^{-1/2}\left[1-0.04\left(\frac{(1+z)M}{230\,M_\odot}\right)^3\right]^{1/2}, \\ \qquad\qquad 230\,M_\odot < (1+z)M \leq 660\,M_\odot; \\ 0 \qquad\qquad 660\,M_\odot < (1+z)M. \end{cases} \tag{2.120}$$

Similarly using Eq. (2.76) we find for advanced LIGO interferometers

$$\left(\frac{S}{N}\right)_{\text{advanced}} = \begin{cases} 13\left(\frac{\epsilon_m}{0.1}\right)^{1/2}\left(\frac{1\,\text{Gpc}}{D(z)}\right)\left(\frac{(1+z)M}{37\,M_\odot}\right)^{5/2}, \\ \qquad\qquad (1+z)M \leq 37\,M_\odot; \\ 13\left(\frac{\epsilon_m}{0.1}\right)^{1/2}\left(\frac{1\,\text{Gpc}}{D(z)}\right)\left(\frac{(1+z)M}{37\,M_\odot}\right) \times \\ \qquad \left[1+3\ln\left(\frac{(1+z)M}{37\,M_\odot}\right) - 3.6\times 10^{-3}\left(\frac{(1+z)M}{37\,M_\odot}\right)^3\right]^{1/2}, \\ \qquad\qquad 37\,M_\odot < (1+z)M \leq 95\,M_\odot; \\ 76\left(\frac{\epsilon_m}{0.1}\right)^{1/2}\left(\frac{1\,\text{Gpc}}{D(z)}\right)\left(\frac{(1+z)M}{95\,M_\odot}\right) \times \\ \qquad \left[1-0.21\left(\frac{(1+z)M}{95\,M_\odot}\right)^{-3} - 0.013\left(\frac{(1+z)M}{95\,M_\odot}\right)^3\right]^{1/2}, \\ \qquad\qquad 95\,M_\odot < (1+z)M \leq 240\,M_\odot; \\ 88\left(\frac{\epsilon_m}{0.1}\right)^{1/2}\left(\frac{1\,\text{Gpc}}{D(z)}\right)\left(\frac{(1+z)M}{240\,M_\odot}\right) \times \\ \qquad \left[1-3\ln\left(\frac{(1+z)M}{620\,M_\odot}\right) - 0.061\left(\frac{(1+z)M}{240\,M_\odot}\right)^{-3}\right]^{1/2}, \\ \qquad\qquad 240\,M_\odot < (1+z)M \leq 410\,M_\odot; \\ 150\left(\frac{\epsilon_m}{0.1}\right)^{1/2}\left(\frac{1\,\text{Gpc}}{D(z)}\right)\left(\frac{(1+z)M}{410\,M_\odot}\right)\left[1-3.0\ln\left(\frac{(1+z)M}{620\,M_\odot}\right)\right]^{1/2}, \\ \qquad\qquad 410\,M_\odot < (1+z)M \leq 620\,M_\odot; \\ 220\left(\frac{\epsilon_m}{0.1}\right)^{1/2}\left(\frac{1\,\text{Gpc}}{D(z)}\right)\left(\frac{(1+z)M}{620\,M_\odot}\right)^{-1/2}\left[1-0.013\left(\frac{(1+z)M}{620\,M_\odot}\right)^3\right]^{1/2}, \\ \qquad\qquad 620\,M_\odot < (1+z)M \leq 2600\,M_\odot; \\ 0 \qquad\qquad 2600\,M_\odot < (1+z)M. \end{cases} \tag{2.121}$$

Finally, using the parameters (2.77) appropriate for LISA, we obtain

$$\left(\frac{S}{N}\right)_{\rm LISA} = \begin{cases} 1.9\times 10^3\,\left(\frac{\epsilon_m}{0.1}\right)^{1/2}\left(\frac{1\,\mathrm{Gpc}}{D(z)}\right)\left(\frac{(1+z)M}{2.0\times 10^5 M_\odot}\right)^{5/2}, \\ \qquad\qquad\qquad\qquad (1+z)M \le 2.0\times 10^5\,M_\odot; \\ \\ 1.9\times 10^3\,\left(\frac{\epsilon_m}{0.1}\right)^{1/2}\left(\frac{1\,\mathrm{Gpc}}{D(z)}\right)\left(\frac{(1+z)M}{2.0\times 10^5 M_\odot}\right) \\ \quad\times\left[1+3\ln\left(\frac{(1+z)M}{2.0\times 10^5 M_\odot}\right)-3.6\times 10^{-3}\left(\frac{(1+z)M}{2.0\times 10^5 M_\odot}\right)^3\right]^{1/2}, \\ \qquad\qquad\qquad\qquad 2.0\times 10^5 M_\odot < (1+z)M \le 1.3\,\mathrm{M}M_\odot; \\ \\ 2.8\times 10^4\,\left(\frac{\epsilon_m}{0.1}\right)^{1/2}\left(\frac{1\,\mathrm{Gpc}}{D(z)}\right)\left(\frac{(1+z)M}{1.3\,\mathrm{M}M_\odot}\right), \\ \qquad\qquad\qquad\qquad 1.3\,\mathrm{M}M_\odot < (1+z)M \le 6.0\,\mathrm{M}M_\odot; \\ \\ 3.4\times 10^4\,\left(\frac{\epsilon_m}{0.1}\right)^{1/2}\left(\frac{1\,\mathrm{Gpc}}{D(z)}\right)\left(\frac{(1+z)M}{6.0\,\mathrm{M}M_\odot}\right)\left[1-3\ln\left(\frac{(1+z)M}{39\,\mathrm{M}M_\odot}\right)-\left(\frac{(1+z)M}{6.0\,\mathrm{M}M_\odot}\right)^{-3}\right]^{1/2}, \\ \qquad\qquad\qquad\qquad 6.0\,\mathrm{M}M_\odot < (1+z)M \le 39\,\mathrm{M}M_\odot; \\ \\ 3.6\times 10^5\,\left(\frac{\epsilon_m}{0.1}\right)^{1/2}\left(\frac{1\,\mathrm{Gpc}}{D(z)}\right)\left(\frac{(1+z)M}{39\,\mathrm{M}M_\odot}\right)^{-1/2}, \\ \qquad\qquad\qquad\qquad 39\,\mathrm{M}M_\odot < (1+z)M \le 41\,\mathrm{M}M_\odot; \\ \\ 3.4\times 10^5\,\left(\frac{\epsilon_m}{0.1}\right)^{1/2}\left(\frac{1\,\mathrm{Gpc}}{D(z)}\right)\left(\frac{(1+z)M}{41\,\mathrm{M}M_\odot}\right)^{-1/2}\left[1-3.8\times 10^{-3}\left(\frac{(1+z)M}{41\,\mathrm{M}M_\odot}\right)^3\right]^{1/2}, \\ \qquad\qquad\qquad\qquad 41\,\mathrm{M}M_\odot < (1+z)M \le 260\,\mathrm{M}M_\odot; \\ \\ 0 \qquad\qquad\qquad\qquad 260\,\mathrm{M}M_\odot < (1+z)M. \end{cases} \tag{2.122}$$

Ringdown

The ringdown SNRs are calculated a little differently from the inspiral and merger SNRs. First, we use the effective energy spectrum (2.65) which yields an estimate of the true SNR obtainable from the model waveform (2.62) that is accurate to within a few tens of percent (see Appendix A). Second, the integral over frequency in the SNR formula (2.36) with the noise spectrum (2.74) and the energy spectrum (2.65) cannot easily be evaluated analytically. Hence, we calculated this integral numerically to produce the plots of ringdown SNR versus BBH mass shown in Figs. 2.4, 2.5 and 2.6.

In the remainder of this appendix we derive approximate formulae for the ringdown SNR as a function of mass, by approximating the ringdown energy spectrum as a delta function at the ringdown frequency [*cf.* Eq. (2.66)]. This approximation yields (see Appendix A and Ref. [106])

$$\langle \rho^2 \rangle = \frac{(1+z)^3 M^2 \mathcal{A}^2 Q[4\mu/M]^2}{20\pi^2 D(z)^2 f_{\rm qnr} S_h[f_{\rm qnr}/(1+z)]}. \tag{2.123}$$

Using Eq. (2.64) and the relation (2.69) between the dimensionless coefficient $\mathcal{A}$ and the radiated energy we can rewrite formula (2.123) as

$$\langle \rho^2 \rangle = \frac{8}{5}\,\frac{1}{F(a)^2}\,\epsilon_r\,\frac{(1+z)M}{S_h[f_{\rm qnr}/(1+z)]}\left[\frac{(1+z)M}{D(z)}\right]^2\left[\frac{4\mu}{M}\right]^2, \tag{2.124}$$

where $\epsilon_r = \epsilon_{\rm ringdown}$ is the fraction of the total mass energy radiated in the ringdown, and

$$F(a) = 1 - \frac{63}{100}(1-a)^{3/10}. \tag{2.125}$$

An equivalent formula was previously obtained by Finn [107].

We find the following numerical result when we insert our assumed values $\epsilon_r = 0.03$ and $a = 0.98$ for the ringdown signal together with the parameters for the initial LIGO interferometer noise curve in the equal-mass case:

$$\left(\frac{S}{N}\right)_{\rm initial} = \begin{cases} 0.08\,\left(\frac{\epsilon_r}{0.03}\right)^{1/2}\left(\frac{200\,{\rm Mpc}}{D(z)}\right)\left(\frac{(1+z)M}{18\,M_\odot}\right)^{5/2} & (1+z)M \le 118\,M_\odot \\ 8.8\,\left(\frac{\epsilon_r}{0.03}\right)^{1/2}\left(\frac{200\,{\rm Mpc}}{D(z)}\right)\left(\frac{(1+z)M}{118\,M_\odot}\right) & 118\,M_\odot < (1+z)M \le 230\,M_\odot \\ 17\,\left(\frac{\epsilon_r}{0.03}\right)^{1/2}\left(\frac{200\,{\rm Mpc}}{D(z)}\right)\left(\frac{(1+z)M}{230\,M_\odot}\right)^{-1/2} & 230\,M_\odot < (1+z)M \le 660\,M_\odot \\ 0 & 660\,M_\odot < (1+z)M. \end{cases} \tag{2.126}$$

The corresponding formulae for advanced LIGO interferometers are

$$\left(\frac{S}{N}\right)_{\text{advanced}} = \begin{cases} 0.71\ \left(\frac{\epsilon_r}{0.03}\right)^{1/2}\ \left(\frac{1\,\text{Gpc}}{D(z)}\right)\ \left(\frac{(1+z)M}{37\,M_\odot}\right)^{5/2} & (1+z)M \leq 240\,M_\odot \\ 77\ \left(\frac{\epsilon_r}{0.03}\right)^{1/2}\ \left(\frac{1\,\text{Gpc}}{D(z)}\right)\ \left(\frac{(1+z)M}{240\,M_\odot}\right) & 240\,M_\odot < (1+z)M \leq 620\,M_\odot \\ 200\ \left(\frac{\epsilon_r}{0.03}\right)^{1/2}\ \left(\frac{1\,\text{Gpc}}{D(z)}\right)\ \left(\frac{(1+z)M}{620\,M_\odot}\right)^{-1/2} & 620\,M_\odot < (1+z)M \leq 2600\,M_\odot \\ 0 & 2600\,M_\odot < (1+z)M. \end{cases} \tag{2.127}$$

Finally, the corresponding formulae for LISA are

$$\left(\frac{S}{N}\right)_{\text{LISA}} = \begin{cases} 96\ \left(\frac{\epsilon_r}{0.03}\right)^{1/2}\left(\frac{1\,\text{Gpc}}{D(z)}\right)\left(\frac{(1+z)M}{0.2\,\text{M}M_\odot}\right)^{5/2} & (1+z)M \leq 1.3\,\text{M}M_\odot \\ 1.0\times 10^4\ \left(\frac{\epsilon_r}{0.03}\right)^{1/2}\left(\frac{1\,\text{Gpc}}{D(z)}\right)\left(\frac{(1+z)M}{1.3\,\text{M}M_\odot}\right) & 1.3\,\text{M}M_\odot < (1+z)M \leq 39\,\text{M}M_\odot \\ 3.1\times 10^5\ \left(\frac{\epsilon_r}{0.03}\right)^{1/2}\left(\frac{1\,\text{Gpc}}{D(z)}\right)\left(\frac{(1+z)M}{39\,\text{M}M_\odot}\right)^{-1/2} & 39\,\text{M}M_\odot < (1+z)M \leq 260\,\text{M}M_\odot \\ 0 & 260\,\text{M}M_\odot < (1+z)M. \end{cases} \tag{2.128}$$

By comparing Eqs. (2.126) – (2.128) with Figs. 2.4 – 2.6 it can be seen that the delta-function energy spectrum approximation is fairly good except for $M \gtrsim 3000 M_\odot$ for advanced LIGO interferometers and $M \gtrsim 3\times 10^8 M_\odot$ for LISA. The approximation fails to capture the high mass tails of the SNR curves.

Bibliography

[1] K. S. Thorne, in *300 Years of Gravitation*, ed. S. W. Hawking and W. Israel (Cambridge University Press, Cambridge, 1987), pp. 330-458.

[2] B. F. Schutz, *Sources of Gravitational Waves*, in NASA, Relativistic Gravitational Experiments in Space, pp. 7-13 (1989).

[3] A. Abramovici, W. E. Althouse, R. W. P. Drever, Y. Gürsel, S. Kawamura, F. J. Raab, D. Shoemaker, L. Sievers, R. E. Spero, K. S. Thorne, R. E. Vogt, R. Weiss, S. E. Whitcomb, and M. E. Zucker, *LIGO: The Laser Interferometer Gravitational-wave Observatory*, Science **256**, 325 (1992).

[4] C. Bradaschia *et al.*, Nucl. Instrum. & Methods **A289**, 518 (1990); also in *Gravitation: A Banff Summer Institute*, ed. R. Mann and P. Wesson (World Scientific, Singapore, 1991).

[5] P. Bender *et al.*, "LISA, Laser interferometer space antenna for gravitational wave measurements: ESA Assessment Study Report", 1994.

[6] Hough, J. *et al.*, in *Gravitational Wave Experiments*, proceedings of the Edoardo Amaldi Conference, edited by E. Coccia, G. Pizzella, and F. Ronga, (World Scientific, Singapore, 1995), p. 50.

[7] P. Bender, I. Ciufolini, K. Danzmann, W. Folkner, J. Hough, D. Robertson, A. Rüdiger, M. Sandford, R. Schilling, B. Schutz, R. Stebbins, T. Summer, P. Touboul, S. Vitale, H. Ward, and W. Winkler, *LISA: Laser Interferometer Space Antenna for the detection and observation of gravitational waves*, Pre-Phase A Report, December 1995 (unpublished).

[8] L. E. Kidder, C. M. Will, and A. G. Wiseman, Phys. Rev. D **47**, 3281 (1993); Class. Quant. Grav. **9** L125 (1992).

[9] G. B. Cook, Phys. Rev. D **50**, 5025 (1994). See especially Fig. 3.

[10] K. S. Thorne, in *Proceedings of the Snowmass 95 Summer Study on Particle and Nuclear Astrophysics*, eds. E.W. Kolb and R. Peccei (World Scientific, Singapore, 1995) (gr-qc/9506086).

[11] A. Ori and K. S. Thorne, in preparation.

[12] D. Lai and A. G. Wiseman, "Innermost Stable Circular Orbit of Inspiraling Neutron-Star Binaries: Tidal Effects, Post-Newtonian Effects and the Neutron-Star Equation of State", gr-qc/9609014.

[13] S. A. Teukolsky and W. H. Press, Astrophys. J. **193**, 443 (1974).

[14] S. Chandrasekhar and S. L. Detweiler, Proc. R. Soc. London **A344**, 441 (1975).

[15] F. Echeverria, Phys. Rev. D **40**, 3194 (1988).

[16] L. S. Finn, Phys. Rev. D **46**, 5236 (1992). See also F. Echeverria, unpublished PhD thesis, California Institute of Technology, addendum to Ch. 2 (1993). This is an addendum to Ref. [15] which shows that the methods used to calculate measurement errors in Refs. [15] and [16] are equivalent.

[17] G. D. Quinlan and S. L. Shapiro, Astrophys. J. **343**, 725 (1989) (especially Fig. 12); *ibid* **356**, 483 (1990).

[18] S. Sigurdsson and L. Hernquist, Nature **364**, 423, 1993.

[19] E. S. Phinney, Astrophys. J. **380**, L17 (1991).

[20] R. Narayan, T. Piran, and A. Shemi, Astrophys. J. **379**, L17 (1991)

[21] E. P. J. Van den Heuvel and D. R. Lorimer, Mon. Not. R. Astron. Soc. **283**, L37-L39 (1996).

[22] A. V. Tutukov and L. R. Yungelson, Mon. Not. R. Astron. Soc. **260** 675, 1993.

[23] H. Yamaoka, T. Shigeyama, and K. Nomoto, Astron. Astrophys. **267**, 433, 1993.

[24] V. M. Lipunov, K. A. Postnov and M. E. Prokhorov, Sternberg Astronomical Institute preprint (1996) (astro-ph/9610016); also astro-ph/9701134.

[25] S. F. P. Zwart and L. R. Yungelson, *Formation and evolution of binary neutron stars*, to appear in Astron. Astrophys.; astro-ph/9710347.

[26] It is also conceivable that the BBH coalescence rates could be higher than these theoretical estimates: high mass stars may have been much more numerous among population III stars due to the lower metallicity at high redshift, so there could be a large population of BBHs that are remnants of population III stars living in galactic halos.

[27] Although there have been suggestions that the globular cluster M15 harbors a black hole of mass $\sim 10^3 M_\odot$ [28], theoretical modeling combined with recent HST observations neither confirm nor rule out this possibility [29].

[28] K. A. Postnov, M. E. Prokhorov and N. I. Shakura, in *High Energy Astrophysics: American and Soviet Perspectives*, Proceedings fromthe U.S.-USSR Workshop on High-Energy Astrophysics, 1989, edited by W. H. G. Lewin, G. W. Clark, R. A. Sunyaev, K. K. Trivers, and D. M. Abramson (National Academy Press, Washington, D.C., 1991), p 316-321.

[29] J. D. Dull *et al.*, Astrophys. J. **481**, 257 (1997); K. Gebhardt *et al.*, Astron. J. **113**, 1026 (1997).

[30] M. Begelman and M. Rees, *Gravity's fatal attraction: Black Holes in the Universe*, W.H. Freeman and Co., Basingstoke, England (1995); and references therein.

[31] R. D. Blandford, in *Active Galactic Nuclei: Saas-Fee Adv Course 20*, ed. T. Courvoisier & M. Mayor (Springer-Verlag, Berlin, 1990); M. J. Rees, Science **247**, 817 (1990).

[32] D. Hils and P. L. Bender, Astrophys. J. **445**, L7 (1995).

[33] E. Poisson, *Measuring black-hole parameters and testing general relativity using gravitational wave data from space-based interferometers*, preprint 1996, gr-qc/9606024.

[34] M. C. Begelman, R. D. Blandford, M. J. Rees, Nature (Londom) **287**, 307 (1980).

[35] H. D. Wahlquist, in "NASA, Relativistic Gravitational Experiments in Space", Report No. SEE N90-19940 12-90, 1989, pp. 14–17.

[36] M. G. Haehnelt, Mon. Not. Roy. Astron. Soc. **269** 199 (1994); astro-ph/9405032.

[37] N. Roos, J.S. Kaastra, C.A. Hummel, Astrophys. J. **409**, 130 (1993).

[38] A. Sillanpaa *et al*, Astrophys. J. **325**, 628 (1988).

[39] C.M. Gaskell, Astrophys. J. **464**, L107 (1996); C.M. Gaskell, in *Jets from Stars and Galaxies*, edited by W. Kundt (Springer, Berlin, 1996) pp. 165–196.

[40] B. F. Schutz, in *The detection of gravitational radiation*, edited by D. Blair, (Cambridge University Press, Cambridge, England, 1989).

[41] L. Blanchet, Phys. Rev. D **54**, 1417 (1996) (gr-qc/9603048).

[42] L. Blanchet, private communication.

[43] By post-n-Newtonian order, we mean $O[(v/c)^{2n}]$ in secular terms and $O[(v/c)^{5+2n}]$ in dissipative, radiation reaction terms ($2n$ orders beyond the leading quadrupole radiation reaction term). This is the standard counting method for post-Newtonian waveforms.

[44] C. Cutler, T. A. Apostolatos, L. Bildsten, L. S. Finn, É. É. Flanagan, D. Kennefick, D. M. Marković, A. Ori, E. Poisson, G. J. Sussman, and K. S. Thorne, Phys. Rev. Lett. **70**, 2984 (1993).

[45] E. Poisson, Phys. Rev. D **52**, 5719 (1995). (gr-qc/9505030).

[46] R. Balasubramanian and S. V. Dhurandhar, Phys. Rev. D **50**, 6080 (1994) (gr-qc/9404009).

[47] C. Cutler and É. É. Flanagan, in preparation.

[48] Families of template waveforms optimized for signal searches are in the early stages of development; see B. S. Sathyaprakash, Phys. Rev. D **40**, R7111 (1994); B. S Sathyaprakash and S. V. Dhurandhar, Phys. Rev. D **44**, 3819 (1991); **49**, 1707 (1994); A. Królak, K. D. Kokkotas, and G. Schäfer, *Proceedings of the 17th Texas Symposium on Relativistic Astrophysics, Ann. N. Y. Acad. Sci*, 1995; T. A. Apostolatos, Phys. Rev. D **52**, 605 (1995).

[49] K. S. Thorne, presentation at the *Intermediate Binary Black Hole* workshop, Caltech, July 1996. The location of the post-Newtonian breakdown can be seen from Fig. 1 of Ref. [45].

[50] A workshop focusing on this issue was held at Caltech in July, 1996.

[51] Even if such methods are not found, post-Newtonian templates should be adequate for searching for inspiral waves even in the IBBH regime; IBBH templates will likely be needed only as a foundation for extracting the waves' information. We also note that the method of Padé approximants has recently been found to improve significantly the convergence of the post-Newtonian series [52]; the implications of this for the IBBH regime are not yet clear.

[52] T. Damour, B. Iyer, and B. S. Sathyaprakash, Phys. Rev. D **57**, 885 (1998).

[53] One can convince oneself of the likelihood of this cleanliness by considering various possible sources of perturbations to the gravitational-wave signal. For solar mass coalescences, the most likely perturbing effect would be due to accretion disks; most likely they will be long gone before the black holes merge. One case where a possible perturbing effect on the gravitational-wave signal may be observable is the stochastic influence of a surrounding stellar cluster on the orbits of members of a SMBH binary during the early stages of the inspiral. While strictly speaking this could make our assumption of the applicability of Wiener optimal filtering invalid for some SMBH inspirals, such inapplicability is not a cause for concern: the SNRs are typically so high anyway that it should be possible to easily detect both the coherent portions of the inspiral radiation and any isolated changes in phase due to close-encounter perturbations.

[54] The Grand Challenge Alliance is an NSF funded collaboration of physicists and computer scientists at eight institutions: University of Texas, Austin; NCSA/University of Illinois; University of North Carolina, Chapel Hill; Cornell University; Syracuse University NPAC; University

of Pittsburgh; Northwestern University; and Penn State University. More information can be found at the WWW address `http://jean-luc.ncsa.uiuc.edu/GC/GC.html`; see also Ref. [55] for a review.

[55] L. S. Finn, in proceedings of GR14; gr-qc/9603004.

[56] S. Chandrasekhar, *The Mathematical Theory of Black Holes*, Oxford University Press, New York, 1983; p. 528.

[57] É. É. Flanagan and S. A. Hughes, *Measuring gravitational waves from binary black hole coalescence: II. The waves' information and its extraction, with and without merger templates*, Phys. Rev. D **57**, 4566 (1998).

[58] C. W. Helstrom, *Statistical Theory of Signal Detection*, (Pergamon, Oxford, 1968).

[59] L. A. Wainstein and V. D. Zubakov, *Extraction of Signals from Noise*, (Prentice-Hall, Englewood Cliffs, NJ,1962).

[60] C. Cutler and É. É. Flanagan, Phys. Rev. D **49**, 2658 (1994).

[61] Our convention for the normalization of the spectral noise density $S_h(f)$ is such that

$$\langle n(t)^2 \rangle = \int_0^\infty S_h(f)\, df,$$

where $n(t)$ is the detector noise ("One-sided spectral noise density"). This determines the constant 4 appearing in Eq. (2.13). Note that the alternative convention used in Refs. [58, 59] results in a factor 2 instead of 4 in Eq. (2.13). In Eq. (29) of Ref. [1], the spectral noise density that is used is the one-sided spectral noise density (as in this paper), and thus the overall factor in front of the integral should be 4, not 2.

[62] S. L. Shapiro and S. A. Teukolsky, *Black Holes, White Dwarfs, and Neutron Stars: The Physics of Compact Objects* (Wiley, New York, 1983).

[63] For instance, if the post-Newtonian expansion is taken to order $3/2$, we would find in the equal mass case (see, *e.g.*, Ref. [64])

$$\frac{dE}{df} = \frac{1}{12}\pi^{2/3} M^{5/3} f^{-1/3} \left[1 - \frac{1}{6}\left(9 + \frac{1}{4}\right)(\pi M f)^{2/3}\right].$$

The correction to the Newtonian formula is ~ 0.24 at $f = f_{\rm merge}$; when taken to higher order, there will be additional corrections. For the purposes of our discussion, these corrections are

not important – an estimate of the SNR that is accurate to a few tens of percent is adequate. Also, the loss in SNR due the phase lag between the approximate, post-Newtonian templates and the true, general-relativistic signal will be small [48].

[64] C. M. Will, in *Relativistic Cosmology*, edited by M. Sasaki (Universal Academy Press, Tokyo, 1994), pp. 83–93.

[65] This is the value predicted by the numerical initial data sets of Ref. [9] at $f = f_{\rm merge} = 0.02/M$; see also the arguments concerning angular momentum in Sec. 2.3.2.

[66] S. R. Brandt and E. Seidel, Phys. Rev. D **52**, 870 (1995) (gr-qc/9412073); the run labeled r3 of a distorted Kerr black hole with $a \sim 0.35$ yields an energy radiated in ringdown waves of $\sim 3\%$ (from Table IV, and also from Fig. 18 which shows that most of the radiated energy can be ascribed to the ringdown waves).

[67] L. L. Smarr, Ph.D dissertation, University of Texas at Austin, unpublished (1975).

[68] S. Detweiler, in *Sources of Gravitational Radiation*, edited by L. L. Smarr (Cambridge University Press, Cambridge, 1979).

[69] See, *e.g.*, J. Baker, A. Abrahams, P. Anninos, S. Brandt, R. Price, J. Pullin, E. Seidel, Phys. Rev. D **55**, 829 (1997).

[70] When we say that a source is visible out to a distance D, we mean that the rate of detection of events is the roughly the same as the rate of occurrence of events within a sphere of radius D. Note that some events within this sphere will be missed, and some outside this sphere will be detected, due to the beaming and orientation effects discussed in Sec. 2.2.3. Rare, optimally oriented sources will be visible out to several times D.

[71] It would be quite simple to improve on this filter. For example, one could divide it by the noise spectral density in order to weight the filter according to the instrumental noise characteristics, *i.e.*, pre-whiten the data stream. The main result of our analysis, the formula (2.18), would also approximately apply to such an improved filtering method.

[72] Note that we distinguish between the number of statistically independent waveform shapes $\mathcal{N}_{\rm shapes}$ in the manifold of waveforms that one is trying to detect using the matched filtering process, and the actual number of templates $\mathcal{N}_{\rm templates}$ used in the computations. The number $\mathcal{N}_{\rm shapes}$ is the volume of the subset of the manifold of signals with SNR $\leq \rho$, in the natural metric induced by the statistical properties of the noise; thus $\mathcal{N}_{\rm shapes}$ depends

on ρ. The number $\mathcal{N}_{\rm templates}$ is defined in Sec. 2.6.1 and is independent of ρ. In general $\mathcal{N}_{\rm templates} < \mathcal{N}_{\rm shapes}$ since the optimum computational method will have less than one template per statistically independent waveform shape. For the purposes of calculating SNR thresholds, $\ln(\mathcal{N}_{\rm templates}) \approx \ln(\mathcal{N}_{\rm shapes})$ to a good approximation.

[73] É. É. Flanagan, in preparation.

[74] P. R. Brady, T. Creighton, C. Cutler, B. F. Schutz, Phys. Rev. D **57**, 2101 (1998).

[75] D. Marković, Phys. Rev. D **48**, 4738 (1993); E.W. Kolb and M.S. Turner, *The Early Universe*, (Addison-Wesley, Redwood, CA, 1990) p. 44.

[76] During the inspiral phase, the timescale over which the frequency of the waves changes is much longer than the instantaneous period, so it makes sense to talk about the frequency of the waves at a certain time. In particular, we can (roughly) talk either about the time or the frequency at which the inspiral ends — the notion of instantaneous frequency is just beginning to break down then.

[77] L. L. Smarr, in *Sources of Gravitational Radiation*, edited by L. L. Smarr (Cambridge University Press, Cambridge, 1979).

[78] P. Anninos, D. Hobill, E. Seidel, L. Smarr, W.-M. Suen, Phys. Rev. Lett. **71**, 2851 (1993); Phys. Rev. D **52**, 2044 (1995).

[79] S.L. Detweiler, Proc. R. Soc. London **A352**, 381 (1977).

[80] D. Christodoulou, Phys. Rev. Lett. **67**, 1486 (1991); K. S. Thorne, Phys. Rev. D **45**, 520 (1992); A. G. Wiseman and C. M. Will, Phys. Rev. D **44**, R2945 (1991).

[81] D. Kennefick, Phys. Rev. D **50** 3587 (1994).

[82] Since ϵ is a scalar quantity, it can only depend on scalar products of $\mathbf{S}_1$, $\mathbf{S}_2$ and $\hat{\mathbf{L}}$ and not on these vectorial quantities themselves. Therefore the number of independent variables that ϵ depends on is six.

[83] J. K. Blackburn and S. Detweiler, Phys. Rev. D **46**, 2318 (1992); the geometry at which $S = 7.5\, m_1$ in their notation.

[84] D. M. Eardley, in *Gravitational Radiation*, ed. N. Deruelle and T. Piran, North-Holland Publishing Co., 1983.

[85] See, for example, K. S. Thorne, Rev. Mod. Phys. **52**, 299 (1980), Eqs. (4.16') and (4.23').

[86] The inequality $|\mathbf{S}_{\rm final}| \leq M^2$ used in deriving Eq. (2.56) should really be $|\mathbf{S}_{\rm final}| \leq (M - E_{\rm rad})^2$, since it is the mass of the final black hole and not the initial total mass of the system that is relevant. An argument parallel to that leading to Eq. (2.58) then yields the inequality $\epsilon_{\rm rad} \gtrsim [1.4 - (1 - \epsilon_{\rm rad})^2]/4$ or $\epsilon_{\rm rad} \gtrsim 0.18$, where $\epsilon_{\rm rad} = E_{\rm rad}/M$. Hence, even if only $\sim 50\%$ of the emitted radiation is quadrupolar, the estimate $\epsilon_{\rm rad} \sim 0.1$ used in Sec. 2.3.2 is probably still fairly realistic.

[87] D. M. Eardley and E. W. Hirschmann, *Comment on "Instabilities in Close Neutron Star Binaries"*, ITP Santa Barbara preprint NSF-ITP-95-165 (gr-qc/9601019).

[88] C. W. Misner *et al.*, *Gravitation* (Freeman, New York, 1973), Sec. 36.6.

[89] B. J. Owen, Phys. Rev. D **53**, 6749 (1996).

[90] E. W. Leaver, Proc. R. Soc. Lond. A **402**, 285 (1985). Leaver's data on the $l = m = 2$ mode, which was used by Echeverria, is unpublished.

[91] K. S. Thorne, Ap. J. **191**, 507 (1974).

[92] Actually the QNR metric perturbation will vanish at the event horizon; one could instead use the boundary of the ergo-region. Also, the ratio $\mathcal{R}$ of the circumferences will be gauge dependent. However, if we expand $\mathcal{R}$ as $\mathcal{R} = 1 + \alpha\mathcal{A} + O(\mathcal{A}^2)$, then the coefficient α will be gauge invariant and we could take $\mathcal{A}_2 = 1/\alpha$.

[93] More specifically, an ellipsoidal solid body of mass M of uniform density whose axes are given by $l^2, l^2[1 \pm (3/5)\sin(\omega t)]$ produces a luminosity $L = 9M^2l^4\omega^6/5^5$; comparing this to the luminosity $\mathcal{A}^2M^2\omega_{\rm qnr}^2/(16\pi)$ for the waveform (2.62) at $t = 0$, identifying $\omega = \omega_{\rm qnr} = 2\pi\,0.13/M$ and taking $l = r_+ = M + \sqrt{M^2 - a^2}$ for $a = 0.97M$ say yields $\mathcal{A} = 0.4$. This crude estimation method clearly does not take into account the potential barrier through which the radiation must propagate (among other things). We imagine a more precise calculation will find a somewhat smaller value of $\mathcal{A}$.

[94] This error can be seen by inserting the parameter values $m = 1000\,\mathrm{kg}$, $f_0 = 1\,\mathrm{Hz}$, and $Q_0 = 10^9$ given in Ref. [3] into the standard equation for suspension thermal noise due to viscous damping, as given in, *e.g.*, Eq. (4.3) of Ref. [95]. The resulting noise level is 3 times larger than the noise level shown in Fig. 7 of Ref. [3] for $10\,\mathrm{Hz} \lesssim f \lesssim 70\,\mathrm{Hz}$. This error was not made in the corresponding figure V.4 of the 1989 LIGO proposal [96]. [K. S. Thorne, private communication]

[95] L. S. Finn and D. F. Chernoff, Phys. Rev. D **47**, 2198 (1993).

[96] R. E. Vogt *et al.*, "Proposal to the National Science Foundation for the Construction, Operation, and Supporting Research and Development of a Laser Interferometer Gravitational-Wave Observatory", California Institute of Technology, 1989 (unpublished).

[97] The $h_{\rm rms}(f) = $ const part of the noise curve happens to have the same frequency dependence that the test masses' thermal noise would have if this noise were due to structural damping [98]. This behavior is accidental: the $h_{\rm rms}(f) =$ const piece of the spectrum is used here merely to more closely approximate the smooth transition between the suspension thermal noise and laser shot noise parts of the spectrum.

[98] A. Gillespie and F. Raab, Phys. Lett. A, **190**, 213 (1994).

[99] C. Cutler, *Angular Resolution of the LISA Gravitational Wave Detector*, gr-qc/9703068; Phys. Rev. D, in press.

[100] See Eq. (32) of Ref. [1]. Note also that our $h_n(f)$ is similar to the quantity $h_{3/\rm yr}$ defined in Ref. [1], which is the same as the quantity denoted $h_{\rm SB}(f)$ in Refs. [3, 10]. These quantities differ from $h_n(f)$ by the factor $\sqrt{\ln \mathcal{N}} \sim 5$, where $\mathcal{N}$ is the number of independent starting times per third of a year that must be tried in the matched filtering search process; see Eq. (34) of Ref. [1]. We omit this factor in our definition of h_n since in paper II [57] we will be discussing SNRs in situations when the waves have already been detected and where the factor $\sqrt{\ln \mathcal{N}}$ is not relevant. The factor instead appears in our SNR thresholds discussed in Sec. 2.6. Note also that our signal-to-noise ratios differ from those in Refs. [3, 10] by an overall factor of $\sqrt{3/2}$, as discussed after Eq. (2.36) above.

[101] We obtained the metric (2.84) in the following way: (i) We took the large Q limit of the matrix C'^{-1}_{ij} of Ref. [16], which was calculated assuming white noise, (ii) We inverted this matrix, took a 2×2 sub-block and re-inverted, thus eliminating (effectively integrating out) the variables V and T. This procedure for eliminating the time-of-arrival variable T is equivalent to the procedure embodied in Eq. (2.28) of Ref. [89]. (iii) We divided by 2 in order to accord with the definition (2.12) of Ref. [89].

[102] This is Eq. (2.15) with $\ln(\mathcal{N}_{\rm shapes})$ replaced by $\ln(\mathcal{N}_{\rm templates})$, *cf.* Ref. [72] above.

[103] In the situation where merger templates are available, the optimum search method would in fact be a combination of inspiral, merger and ringdown searches, in which the entire inspiral-merger-ringdown signal as a whole is searched for using matched filtering.

[104] Here we are assuming that we have a fair idea of the range of durations and bandwidths of merger waves from representative supercomputer simulations. Without such information, a more appropriate, conservative value for $\mathcal{N}_{\rm bins}$ might be ~ 300. This would increase $\mathcal{R}$ from 3.5 to ~ 10, corresponding to a reduction in event rate of ~ 3. Thus, information from the simulations will be important for detecting the waves.

[105] The quantity $\mathcal{N}_{\rm shapes,max}$ is also approximately the total of waveform shapes of duration less than or equal to T, with bandwidth Δf and with SNR $\leq \rho$ which are distinguishable in the interferometer noise [57].

[106] To see that angle-averaging the approximate formula (2.96) yields the formula (2.123) for the ringdown SNR, corresponding to the approximate delta function energy spectrum (2.66), proceed as follows. Starting from Eq. (2.107), average over the angles θ,φ,ψ,ι and β using Eqs. (2.40) and (2.63). This yields

$$\langle h_0(\theta,\varphi,\psi,\iota,\beta)^2\rangle = \frac{1}{10\pi}\frac{\mathcal{A}^2M^2}{r^2}.$$

Substitute this into Eq. (2.96), make the replacement $S_h \rightarrow S_h(f_{\rm qnr})$, and make the appropriate substitutions to account for cosmological effects as explained in Sec. 2.2.3 to obtain Eq. (2.123).

[107] The small z, equal-mass limit of Eq. (2.124) agrees with the large Q limit of Eq. (4.7) of Ref. [16] when that equation is multiplied by a correction factor of 2.

Chapter 3

Measuring gravitational waves from binary black hole coalescences: II. The waves' information and its extraction, with and without templates

Coauthored with Éanna É. Flanagan; published in *Physical Review D* [Phys. Rev. D **57**, 4566 (1998)].

Abstract

We discuss the extraction of information from detected binary black hole (BBH) coalescence gravitational waves by the ground-based interferometers LIGO and VIRGO, and by the space-based interferometer LISA. We focus on the merger phase that occurs after the gradual inspiral and before the ringdown. Our results are: (i) If numerical relativity simulations have not produced template merger waveforms before BBH events are detected, one can study the merger waves using simple band-pass filters. For BBHs smaller than about 40 $M_\odot$ detected via their inspiral waves, the band-pass filtering signal-to-noise ratio indicates that the merger waves should typically be just barely visible in the noise for initial and advanced LIGO interferometers. (ii) We derive an optimized maximum-likelihood method for extracting a best-fit merger waveform from the noisy detector output; one "perpendicularly projects" this output onto a function space (specified using wavelets) that incorporates our (possibly sketchy) prior knowledge of the waveforms. An extension of the method allows one to extract the BBH's two independent waveforms from outputs of several interferometers. (iii) We propose a computational strategy for numerical relativists to pursue, if they successfully produce computer codes for generating merger waveforms, but if running the codes is too expensive to permit an extensive survey of the merger parameter space. In this case, for LIGO/VIRGO data analysis purposes, it would be advantageous to do a coarse survey of the parameter space aimed at exploring several qualitative issues and at determining the ranges of the several key parameters which we describe. (iv) A complete set of templates could be used to test the nonlinear dynamics of general relativity and to measure some of the binary's parameters via matched filtering. We estimate the number of bits of information obtainable from the merger waves (about 10 to 60 for LIGO/VIRGO; up to 200 for LISA), estimate the information loss due to template numerical errors

or sparseness in the template grid, and infer approximate requirements on template accuracy and spacing.

3.1 Introduction and Summary

3.1.1 Gravitational waves from binary black holes

With the ground-based gravitational-wave observatories LIGO [1], VIRGO [2], and GEO600 [3] expected to be taking data within the next few years, and with the space-based observatory LISA [4, 5, 6] in planning and development, much effort is currently going into understanding gravitational-wave sources and associated data analysis issues. One potentially interesting and important source is the coalescences of binary black holes (BBHs). Such systems will be detectable to large distances by ground-based interferometers (factors of order ten further than binary neutron star systems) and over a wide range of masses. If the birthrates of BBH systems are not too low, they could be the most commonly detected type of compact binary gravitational-wave source.

The evolution of BBH systems and their emitted gravitational waves can be roughly divided into three epochs [7]: an adiabatic *inspiral*, in which the evolution is driven by radiation reaction, terminating roughly at the innermost stable circular orbit [8, 9]; a violent, dynamic *merger*; and a final *ringdown* in which the emitted radiation is dominated by the $l = m = 2$ quasinormal mode of the final Kerr black hole. Gravitational waves from the merger epoch could be rich with information about relativistic gravity in a highly nonlinear, highly dynamical regime which is poorly understood today.

Depending on the system's mass, some BBH coalescence events will be most easily detected by searching for the inspiral waves, others by searching for the ringdown, and others by searching for the merger. In the previous chapter, we analyzed the prospects for detecting BBH events using these three different types of searches, for initial and advanced LIGO interferometers and for LISA. Once a BBH event has been detected, the location of the three different phases of the waves in the data stream will be known to a fair approximation, although it will not necessarily be the case that all three phases will be detectable.

Waveform models or templates for the three epochs will be useful both for searches for BBH events using matched filtering, and also for interpreting and extracting information from the observed waveforms. At present, there is a reasonably good theoretical understanding of the waves generated during the inspiral and the ringdown [7, 10], whereas the merger is very poorly under-

stood: no merger templates exist as yet. Theoretical understanding of merger dynamics will eventually come from numerical relativity. One rather large effort to compute the dynamics of BBH mergers is the American Grand Challenge Alliance, an NSF funded collaboration of physicists and computer scientists at eight institutions [11, 12]; similar efforts are underway elsewhere. Modeling BBH mergers is an extremely difficult task; the numerical relativists who are writing codes for simulating BBH mergers are beset with many technical difficulties.

When the first BBH coalescences are detected, our theoretical understanding of BBH mergers could be in one of four possible states: (i) *No information:* supercomputer simulations have not yet successfully evolved any BBH mergers, so no information about merger waves is available. (ii) *Information limited in principle:* some information about BBH mergers is available, but numerical relativists are unable to produce arbitrary merger templates. For example, supercomputer codes might only be able to simulate some special class of BBH mergers (*e.g.*, those with vanishing initial spins, or equal mass BBHs); or, it could be that it is not possible to produce accurate waveforms, but more qualitative information about the merger (such as its duration) is available. (iii) *Information limited in practice:* accurate waveforms can be obtained for fully general BBH mergers, but each run of the codes to produce a template is so expensive in terms of computer time and cost that only a small number of representative template shapes can be computed and stored. (The total number of template shapes required to cover the entire range of behaviors of BBH mergers is likely to be in the range of thousands to millions or more.) (iv) *Full information:* a complete set of templates has been computed and is available for data analysis. This possibility seems rather unlikely in the time frame of the first detections of BBH coalescences.

Concomitant to these four states are three possible scenarios for data analysis of the waves from the merger epoch. The first possibility [corresponding to state (i) above] is that numerical computations provide no input to aid gravitational-wave data analysis. With no templates to guide the interpretation of the measured waveform, it will not be possible to obtain information about the BBH source or about strong-field general relativity from the merger waves. One's goal will simply be to measure as accurately as possible the merger waveform's shape. For this waveform shape measurement, one should make use of all possible prior information obtainable from analyses of the inspiral and/or ringdown signals, if they are detectable (see Sec. 3.1.2 below).

Second [states (ii) and (iii) above], if only a few representative simulations and associated templates are available, one might simply perform a qualitative comparison between the measured waveform and templates in order to deduce qualitative information about the BBH source. For in-

stance, simulations might demonstrate a strong correlation between the duration of the merger (in units of the total mass of the system) and the spins of the binary's black holes; a measurement of the merger's duration would then give some information about the binary's spins, without having to find a template that exactly matched the measured waveform. In this scenario, when reconstructing the merger waveform from the noisy data, one should use the any prior information from the measured inspiral and/or ringdown waves, and in addition the prior information (for example the expected range of frequencies) one has about the merger waveforms' behaviors from the representative supercomputer simulations.

The third scenario consists of matched filtering the data stream with merger templates in order to measure the parameters of the binary and to test general relativity. This will certainly be feasible if one has a complete set of merger templates [state (iv)]. It may also be feasible when information about BBH mergers is "limited in practice" [state (iii)]: it may be possible to perform several runs of the supercomputer code, concentrated in the appropriate small region of parameter space compatible with one's measurements from the inspiral and ringdown waves, in an effort to match the observed waveforms.

3.1.2 What can be learned from BBH waves

Different types of information will be obtainable from the three different phases of the gravitational wave signal. If the inspiral and ringdown phases are strong enough to be measurable, they will be easier to analyze than the merger phase, and the information they yield via matched filtering will be used as "prior information" in attempting to analyze the merger phase. Matched filtering of the inspiral will allow measurements of the (redshifted) masses of the two black holes, the direction to the source, the arrival time, orbital phase, and direction of orbital angular momentum at some fiducial frequency, the luminosity distance to the source, and some information about the black holes' spins. See, for example, Refs. [13, 14, 15, 16, 17, 18] for estimates of anticipated measurement accuracies for these parameters [19]. From the ringdown waves, one can measure the mass M and dimensionless spin parameter a of the final merged black hole, with an accuracy of roughly [16, 17]

$$\begin{aligned} \Delta a &\simeq \frac{6(1-a)^{1.06}}{(S/N)_{\text{ringdown}}}, \\ \frac{\Delta M}{M} &\simeq \frac{2(1-a)^{9/20}}{(S/N)_{\text{ringdown}}}, \end{aligned} \tag{3.1}$$

where $(S/N)_{\text{ringdown}}$ is the ringdown's measured matched filtering signal-to-noise ratio (SNR). (However, note that for low mass BBH events which are detected via their inspiral signals, the ringdown waves will be detectable only for $\sim 1\%$ of the events [20].)

If merger templates are available, one could hope to use matched filtering to measure the system's parameters and to test general relativity. If one has no prior information about the detected BBH system, one would simply filter the merger data with all merger templates available, potentially a large number. However, if the inspiral and/or the ringdown signals have already been measured, some information of the type discussed in the previous paragraph will be available. In such cases the total number of merger templates needed will be reduced—one need consider only templates whose parameters are commensurate with the inspiral/ringdown measurements. Such inspiral and ringdown information will be invaluable if our understanding of the merger waves is "limited in practice," as discussed in Sec. 3.1.1.

The primary goal when one attempts to match a merger template with gravitational-wave data will be to provide a test of general relativity rather than to measure parameters. A good match between the measured waveform and a numerical template would constitute a strong test of general relativity in the most extreme of domains: highly nonlinear, rapidly dynamical, highly nonspherical spacetime warpage. It would also provide the oft-quoted unambiguous detection of black holes. (Such an unambiguous detection could also come from a measurement of quasinormal ringing.) A close match between measured and predicted waveforms for BBH mergers might constrain theories of gravity that generalize general relativity. The inspiral portion of the waveform for neutron star-neutron star mergers will strongly constrain the dimensionless parameter ω of Brans-Dicke theory [21]. Unfortunately, the most theoretically natural class of generalizations of general relativity compatible with known experiments ("scalar-tensor theories" [22]) may not be constrained by BBH measurements, since black holes, unlike neutron stars, cannot have any scalar hair in such theories [23].

Matched filtering of the merger waves could also be useful in measuring some of the system's parameters, such as the total mass M or the spin parameter a of the final black hole [24]. These measurements could provide additional information about the source, over and above that obtainable from the inspiral and ringdown signals. For instance, in some cases the total mass of the system may be largely unconstrained from an inspiral measurement, while the ringdown may not be detectable; in such cases the total mass might be extractable from the merger waves.

3.1.3 Extracting the waves' information: our analyses, suggested tools, and results

The principal purposes of this chapter are: (i) to suggest a data analysis method that can be used in the absence of templates to obtain from the noisy data stream a "best-fit" merger waveform shape; and (ii) to provide input to numerical relativity simulations by deriving some requirements that numerical templates must satisfy in order to be as useful as possible for data analysis purposes, and by highlighting the kinds of information that such simulations can provide, other than merger templates, that can aid BBH merger data analysis.

We first consider analysis of a detected merger without templates from numerical relativity. In this case, observers will likely resort to simple band-pass filters to study the merger waves. The first question to address in this context is whether the merger signal is likely to even be *visible*; that is, whether the signal will stand out above the background noise level in the band-pass filtered detector output. In Sec. 3.3 we estimate band-pass filtering signal to noise ratios (SNRs) for the merger waves using the results of the previous chapter. We find that for BBHs that have been detected via their inspiral waves, these band-pass filtering SNRs are of order unity for initial and advanced LIGO interferometers; thus the merger signal will typically be just barely visible above the noise if at all. Only the somewhat rarer, close events will have easily visible merger signals. For LISA, by contrast, we estimate that band-pass filtering SNRs will typically be $\gtrsim 400$, so the merger waves will be easily visible.

When templates are not available, one's goal will be to reconstruct as well as possible the merger waveform from the noisy data stream. In Sec. 3.4 we use Bayesian statistics and the framework of maximum likelihood estimation to sketch an optimized method for performing such a reconstruction. The method is based on a "perpendicular projection" of the observed signal onto an appropriate function space that encodes all of our (possibly sketchy) prior knowledge about the waveforms. We argue that the best type of "basis functions" to use to specify this function space are wavelets, functions which allow simultaneous localization in time and frequency. We develop the reconstruction technique in detail using the language of wavelets, and also show that the operation of "perpendicular projection" onto the function space is a special case of Wiener optimal filtering. In Appendix A, we describe an extension of the method to a network of several gravitational-wave detectors, which allows one to reconstruct the two independent polarizations $h_+(t)$ and $h_\times(t)$ of the merger waves. This method for a network is an extension and generalization of a method previously suggested by Gürsel and Tinto [25].

Our waveform reconstruction algorithm comes in two versions: a simple version incorporating the above mentioned "perpendicular projection," described in Sec. 3.4.1, and a more general and powerful version that allows one to build in more prior information, described in Sec. 3.4.2. If one's prior information consists only of the signal's bandwidth, then the best-fit reconstructed waveform is just the band-pass filtered data stream. However, one can also build in as input to the method the expected duration of the signal, the fact that it must match up smoothly to the measured inspiral waveform, *etc.*; in such cases the reconstructed waveform differs from the band-pass filtered data stream.

In Sec. 3.5, we discuss the types of information that representative supercomputer simulations could provide, short of providing a complete set of merger templates [*i.e.* in states (ii) and (iii) above], that would be useful for data analysis. Such qualitative information about BBH merger waveforms would be useful in two ways: as prior information for signal reconstruction, and as a basis for comparisons with the reconstructed waveforms in order to make qualitative deductions about the BBH source, as mentioned above.

We turn next to issues concerning the use of numerical relativity templates in data analysis. Using matched filtering, templates can be used to make measurements of the binary's physical parameters (masses, vectorial spin angular momenta, *etc.*) which are independent of any such measurements from the inspiral and ringdown waves; and to make quantitative tests of general relativity. These measurements and tests will be possible with modest accuracy with LIGO/VIRGO, and with extremely high accuracy with LISA (for which the merger matched filtering SNRs are typically $\gtrsim 10^4$ [7]). To be useful for such purposes, the merger templates must satisfy certain accuracy requirements. In Sec. 3.6 we derive an approximate accuracy criterion [Eq. (3.49)] that numerical relativists can use to ensure that the waveforms they produce are sufficiently accurate. This formula is derived from two requirements: first, that template inaccuracies cause a loss in event rate of no more than 3% when searching for merger waves with matched filtering; and second, when measuring the BBH parameters, that the systematic errors due to template inaccuracies be smaller than the statistical errors from detector noise.

In Sec. 3.7 we re-address the issue of template accuracy, and also the issue of the spacing of templates in parameter space in the construction of a grid of templates, using the mathematical machinery of information theory. In information theory, a quantity called "information" can be associated with any measurement: it is simply the base 2 logarithm of the number of distinguishable measurement outcomes [26, 27]. We specialize the notions of information theory to gravitational

wave measurements, and define two different types of information: (i) a "total" information $I_{\rm total}$, the base 2 logarithm of the total number of waveform shapes that could have been distinguished by the measurement; and (ii) a "source" information $I_{\rm source}$, the base 2 logarithm of the total number of waveform shapes that could have been distinguished by the measurement *and* that could have been generated by BBH mergers (*i.e.*, the number of BBH sources that the measurement could have distinguished).

We give precise definitions of $I_{\rm total}$ and $I_{\rm source}$ [Eqs. (3.62) and (3.71)] in Sec. 3.7. In Appendix B, we derive simple analytic approximations for $I_{\rm total}$ and $I_{\rm source}$, expressing them in terms of the merger's matched filtering SNR ρ, the number of independent data points $\mathcal{N}_{\rm bins}$ in the observed signal, and the number of parameters $\mathcal{N}_{\rm param}$ on which merger templates have a significant dependence. In Sec. 3.7.3, we estimate the loss $\delta I_{\rm source}$ in source information that would result from template inaccuracies [Eq. (3.80)]; demanding that $\delta I_{\rm source} \lesssim 1$ then allows us to re-derive the criterion for the template accuracy requirements obtained in Sec. 3.6. We also estimate the loss in information $\delta I_{\rm source}$ that would result from having insufficiently closely spaced templates in a template grid [Eq. (3.84)], and we deduce an approximate criterion for how closely templates must be spaced.

3.2 Notation and Conventions

In this section we introduce some notations that will be used throughout this chapter. We use geometrized units in which Newton's gravitational constant G and the speed of light c are unity. For any function of time $a(t)$, we will use a tilde to represent that function's Fourier transform:

$$\tilde{a}(f) = \int_{-\infty}^{\infty} dt\, e^{2\pi i f t} a(t). \tag{3.2}$$

The output strain amplitude $s(t)$ of a detector can be written

$$s(t) = h(t) + n(t), \tag{3.3}$$

where $h(t)$ is the gravitational wave signal and $n(t)$ is the detector noise. Throughout this chapter we will assume, for simplicity, that the noise is stationary and Gaussian. The statistical properties

of the noise determine an inner product on the space of waveforms $h(t)$, given by

$$(h_1 \,|\, h_2) = 4\,\mathrm{Re} \int_0^\infty df \frac{\tilde{h}_1(f)^* \, \tilde{h}_2(f)}{S_h(f)}; \tag{3.4}$$

see, for example, Refs. [28, 13]. In Eq. (3.4), $S_h(f)$ is the one-sided power spectral density of strain noise $n(t)$ [29].

For any waveform $h(t)$, the matched filtering SNR ρ is given by

$$\rho^2 = (h \,|\, h) = 4 \int_0^\infty df \, \frac{|\tilde{h}(f)|^2}{S_h(f)}. \tag{3.5}$$

On several occasions we shall be interested in finite stretches of data of length T, represented as a vector of numbers instead of as a continuous function. If Δt is the sampling time, this vector is

$$\mathbf{s} = (s^1, \ldots, s^{\mathcal{N}_{\mathrm{bins}}}), \tag{3.6}$$

where $\mathcal{N}_{\mathrm{bins}} = T/\Delta t$, $s^j = s[t_{\mathrm{start}} + (j-1)\Delta t]$, $1 \le j \le \mathcal{N}_{\mathrm{bins}}$, and t_{start} is the starting time. The quantity $\mathcal{N}_{\mathrm{bins}}$ is the number of independent real data points (number of bins) in the measured signal. The gravitational wave signal $h(t)$ and the noise $n(t)$ can similarly be represented in this way, so that $\mathbf{s} = \mathbf{h} + \mathbf{n}$. We adopt the geometrical viewpoint of Dhurandhar and Schutz [30], regarding $\mathbf{s}$ as an element of an abstract vector space V of dimension $\mathcal{N}_{\mathrm{bins}}$, and the sample points s^j as the components of $\mathbf{s}$ on a time domain basis $\{\mathbf{e}_1, \ldots, \mathbf{e}_{\mathcal{N}_{\mathrm{bins}}}\}$ of V:

$$\mathbf{s} = \sum_{j=1}^{\mathcal{N}_{\mathrm{bins}}} s^j \, \mathbf{e}_j. \tag{3.7}$$

Taking a finite Fourier transform of the data stream can be regarded as a change of basis of V. Thus, a frequency domain basis $\{\mathbf{d}_k\}$ of V is given by the finite Fourier transform

$$\mathbf{d}_k = \sum_{j=1}^{\mathcal{N}_{\mathrm{bins}}} \mathbf{e}_j \exp\{2\pi i j k / \mathcal{N}_{\mathrm{bins}}\}, \tag{3.8}$$

where $-(\mathcal{N}_{\mathrm{bins}} - 1)/2 \le k \le (\mathcal{N}_{\mathrm{bins}} - 1)/2$. The corresponding frequencies $f_k = k/T$ run from $-1/(2\Delta t)$ to $1/(2\Delta t)$ [31].

More generally, if we band-pass filter the data stream down to a frequency interval of length

Δf, then a stretch of band-pass filtered data of duration T will have

$$\mathcal{N}_{\rm bins} = 2T\Delta f \tag{3.9}$$

independent real data points. In this case also we regard the set of all such stretches of data as an abstract linear space V of dimension $\mathcal{N}_{\rm bins}$.

On an arbitrary basis of V, we define the matrices Γ_{ij} and Σ^{ij} by

$$\langle n^i\, n^j \rangle \equiv \Sigma^{ij}, \tag{3.10}$$

$$\Gamma_{ij}\, \Sigma^{jk} = \delta^i_k; \tag{3.11}$$

i.e., the matrices $\mathbf{\Gamma}$ and $\mathbf{\Sigma}$ are inverses of each other. In Eq. (3.10) the angle brackets mean expected value. On the time domain basis $\{\mathbf{e}_1, \ldots, \mathbf{e}_{\mathcal{N}_{\rm bins}}\}$ we have

$$\Sigma^{jk} = C_n(t_j - t_k), \tag{3.12}$$

where $t_j = t_{\rm start} + (j-1)\Delta t$, and $C_n(\tau) = \langle n(t) n(t+\tau) \rangle$ is the noise correlation function given by

$$C_n(\tau) = \int_0^\infty df\, \cos[2\pi f \tau]\, S_h(f). \tag{3.13}$$

We define an inner product on the space V by

$$(\mathbf{h}_1 \,|\, \mathbf{h}_2) = \Gamma_{ij} h_1^i h_2^j. \tag{3.14}$$

This is a discrete version of the inner product (3.4): the two inner products coincide in the limit $\Delta t \to 0$, for waveforms which vanish outside of the time interval of length T [16].

Throughout this chapter we shall use interchangeably the notations $h(t)$ and $\mathbf{h}$ for a gravitational waveform. We shall also for the most part not need to distinguish between the inner products (3.4) and (3.14). Some generalizations of these notations and definitions to a network of several detectors are given in Appendix A.

For any detector output $\mathbf{s} = \mathbf{h} + \mathbf{n}$, we define

$$\rho(\mathbf{s}) \equiv \sqrt{(\mathbf{s} \,|\, \mathbf{s})}, \tag{3.15}$$

which we call the *magnitude* of the stretch of data $\mathbf{s}$. From Eqs. (3.10) and (3.14) it follows that

$$\langle \rho(\mathbf{s})^2 \rangle = \rho^2 + \mathcal{N}_{\rm bins}, \tag{3.16}$$

where ρ^2 is the matched filtering SNR squared (3.5) of the signal $\mathbf{h}$, and that

$$\sqrt{\langle\, [\Delta\rho(\mathbf{s})^2]^2 \,\rangle} = \sqrt{4\rho^2 + 2\mathcal{N}_{\rm bins}}, \tag{3.17}$$

where $\Delta\rho(\mathbf{s})^2 \equiv \rho(\mathbf{s})^2 - \langle\rho(\mathbf{s})^2\rangle$. Thus, the magnitude $\rho(\mathbf{s})$ is approximately the same as the matched filtering SNR ρ in the limit $\rho \gg \sqrt{\mathcal{N}_{\rm bins}}$ (large SNR squared per frequency bin), but is much larger than ρ when $\rho \ll \sqrt{\mathcal{N}_{\rm bins}}$. The quantity $\rho(\mathbf{s})$ will be of most use in our information theory calculations in Sec. 3.7 and Appendix B.

The space V equipped with the inner product (3.14) forms a Euclidean vector space. We will also be concerned with sets of gravitational waveforms $\mathbf{h}(\boldsymbol{\theta})$ that depend on a finite number n_p of parameters $\boldsymbol{\theta} = (\theta^1, \ldots, \theta^{n_p})$. For example, inspiral waveforms form a set of this type, where $\boldsymbol{\theta}$ are the parameters describing the binary source. We will denote by $\mathcal{S}$ the manifold of signals $\mathbf{h}(\boldsymbol{\theta})$, which is a submanifold of dimension n_p of the vector space V. We will adopt the convention that Roman indices i, j, k, ... will run from 1 to $\mathcal{N}_{\rm bins}$, and that a symbol such as v^i will denote some vector in the space V. Greek indices α, β, γ will run from 1 to n_p, and a vector v^α will denote a vector field on the manifold $\mathcal{S}$. The inner product (3.14) induces a natural Riemannian metric on the manifold $\mathcal{S}$ given by

$$ds^2 = \left(\frac{\partial \mathbf{h}}{\partial \theta^\alpha} \,\middle|\, \frac{\partial \mathbf{h}}{\partial \theta^\beta} \right) d\theta^\alpha d\theta^\beta. \tag{3.18}$$

We shall denote this metric by $\Gamma_{\alpha\beta}$ and its inverse by $\Sigma^{\alpha\beta}$, relying on the index alphabet to distinguish these quantities from the quantities (3.10) and (3.11). For more details on this geometric picture, see, for example, Ref. [13].

We shall use the word *detector* to refer to either a single interferometer or a resonant mass antenna, and the phrase *detector network* to refer to a collection of detectors operated in tandem. Note that this terminology differs from that adopted in, for example, Ref. [28], where our "detector network" is called a "detector."

Finally, we will use bold faced vectors like $\mathbf{a}$ to denote either vectors in three dimensional space, or vectors in the $\mathcal{N}_{\rm bins}$-dimensional space V, or vectors in the n_p dimensional space of signal parameters. In Appendix A, we will use arrowed vectors ($\vec{a}$) to denote elements of the linear space

of the output of a detector network.

3.3 Analysis of merger waves without templates: visibility of the merger after band-pass filtering

We first consider merger wave data analysis when matched filtering is not possible. One's primary goal in this case will be to reconstruct a "best-guess" estimate of the merger waveform [32] from the measured data. If some (perhaps very few) supercomputer templates are available, it may then be possible to interpret the reconstructed waveform and obtain some qualitative information about the source.

One very simple procedure that could be used to estimate the waveform shape is simply to band-pass filter the data stream according to our prior prejudice about the frequency band of the merger waves. However, even after such band-pass filtering, the merger signal may be dominated by detector noise and may not be visible.

In this section, we estimate the visibility of the merger signal after band-pass filtering by calculating band-pass filtering SNRs using the results of Ref. [7]. A signal will be visible if its band-pass filtering SNR is large compared to unity [7]. We consider only signals that are detected via their inspiral waves — in other words, low-mass BBH systems. We first consider the visibility of the last few cycles of the inspiral. By continuity, one might expect that if the last few inspiral cycles are visible, then at least the early part of the merger signal will be as well. We then consider the visibility of the merger signal itself.

3.3.1 Visibility of inspiral waveform

If a BBH event has been detected via its inspiral signal, it follows that the matched filtering inspiral SNR must be $\gtrsim 6$ [33]. It does not follow, however, that the inspiral is visible in the data stream. For neutron star-neutron star binaries the reverse is usually the case: the amplitude of the signal is less than the noise, and the signal would be invisible without matched filtering.

The dominant harmonic of the inspiral waveform can be written as

$$h(t) = h_{\rm amp}(t)\cos[\Phi(t)], \tag{3.19}$$

where the amplitude $h_{\rm amp}(t)$ and instantaneous frequency $f(t)$ [given by $2\pi f(t) = d\Phi/dt$] are

slowly evolving. For such waveforms, the SNR squared obtained using band-pass filtering is approximately given by the matched filtering SNR squared *per cycle* [*cf.* Eq. (2.10) of Ref. [7]]:

$$\begin{aligned}\left(\frac{S}{N}\right)^2_{\text{band-pass}} &\approx \left(\frac{S}{N}\right)^2_{\text{matched, per cycle}} \\ &= \left[\frac{h_{\text{amp}}\left[t(f)\right]}{h_{\text{rms}}(f)}\right]^2 . \end{aligned} \tag{3.20}$$

In Eq. (3.20), $t(f)$ denotes the time at which the frequency is f, and $h_{\text{rms}}(f) \equiv \sqrt{f S_h(f)}$. Note that the band-pass filtering SNR (3.20) is evaluated at a specific frequency; when one discusses matched filtering SNRs, an integral over a frequency band has been performed. We next insert the value of $h_{\text{amp}}[t(f)]^2$ for the leading-order approximation to the inspiral waves and take an rms average over source orientations and polarizations [34, 7], which yields

$$\left(\frac{S}{N}\right)^2_{\text{band-pass}} = \frac{4\pi^{4/3}[(1+z)M]^{10/3} f^{4/3}}{25 D(z)^2 h_{\text{rms}}(f)^2}. \tag{3.21}$$

Here, M is the binary's total mass, z its cosmological redshift, and $D(z)$ its luminosity distance. We have also specialized to equal masses.

In Eq. (4.1) of Ref. [7] we introduced an analytic formula for a detector's noise spectrum, which, by specialization of its parameters, could describe to a good approximation either an initial LIGO interferometer, an advanced LIGO interferometer, or a space-based LISA interferometer. We now insert that formula into Eq. (3.20), and specialize to the frequency

$$f = f_{\text{merge}} = \frac{\gamma_m}{(1+z)M}, \tag{3.22}$$

where $\gamma_m = 0.02$. The frequency f_{merge} is approximately the location of the transition from inspiral to merger, as estimated in Ref. [7]. This yields

$$\left(\frac{S}{N}\right)^2_{\text{band-pass}} \approx \frac{4\pi^{4/3}[(1+z)M]^5 \gamma_m^{-5/3} \alpha^3 f_m^3}{5 D(z)^2 h_m^2}, \tag{3.23}$$

where α, h_m and f_m are the parameters used in Ref. [7] to describe the noise curve. Equation (3.23) is valid only when the redshifted mass $(1+z)M$ is smaller than $\gamma_m/\alpha f_m$.

For initial LIGO interferometers, appropriate values of h_m, f_m and α are given in Eq. (4.2) of

Ref. [7]. Inserting these values into Eq. (3.23) gives

$$\left(\frac{S}{N}\right)_{\text{band-pass}} \sim 1.1 \left[\frac{200\,\text{Mpc}}{D(z)}\right] \left[\frac{(1+z)M}{20\,M_\odot}\right]^{5/2}. \tag{3.24}$$

This result is valid for $(1+z)M \lesssim 18M_\odot$. Now, the SNR obtained by matched filtering the inspiral signal is approximately [7]

$$\left(\frac{S}{N}\right)_{\text{matched}} \sim 2.6 \left[\frac{200\,\text{Mpc}}{D(z)}\right] \left[\frac{(1+z)M}{20\,M_\odot}\right]^{5/6}, \tag{3.25}$$

and the SNR (3.25) must be $\gtrsim 6$ [33], since, by assumption, the inspiral has been detected. By eliminating the luminosity distance $D(z)$ between Eqs. (3.24) and (3.25) we find that the band-pass filtering SNR for the last few cycles of inspiral for detected binaries satisfies

$$\left(\frac{S}{N}\right)_{\text{band-pass}} \gtrsim 2.5 \left[\frac{(1+z)M}{20\,M_\odot}\right]^{5/3}. \tag{3.26}$$

Therefore, the last few cycles of the inspiral should be individually visible above the noise for BBH events with $5M_\odot \lesssim M \lesssim 20M_\odot$ detected by initial LIGO interferometers.

We now repeat the above calculation with the values of h_m, f_m, and α appropriate for advanced LIGO interferometers, given in Eq. (4.3) of Ref. [7]. The band-pass filtering SNR for advanced interferometers is

$$\left(\frac{S}{N}\right)_{\text{band-pass}} \sim 1.6 \left[\frac{1\,\text{Gpc}}{D(z)}\right] \left[\frac{(1+z)M}{20\,M_\odot}\right]^{5/2}, \tag{3.27}$$

and the SNR obtained by matched filtering the inspiral signal is

$$\left(\frac{S}{N}\right)_{\text{matched}} \sim 16 \left[\frac{1\,\text{Gpc}}{D(z)}\right] \left[\frac{(1+z)M}{20\,M_\odot}\right]^{5/6}, \tag{3.28}$$

for $(1+z)M \lesssim 37M_\odot$ [7]. With the assumption that $(S/N)_{\text{matched}} \gtrsim 6$, we find

$$\left(\frac{S}{N}\right)_{\text{band-pass}} \gtrsim 0.6 \left[\frac{(1+z)M}{20\,M_\odot}\right]^{5/3} \tag{3.29}$$

for $(1+z)M \lesssim 37M_\odot$. Thus the last few cycles of BBH inspirals with $(1+z)M \lesssim 37M_\odot$ should typically be just barely visible above the noise for advanced LIGO interferometers, depending on the binary's total mass.

Although we do not explore here larger mass BBHs, in many cases for these systems also the

last few cycles of inspiral will be visible; this can be seen by combining Eq. (3.20) with Figs. 4 and 5 of Ref. [7].

For LISA, Eq. (3.23) combined with Eq. (4.4) of Ref. [7] yields

$$\left(\frac{S}{N}\right)_{\text{band-pass}} \sim 400 \left[\frac{1\,\text{Gpc}}{D(z)}\right] \left[\frac{(1+z)M}{10^5\,M_\odot}\right]^{5/2} \tag{3.30}$$

for $(1+z)M \lesssim 10^5\,M_\odot$, with larger values for $10^5\,M_\odot \lesssim (1+z)M \lesssim 3\times 10^7\,M_\odot$. Individual cycles of inspiral should be clearly visible with LISA.

3.3.2 Visibility of merger waveform

Consider now the merger waveform itself. In Ref. [7] we showed that

$$\left(\frac{S}{N}\right)_{\text{band-pass, merger}} \approx \frac{1}{\sqrt{\mathcal{N}_{\text{bins}}}} \left(\frac{S}{N}\right)_{\text{matched, merger}}, \tag{3.31}$$

where $\mathcal{N}_{\text{bins}} = 2T\Delta f$ is as discussed in Sec. 3.2. We also estimated [Eq. (3.26) of Ref. [7]] that for the merger waves,

$$\sqrt{\mathcal{N}_{\text{bins}}} \sim 5, \tag{3.32}$$

although there is a large uncertainty in this estimate.

Consider the band-pass filtering SNR for the merger for events that have been detected via matched filtering of the inspiral. For initial LIGO interferometers, combining Eqs. (B4) and (B10) of Ref. [7], Eqs. (3.31) and (3.32), and the threshold for detection [33]

$$\left(\frac{S}{N}\right)_{\text{matched, inspiral}} \gtrsim 6 \tag{3.33}$$

yields

$$\left(\frac{S}{N}\right)_{\text{band-pass, merger}} \gtrsim 0.8 \left[\frac{(1+z)M}{20M_\odot}\right]^{5/3} \tag{3.34}$$

for $(1+z)M \lesssim 18M_\odot$. Repeating this analysis for advanced LIGO interferometers [using Eqs. (B5) and (B11) of Ref. [7]] yields

$$\left(\frac{S}{N}\right)_{\text{band-pass, merger}} \gtrsim 0.2 \left[\frac{(1+z)M}{20M_\odot}\right]^{5/3} \tag{3.35}$$

for $(1+z)M \lesssim 37M_\odot$ [35].

The SNR values (3.34) and (3.35) indicate that for typical inspiral-detected BBH systems with $M \lesssim 20M_\odot$ (initial interferometers) or $M \lesssim 40M_\odot$ (advanced interferometers), the merger signal will not be easily visible in the noise, and that only relatively rare, nearby events will have easily visible merger signals. This conclusion is somewhat tentative because of the uncertainty in the estimates of $\mathcal{N}_{\rm bins}$ and of the energy spectra discussed in Ref. [7]. Also the actual visibility will probably vary considerably from event to event. However, our crude visibility argument suggests that the prospects for accurately recovering the merger waveform are good only for the stronger detected merger signals.

This conclusion only applies to low mass BBH systems which are detected via their inspiral waves. For higher mass systems which are detected directly via their merger and/or ringdown waves, the merger signal should be visible above the noise after appropriate band-pass filtering (*cf.* Figs. 4 and 5 of [7], dividing the matched filtering SNRs presented there by $\sqrt{\mathcal{N}_{\rm bins}} \sim 5$). Moreover, most merger events detected by LISA will have band-pass filtering SNRs $\gg 1$, as can be seen from Fig. 6 of Ref. [7], and thus should be easily visible.

3.4 Analysis of merger waves without templates: a method of extracting a best-guess waveform from the noisy data stream

In the absence of templates we would like to reconstruct from the data a best-guess estimate of the merger waveform. Any waveform-reconstruction method should use all available prior knowledge about the waveform. We will hopefully know from representative simulations and perhaps from the measured inspiral/ringdown the following: the approximate starting time of the merger waveform, the fact that it starts off strongly (smoothly joining on to the inspiral) and eventually dies away in quasinormal ringing, and its approximate bandwidth and duration. When both the inspiral and the ringdown are strong enough to be detectable, the duration of the merger waveform will be fairly well known, as will the frequency $f_{\rm qnr}$ of the ringdown onto which the merger waveform must smoothly join.

In this section, we suggest a method for reconstructing the waveform which uses such prior information, based on the technique of maximum likelihood estimation [36, 37]. We shall describe this method in the context of a single detector. However, in a few years there will be in operation a network of detectors (both interferometers [1, 2, 3] and resonant mass antennae), and from the outputs of these detectors one would like to reconstruct the two polarization components $h_+(t)$ and

$h_\times(t)$ of the merger waves. In Appendix A we extend this section's waveform-estimation method to an arbitrary number of detectors, which yields a method of reconstructing the two waveforms $h_+(t)$ and $h_\times(t)$.

The use of maximum likelihood estimators has been discussed extensively by many authors in the context of gravitational waves of a known functional form, depending only on a few parameters [28, 13, 14, 38, 39]. Here we consider their application to wave bursts of largely unknown shape. The resulting data analysis methods which we derive are closely related mathematically to the methods discussed previously [28, 13, 14, 38, 39], but are considerably different in operational terms and in implementation.

3.4.1 Derivation of data analysis method

Suppose our prior information includes the fact that the merger waveform lies inside some time interval of duration T, and inside some frequency interval of length Δf. We define $\mathcal{N}_{\text{bins}} = 2T\Delta f$, *cf.* Sec. 3.2 above. We assume that we are given a stretch of data of duration $T' > T$ and with sampling time $\Delta t < 1/(2\Delta f)$. These data lie in a linear space V of dimension

$$\mathcal{N}'_{\text{bins}} = T'/\Delta t. \tag{3.36}$$

Thus, $\mathcal{N}'_{\text{bins}}$ is the number of independent data points, and $\mathcal{N}_{\text{bins}}$ is the number of independent data points in that subset of the data which we expect to contain the merger signal. Note that these definitions modify the conventions of Sec. 3.2, where the dimension of V was denoted $\mathcal{N}_{\text{bins}}$; we will use, unmodified, the other conventions of Sec. 3.2.

In our analysis, we will allow the basis of the vector space V to be arbitrary. However, we will occasionally specialize to the time-domain and frequency-domain bases discussed in Sec. 3.2. We will also consider wavelet bases. Wavelet bases can be regarded as any set of functions $w_{ij}(t)$ such that $w_{ij}(t)$ is approximately localized in time at the time $t_i = t_{\text{start}} + (i/n_T)T'$, and in frequency at the frequency $f_j = (j/n_F)(\Delta t)^{-1}$; their advantage is that they simultaneously encode time domain and frequency domain information. The index i runs from 1 to n_T and j from $-(n_F - 1)/2$ to $(n_F - 1)/2$. Clearly the number of frequency bins n_F and the number of time bins n_T must satisfy $n_T n_F = \mathcal{N}'_{\text{bins}}$, but otherwise they can be arbitrary; typically $n_T \sim n_F \sim \sqrt{\mathcal{N}'_{\text{bins}}}$. Also, the

functions w_{ij} usually all have the same shape:

$$w_{ij}(t) \propto \varphi\left[f_j(t - t_i)\right] \tag{3.37}$$

for some function φ. For our considerations, the shape of φ is not of critical importance. Note that families of wavelets discussed in the literature are often over-complete; here we are considering bases of the vector space V, which by definition are simply complete.

Let $p^{(0)}(\mathbf{h})$ be the probability distribution function (PDF) that summarizes our prior information about the waveform. A standard Bayesian analysis shows that the PDF of $\mathbf{h}$ given the measured data stream $\mathbf{s}$ is [28, 16]

$$p(\mathbf{h} \,|\, \mathbf{s}) = \mathcal{K}\, p^{(0)}(\mathbf{h}) \exp\left[-\Gamma_{ij}(h^i - s^i)(h^j - s^j)/2\right], \tag{3.38}$$

where the matrix Γ_{ij} is defined in Eq. (3.11) and $\mathcal{K}$ is a normalization constant. In principle this PDF gives complete information about the measurement. Maximizing the PDF gives the maximum likelihood estimator for the merger waveform $\mathbf{h}$. This estimator, $\mathbf{h}(\mathbf{s})$, will in general will be some non-linear function of $\mathbf{s}$. The effectiveness of the resulting waveform estimator will depend on how much prior information about the waveform shape can be encoded in the prior PDF $p^{(0)}$.

One of the simplest possibilities is to take $p^{(0)}$ to be concentrated on some linear subspace U of the space V, and to be approximately constant inside this subspace. A multivariate Gaussian with widths very small in some directions and very broad in others would accomplish this to a good approximation. For such choices of prior PDF $p^{(0)}$, the resulting maximum likelihood estimator [the function $\mathbf{h} = \mathbf{h}(\mathbf{s})$ that maximizes the PDF (3.38)] is simply the perpendicular projection P_U of $\mathbf{s}$ into U:

$$\mathbf{h}_{\text{best-fit}}(\mathbf{s}) = P_U(\mathbf{s}), \tag{3.39}$$

where

$$P_U(\mathbf{s}) \equiv \sum_{i,j=1}^{n_U} u^{ij}\, (\mathbf{u}_j \,|\, \mathbf{s})\ \mathbf{u}_i. \tag{3.40}$$

Here, $\mathbf{u}_1, \ldots, \mathbf{u}_{n_U}$ is an arbitrary basis of U, n_U is the dimension of U, $u^{ij}u_{jk} = \delta^i_j$ and $u_{jk} = (\mathbf{u}_j \,|\, \mathbf{u}_k)$.

The method of filtering (3.39) is a special case of Wiener optimal filtering: it is equivalent to matched filtering with templates consisting of linear combinations of the basis functions $\mathbf{u}_i$. (The

equivalence between maximum likelihood estimation and Wiener optimal filtering in more general contexts has been shown by Echeverria [40].) To show this, define a family of template waveforms that depends on parameters $a_1, \ldots, a_{n_U}$ by

$$h(t; a_j) = \sum_{j=1}^{n_U} a_j u_j(t), \tag{3.41}$$

where $u_j(t)$ are the functions of time corresponding to the basis elements $\mathbf{u}_j$ of U. The SNR for any template $h(t)$ with the data stream $s(t)$ is

$$\frac{S}{N}[h(t)] \equiv \frac{(\mathbf{h} \,|\, \mathbf{s})}{\sqrt{(\mathbf{h} \,|\, \mathbf{h})}}. \tag{3.42}$$

The best-fit signal given by the optimal filtering method is the template which maximizes the SNR (3.42), *i.e.*, the template $h(t; \hat{a}_j)$ such that

$$\frac{S}{N}[h(t; \hat{a}_j)] = \max_{a_1, \ldots, a_{n_U}} \frac{S}{N}[h(t; a_j)]\,. \tag{3.43}$$

From Eqs. (3.40)–(3.42) it follows that $P_U(\mathbf{s}) = h(t; \hat{a}_j)$. Thus, computing the perpendicular projection (3.40) of $\mathbf{s}$ into U is equivalent to matched filtering with the template family (3.41).

To summarize, the maximum likelihood estimator (3.39) gives a general procedure for specifying a filtering algorithm adapted to a given linear subspace U of the space of signals V. We now discuss some general issues regarding the choice of U. At the very least, we would like our choice to effect truncation of the measured data stream in both the time and frequency domains, down to the intervals of time and frequency in which we expect the merger waveform to lie. Because of the uncertainty principle, such a truncation cannot be done exactly. Moreover, for fixed specific intervals of time and frequency, there are different, inequivalent ways of approximately truncating the signal to these intervals [41]. The differences between the inequivalent methods are essentially due to aliasing effects. Such effects cannot always be neglected in the analysis of merger waveforms, because the duration $T \sim 10M - 100M$ [7] of the waveform is probably only a few times larger than the reciprocal of the highest frequency of interest.

The simplest method of truncating in frequency, band-pass filtering, is to a good approximation a projection of the type (3.39) that we are considering. Let $\mathbf{d}_k$ [*cf.* Eq. (3.8)] be a frequency domain basis of V. For a given frequency interval $[f_{\text{char}} - \Delta f/2, f_{\text{char}} + \Delta f/2]$, let U be the subspace of V spanned by the elements $\mathbf{d}_j$ with $|f_{\text{char}} - f_j| < \Delta f/2$, *i.e.*, the span of the basis elements

that correspond to the given frequency interval. Then the projection operation P_U is to a moderate approximation just the band-pass filter:

$$P_U \left[\sum_{j=1}^{\mathcal{N}'_{\rm bins}} s^j \, \mathbf{d}_j \right] \approx \sum{}' s^j \, \mathbf{d}_j, \tag{3.44}$$

where the notation $\sum'$ means that the sum is taken only over the appropriate range of frequencies. The relation (3.44) follows from the fact that the basis $\mathbf{d}_j$ is approximately orthogonal with respect to the noise inner product (3.14): different frequency components of the noise are statistically independent up to small aliasing corrections of the order of $\sim 1/(f_{\rm char}T')$. Thus, if our *a priori* information is that the signal lies within a certain frequency interval, then the maximum likelihood estimate of the signal is approximately given by passing the data stream through a band-pass filter.

Truncating in the time domain, on the other hand, is not a projection of the type (3.39). If our prior information is that the signal vanishes outside a certain interval of time, then simply discarding the data outside of this interval will not give the maximum likelihood estimate of the signal. This is because of statistical correlations between sample points just inside and just outside of the time interval: the measured data stream outside the interval gives information about what the noise inside the interval is likely to be. These correlation effects become unimportant in the limit $T f_{\rm char} \to \infty$, but for BBH merger signals $T f_{\rm char}$ is probably $\lesssim 20$ [7]. The correct maximum likelihood estimator of the waveform, when our prior information is that the signal vanishes outside of a certain time interval, is given by Eq. (3.40) with the basis $\{\mathbf{u}_1, \ldots, \mathbf{u}_{n_U}\}$ replaced by the appropriate subset of the time-domain basis $\{\mathbf{e}_1, \ldots, \mathbf{e}_{\mathcal{N}'_{\rm bins}}\}$.

Our suggested choice of subspace U and corresponding specification of a filtering method is as follows. Pick a wavelet basis $\mathbf{w}_{ij}$ of the type discussed above. (The filtering method will depend only weakly on which wavelet basis is chosen.) Then, the subspace U is taken to be the span of a suitable subset of this wavelet basis, chosen according to our prior information about the bandwidth and duration of the signal. The dimension of U will be $n_U = \mathcal{N}_{\rm bins} = 2T\Delta f$.

In more detail, the filtering method would work as follows. First, band-pass filter the data stream and truncate it in time, down to intervals of frequency and time that are several times larger than are ultimately required, in order to reduce the number of independent data points $\mathcal{N}'_{\rm bins}$ to a manageable number. Second, for the wavelet basis $\mathbf{w}_{ij}$ of this reduced data set, calculate the matrix $w_{ij\,i'j'} = (\mathbf{w}_{ij} \,|\mathbf{w}_{i'j'})$. Recall that the index i corresponds to a time t_i, and the index j to a frequency f_j [c.f. the discussion preceding Eq. (3.37)]. Third, pick out the sub-block $\bar{w}_{ij\,i'j'}$ of the

matrix $w_{ij\,i'j'}$ for which the times t_i and $t_{i'}$ and frequencies f_j and $f_{j'}$ lie in the required intervals. Invert this matrix to obtain $\bar{w}^{ij\,i'j'}$. The best-fit waveform is then given by

$$\mathbf{h}_{\rm best-fit} = \sum_{ij}{}' \sum_{i'j'}{}' \bar{w}^{ij\,i'j'} \; (\mathbf{s} \,|\, \mathbf{w}_{i'j'}) \; \mathbf{w}_{ij}, \tag{3.45}$$

where $\sum'$ means the sum over the required time and frequency intervals.

3.4.2 Extension of method to incorporate other types of prior information

A waveform reconstruction method more sophisticated than (3.39) can be obtained by generalizing the above analysis. Suppose that the prior PDF $p^{(0)}(\mathbf{h})$ is a general multivariate Gaussian in $\mathbf{h}$, such as

$$p^{(0)}(\mathbf{h}) \propto \exp\left[-\frac{1}{2}\sum_{ij}\frac{(h_{ij}-\bar{h}_{ij})^2}{\alpha_{ij}^2}\right], \tag{3.46}$$

where h^{ij} are the expansion coefficients of the signal $\mathbf{h}$ on some fixed wavelet basis $\mathbf{w}_{ij}$. By making suitable choices of the parameters $\bar{h}_{ij}$ and α_{ij}, such a PDF could be chosen to encode the information that the frequency content of the signal at early times is concentrated near $f_{\rm merge}$, that the signal joins smoothly onto the inspiral waveform, that at the end of merger the dominant frequency component is that of quasi-normal ringing, *etc.* For any such prior PDF, it is straightforward to calculate the corresponding maximum likelihood estimator. If the prior PDF has expected value $\mathbf{h}_0$ and variance-covariance matrix $\mathbf{\Sigma}_0$, then the estimator is

$$\mathbf{h}_{\rm best-fit}(\mathbf{s}) = \left[\mathbf{\Sigma}^{-1} + \mathbf{\Sigma}_0^{-1}\right]^{-1} \cdot \left[\mathbf{\Sigma}^{-1}\cdot\mathbf{s} + \mathbf{\Sigma}_0^{-1}\cdot\mathbf{h}_0\right]. \tag{3.47}$$

Such an estimator could be calculated numerically.

3.5 Using information from representative numerical simulations

In this section we propose a computational strategy for numerical relativists to pursue, if they successfully produce computer codes capable of simulating BBH mergers, but if running such codes is too expensive to permit an extensive survey of the merger parameter space. In this case, for data analysis purposes, it would be very useful to do a coarse survey of the BBH parameter space, with the aim of answering several qualitative questions and determining the range of several key parameters. Below we discuss several such issues, and describe how an understanding of them may impact

data analysis.

One of the most important questions is: what is the approximate duration of the merger signal, and how does it depend on parameters such as the initial spins of the black holes and the mass ratio? The range of merger signal durations will be an important input to algorithms for searching for merger waves (the "noise-monitoring" technique described in Refs. [7, 42]) and algorithms for reconstructing the waveform from the data (see Sec. 3.4), particularly for cases in which the ringdown and/or inspiral signals are too weak to be seen in the data stream. Moreover, the duration of the waveform (together with its bandwidth) approximately determines the amount by which the SNR from band-pass filtering is lower than the matched filtering SNR obtained with merger templates [*cf.* Eq. (3.31)]. If it turns out that the duration is long (or, more relevantly, if $\mathcal{N}_{\rm bins}$ is greater than our estimate of ~ 30), then the merger SNR will be badly degraded if templates are not available. Although the noise-monitoring technique will likely be useful for detecting merger waves, it will be difficult to reconstruct the waveform if $\mathcal{N}_{\rm bins}$ is too large.

A similar question is the frequency bandwidth in which most of the merger waves' power is concentrated. In Ref. [7] we assumed that when one excises in the time domain the ringdown portion of the signal, the remaining signal has no significant power at frequencies above the quasi-normal ringing frequency of the final Kerr black hole. However, this assumption may not be valid; if it is not, signal searches and waveform reconstruction methods will need to incorporate this high-frequency power. As with the signal's duration, the range of bandwidths of merger waveforms will be an input to algorithms for reconstructing the merger waveform from the noisy data (see Sec. 3.4).

Another issue is how much energy is radiated in the merger compared to the energy radiated in the ringdown. Operationally, this question reduces to asking what proportion of the total waveform produced during the coalescence can be accurately fit by the ringdown's decaying sinusoid. In the preceding chapter, we argued that if the spins of the black holes are large and aligned with one another and the orbital angular momentum, then the system has too much angular momentum for it to be lost solely through the ringdown, so that ringdown waves should not dominate the merger. On the other hand, if the spins of the black holes are small or not aligned, most of the radiated energy might well come out in ringdown waves. It may turn out that the ratio of energy radiated in the merger to that in the ringdown is small for all but a small set of merger parameters, which could have a great influence on BBH event searches.

It would be useful to know if the waveforms contain a strong signature of an "innermost stable circular orbit" (ISCO) [8, 9, 43], as has commonly been assumed. In the extreme mass ratio limit

$\mu \ll M$, there is such an orbit; when the smaller black hole reaches it, there is a sharp drop in the radiated energy per unit logarithmic frequency $dE/d\ln f$ [44]. However, there may not be such a sharp feature in the $dE/d\ln f$ plot in the equal-mass case, especially if the timescale over which the orbital instability operates is comparable to the radiation reaction timescale.

Finally, it would be useful to know how much of the merger can be described as higher order QNR modes. By convention, we have been calling that phase of the coalescence which is dominated by the most slowly damped, $l = m = 2$ mode the ringdown phase; but, before this mode dominates, QNR modes with different values of l and/or m are likely to be present. After the merger has evolved to the point when the merged object can be accurately described as a linear perturbation about a stationary black hole background, there might or might not be any significant subsequent period of time before the higher order modes have decayed away so much as to be undetectable. If simulations predict that higher order QNR modes are strong for a significant period of time, then these higher order QNR modes should be found by the normal ringdown search of the data stream; no extra search should be needed.

3.6 Accuracy requirements for merger waveform templates

For the remainder of the chapter, we consider data analysis of merger waves using supercomputer templates. These templates will unavoidably contain numerical errors: if the physical waveform for some source is $h(t;\boldsymbol{\theta})$, where the components of $\boldsymbol{\theta} = (\theta^1, \ldots, \theta^{n_p})$ are the various parameters upon which the waveform depends, then numerical simulations will predict the waveform $h(t;\boldsymbol{\theta}) + \delta h(t;\boldsymbol{\theta})$. One would like the numerical error $\delta h(t;\boldsymbol{\theta})$ to be small enough not to have a significant effect on signal searches, parameter extraction or any other types of data analysis that might be carried out using the template waveforms. In this section we suggest an approximate rule of thumb [Eq. (3.49)] for estimating when numerical errors are sufficiently small, and discuss its meaning and derivation.

3.6.1 Accuracy criterion and implementation

The accuracy criterion can be simply expressed in terms of the inner product introduced in Sec. 3.2 above [which is defined by Eq. (3.4) or alternatively by Eqs. (3.11)–(3.14)]: for a given template

$h(t)$, our rule of thumb is that the numerical error $\delta h(t)$ should be small enough that the quantity

$$\Delta \equiv \frac{1}{2}\frac{(\delta h|\delta h)}{(h|h)} \tag{3.48}$$

satisfies

$$\Delta \lesssim 0.01 \ . \tag{3.49}$$

(The fractional loss in event detection rate in signal searches is $\sim 3\Delta$, so the value 0.01 corresponds to a 3% loss in event rate; see Sec. 3.6.2.) If the errors at each data point $h_j = h(t_j)$ are uncorrelated, then Eq. (3.49) translates into a fractional accuracy for each data point of about $0.01/\sqrt{N_{\rm bins}}$. If the errors add coherently in the integral (3.48), the fractional accuracy requirement will be more stringent.

It should be straightforward in principle to ensure that numerical templates satisfy Eq. (3.49). Let us schematically denote a numerically generated template as $h_{\rm num}(t,\varepsilon)$, where ε represents the set of tolerances (grid size, size of time steps, *etc.*) that govern the accuracy of the calculation. (Representing this set of parameters by a single tolerance ε is an oversimplification but is adequate for the purposes of our discussion.) One can then iterate one's calculations varying ε in order to obtain sufficiently accurate templates, using the following standard type of procedure: First, calculate the template $h_{\rm num}(t,\varepsilon)$. Second, calculate the more accurate template $h_{\rm num}(t,\varepsilon/2)$. Third, make the identifications

$$\begin{aligned} h(t) &\equiv h_{\rm num}(t,\varepsilon/2), \\ \delta h(t) &\equiv h_{\rm num}(t,\varepsilon/2) - h_{\rm num}(t,\varepsilon), \end{aligned} \tag{3.50}$$

and insert these quantities in Eq. (3.48) to calculate Δ. This allows one to assess the accuracy of the template $h_{\rm num}(t,\varepsilon)$. Finally, iterate until Eq. (3.49) is satisfied.

3.6.2 Derivation and meaning of accuracy criterion

The required accuracy of numerical templates depends on how and for what purpose they are used. As discussed in the Introduction, merger templates might be used in several different ways: (i) They might be used as search templates for signal searches using matched filtering. Such searches will probably not be feasible, at least initially, as they would require the computation of an inordinately large number of templates. (ii) For BBH events that have already been detected via matched filtering

of the inspiral or ringdown waves, or by the noise-monitoring detection technique [7, 42] applied to the merger waves, the merger templates might be used for matched filtering in order to measure the binary's parameters and test general relativity. (iii) If only a few, representative supercomputer simulations and their associated waveform templates are available, one might simply perform a qualitative comparison between the measured waveform and templates in order to deduce qualitative information about the BBH source. In this section we estimate the accuracy requirements for the first two of these uses of merger templates.

Consider first signal searches using matched filtering. The expected SNR ρ obtained for a waveform $h(t)$ when using a template $h_T(t)$ is [45]

$$\rho = \frac{(h|h_T)}{\sqrt{(h_T|h_T)}}. \tag{3.51}$$

Substituting $h_T(t) = h(t) + \delta h(t)$ into Eq. (3.51) and expanding to second order in δh, we find that the fractional loss in SNR produced by the numerical error $\delta h(t)$ is

$$\frac{\delta\rho}{\rho} = \Delta_1 + O[(\delta h)^3], \tag{3.52}$$

where

$$\Delta_1 \equiv \frac{1}{2}\left[\frac{(\delta h|\delta h)}{(h|h)} - \frac{(\delta h|h)^2}{(h|h)^2}\right]. \tag{3.53}$$

Note that the quantity Δ_1 is proportional to $(\delta h_1|\delta h_1)$, where δh_1 is the component of δh perpendicular to h. Thus, a numerical error of the form $\delta h(t) \propto h(t)$ will not contribute to the fractional loss in SNR. This is to be expected, since the quantity (3.51) is independent of the absolute normalization of the templates $h_T(t)$.

The event detection rate is proportional to the cube of the SNR, and hence the fractional loss in event rate resulting from template inaccuracies is approximately $3\delta\rho/\rho$ [45]. If one demands that the fractional loss in event rate be less than, say, 3% one obtains the criterion [46]

$$\Delta_1 \leq 0.01. \tag{3.54}$$

From Eqs. (3.48) and (3.53), $\Delta_1 \leq \Delta$, so the condition (3.54) is less stringent than the condition (3.49). The justification for imposing the more stringent criterion (3.49) rather than (3.54) derives from the use of templates for parameter extraction. We now turn to a discussion of this issue.

In principle, one could hope to measure all of the 15 parameters on which the merger waveforms depend by combining the outputs of several detectors with a complete bank of templates (although in practice the accuracy with which some of those 15 parameters can be measured is not likely to be very good). In the next few paragraphs we derive an approximate condition on Δ [Eq. (3.60)] which results from demanding that the systematic errors in the measured values of all the parameters be small compared to the statistical errors due to detector noise. (We note that one would also like to use matched filtering to test general relativity with merger waves; the accuracy criterion that we derive for parameter measurement will also approximately apply to tests of general relativity.)

Recall that we write the waveform as $h(t;\,\boldsymbol{\theta})$. Let $\hat{\theta}^\alpha$, $1 \leq \alpha \leq n_p$, be the best-fit values of θ^α given by the matched-filtering process. The quantities $\hat{\theta}^\alpha$ depend on the detector noise and are thus random variables. In the high SNR limit, the variables $\hat{\theta}^\alpha$ have a multivariate Gaussian distribution with (see, *e.g.*, Ref. [13])

$$\langle \delta\hat{\theta}^\alpha \; \delta\hat{\theta}^\beta \rangle = \Sigma^{\alpha\beta}, \tag{3.55}$$

where $\delta\hat{\theta}^\alpha \equiv \hat{\theta}^\alpha - \langle\hat{\theta}^\alpha\rangle$ and the matrix $\Sigma^{\alpha\beta}$ is defined after Eq. (3.18). The systematic error $\Delta\theta^\alpha$ in the inferred values of the parameters θ^α due to the template error δh can be shown to be approximately

$$\Delta\theta^\alpha = \Sigma^{\alpha\beta} \left(\frac{\partial h}{\partial\theta^\beta} \middle| \delta h \right). \tag{3.56}$$

From Eqs. (3.55) and (3.56), in order to guarantee that the systematic error in each of the parameters be smaller than some number ε times that parameter's statistical error, we must have

$$||\delta h_{||}||^2 \equiv \left(\delta h_{||} | \delta h_{||} \right) \leq \varepsilon^2. \tag{3.57}$$

Here $\delta h_{||}$ is the component of δh parallel to the tangent space of the manifold of signals $\mathcal{S}$ discussed in Sec. 3.2. It is given by

$$\delta h_{||} = \Sigma^{\alpha\beta} \left(\delta h \middle| \frac{\partial h}{\partial\theta^\alpha} \right) \frac{\partial h}{\partial\theta^\beta}. \tag{3.58}$$

The magnitude $||\delta h_{||}||$ depends on details of the number of parameters, and on how the waveform $h(t, \boldsymbol{\theta})$ varies with these parameters. However, a strict upper bound is

$$||\delta h_{||}|| \leq ||\delta h||. \tag{3.59}$$

If we combine Eqs. (3.48), (3.57) and (3.59) we obtain

$$\Delta \leq \frac{\varepsilon^2}{2\rho^2}. \tag{3.60}$$

Inserting reasonable estimates for ρ and ε ($\rho \simeq 7$, $\varepsilon \simeq 1$) we recover the criterion (3.49) [47]. In Sec. 3.7 we give an alternative derivation of Eq. (3.60) using information theory.

The value $\rho \simeq 7$ leading to the criterion (3.49) is appropriate for ground based interferometers [7]. However, much higher SNRs are expected for LISA; see, *e.g.*, Ref. [7]. Thus, numerical templates used for testing relativity and measuring parameters with LISA data will have to be substantially more accurate than those used with data from ground based instruments.

3.7 Number of bits of information obtainable from the merger signal and implications for template construction

In information theory, a quantity called "information" (analogous to entropy) can be associated with any measurement process: it is simply the base 2 logarithm of the number of distinguishable measurement outcomes [26, 27]. Equivalently, it is the number of bits required to store the knowledge gained from the measurement. In this section we specialize the notions of information theory to gravitational wave measurements, and estimate the number of bits of information which one can gain in different cases.

3.7.1 Total information gain

First consider the situation in which templates are unavailable. Suppose that our prior information describing the signal is that it lies inside some frequency band of length Δf and inside some time interval of duration T. We denote by $I_{\rm total}$ the base 2 logarithm of the number of waveforms $\mathbf{h}$ that are distinguishable by the measurement, that are compatible with our prior information, and that are compatible with our measurement of the detector output's magnitude $\rho(\mathbf{s})$ [48]. Note that the vast majority of these $2^{I_{\rm total}}$ waveforms are completely irrelevant to BBH mergers: the merger signals are a small subset (the manifold $\mathcal{S}$) of all distinguishable waveforms with the above characteristics. The quantity $I_{\rm total}$ characterizes the information gain in a measurement when we do not have prior information about which waveforms are relevant. Note also that $I_{\rm total}$ quantifies the information gained from the measurement about the merger waveform shape, but in the absence of templates,

we do not learn anything about the BBH source.

A precise definition of the total information gain I_{total} is as follows. Let T and Δf be *a priori* upper bounds for the durations and bandwidths of merger signals, and let V be the vector space of signals with duration $\leq T$ inside the relevant frequency band. This vector space V has dimension $\mathcal{N}_{\text{bins}} = 2T\Delta f$. Let $p^{(0)}(\mathbf{h})$ be the PDF describing our prior information about the gravitational wave signal [49], and let $p(\mathbf{h}\,|\,\mathbf{s})$ denote the posterior PDF for $\mathbf{h}$ after the measurement, *i.e.*, the PDF for $\mathbf{h}$ given that the detector output is $\mathbf{s}$. A standard Bayesian analysis shows that $p(\mathbf{h}\,|\,\mathbf{s})$ will be given by

$$p(\mathbf{h}\,|\,\mathbf{s}) = \mathcal{K}\, p^{(0)}(\mathbf{h})\, \exp\left[-\left(\mathbf{s}-\mathbf{h}\,|\,\mathbf{s}-\mathbf{h}\right)/2\right] \tag{3.61}$$

where $\mathcal{K}$ is a normalization constant [16]. Finally, let $p[\mathbf{h}\,|\,\rho(\mathbf{s})]$ be the PDF of $\mathbf{h}$ given that the magnitude of $\mathbf{s}$ is $\rho(\mathbf{s})$. We define I_{total} to be

$$I_{\text{total}} \equiv \int d\mathbf{h}\; p(\mathbf{h}\,|\,\mathbf{s}) \log_2 \left[\frac{p(\mathbf{h}\,|\,\mathbf{s})}{p[\mathbf{h}\,|\,\rho(\mathbf{s})]}\right]. \tag{3.62}$$

By this definition, I_{total} is the *relative information* of the PDFs $p[\mathbf{h}\,|\,\rho(\mathbf{s})]$ and $p(\mathbf{h}\,|\,\mathbf{s})$ [27]. In Appendix B we show that the quantity (3.62) in fact represents the base 2 logarithm of the number of distinguishable wave shapes that could have been measured and that are compatible with the magnitude $\rho(\mathbf{s})$ of the data stream [48]. Thus, one learns I_{total} bits of information about the waveform $\mathbf{h}$ when one goes from knowing only the magnitude $\rho(\mathbf{s}) = ||\mathbf{s}||$ of the detector output to knowing the actual detector output $\mathbf{s}$.

We also show in Appendix B that in the limit of no prior information other than T and Δf, we have

$$I_{\text{total}} = \frac{1}{2}\mathcal{N}_{\text{bins}}\, \log_2\left[\rho(\mathbf{s})^2/\mathcal{N}_{\text{bins}}\right] + O[\ln \mathcal{N}_{\text{bins}}]. \tag{3.63}$$

The formula (3.63) is valid in the limit of large $\mathcal{N}_{\text{bins}}$ for fixed $\rho(\mathbf{s})^2/\mathcal{N}_{\text{bins}}$, and moreover applies only when

$$\rho(\mathbf{s})^2/\mathcal{N}_{\text{bins}} > 1; \tag{3.64}$$

see below for further discussion of this point.

There is a simple and intuitive way to understand the result (3.63). Fix the gravitational waveform, $\mathbf{h}$, considered as a point in the $\mathcal{N}_{\text{bins}}$-dimensional Euclidean space V. What is measured is the detector output $\mathbf{s} = \mathbf{h} + \mathbf{n}$, whose location in V is displaced from $\mathbf{h}$. The direction and magnitude of the displacement depend upon the particular instance of the noise $\mathbf{n}$. However, if we average over

an ensemble of noise realizations, the displacement due to the noise is in a random direction and has rms magnitude $\sqrt{\mathcal{N}_{\rm bins}}$ (since on an appropriate basis each component of $\mathbf{n}$ has rms value 1). Therefore, all points $\{\mathbf{h}'\}$ lying inside a hypersphere of radius $\sqrt{\mathcal{N}_{\rm bins}}$ centered on $\mathbf{h}$ are effectively indistinguishable from each other. The volume of such a hypersphere is

$$C_{\mathcal{N}_{\rm bins}}(\sqrt{\mathcal{N}_{\rm bins}})^{\mathcal{N}_{\rm bins}}, \tag{3.65}$$

where $C_{\mathcal{N}_{\rm bins}}$ is a constant whose value is unimportant. When we measure a detector output $\mathbf{s}$ with magnitude $\rho(\mathbf{s})$, the set of signals $\mathbf{h}$ that could have given rise to an identical measured $\rho(\mathbf{s})$ will form a hypersphere of radius $\sim \rho(\mathbf{s})$ and volume

$$C_{\mathcal{N}_{\rm bins}}\rho(\mathbf{s})^{\mathcal{N}_{\rm bins}}. \tag{3.66}$$

The number of distinguishable signals in this large hypersphere will be approximately the ratio of the two volumes (3.65) and (3.66); the base 2 logarithm of this ratio is the quantity (3.63).

Equation (3.63) expresses the information gain as a function of the magnitude of the measured detector output $\mathbf{s}$. We now re-express this information gain in terms of properties of the gravitational-wave signal $\mathbf{h}$. For a given $\mathbf{h}$, Eqs. (3.16) and (3.17) show that the detector output's magnitude $\rho(\mathbf{s})$ will be approximately given by

$$\rho(\mathbf{s})^2 \approx \rho^2 + \mathcal{N}_{\rm bins} \pm \sqrt{\mathcal{N}_{\rm bins}}. \tag{3.67}$$

Here $\rho^2 = ||\mathbf{h}||^2$ is the SNR squared (2.13) that would be achieved if matched filtering were possible (if templates were available). We use ρ as a convenient measure of signal strength; in this context, it is meaningful even in situations where templates are unavailable and matched filtering cannot be carried out. The last term in Eq. (3.67) gives the approximate size of the statistical fluctuations in $\rho(\mathbf{s})^2$. We now substitute Eq. (3.67) into Eq. (3.63) and obtain

$$I_{\rm total} = \frac{1}{2}\mathcal{N}_{\rm bins}\,\log_2\left[1+\rho^2/\mathcal{N}_{\rm bins}\right] \times \left[1 + O\left(\frac{\ln \mathcal{N}_{\rm bins}}{\mathcal{N}_{\rm bins}}\right) + O\left(\frac{1}{\sqrt{\mathcal{N}_{\rm bins}}}\right)\right]. \tag{3.68}$$

Also, the condition (3.64) for the applicability of Eq. (3.63), when expressed in terms of ρ instead of $\rho(\mathbf{s})$, becomes

$$\frac{\rho^2}{\mathcal{N}_{\rm bins}} \pm \frac{1}{\sqrt{\mathcal{N}_{\rm bins}}} \geq 0, \tag{3.69}$$

which will be satisfied with high probability when $\rho \gg \mathcal{N}_{\rm bins}^{1/4}$ [50]. In the regime $\rho \lesssim \mathcal{N}_{\rm bins}^{1/4}$, the condition (3.64) is typically not satisfied and the formula (3.63) does not apply; we show in Appendix B that in this case the information gain (3.62) is usually very small, depending somewhat on the prior PDF $p^{(0)}(\mathbf{h})$. [In contexts other than BBH merger waveforms, the information gain can be large in the regime $\rho \ll \mathcal{N}_{\rm bins}^{1/4}$ if the prior PDF $p^{(0)}(\mathbf{h})$ is very sharply peaked. For example, when one considers measurements of binary neutron star inspirals with advanced LIGO interferometers, the information gain in the measurement is large even though typically one will have $\rho \ll \mathcal{N}_{\rm bins}^{1/4}$, because we have very good prior information about inspiral waveforms.]

As an example, a typical detected BBH event might have a merger SNR of $\rho \sim 10$, and $\mathcal{N}_{\rm bins}$ might be 30 [7]. Then, Eq. (3.68) tells us that $\sim 3 \times 10^9 \approx 2^{32}$ signals of the same magnitude could have been distinguished, thus the information gained is ~ 32 bits. More generally, for ground based interferometers we expect ρ to lie in the range $5 \lesssim \rho \lesssim 100$ [7], and therefore $10\,\text{bits} \lesssim I_{\rm total} \lesssim 120\,\text{bits}$; and for LISA we expect ρ to typically lie in the range $10^3 \lesssim \rho \lesssim 10^5$ so that $200\,\text{bits} \lesssim I_{\rm total} \lesssim 400\,\text{bits}$.

3.7.2 Source information gain

Consider next the situation in which a complete family of accurate theoretical template waveforms $\mathbf{h}(\boldsymbol{\theta})$ are available for the merger. Without templates, we gain $I_{\rm total}$ bits of information about the shape of the waveform in a measurement. With templates, some—but not all—of this information can be translated into information about the BBH source. For instance, suppose in the example considered above that the number of distinguishable waveforms that could have come from BBH mergers and that are distinguishable in the detector noise is 2^{25}. (This number must be less that the total number $\sim 2^{32}$ of distinguishable waveform shapes, since waveforms from BBH mergers will clearly not fill out the entire function space V of possible waveforms.) In this example, by identifying which template best fits the detector output, we can gain ~ 25 bits of information about the BBH source (*e.g.* about the black holes' masses or spins). We will call this number of bits of information $I_{\rm source}$; clearly $I_{\rm source} \leq I_{\rm total}$ always.

What of the remaining $I_{\rm total} - I_{\rm source}$ bits of information (7 bits in the above example)? If the detector output is close to one of the template shapes, this closeness can be regarded as evidence in favor of the theory of gravity (general relativity) used to compute the templates, so the $I_{\rm total} - I_{\rm source}$ bits can be viewed as information about the validity of general relativity. If one computed templates in more general theories of gravity, one could in principle translate those $I_{\rm total} - I_{\rm source}$ bits into

a quantitative form and obtain constraints on the parameters entering into the gravitational theory. However, with only general-relativistic templates at one's disposal, the information contained in the $I_{\rm total} - I_{\rm source}$ bits will simply result in a qualitative confirmation of general relativity, in the sense that one of the general relativistic templates will fit the data well.

A precise definition of $I_{\rm source}$ is as follows. Let $p(\boldsymbol{\theta} \,|\, \mathbf{s})$ denote the probability distribution for the source parameters $\boldsymbol{\theta}$ given the measurement $\mathbf{s}$. This PDF is given by a formula analogous to Eq. (3.61) [16]

$$p(\boldsymbol{\theta} \,|\, \mathbf{s}) = \mathcal{K} p^{(0)}(\boldsymbol{\theta}) \, \exp\left[- \left(\mathbf{s} - \mathbf{h}(\boldsymbol{\theta}) \,|\, \mathbf{s} - \mathbf{h}(\boldsymbol{\theta}) \right) / 2 \right], \tag{3.70}$$

where $p^{(0)}(\boldsymbol{\theta})$ is the prior PDF for $\boldsymbol{\theta}$ and $\mathcal{K}$ is a normalization constant. Let $p[\boldsymbol{\theta} \,|\, \rho(\mathbf{s})]$ be the posterior PDF for $\boldsymbol{\theta}$ given that the magnitude of the measured signal is $\rho(\mathbf{s})$. Then we define

$$I_{\rm source} \equiv \int d\boldsymbol{\theta} \; p(\boldsymbol{\theta} \,|\, \mathbf{s}) \log_2 \left[\frac{p(\boldsymbol{\theta} \,|\, \mathbf{s})}{p[\boldsymbol{\theta} \,|\, \rho(\mathbf{s})]} \right]. \tag{3.71}$$

The number of bits (3.71) gained about the source will clearly depend on the details of how the gravitational waveforms depend on the source parameters, on the prior expected ranges of these parameters, *etc.* In Appendix B we argue that to a rather crude approximation, $I_{\rm source}$ should be given by the formula (3.68) with $\mathcal{N}_{\rm bins}$ replaced by the number of parameters $\mathcal{N}_{\rm param}$ on which the waveform has a significant dependence:

$$I_{\rm source} \approx \frac{1}{2} \mathcal{N}_{\rm param} \, \log_2 \left[1 + \rho^2 / \mathcal{N}_{\rm param} \right]. \tag{3.72}$$

Note that the quantity $\mathcal{N}_{\rm param}$ should be bounded above by the quantity n_p discussed in Sec. 3.2, but may be somewhat smaller than n_p. This will be the case if the waveform depends only very weakly on some of the parameters θ^α. Equation (3.72) is only valid when $\mathcal{N}_{\rm param} \leq \mathcal{N}_{\rm bins}$. For BBH mergers we expect $\mathcal{N}_{\rm param} \lesssim 15$, which from Eq. (3.72) predicts that $I_{\rm source}$ lies in the range $\sim$ 10 bits to $\sim$ 70 bits for SNRs ρ in the range 5 to 100 (the expected range for ground based interferometers [7]), and $\sim$ 100 bits to $\sim$ 200 bits for ρ in the range 10^3 to 10^5 expected for LISA [7].

3.7.3 Loss of source information due to template inaccuracies or to sparseness in the lattice of templates

As discussed in Sec. 3.6, templates will contain unavoidable numerical errors. We now analyze how such errors affect the source information gained, and use this analysis to infer the maximum allowable template error. We write

$$\mathbf{h}_T(\boldsymbol{\theta}) = \mathbf{h}(\boldsymbol{\theta}) + \delta\mathbf{h}(\boldsymbol{\theta}), \tag{3.73}$$

where $\mathbf{h}(\boldsymbol{\theta})$ denotes the true waveform, $\mathbf{h}_T(\boldsymbol{\theta})$ the numerical template, and $\delta\mathbf{h}(\boldsymbol{\theta})$ the numerical error. Clearly, the numerical error will reduce the information (3.71) one obtains about the source. To make an estimate of the reduction, we model the numerical error as a random process with

$$\langle \delta h_i \, \delta h_j \rangle = \mathcal{C}_{ij}, \tag{3.74}$$

where for simplicity we take $\mathcal{C}_{ij} = \lambda\Gamma_{ij}$ for some constant λ. Here Γ_{ij} is the matrix introduced in Eq. (3.11). The expected value of $(\delta\mathbf{h} \,|\, \delta\mathbf{h})$ is then given by, from Eq. (3.14),

$$\begin{aligned} \langle\, (\delta\mathbf{h} \,|\, \delta\mathbf{h}) \,\rangle &= \Sigma^{ij} \langle \delta h_i \delta h_j \rangle \\ &= \Sigma^{ij}\, \lambda\Gamma_{ij} = \lambda\mathcal{N}_{\text{bins}}, \end{aligned} \tag{3.75}$$

where we have used Eq. (3.10). We can write λ in terms of the quantity Δ discussed in Sec. 3.6 by combining Eqs. (3.48) and (3.75), yielding

$$\lambda = 2\Delta \frac{\rho^2}{\mathcal{N}_{\text{bins}}}. \tag{3.76}$$

The information I'_{source} which one obtains when measuring with inaccurate templates can be calculated by treating the sum of the detector noise $\mathbf{n}$ and the template numerical error $\delta\mathbf{h}$ as an effective noise $\mathbf{n}^{(\text{eff})}$. This effective noise is characterized by the covariance matrix

$$\langle n_i^{(\text{eff})}\, n_j^{(\text{eff})} \rangle = \Gamma_{ij} + \lambda\Gamma_{ij}. \tag{3.77}$$

Thus, in this simplified model, the effect of the numerical error is to increase the noise by a factor $\sqrt{1+\lambda}$. The new information gain I'_{source} is therefore given by Eq. (3.72) with ρ replaced by an

effective SNR ρ', where

$$(\rho')^2 = \frac{\rho^2}{1+\lambda}. \tag{3.78}$$

If we now combine Eqs. (3.72), (3.76) and (3.78), we find that the loss in information due to template inaccuracy

$$\delta I_{\text{source}} = I_{\text{source}} - I'_{\text{source}} \tag{3.79}$$

is given by

$$\delta I_{\text{source}} = \rho^2 \left(\frac{\rho^2}{\mathcal{N}_{\text{param}} + \rho^2} \right) \left(\frac{\mathcal{N}_{\text{param}}}{\mathcal{N}_{\text{bins}}} \right) \Delta + O(\Delta^2). \tag{3.80}$$

To ensure that $\delta I_{\text{source}} \lesssim 1$ bit, we therefore must have

$$\Delta \lesssim \frac{1}{\rho^2} \left(\frac{\mathcal{N}_{\text{param}} + \rho^2}{\rho^2} \right) \left(\frac{\mathcal{N}_{\text{bins}}}{\mathcal{N}_{\text{param}}} \right). \tag{3.81}$$

This condition is a more accurate version of the condition (3.60) that was derived in Sec. 3.6. It approximately reduces to (3.60) for typical BBH events (except in the unrealistic limit $\rho^2 \ll \mathcal{N}_{\text{param}}$), since $\mathcal{N}_{\text{param}} \sim 10$ and $10 \lesssim \mathcal{N}_{\text{bins}} \lesssim 100$ [7].

Turn next to the issue of the required degree of fineness of a template lattice, that is, how close in parameter space successive templates must be to one another. We parameterize the fineness by a dimensionless parameter $\varepsilon_{\text{grid}}$: the lattice is required to have the property that for any possible true signal $\mathbf{h}(\boldsymbol{\theta})$, there exists some template $\mathbf{h}(\boldsymbol{\theta}^*)$ in the lattice with

$$\frac{(\mathbf{h}(\boldsymbol{\theta}) \,|\, \mathbf{h}(\boldsymbol{\theta}^*))}{\sqrt{(\mathbf{h}(\boldsymbol{\theta}) \,|\, \mathbf{h}(\boldsymbol{\theta}))}\, \sqrt{(\mathbf{h}(\boldsymbol{\theta}^*) \,|\, \mathbf{h}(\boldsymbol{\theta}^*))}} \geq 1 - \varepsilon_{\text{grid}}. \tag{3.82}$$

The quantity $1 - \varepsilon_{\text{grid}}$ is called the minimal match [45]. Suppose that one defines a metric on the space V of templates using the norm associated with the inner product (3.14). It then follows from Eq. (3.82) that the largest possible distance D_{max} between an incoming signal $\mathbf{h}(\boldsymbol{\theta})$ and some rescaled template $\mathcal{A}\mathbf{h}(\boldsymbol{\theta}^*)$ with $\mathcal{A} > 0$ is

$$D_{\text{max}} = \sqrt{2\varepsilon_{\text{grid}}}\, \rho, \tag{3.83}$$

where ρ is the matched filtering SNR (2.13) of the incoming signal.

We can view the discreteness in the template lattice as roughly equivalent to an ignorance on our part about the location of the manifold $\mathcal{S}$ of true gravitational wave signals between the lattice

points. The maximum distance any correct waveform $\mathbf{h}(\boldsymbol{\theta})$ could be away from where we may think it should be (where our guess is for example obtained by linearly extrapolating from the nearest points on the lattice) is of order $D_{\rm max}$. We can crudely view this ignorance as equivalent to a numerical error $\delta\mathbf{h}$ in the templates of magnitude $||\delta\mathbf{h}|| = D_{\rm max}$. Combining Eqs. (3.48), (3.80) and (3.83) shows that the loss of information $\delta I_{\rm source}$ due to the discreteness of the grid should therefore be of order

$$\delta I_{\rm source} \sim \rho^2 \left(\frac{\rho^2}{\mathcal{N}_{\rm param} + \rho^2}\right) \left(\frac{\mathcal{N}_{\rm param}}{\mathcal{N}_{\rm bins}}\right) \varepsilon_{\rm grid}. \tag{3.84}$$

The grid fineness $\varepsilon_{\rm grid}$ should be chosen to ensure that $\delta I_{\rm source}$ is small compared to unity, while also taking into account that the fractional loss in event detection rate for signal searches due to the coarseness of the grid will be $\lesssim 3\varepsilon_{\rm grid}$; see Sec. 3.6.2 above and Refs. [45, 46]

3.8 Conclusions

Templates from numerical relativity for the merger phase of BBH coalescences will be a great aid to the analysis of detected BBH events. A complete bank of templates could be used to implement a matched filtering analysis of merger data, which would allow measurements of the binary's parameters and tests of general relativity in a strong field, highly dynamic regime. Such matched filtering may also be possible without a complete bank of templates, if iterative supercomputer simulations are carried out in tandem with data analysis. A match of the detected waves with such templates will be a triumph for the theory of general relativity and an unambiguous signature of the existence of black holes. Qualitative information from representative supercomputer simulations will also be useful, both as an input to algorithms for extracting the merger waveform's shape from the noisy interferometer data stream, and as an aid to interpreting the observed waveforms and making deductions about the waves' source.

We have derived, using several rather different conceptual starting points, accuracy requirements that numerical templates must satisfy in order for them to be useful as data analysis tools. We first considered matched filtering signal searches using templates; here the loss in event rate due to template inaccuracies is simply related to the degradation in SNR, and leads to a criterion on template accuracy. Approximately the same criterion is obtained when one demands that the systematic errors in parameter extraction be small compared to the detector-noise induced statistical

errors. Finally, we quantified the information that is encoded in the merger waveforms using the framework of information theory, and deduced how much of the information is lost due to template inaccuracies or to having insufficiently many templates. We deduced approximate requirements that templates must satisfy (in terms both of individual template accuracy and of spacing between templates) in order that all of the waveform's information can be extracted.

The theory of maximum likelihood estimation is a useful starting point for deriving algorithms for reconstructing the gravitational waveforms from the noisy interferometer output. In this chapter we have discussed and derived such algorithms in the contexts both of a single detector and of a network of several detectors; these algorithms can be tailored to build-in many different kinds of prior information about the waveforms.

Acknowledgements

We thank Kip Thorne for suggesting this project to us, and for his invaluable encouragement and detailed comments on the paper. We thank David Chernoff for some helpful conversations. This research was supported in part by NSF grants PHY–9424337, PHY–9220644, PHY–9514726, and NASA grant NAGW–2897. S. A. H. gratefully acknowledges the support of a National Science Foundation Graduate Fellowship, and É. F. likewise acknowledges the support of Enrico Fermi and Sloan Foundation fellowships.

Appendix A Waveform reconstruction with a detector network

In this appendix we describe how to extend the filtering methods discussed in Sec. 3.4 above from a single detector to a network of an arbitrary number of detectors. The underlying principle is again simply to use the maximum likelihood estimator of the waveform shape. We also explain the relationship between our waveform reconstruction method and the method of Gürsel and Tinto [25]. Secs. A and A below overlap somewhat with analyses by L. S. Finn [51]. Finn uses similar mathematical techniques to analyze measurements of a stochastic background and waves of well-understood form with multiple detectors, applications which are rather different from ours.

We start by establishing some notations for a detector network; these notations and conventions follow those of Appendix A of Ref. [13]. The output of such a network can be represented as a vector $\vec{s}(t) = [s_1(t), \ldots, s_{n_d}(t)]$, where n_d is the number of detectors, and $s_a(t)$ is the strain amplitude read out from the ath detector [52]. There will be two contributions to the detector output $\vec{s}(t)$—the detector network noise $\vec{n}(t)$ (a vector random process), and the true gravitational-wave signal $\vec{h}(t)$:

$$\vec{s}(t) = \vec{h}(t) + \vec{n}(t). \tag{3.85}$$

We will assume that the detector network noise is stationary and Gaussian. This assumption is not very realistic, but understanding the optimal method of waveform reconstruction with this idealized assumptions is an important first step towards more sophisticated waveform reconstruction algorithms adapted to realistic detector noise. With this assumption, the statistical properties of the detector network noise can be described by the auto-correlation matrix

$$C_n(\tau)_{ab} = \langle n_a(t+\tau) n_b(t) \rangle - \langle n_a(t+\tau) \rangle \langle n_b(t) \rangle, \tag{3.86}$$

where the angular brackets mean an ensemble average or a time average. Twice the Fourier transform of the correlation matrix is the power spectral density matrix:

$$S_h(f)_{ab} = 2 \int_{-\infty}^{\infty} d\tau \, e^{2\pi i f \tau} C_n(\tau)_{ab}. \tag{3.87}$$

The off-diagonal elements of this matrix describe the effects of correlations between the noise sources in the various detectors, while each diagonal element $S_h(f)_{aa}$ is just the usual power spectral density of the noise in the ath detector. We assume that the functions $S_h(f)_{ab}$ for $a \neq b$ have

been measured for each pair of detectors.

The Gaussian random process $\vec{n}(t)$ determines a natural inner product on the space of functions $\vec{h}(t)$, which generalizes the single-detector inner product (3.4). The inner product is defined so that the probability that the noise takes a specific value $\vec{n}_0(t)$ is

$$p[\vec{n} = \vec{n}_0] \propto e^{-(\vec{n}_0|\vec{n}_0)/2}. \tag{3.88}$$

It is given by

$$\left(\vec{g}\,|\,\vec{h}\right) \equiv 4\,\mathrm{Re}\int_0^\infty df\ \tilde{g}_a(f)^*\left[\mathbf{S}_h(f)^{-1}\right]^{ab}\tilde{h}_b(f). \tag{3.89}$$

See, *e.g.*, Appendix A of Ref. [13] for more details.

Turn, now, to the relation between the gravitational wave signal $h_a(t)$ seen in the ath detector, and the two independent polarization components $h_+(t)$ and $h_\times(t)$ of the waves. Let $\mathbf{x}_a$ be the position and $\mathbf{d}_a$ the polarization tensor of the ath detector in the detector network. By polarization tensor we mean that tensor $\mathbf{d}_a$ for which the detector's output $h_a(t)$ is given in terms of the waves' transverse traceless strain tensor $\mathbf{h}(\mathbf{x},t)$ by

$$h_a(t) = \mathbf{d}_a : \mathbf{h}(\mathbf{x}_a, t), \tag{3.90}$$

where the colon denotes a double contraction. A gravitational wave burst coming from the direction of a unit vector $\mathbf{m}$ will have the form

$$\mathbf{h}(\mathbf{x},t) = \sum_{A=+,\times} h_A(t+\mathbf{m}\cdot\mathbf{x})\,\mathbf{e}^A_{\mathbf{m}}, \tag{3.91}$$

where $\mathbf{e}^+_{\mathbf{m}}$ and $\mathbf{e}^\times_{\mathbf{m}}$ are a basis for the transverse traceless tensors perpendicular to $\mathbf{m}$, normalized according to $\mathbf{e}^A_{\mathbf{m}} : \mathbf{e}^B_{\mathbf{m}} = 2\delta^{AB}$. Combining Eqs. (3.90) and (3.91) and switching to the frequency domain using the convention (3.2) yields

$$\tilde{h}_a(f) = F^A_a(\mathbf{m})\,\tilde{h}_A(f)\,e^{-2\pi i f\tau_a(\mathbf{m})}, \tag{3.92}$$

where the quantities

$$F^A_a(\mathbf{m}) \equiv \mathbf{e}^A_{\mathbf{m}} : \mathbf{d}_a, \tag{3.93}$$

for $A = +, \times$, are detector beam-pattern functions for the ath detector [34] and $\tau_a(\mathbf{m}) \equiv \mathbf{m}\cdot\mathbf{x}_a$ is

the time delay at the ath detector relative to the origin of coordinates.

Derivation of posterior probability distribution

We now construct the PDF $\mathcal{P}[\mathbf{m}, h_+(t), h_\times(t)|\vec{s}(t)]$ for the gravitational waves to be coming from direction $\mathbf{m}$ with waveforms $h_+(t)$ and $h_\times(t)$, given that the output of the detector network is $\vec{s}(t)$. Let $p^{(0)}(\mathbf{m})$ and $p^{(0)}[h_A(t)]$ be the prior probability distributions for the sky position $\mathbf{m}$ (presumably a uniform distribution on the unit sphere) and waveform shapes $h_A(t)$, respectively. A standard Bayesian analysis along the lines of that given in Ref. [16] and using Eq. (3.88) gives

$$\mathcal{P}[\mathbf{m}, h_A(t)|\vec{s}(t)] = \mathcal{K}\, p^{(0)}(\mathbf{m})\, p^{(0)}[h_A(t)] \times \exp\left[-\left(\vec{s}-\vec{h}\,|\,\vec{s}-\vec{h}\right)/2\right], \tag{3.94}$$

where $\mathcal{K}$ is a normalization constant and $\vec{h}$ is understood to be the function of $\mathbf{m}$ and $h_A(t)$ given by (the Fourier transform of) Eq. (3.92).

We next simplify Eq. (3.94) by reducing the argument of the exponential from a double sum over detectors to a single sum over detector sites. In the next few paragraphs we carry out this reduction, leading to Eqs. (3.102) and (3.103) below. We assume that each pair of detectors in the network comes in one of two categories: (i) pairs of detectors at the same detector site, which are oriented the same way, and thus share common detector beam pattern functions $F_a^A(\mathbf{m})$ (for example the 2 km and 4 km interferometers at the LIGO Hanford site); or (ii) pairs of detectors at widely separated sites, for which the detector noise is effectively uncorrelated. Under this assumption we can arrange for the matrix $\mathbf{S}_h(f)$ to have a block diagonal form, with each block corresponding to a detector site, by choosing a suitable ordering of detectors in the list $(1, \ldots, n_d)$. Let us denote the detector sites by Greek indices $\alpha, \beta, \gamma \ldots$, so that α runs from 1 to n_s, where n_s is the number of sites. Let $\mathcal{D}_\alpha$ be the subset of the detector list $(1, \ldots, n_d)$ containing the detectors at the αth site, so that any sum over detectors can be rewritten

$$\sum_{a=1}^{n_d} = \sum_{\alpha=1}^{n_s} \sum_{a\,\in\mathcal{D}_\alpha} . \tag{3.95}$$

Thus, for example, for a 3 detector network with 2 detectors at the first site and one at the second, $\mathcal{D}_1 = \{1, 2\}$ and $\mathcal{D}_2 = \{3\}$. Let $F_\alpha^A(\mathbf{m})$ denote the common value of the beam pattern functions (3.93) for all the detectors at site α. Let $\mathbf{S}_\alpha(f)$ denote the αth diagonal sub-block of the matrix

$\mathbf{S}_h(f)$. Then if we define

$$\Lambda = \left(\vec{s} - \vec{h} \,|\, \vec{s} - \vec{h}\right), \tag{3.96}$$

[the quantity which appears in the exponential in Eq. (3.94)], we obtain from Eq. (3.89)

$$\Lambda = \sum_{\alpha=1}^{n_s} 4\mathrm{Re} \int_0^\infty df \sum_{a,b \in \mathcal{D}_\alpha} \left[\tilde{s}_a(f)^* - \tilde{h}_a(f)^*\right] \times \left[\mathbf{S}_\alpha(f)^{-1}\right]^{ab} \times \left[\tilde{s}_b(f) - \tilde{h}_b(f)\right]. \tag{3.97}$$

Next, we note from Eq. (3.92) that the value of $\tilde{h}_a$ will be the same for all detectors at a given site α. If we denote this common value by $\tilde{h}_\alpha$, then we obtain after some manipulation of Eq. (3.97)

$$\Lambda = \sum_{\alpha=1}^{n_s} 4\,\mathrm{Re} \int_0^\infty df \left\{ \frac{|\tilde{s}_\alpha(f) - \tilde{h}_\alpha(f)|^2}{S_\alpha^{(\mathrm{eff})}(f)} + \Delta_\alpha(f) \right\}. \tag{3.98}$$

The meanings of the various symbols in Eq. (3.98) are as follows. The quantity $S_\alpha^{(\mathrm{eff})}(f)$ is defined by

$$\frac{1}{S_\alpha^{(\mathrm{eff})}(f)} \equiv \sum_{a,b \in \mathcal{D}_\alpha} \left[\mathbf{S}_\alpha(f)^{-1}\right]^{ab}, \tag{3.99}$$

and can be interpreted as the effective overall noise spectrum for site α [53]. The quantity s_α is given by

$$\tilde{s}_\alpha(f) \equiv S_\alpha^{(\mathrm{eff})}(f) \sum_{a,b \in \mathcal{D}_\alpha} \left[\mathbf{S}_\alpha(f)^{-1}\right]^{ab} \tilde{s}_b(f), \tag{3.100}$$

and is, roughly speaking, the mean output strain amplitude of site α. Finally,

$$\Delta_\alpha(f) \equiv \sum_{a,b \in \mathcal{D}_\alpha} \tilde{s}_a(f)^* \tilde{s}_b(f) \left\{ \left[\mathbf{S}_\alpha(f)^{-1}\right]^{ab} - S_\alpha^{(\mathrm{eff})}(f) \sum_{c,d \in \mathcal{D}_\alpha} \left[\mathbf{S}_\alpha(f)^{-1}\right]^{ac} \left[\mathbf{S}_\alpha(f)^{-1}\right]^{db} \right\}. \tag{3.101}$$

The quantity Δ_α is independent of $\mathbf{m}$ and $h_A(t)$, and is therefore irrelevant for our purposes; it can be absorbed into the normalization constant $\mathcal{K}$ in Eq. (3.94). This unimportance of Δ_α occurs because we are assuming that there is some signal present. The term Δ_α is very important, however, in situations where one is trying to assess the probability that some signal (and not just noise) is present in the outputs of the detector network. In effect, it encodes the discriminating power against noise bursts which is due to the presence of detectors with different noise spectra at one site (*e.g.*, the 2km and 4km interferometers at the LIGO Hanford site). We drop the term Δ_α from now on.

The probability distribution for the waveform shapes and sky direction is now given by, from

Eqs. (3.94), (3.96) and (3.98),

$$\mathcal{P}[\mathbf{m}, h_A(t)|\vec{s}(t)] = \mathcal{K}\, p^{(0)}(\mathbf{m})\, p^{(0)}[h_A(t)]\, e^{-\Lambda'/2}, \tag{3.102}$$

where

$$\Lambda' = \sum_{\alpha=1}^{n_s} 4\,\mathrm{Re} \int_0^\infty df\ \frac{|\tilde{s}_\alpha(f) - \tilde{h}_\alpha(f)|^2}{S_\alpha^{(\mathrm{eff})}(f)}. \tag{3.103}$$

Finally, we express this probability distribution directly in terms of the waveforms $h_+(t)$ and $h_\times(t)$ by substituting Eq. (3.92) into Eq. (3.103), which gives

$$\Lambda' = 4\mathrm{Re} \int_0^\infty df \Big\{ \sum_{A,B=+,\times} \Theta^{AB}(f,\mathbf{m}) \left[\tilde{h}_A(f)^* - \tilde{\hat{h}}_A(f)^*\right] \left[\tilde{h}_B(f) - \tilde{\hat{h}}_B(f)\right] + \mathcal{S}(f,\mathbf{m}) \Big\}. \tag{3.104}$$

Here

$$\Theta^{AB}(f,\mathbf{m}) \equiv \sum_{\alpha=1}^{n_s} \frac{F_\alpha^A(\mathbf{m}) F_\alpha^B(\mathbf{m})}{S_\alpha^{(\mathrm{eff})}(f)}, \tag{3.105}$$

$$\tilde{\hat{h}}_A(f) \equiv \Theta_{AB}(f,\mathbf{m}) \sum_{\alpha=1}^{n_s} F_\alpha^B(\mathbf{m}) \tilde{s}_\alpha(f)\, e^{2\pi i f \tau_\alpha(\mathbf{m})}, \tag{3.106}$$

where Θ_{AB} is the inverse matrix to Θ^{AB}, and

$$\mathcal{S}(f,\mathbf{m}) = \sum_\alpha |\tilde{s}_\alpha(f)|^2 - \Theta^{AB} \tilde{\hat{h}}_A(f)^* \tilde{\hat{h}}_B(f). \tag{3.107}$$

Estimating the waveform shapes and the direction to the source

Equations (3.102) and (3.104) constitute one of the main results of this appendix, and give the final and general PDF for $\mathbf{m}$ and $h_A(t)$. In the next few paragraphs we discuss its implications. As mentioned at the start of the appendix, we are primarily interested in situations where the direction $\mathbf{m}$ to the source is already known. However, as an aside, we now briefly consider the more general context where the direction to the source as well as the waveform shapes are unknown.

Starting from Eq. (3.102), one could use either maximum likelihood estimators or so-called Bayes estimators [13, 54, 55, 56] to determine "best-guess" values of $\mathbf{m}$ and $h_A(t)$. Bayes estimators have significant advantages over maximum likelihood estimators but are typically much more difficult to compute, as explained in, for example, Appendix A of Ref. [13]. The Bayes estimator for the direction to the source will be given by first integrating Eq. (3.102) over all waveform shapes,

which yields

$$\mathcal{P}[\mathbf{m}|\vec{s}(t)] = \mathcal{K}p^{(0)}(\mathbf{m})\,\mathcal{D}(\mathbf{m})\;\exp\left[-2\int_0^\infty df\,\mathcal{S}(f,\mathbf{m})\right], \tag{3.108}$$

where $\mathcal{D}(\mathbf{m})$ is a determinant-type factor that is produced by integrating over the waveforms $h_A(t)$. This factor encodes the information that the detector network has greater sensitivity in some directions than in others, and that other things being equal, a signal is more likely to have come from a direction in which the network is more sensitive. The Bayes estimator of $\mathbf{m}$ is now obtained simply by calculating the expected value of $\mathbf{m}$ with respect to the probability distribution (3.108). The simpler, maximum likelihood estimator of $\mathbf{m}$ is given by choosing the values of $\mathbf{m}$ [and of $h_A(t)$] which maximize the probability distribution (3.102), or equivalently by minimizing the quantity

$$\int_0^\infty df\,\mathcal{S}(f,\mathbf{m}). \tag{3.109}$$

Let us denote this value of $\mathbf{m}$ by $\mathbf{m}_{\rm ML}(\vec{s})$. Note that the quantity (3.109) encodes all information about time delays between the signals detected at the various detector sites; as is well known, directional information is obtained primarily through time delay information [54].

In Ref. [25], Gürsel and Tinto suggest a method of estimating $\mathbf{m}$ from $\vec{s}(t)$ for a network of three detectors. For white noise and for the special case of one detector per site, the Gürsel-Tinto estimator is the same as the maximum likelihood estimator $\mathbf{m}_{\rm ML}(\vec{s})$ just discussed, with one major modification: in Sec. V of Ref. [25], Gürsel and Tinto prescribe discarding those Fourier components of the data whose SNR is below a certain threshold as the first stage of calculating their estimator.

Turn, now, to the issue of estimating the waveform shapes $h_+(t)$ and $h_\times(t)$. In general situations where both $\mathbf{m}$ and $h_A(t)$ are unknown, the best way to proceed in principle would be to integrate the probability distribution (3.102) over all solid angles $\mathbf{m}$ to obtain a reduced probability distribution $\mathcal{P}[h_A(t)|\vec{s}(t)]$ for the waveform shapes, and to use this reduced probability distribution to make estimators of $h_A(t)$. However, such an integration cannot be performed analytically and would not be easy numerically; in practice simpler estimators will likely be used. One such simpler estimator is the maximum likelihood estimator of $h_A(t)$ obtained from Eq. (3.102). In the limit of no prior information about the waveform shape when the PDF $p^{(0)}[h_A(t)]$ is very broad, this maximum likelihood estimator is simply $\hat{h}_A(t)$ evaluated at the value $\mathbf{m}_{\rm ML}(\vec{s})$ of $\mathbf{m}$ discussed above.

For BBH mergers, in many cases the direction $\mathbf{m}$ to the source will have been measured from the inspiral portion of the waveform, and thus for the purposes of estimating the merger waveform's

shape, $\mathbf{m}$ can be regarded as known. The probability distribution for $h_A(t)$ given $\mathbf{m}$ and $\vec{s}(t)$ is, from Eq. (3.102),

$$\mathcal{P}[h_A(t) \,|\, \mathbf{m}, \vec{s}(t)] = \mathcal{K}' \, p^{(0)}[h_A(t)] \, e^{-\Lambda''/2}. \tag{3.110}$$

Here $\mathcal{K}'$ is a normalization constant, and Λ'' is given by Eq. (3.104) with the term $\mathcal{S}(f, \mathbf{m})$ omitted. The maximum likelihood estimator of $h_A(t)$ obtained from this probability distribution in the limit of no prior information is again just $\hat{h}_A(t)$. The formula for the estimator $\hat{h}_A(t)$ given by Eqs. (3.99), (3.100), (3.105) and (3.106) is one of the key results of this appendix. It specifies the best-fit waveform shape as a unique function of the detector outputs $s_a(t)$ for any detector network.

Incorporating prior information

In Sec. 3.4, we suggested a method of reconstruction of the merger waveform shape, for a single detector, which incorporated assumed prior information about the waveform's properties. In this appendix, our discussion so far has neglected all prior information about the shape of the waveforms $h_+(t)$ and $h_\times(t)$. We now discuss waveform estimation for a detector network, incorporating prior information, for fixed sky direction $\mathbf{m}$.

With a few minor modifications, the entire discussion of Sec. 3.4 can be applied to a detector network. First, the linear space V should be taken to be the space of pairs of waveforms $\{h_+(t), h_\times(t)\}$, suitably discretized, so that the dimension of V is $2T'/\Delta t$. Second, the inner product (3.14) must be replaced by a discrete version of the inner product

$$(\{h_+, h_\times\} | \{k_+, k_\times\}) \equiv 4\mathrm{Re} \int_0^\infty df \, \Theta^{AB}(f, \mathbf{m}) \tilde{h}_A(f)^* \, \tilde{k}_B(f), \tag{3.111}$$

since the inner product (3.111) plays the same role in the probability distribution (3.110) as the inner product (3.14) plays in the distribution (3.38). Third, the estimated waveforms $\{\hat{h}_+(t), \hat{h}_\times(t)\}$ given by Eq. (3.106) take the place of the measured waveform $\mathbf{s}$ in Sec. 3.4, for the same reason. Fourth, the wavelet basis used to specify the prior information must be replaced by a basis of the form $\{w_{ij}^+(t), w_{kl}^\times(t)\}$, where $w_{ij}^+(t)$ is a wavelet basis of the type discussed in Sec. 3.4 for the space of waveforms $h_+(t)$, and similarly for $w_{kl}^\times(t)$. The prior information about, for example, the assumed duration and bandwidths of the waveforms $h_+(t)$ and $h_\times(t)$ can then be represented exactly as in Sec. 3.4. With these modifications, the remainder of the analyses of Sec. 3.4 apply directly to a network of detectors. Thus the "perpendicular projection" estimator (3.39) and the more general

estimator (3.47) can both be applied to a network of detectors.

The Gürsel-Tinto waveform estimator

As mentioned in Sec. 3.4 above, Gürsel and Tinto have suggested an estimator of the waveforms $h_+(t)$ and $h_\times(t)$ for networks of three detector sites with one detector at each site when the direction $\mathbf{m}$ to the source is known [57]. In our notation, the construction of that estimator can be summarized as follows. First, assume that the estimator is some linear combination of the outputs of the independent detectors corrected for time delays:

$$\tilde{\hat{h}}_A^{(GT)}(f) = \sum_{\alpha=1}^{3} w_A^\alpha(\mathbf{m})\, e^{2\pi i f \tau_\alpha(\mathbf{m})}\, \tilde{s}_\alpha(f). \tag{3.112}$$

Here $\tilde{\hat{h}}_A^{(GT)}$ is the Gürsel-Tinto ansatz for the estimator, and w_A^α are some arbitrary constants that depend on $\mathbf{m}$. [Since there is only one detector per site we can neglect the distinction between the output $\tilde{s}_a(f)$ of an individual detector and the output $\tilde{s}_\alpha(f)$ of a detector site.] Next, demand that for a noise-free signal, the estimator reduces to the true waveforms $h_A(t)$. From Eqs. (3.85) and (3.92) above, this requirement is equivalent to

$$\sum_{\alpha=1}^{3} w_A^\alpha(\mathbf{m})\, F_\alpha^B(\mathbf{m}) = \delta_A^B. \tag{3.113}$$

There is a two dimensional linear space of tensors w_A^α which satisfy Eq. (3.113). Finally, choose w_A^α subject to Eq. (3.113) to minimize the expected value with respect to the noise of the quantity

$$\sum_{A=+,\times} \int dt\, |\hat{h}_A^{(GT)}(t) - h_A(t)|^2, \tag{3.114}$$

where $\hat{h}_A^{(GT)}(t)$ is given as a functional of $h_A(t)$ and the detector noise $n_\alpha(t)$ by Eqs. (3.85), (3.92) and (3.112).

It is straightforward to show by a calculation using Lagrange multipliers that the resulting estimator is [58]

$$\hat{h}_A^{(GT)}(t) = \hat{h}_A(t). \tag{3.115}$$

In other words, the Gürsel-Tinto estimator coincides with the maximum likelihood estimators of $h_+(t)$ and $h_\times(t)$ discussed in this appendix in the case of little prior information. However, the

estimators discussed here generalize the Gürsel-Tinto estimator by allowing an arbitrary number of detectors per site [with the effective output and effective noise spectrum of a site being given by Eqs. (3.100) and (3.99) above], by allowing an arbitrary number of sites, and by allowing one to incorporate prior information about the waveform shapes.

Appendix B Measures of information

In this appendix we substantiate the claims concerning information theory made in Sec. 3.7 of the body of the paper. First, we argue that the concept of the "relative information" of two PDFs introduced in Eq. (3.62) has the interpretation we ascribed to it: it is the base 2 logarithm of the number of distinguishable measurement outcomes. Second, we derive the approximations (3.68) and (3.72).

Consider first the issue of ascribing to any measurement process a "number of bits of information gained" from that process, which corresponds to the base 2 logarithm of the number of distinguishable possible outcomes of the measurement. If $p^{(0)}(\mathbf{x})$ is the PDF for the measured quantities $\mathbf{x} = (x^1, \ldots, x^n)$ before the measurement, and $p(\mathbf{x})$ is the corresponding PDF after the measurement, then the relative information of these two PDFs is defined to be [27]

$$I = \int d^n\mathbf{x}\, p(\mathbf{x})\, \log_2 \left[\frac{p(\mathbf{x})}{p^{(0)}(\mathbf{x})}\right]. \tag{3.116}$$

In simple examples, it is easy to see that the quantity (3.116) reduces to the number of bits of information gained in the measurement. For instance, if $\mathbf{x} = (x^1)$ and the prior PDF $p^{(0)}$ constrains x^1 to lie in some range of size X, and if after the measurement x^1 is constrained to lie in a small interval of size Δx, then $I \approx \log_2(X/\Delta x)$, as one would expect. In addition, the quantity (3.116) has the desirable feature that it is coordinate independent, *i.e.*, that the same answer is obtained when one makes a nonlinear coordinate transformation on the manifold parameterized by $(x^1, \ldots, x^n)$ before evaluating (3.116). For these reasons, in any measurement process, the quantity (3.116) can be interpreted as the number of bits of information gained.

Explicit formula for the total information

As a foundation for deriving the approximate formula (3.68), we derive in this subsection an explicit formula [Eq. (3.128)] for the total information gain (3.62) in a gravitational wave measurement. We shall use a basis of V where the matrix (3.11) is unity, and for ease of notation we shall denote by $\mathcal{N}$ the quantity $\mathcal{N}_{\text{bins}}$.

First, we assume that the prior PDF $p^{(0)}(\mathbf{h})$ appearing in Eq. (3.61) is a function only of $h = ||\mathbf{h}||$. In other words, all directions in the vector space V are taken to be, *a priori*, equally likely, when one measures distances and angles with the inner product (3.14). It would be more realistic

to make such an assumption with respect to a noise-independent inner product like $(h_1 \,|\, h_2) \equiv \int dt h_1(t) h_2(t)$, but if the noise spectrum $S_h(f)$ does not vary too rapidly within the bandwidth of interest, the distinction is not too important and our assumption will be fairly realistic. We write the prior PDF as [59]

$$\begin{aligned} p^{(0)}(\mathbf{h})\, d^{\mathcal{N}} h &= \frac{2\pi^{\mathcal{N}/2}}{\Gamma(\mathcal{N}/2)}\, h^{\mathcal{N}-1}\, p^{(0)}(h) dh \\ &\equiv \bar{p}^{(0)}(h)\, dh. \end{aligned} \tag{3.117}$$

The quantity $\bar{p}^{(0)}(h)\, dh$ is the prior probability that the signal $\mathbf{h}$ will have an SNR $||\mathbf{h}||$ between h and $h + dh$. The exact form of the PDF $\bar{p}^{(0)}(h)$ will not be too important for our calculations below. A moderately realistic choice is $\bar{p}^{(0)}(h) \propto 1/h^3$ with a cutoff at some $h_1 \ll 1$. Note however that the choice $p^{(0)}(\mathbf{h}) = 1$ corresponding to $\bar{p}^{(0)}(h) \propto h^{\mathcal{N}-1}$ is very unrealistic. Below we shall assume that $\bar{p}^{(0)}(h)$ is independent of $\mathcal{N}$.

We next write Eq. (3.61) in a more explicit form. Without loss of generality we can take

$$\mathbf{s} = (s^1, \ldots, s^{\mathcal{N}}) = (s, 0, \ldots, 0), \tag{3.118}$$

where $s = \rho(\mathbf{s}) = ||\mathbf{s}||$. Then, writing $(\mathbf{s}|\mathbf{h}) = sh\cos\theta$ and using the useful identity

$$d^{\mathcal{N}} h = \frac{2\pi^{(\mathcal{N}-1)/2}}{\Gamma\left[(\mathcal{N}-1)/2\right]}\, \sin(\theta)^{\mathcal{N}-2}\, h^{\mathcal{N}-1}\, d\theta\, dh, \tag{3.119}$$

we can write

$$p(\mathbf{h} \,|\, \mathbf{s})\, d^{\mathcal{N}} h = \mathcal{K}_1\, \bar{p}^{(0)}(h) \sin(\theta)^{\mathcal{N}-2}\, \exp\left[-\frac{1}{2}\left(s^2 + h^2 - 2sh\cos\theta\right)\right] dh\, d\theta, \tag{3.120}$$

where $\mathcal{K}_1$ is a constant. If we define the function $F_{\mathcal{N}}(x)$ by

$$F_{\mathcal{N}}(x) \equiv \frac{1}{2}\int_0^{\pi} d\theta\, \sin(\theta)^{\mathcal{N}-2}\, e^{x\cos\theta}, \tag{3.121}$$

then $\mathcal{K}_1$ is determined by the normalization condition

$$1 = 2\mathcal{K}_1 \int_0^{\infty} dh\, e^{-(s^2+h^2)/2}\, F_{\mathcal{N}}(sh)\, \bar{p}^{(0)}(h). \tag{3.122}$$

We next calculate the PDF $p[\mathbf{h} \,|\, \rho(\mathbf{s})]$ appearing in the denominator in Eq. (3.62). From Bayes's

theorem, this PDF is given by

$$p[\mathbf{h} \mid \rho(\mathbf{s})] = \mathcal{K}\, p^{(0)}(\mathbf{h})\, p[\rho(\mathbf{s}) \mid \mathbf{h}], \tag{3.123}$$

where $p[\rho(\mathbf{s}) \mid \mathbf{h}]$ is the PDF for $\rho(\mathbf{s})$ given that the gravitational wave signal is $\mathbf{h}$, and $\mathcal{K}$ is a normalization constant. Using the fact that $p(\mathbf{s} \mid \mathbf{h}) \propto \exp\left[-(\mathbf{s}-\mathbf{h})^2\right]$, we find using Eq. (3.119) that

$$p(\mathbf{s} \mid \mathbf{h})\, d^{\mathcal{N}} s = \frac{2^{1-\mathcal{N}/2}}{\sqrt{\pi}\Gamma\left[(\mathcal{N}-1)/2\right]} \sin(\theta)^{\mathcal{N}-2}\, s^{\mathcal{N}-1} \exp\left[-\frac{1}{2}\left(s^2 + h^2 - 2sh\cos\theta\right)\right] ds\, d\theta. \tag{3.124}$$

Integrating over θ now yields from Eq. (3.121)

$$p[\rho(\mathbf{s}) = s \mid \mathbf{h}]\, ds \;\propto\; s^{\mathcal{N}-1} e^{-(s^2+h^2)/2}\, F_{\mathcal{N}}(sh)\, ds. \tag{3.125}$$

Now combining Eqs. (3.119), (3.123), and (3.125) yields

$$p[\mathbf{h} \mid \rho(\mathbf{s})]\, d^{\mathcal{N}} h = \mathcal{K}_2\, \bar{p}^{(0)}(h)\; e^{-[\rho(\mathbf{s})^2+h^2]/2}\; F_{\mathcal{N}}[\rho(\mathbf{s})h]\; \sin(\theta)^{\mathcal{N}-2}\, dh\, d\theta, \tag{3.126}$$

where from Eq. (3.122) the normalization constant is given by

$$\mathcal{K}_2 = \frac{2\Gamma(\mathcal{N}/2)}{\sqrt{\pi}\Gamma[(\mathcal{N}-1)/2]}\, \mathcal{K}_1. \tag{3.127}$$

We can now calculate the information I_{total} by combining Eqs. (3.62), (3.120), (3.121), (3.126), and (3.127). The result is

$$I_{\text{total}}[\rho(\mathbf{s}), \mathcal{N}] = -\log_2\left[\frac{2\Gamma(\mathcal{N}/2)}{\sqrt{\pi}\Gamma[(\mathcal{N}-1)/2]}\right] - \int_0^\infty dh\, p^{(1)}(h)\, G_{\mathcal{N}}[\rho(\mathbf{s})h], \tag{3.128}$$

where

$$G_{\mathcal{N}}(x) \equiv \frac{x F'_{\mathcal{N}}(x)}{\ln 2\, F_{\mathcal{N}}(x)} - \log_2 F_{\mathcal{N}}(x), \tag{3.129}$$

and

$$p^{(1)}(h) \equiv 2\mathcal{K}_1\, \bar{p}^{(0)}(h)\; e^{-(\rho(\mathbf{s})^2+h^2)/2}\; F_{\mathcal{N}}[\rho(\mathbf{s})h]. \tag{3.130}$$

Equations (3.122), (3.121), and (3.128)–(3.130) now define explicitly the total information I_{total} as a function of the parameters $\rho(\mathbf{s})$ and $\mathcal{N}$ and of the prior PDF $\bar{p}^{(0)}(h)$.

Approximate formula for the total information

We now derive the approximate formula (3.68) for the total information. Let $\rho_b^2 = \rho(\mathbf{s})^2/\mathcal{N}$; we will consider the limit of large $\rho(\mathbf{s})$ and $\mathcal{N}$ but fixed ρ_b. Our analysis will divide into two cases, depending on whether $\rho_b > 1$ or $\rho_b \leq 1$. We first consider the case $\rho_b > 1$. In the large $\mathcal{N}$ limit the result for $\rho_b > 1$ will be independent of the prior PDF $\bar{p}^{(0)}(h)$, which we assume has no dependence on $\mathcal{N}$.

The first term in Eq. (3.128) is the expected value $\langle G_{\mathcal{N}}[\rho(\mathbf{s})h]\rangle$ of $G_{\mathcal{N}}[\rho(\mathbf{s})h]$ with respect to the PDF (3.130). If we change the variable of integration in this term from h to $u = h/\sqrt{\mathcal{N}}$, we find

$$\langle\, G_{\mathcal{N}}[\rho(\mathbf{s})h]\,\rangle \propto \int_0^\infty du\; \bar{p}^{(0)}(\sqrt{\mathcal{N}}u)\; e^{-\mathcal{N}(\rho_b^2+u^2)/2}\; F_{\mathcal{N}}(\mathcal{N}\rho_b u)\; G_{\mathcal{N}}(\mathcal{N}\rho_b u). \tag{3.131}$$

From Eq. (3.121) it is straightforward to show that in the limit of large $\mathcal{N}$,

$$F_{\mathcal{N}}(\mathcal{N}z) \approx \frac{1}{2} e^{\mathcal{N}q(\theta_c)} \sqrt{\frac{2\pi}{\mathcal{N}|q''(\theta_c)|}}, \tag{3.132}$$

for fixed z. Here $q(\theta)$ is the function

$$q(\theta) = z\cos\theta + \ln\sin\theta, \tag{3.133}$$

and $\theta_c = \theta_c(z)$ is the value of θ which maximizes the function $q(\theta)$, given implicitly by

$$z\sin^2\theta_c = \cos\theta_c. \tag{3.134}$$

We similarly find that

$$F'_{\mathcal{N}}(\mathcal{N}z) \approx \frac{1}{2} e^{\mathcal{N}q(\theta_c)} \sqrt{\frac{2\pi}{\mathcal{N}|q''(\theta_c)|}}\, \cos\theta_c. \tag{3.135}$$

It is legitimate to use the approximations (3.132) and (3.135) in the integral (3.131) since the value $u_{\max}(\mathcal{N}, \rho_b)$ of u at which the PDF $p^{(1)}(\mathcal{N}\rho_b u)$ is a maximum approaches at large $\mathcal{N}$ a constant $u_{\max}(\rho_b)$ which is independent of $\mathcal{N}$, as we show below.

Inserting the approximation (3.132) into Eq. (3.131) and identifying $z = \rho_b u$, we find that the PDF (3.130) is proportional to

$$\exp\left[\mathcal{N}\mathcal{Q}(u) + O(1)\right], \tag{3.136}$$

where

$$\mathcal{Q}(u) = -\frac{1}{2}(\rho_b^2 + u^2) + q(\theta_c) \tag{3.137}$$

and $\theta_c = \theta_c(z) = \theta_c(\rho_b u)$. From Eqs. (3.133) and (3.134) one finds that $\mathcal{Q}$ has a local maximum at

$$u = u_{\max} = \sqrt{\rho_b^2 - 1} \tag{3.138}$$

at which point θ_c is given by $\sin\theta_c = 1/\rho_b$. The form of the PDF (3.136) now shows that at large $\mathcal{N}$,

$$\langle G_{\mathcal{N}}(\mathcal{N}\rho_b u)\rangle \approx\ G_{\mathcal{N}}(\mathcal{N}\rho_b u_{\max}). \tag{3.139}$$

Finally, if we combine Eqs. (3.128), (3.132)–(3.135), (3.138) and (3.139) and use Stirling's formula to approximate the Gamma functions, we obtain Eq. (3.63).

Turn, next, to the case $\rho_b < 1$. In this case the function $\mathcal{Q}$ does not have a local maximum, and the dominant contribution to the integral (3.131) at large $\mathcal{N}$ comes from $h \sim O(1)$ (rather than from $h \sim \sqrt{\mathcal{N}}$, $u \sim O(1)$ as was the case above). From Eq. (3.121) we obtain the approximations

$$F_{\mathcal{N}}(\sqrt{\mathcal{N}}w) = \sqrt{\frac{\pi}{2\mathcal{N}}}\, e^{w^2/2}\, \left[1 + O(1/\sqrt{\mathcal{N}})\right] \tag{3.140}$$

and

$$F'_{\mathcal{N}}(\sqrt{\mathcal{N}}w) = \sqrt{\frac{\pi}{2}}\, \frac{w}{\mathcal{N}}\, e^{w^2/2}\, \left[1 + O(1/\sqrt{\mathcal{N}})\right], \tag{3.141}$$

which are valid for fixed w at large $\mathcal{N}$. Using Eqs. (3.140), (3.141), and (3.128) – (3.130), and using Stirling's formula again we find that

$$I_{\text{total}} \approx \frac{1}{2}\rho_b^2\, \frac{\int_0^\infty dh\, \bar{p}^{(0)}(h)\, \exp\left[-(1-\rho_b^2)h^2/2\right]\, h^2}{\int_0^\infty dh\, \bar{p}^{(0)}(h)\, \exp\left[-(1-\rho_b^2)h^2/2\right]}. \tag{3.142}$$

For simplicity we now take $\bar{p}^{(0)}(h)$ to be a Gaussian centered at zero with width h^2_{prior}; this yields

$$I_{\text{total}} \approx \frac{1}{2}\left[\frac{\rho_b^2 h^2_{\text{prior}}}{1 + (1-\rho_b^2)h^2_{\text{prior}}}\right]. \tag{3.143}$$

From Eq. (3.67), the parameter ρ_b is given by

$$\rho_b^2 = 1 + \frac{\rho^2}{\mathcal{N}_{\text{bins}}} \pm \frac{1}{\sqrt{\mathcal{N}_{\text{bins}}}}, \tag{3.144}$$

where the last term denotes the rms magnitude of the statistical fluctuations. Since we are assuming that $\rho_b < 1$, it follows that $\rho_b^2 \approx 1 - 1/\sqrt{\mathcal{N}_{\rm bins}}$, and therefore we obtain from Eq. (3.143)

$$I_{\rm total} \approx \frac{1}{2}\min\left[h_{\rm prior}^2, \sqrt{\mathcal{N}_{\rm bins}}\right]. \tag{3.145}$$

Thus, if $h_{\rm prior} \lesssim 1$, the total information gain is $\lesssim 1$ also.

Approximate formula for the source information

We now turn to a discussion of the approximate formula (3.72) for the information (3.71) obtained about the source of the gravitational waves. In general, the measure of information (3.71) depends in a complex way on the prior PDF $p^{(0)}(\mathbf{h})$, and on how the waveform $\mathbf{h}(\boldsymbol{\theta})$ depends on the source parameters $\boldsymbol{\theta}$. We can evaluate the information $I_{\rm source}$ explicitly in the simple and unrealistic model where the dependence on the source parameters $\boldsymbol{\theta}$ is linear and where there is little prior information. In this case the manifold of possible signals is a linear subspace (with dimension $\mathcal{N}_{\rm param}$) of the linear space of all possible signals (which has dimension $\mathcal{N}$). The integral (3.71) then reduces to an integral analogous to (3.62), and we obtain the formula (3.72) in the same way as we obtained Eq. (3.68). The result (3.72) is clearly a very crude approximation, as the true manifold of merger signals is very curved and nonlinear. Nevertheless, it seems likely that the formula (3.72) will be valid for some effective number of parameters $\mathcal{N}_{\rm param}$ that is not too much different from the true number of parameters on which the waveform depends.

Bibliography

[1] A. Abramovici, W. E. Althouse, R. W. P. Drever, Y. Gürsel, S. Kawamura, F. J. Raab, D. Shoemaker, L. Sievers, R. E. Spero, K. S. Thorne, R. E. Vogt, R. Weiss, S. E. Whitcomb, and M. E. Zucker, *LIGO: The Laser Interferometer Gravitational-wave Observatory*, Science **256**, 325 (1992).

[2] C. Bradaschia *et al.*, Nucl. Instrum. & Methods **A289**, 518 (1990); also in *Gravitation: a Banff Summer Institute*, edited by R. Mann and P. Wesson (World Scientific, Singapore, 1991).

[3] J. Hough *et. al*, "GEO600, Proposal for a 600 m Laser-Interferometric Gravitational Wave Antenna", 1994 (unpublished).

[4] P. Bender *et al.*, "LISA, Laser interferometer space antenna for gravitational wave measurements: ESA assessment Study Report," 1994.

[5] J. Hough *et al.*, in *Gravitational Wave Experiments*, proceedings of the Edoardo Amaldi Conference, edited by E. Coccio, G. Pizzella, and F. Ronga (World Scientific, Singapore, 1995), p. 50.

[6] P. Bender, I. Ciufolini, K. Danzmann, W. Folkner, J. Hough, D. Robertson, A. Rüdiger, M. Sandford, R. Schilling, B. Schutz, R. Stebbins, T. Summer, P. Touboul, S. Vitale, H. Ward, and W. Winkler, "LISA: Laser Interferometer Space Antenna for the detection and observation of gravitational waves", pre-phase A report, 1995 (unpublished).

[7] É. É. Flanagan and S. A. Hughes, Phys. Rev. D **57**, 4535 (1998).

[8] L. E. Kidder, C. M. Will, and A. G. Wiseman, Phys. Rev. D **47**, 3281 (1993); Class. Quant. Grav. **9**, L125 (1992).

[9] G. B. Cook, Phys. Rev. D **50**, 5025 (1994). See especially Fig. 3.

[10] For the purpose of this paper, we consider the "intermediate binary black hole regime" $6M \lesssim r \lesssim 12M$ discussed in Ref. [7] to be part of the inspiral epoch.

[11] More information regarding the binary black hole Grand Challenge Alliance can be found at `http://www.npac.syr.edu/projects/bh/`; see also Ref. [12] for a review.

[12] L. S. Finn, in proceedings of GR 14, gr-qc/9603004.

[13] É. E. Flanagan and C. Cutler, Phys. Rev. D **49**, 2658 (1994).

[14] K. D. Kokkotas, A. Królak, and G. Tsegas, Class. Quant. Grav. **11**, 1901 (1994); P. Jaranowski, K. D. Kokkotas, A. Królak, and G. Tsegas, Class. Quant. Grav. **13**, 1279 (1996).

[15] E. Poisson and C. M. Will, Phys. Rev. D **52**, 848 (1995).

[16] L. S. Finn, Phys. Rev. D **46**, 5236 (1992). See also Ref. [40], which is an addendum to Ref. [17] that shows that the methods used to calculate measurement errors in Refs. [17] and [16] are equivalent.

[17] F. Echeverria, Phys. Rev. D **40**, 3194 (1988).

[18] For quantitative analyses of parameter extraction accuracies with LISA see C. Cutler, gr-qc/9703068 [Phys. Rev. D, in press]; M. Peterseim, O. Jennrich, K. Danzmann, *et al.*, Class. Quant. Grav. **14**, 1507 (1997); O. Jennrich, M. Peterseim, K. Danzmann, *et al.*, Class. Quant. Grav. **14**, 1525 (1997).

[19] The accuracy with which the various waveform parameters will be measurable is currently known only to factors of order 2. Statistical errors in maximum likelihood estimators have been calculated in the high SNR approximation [28, 13, 14, 15], and more accurately using Monte-Carlo simulations [39]. However, ultimately one should use estimators (for example Bayes estimators) which perform better than maximum likelihood estimators [13, 54, 55, 56]. In addition, all analyses to date have neglected waveform modulation due to the spin-induced precession of the orbital plane, an effect which will be important for BBHs with rapidly spinning BHs [60, 61]. Thus the true parameter-measurement accuracies are still somewhat uncertain.

[20] The fraction of events with ringdown SNR greater than some threshold $\rho_{\rm ring}$ is approximately $\rho_{\rm insp}^3/(\alpha\,\rho_{\rm ring})^3$, where $\rho_{\rm insp}$ is the detection threshold for inspiral SNRs, and α is the ratio between the actual inspiral and ringdown SNRs. This assumes that all events are detected via their inspiral signals and thus have inspiral SNRs larger than $\rho_{\rm insp}$. Equations (B4), (B5), (B16) and (B17) of Ref. [7] imply that $\alpha \sim 30$ for initial and advanced LIGO interferometers for $M \lesssim 50\,M_\odot$. Taking $\rho_{\rm ring} = 1$ and using the typically discussed inspiral SNR threshold of $\rho_{\rm insp} = 6$ [33], one obtains that the fraction is about 1%.

[21] C. M. Will, Phys. Rev. D **50**, 6058 (1994); see also Ref. [14].

[22] T. Damour and G. Esposito-Farese, Phys. Rev. Lett. **70**, 2220 (1993); T. Damour and K. Nordtvedt, Phys. Rev. D **48**, 3436 (1993).

[23] J. Bekenstein, to appear in the proceedings of the Second Sakharov Conference in Physics, gr-qc/9605059.

[24] We discuss only Wiener optimal filtering, but note that there are more sophisticated nonlinear filtering methods [13, 54, 55, 56] that could be used to give better results for parameter measurements (see Ref. [19]). The use of such methods would be more computationally intensive than linear filtering, but on the other hand, vast amounts of supercomputer time would have already been expended to generate merger templates.

[25] Y. Gürsel and M. Tinto, Phys. Rev. D **40**, 3884 (1989).

[26] L. Brillouin, *A Physical Theory of Information* (IBM Watson Laboratories, New York, 1952).

[27] T. M. Cover and J. A. Thomas, *Elements of Information Theory* (Wiley, New York, 1991).

[28] L. S. Finn and D. F. Chernoff, Phys. Rev. D **47**, 2198 (1993).

[29] Our convention for the normalization of the spectral noise density $S_h(f)$ is such that

$$\langle n(t)^2 \rangle = \int_0^\infty S_h(f)\, df.$$

[30] S. V. Dhurandhar and B. F. Schutz, Phys. Rev. D **50**, 2390 (1994).

[31] Strictly speaking this is not a real basis, but a real basis could be obtained to by taking $\mathbf{d}_0$ and the real and imaginary parts of $\mathbf{d}_k$ for $k > 0$.

[32] When a complete set of theoretical templates is available so that matched filtering can be carried out, reconstructing the "best-fit" waveform is of course trivial: it is just the template which maximizes the signal to noise ratio.

[33] C. Cutler, T. A. Apostolatos, L. Bildsten, L. S. Finn, É. É. Flanagan, D. Kennefick, D. M. Marković, A. Ori, E. Poisson, G. J. Sussman, and K. S. Thorne, Phys. Rev. Lett. **70**, 2984 (1993).

[34] K. S. Thorne, in *300 Years of Gravitation*, edited by S. W. Hawking and W. Israel (Cambridge University Press, Cambridge, 1987), pp. 330–458.

[35] Contrary to one's intuition, the value (3.35) for advanced interferometers is lower than the value (3.34) for initial interferometers. This is because the advanced interferometers can detect inspirals with lower band-pass filtering SNRs than the initial interferometers, due to the larger number of cycles of the inspiral signal in the advanced interferometer's bandwidth.

[36] L. A. Wainstein and V. D . Zubakov, *Extraction of Signals from Noise*, (Prentice-Hall, Englewood Cliffs, NJ, 1962).

[37] C. W. Helstrom, *Statistical Theory of Signal Detection*, (Pergamon, Oxford, 1968).

[38] P. Jaranowski and A. Krolak, Phys. Rev. D **49**, 1723 (1994); P. Jaranowski, K. D. Kokkotas, A. Krolak, G. Tsegas, Class. Quant. Grav. **13**, 1279 (1996).

[39] R. Balasubramanian, B. S. Sathyaprakash, S. V. Dhurandhar, Phys. Rev. D **53** 3033 (1996); **54** 1860 (1996); R. Balasubramanian, S. V. Dhurandhar, *ibid* **57**, 3408; C. Cutler, unpublished.

[40] F. Echeverria, unpublished PhD thesis, California Institute of Technology, addendum to Ch. 2 (1993).

[41] For example, one can first truncate the signal in the time domain, then perform a finite Fourier transform, and then throw away the Fourier coefficients outside the frequency range of interest. Or, one can first band-pass filter the data stream, and then truncate in the time domain.

[42] É. É. Flanagan, in preparation.

[43] D. Lai and A. G. Wiseman, Phys. Rev. D **54**, 3958 (1996).

[44] A. Ori and K. S. Thorne, in preparation.

[45] B. J. Owen, Phys. Rev. D **53**, 6749 (1996).

[46] In fact, for detection purposes, the criterion (3.54) is a little more stringent than need be: When one attempts to detect the signal, one computes the maximum overlap between the data stream and all possible templates, and thus the relevant quantity to calculate is [45]

$$\max_{\Delta\boldsymbol{\theta}} \frac{(\mathbf{h}(\boldsymbol{\theta}) \,|\, \mathbf{h}_T(\boldsymbol{\theta}+\Delta\boldsymbol{\theta}))}{\sqrt{(\mathbf{h}_T(\boldsymbol{\theta}+\Delta\boldsymbol{\theta}) \,|\, \mathbf{h}_T(\boldsymbol{\theta}+\Delta\boldsymbol{\theta}))}},$$

which is larger than

$$\frac{(\mathbf{h}(\boldsymbol{\theta}) \,|\, \mathbf{h}_T(\boldsymbol{\theta}))}{\sqrt{(\mathbf{h}_T(\boldsymbol{\theta}) \,|\, \mathbf{h}_T(\boldsymbol{\theta}))}}.$$

However, we neglect this effect here as it is not possible to calculate it in the absence of a model waveform $\mathbf{h}(\boldsymbol{\theta})$ for merger waves. For inspiral waves, relatively crude templates will suffice to detect the waves, and more accurate templates will be needed to measure parameters.

[47] Criterion (3.60) is probably rather more stringent than need be: the left hand side of Eq. (3.59) is likely smaller than the right hand side by a factor $\sim \sqrt{n_p/\mathcal{N}_{\rm bins}}$, where n_p is the number of parameters and $\mathcal{N}_{\rm bins}$ is the dimension of the total space of signals V.

[48] No significant changes would result from changing the requirement "have the same magnitude as the measured signal" to "have a magnitude which is smaller than or equal to that of the measured signal"; the numerical value of the information would be about the same. The reason we insert this requirement into our definition of information [so that we use the PDF $p[\mathbf{h} \mid \rho(\mathbf{s})]$ in Eq. (3.62) rather than the PDF $p^{(0)}(\mathbf{h})$] is that the resulting notion of information is more useful and relevant than the notion obtained from using $p^{(0)}(\mathbf{h})$. If one were to use the PDF $p^{(0)}$, the resulting "information gain in the measurement" would be the same for all detected signals, whether the SNR be 10 or 1000.

[49] The PDF $p^{(0)}(\mathbf{h})$ describes all one's prior information about the signal $\mathbf{h}$, except for the information that the maximum expected duration is T and that the maximum expected bandwidth is Δf; that information is already encoded in the choice of the space V.

[50] Note that the regime $\rho \gg \mathcal{N}_{\text{bins}}^{1/4}$ coincides with the regime in which the signal is detectable using the noise-monitoring search method discussed in Refs. [7, 42].

[51] L. S. Finn, in preparation.

[52] Note that in Appendix A of Ref. [13], this quantity was denoted $\mathbf{s}(t)$ rather than $\vec{s}(t)$. Here we use the alternative notation $\vec{s}(t)$ since the notation $\mathbf{s}$ has already been used in Sec. 3.4 to denote the vector (3.6).

[53] The effective site noise $S_\alpha^{(\text{eff})}(f)$ is also the relevant quantity which governs the sensitivity of a given site to stochastic gravitational waves; see Eq. (3.13) of É. É. Flanagan, Phys. Rev. D **48**, 2389 (1993).

[54] B. F. Schutz, in *The Detection of Gravitational Radiation*, edited byD. Blair, (Cambridge University Press, Cambridge, England, 1989).

[55] M. H. A. Davis, in *Gravitational Wave Data Analysis*, edited by B. F. Schutz, (Kluwer Academic, Boston, 1989).

[56] D. Nicholson and A. Vecchio, Phys. Rev. D **57**, 4588 (1997).

[57] See Eqs. (4.17)–(4.22) and Appendix C of Ref. [25].

[58] In fact, this result is independent of the specific choice (3.114) of norm on the space of waveform pairs $\{h_+(t), h_\times(t)\}$.

[59] In Eqs. (3.117), (3.119), (3.120), (3.124), and (3.126) we omit factors of $\mathcal{N} - 2$ dimensional solid angle elements $d\Omega^{\mathcal{N}-2}/C_{\mathcal{N}-2}$ which integrate to one. Thus, the equals symbol in these

equations should be interpreted to mean that the PDFs on the LHS and RHS will produce identical expected values of functions that depend on θ and h only.

[60] T. A. Apostolatos, C. Cutler, G. J. Sussman, and K. S. Thorne, Phys. Rev. D **49**, 6274 (1994).

[61] L. E. Kidder, Phys. Rev. D **52**, 821 (1995).

Chapter 4

Detector networks for measuring the final merger of binary neutron star coalescence in gravitational waves

To be submitted to *Physical Review D*.

Abstract

The final merger of binary neutron star systems will produce gravitational waves that are sensitive to neutron star structure. Observations of this final merger by gravitational-wave observatories have the potential to teach us about details of this structure, such as the equation of state of dense matter. Such observations will probably only be possible using a combination of broad-band detectors, such as LIGO and VIRGO, and narrow-band detectors, such as resonant spherical antennae or dual-recycled laser interferometers. In this chapter, I present an algorithm for configuring a network of gravitational-wave detectors, which, in accordance with one's prior information, will optimally measure gravitational waves associated with the final merger. Application of this algorithm to simple models of the binary neutron star coalescence waveform indicates that gravitational-wave observations may be able to provide high quality measurements of the merger when laser interferometers have reached "advanced" sensitivity levels. Even in this era, however, such measurement is likely to be an arduous task, requiring measurements of a large number of events using several narrow-band detectors in concert with broad-band detectors in order to understand gross details of the merger.

4.1 Introduction

4.1.1 Overview and motivation

Construction of the LIGO gravitational-wave observatories is well underway; the first science run is planned for the year 2002 [1]. European and Japanese interferometers, such as VIRGO[2], GEO600 [3], and TAMA [4] are also under construction and should begin operation in roughly the same time

frame; and an Australian consortium, ACIGA [5] offers the promise of a long-baseline interferometer in the Southern hemisphere in the next decade. One astrophysical source to which such observatories should be very sensitive is the coalescence of binary neutron star (NS-NS) systems. LIGO and VIRGO are well designed to measure the slow, adiabatic "inspiral" of such systems [6], in which the orbit slowly decays due to gravitational radiation reaction. Theory and observations suggest that such systems should coalesce at the rate of about several $\times 10^{-4}$–10^{-5} year^{-1}Galaxy^{-1} [7]. If these estimates of the coalescence rate are correct, gravitational-wave observatories may be able to make measurements of about 100 NS-NS coalescences per year when their sensitivities reach "advanced" levels [8] circa 2010.

The self-gravity of neutron stars is so strong that the stars are hardly deformed during the inspiral (*i.e.*, while the frequency f of emitted gravitational radiation is $\lesssim$ 1 kHz). Thus, details of neutron star structure are mostly irrelevant to the radiation emitted in this frequency band. The inspiral waveform instead depends on just a few "clean" parameters: the masses and spins of the two neutron stars, and orbital elements of the binary (such as its eccentricity and the angles between the orbital and spin angular momentum vectors). Measuring the inspiral waveform thus measures these parameters, in some cases to phenomenal accuracy. For example, one particular combination of the masses, the "chirp mass," $\mathcal{M} = (m_1 m_2)^{3/5}/(m_1 + m_2)^{1/5}$, can be measured to a fractional accuracy of about 0.1% or better; see, *e.g.*, [9] for a recent discussion of parameter measurement accuracy with neutron star inspiral measurements.

During the inspiral, the gravitational-wave frequency monotonically "chirps" upwards as the stars spiral together. Eventually, when the frequencies are $\sim$ 1 kHz, the neutron stars have spiraled so close together that they exhibit significant deformations, and may in fact come into contact with each other. The waveform at these frequencies depends on the sizes of the stars, their equation of state, and the hydrodynamic details of the merger. A measurement of this "merger" waveform has the potential to teach us about the relationship of neutron star mass to radius, the equation of state of dense nuclear matter [10], and hydrodynamic processes that may occur during the merger, such as the formation of a bar of dense matter, or the formation of a black hole.

At the frequencies near 1 kHz where the gravitational waveform depends on neutron star structure, the sensitivity of broad-band detectors such as LIGO and VIRGO is badly degraded by photon shot noise — the rms strain noise in this frequency band scales with frequency as $f^{3/2}$. Near 1 kHz, the characteristic gravitational-wave strain of a NS-NS system 200 Mpc from the earth is of order (a few) $\times 10^{-22}$, whereas the characteristic noise strain is of order 10^{-21}. At first sight, one might

think that there is little hope of being able to learn about the NS-NS merger using gravitational-wave measurements. However, it may be possible to do better by combining broad-band detectors with narrow-band detectors. Narrow-band detectors have very good sensitivity in some narrow bandwidth — for example, a "dual-recycled" laser interferometer (discussed in greater detail below) has a strain sensitivity of about 10^{-23} in a band of roughly 1 Hz near 1000 Hz. The issue of combining a broad-band interferometer with a "xylophone" of several narrow-band detectors has been discussed generally in [20, 21], and discussed with a particular focus on measuring NS-NS merger in [11, 12]. These last two papers point out that the energy spectrum of emitted gravitational waves is likely to fall off very sharply as neutron stars merge. A xylophone of narrow-band detectors is thus well-suited for determining the frequency at which the sharp fall off occurs: detectors in the xylophone at frequencies below the fall-off will "ring," whereas those above will be silent.

There are several efforts underway geared towards producing gravitational-wave detectors with good sensitivity in a narrow band at high frequencies. One approach uses resonant masses detectors. Bar detectors, similar to those used for several decades in searches for gravitational waves, are currently operational in the United States, Italy, and Australia [13]. Future resonant masses might be constructed with a spherical geometry, which yields very good sensitivity to both wave polarizations over the entire sky. Spherical detector projects are planned in the United States, Europe, and Brazil [14]. Other well-analyzed narrow-band detectors are based on laser interferometry. Two such designs are dual-recycled interferometers, discussed at length in [15, 17, 18], and resonant sideband extraction, discussed in [19]. Conceptually, these two schemes are quite similar. The experimenter introduces a mirror on the output port of the interferometer which reflects signal sidebands back into the interferometer. This reflected signal resonates between the two arms and builds up at some chosen frequency f_{GW}. This frequency can be tuned by adjusting the position of this signal recycling mirror. The interferometer thus resonates with a particular monochromatic gravitational-wave signal. It then has very good noise performance in some narrow band near f_{GW}, but it has very poor performance outside this band. See [15, 17, 18, 19] for extended discussion of these techniques.

It seems likely that viable techniques will exist for achieving good narrow-band sensitivity to gravitational waves, especially by the time that broad-band detectors reach advanced sensitivity levels. The ideal detector network for measuring neutron star coalescence is likely to be a combination of broad-band and narrow-band detectors: the broad-band detectors will be able to measure the inspiral with very good accuracy, and a "xylophone" of narrow-band detectors will be able to measure and provide information about the final merger waveform.

4.1.2 Approach of this chapter

The question of interest then becomes: What is the optimal detector network configuration for measuring the merger? Given that little is likely to be known about the merger, prior to measurement, one would like the detector network to provide as much information about the merger waveform as possible, especially since the number of narrow-band detectors is likely to be limited by expense and other practical considerations. (For example, narrow-band laser interferometers will need to operate within the same vacuum system as the broad-band interferometers — the amount of space available will limit the number of detectors that can be run simultaneously.)

Put the question another way: suppose that the NS-NS coalescence waveform depends crucially on some parameter λ. For example, λ might represent the frequency at which the energy carried off by gravitational waves falls by several orders of magnitude; or, it could represent the frequency at which a bar (formed in the hydrodynamic detritus of the final merger) strongly radiates for several cycles. The optimal network would then be the combination of broad-band and narrow-band detectors that measures λ with as little error as possible.

In this chapter, I present an algorithm for designing such a detector network. The approach is based on probability distributions, which in turn are based on the Bayesian/maximum likelihood approach advocated by Finn [24]. Three probability distributions play a crucial role in this analysis. The first is the *posterior* distribution, $P_{\rm post}$. This quantity is the probability distribution for a parameter λ after a measurement has been made. In [24], Finn shows how to calculate $P_{\rm post}$; it turns out to depend on the parameter value $\hat{\lambda}$ that is actually present in the data, the signal-to-noise ratio (SNR), and the *prior* probability distribution, p_0. The prior probability (which is the second important distribution that will be used in this chapter) encapsulates all that is known about λ's distribution prior to measurement. Because the posterior distribution depends upon $\hat{\lambda}$, it will be denoted $P_{\rm post}(\lambda|\hat{\lambda})$. From it, one can compute the quantities

$$\begin{aligned} \bar{\lambda}_{\rm post} &= \int \lambda P_{\rm post}(\lambda|\hat{\lambda})\, d\lambda, \\ \sigma^2_{\rm post} &= \int (\lambda - \bar{\lambda}_{\rm post})^2 P_{\rm post}(\lambda|\hat{\lambda})\, d\lambda. \end{aligned} \tag{4.1}$$

The mean $\bar{\lambda}_{\rm post}$ is the value of λ we would expect to find if it were possible to repeat the NS-NS merger measurement many times; $\sigma_{\rm post}$ is indicative of the error that one expects in any measurement. Typically, the measured value of λ will be within $\sigma_{\rm post}$ of $\bar{\lambda}_{\rm post}$.

The quantities $P_{\rm post}(\lambda|\hat{\lambda})$, $\bar{\lambda}$, and $\sigma_{\rm post}$ are very useful quantities for assessing measurement quality *after* measurement. For my purposes, however, this is not sufficient. What is needed is a quantity that can be used to anticipate — *given our best prior knowledge of the signal* — the quality with which the signal parameters *will be* measured. By treating the characteristics of the noise as variational parameters, one can then minimize the anticipated error. This is effectively an algorithm for designing an "optimal" detector network — "optimal" in the sense that the network it designs minimizes this anticipated measurement error.

To this end, I introduce the third distribution that is used in this chapter: the *anticipated* probability distribution for λ. This distribution gives the best-guess of the posterior distribution for a particular measurement, modulo our ignorance regarding the value of $\hat{\lambda}$. It is constructed by integrating out the $\hat{\lambda}$ dependence, weighting the integral according to our prejudices regarding $\hat{\lambda}$'s likely value. More precisely,

$$P_{\rm ant}(\lambda) = \int P_{\rm post}(\lambda|\hat{\lambda}) p_0(\hat{\lambda})\, d\hat{\lambda}. \tag{4.2}$$

Analogous to the posterior mean and variance (4.1) are the anticipated mean and variance:

$$\begin{aligned} \bar{\lambda}_{\rm ant} &= \int \lambda P_{\rm ant}(\lambda)\, d\lambda, \\ \sigma^2_{\rm ant} &= \int (\lambda - \bar{\lambda}_{\rm ant})^2 P_{\rm ant}(\lambda)\, d\lambda. \end{aligned} \tag{4.3}$$

By minimizing $\sigma^2_{\rm ant}$ with respect to the network's noise characteristics, one obtains the optimal network — the network that, given our prior knowledge of λ's distribution, measures λ most accurately:

$$\nabla_{(\text{noise parameters})} \sigma^2_{\rm ant} = 0 \longmapsto \text{The optimal detector network.} \tag{4.4}$$

Note that, since $P_{\rm post}$ depends upon SNR, the anticipated probability distribution — and hence the choice of optimal detector network — depends upon SNR. This would appear to be a weakness of this algorithm: the network design depends upon the anticipated SNR. However, I would argue that it is favorable to leave the anticipated SNR in the algorithm as an adjustable parameter, for the following reasons. First, to properly eliminate SNR as a parameter, it would have to be integrated out using a correctly constructed probability density for its distribution. Although there currently are estimates of the NS-NS coalescence rate upon which one could construct such a distribution, these estimates are uncertain by at least an order of magnitude. Thus, it is probably not useful to integrate out the SNR dependence, at least not now. Second, by the time that observatories like LIGO reach

advanced sensitivity levels, they may be detecting a large number of NS-NS coalescences every year. If this is the case, observers may choose to look for the merger in only the strongest signals — those signals are most likely to provide information about the details of the merger. On the other hand, if our current best estimates of NS-NS coalescence are overly optimistic, there may only be a few events per year, even when advanced sensitivities are reached. Observers will not have the luxury of using only strong signals, and will need to analyze weak signals as much as possible. Thus, I leave the SNR as a free parameter in order that the detector network design algorithm can be tailored to the SNR levels that turn out to be appropriate.

To test this algorithm, I apply it to two models of the NS-NS coalescence waveform. The first is a simple toy model in which the emitted gravitational waves are abruptly cut-off at some frequency. The spectrum of such waves is rather sharp — the cut-off frequency is a very clear, well-defined signature of the merger. I find that detector networks designed with the algorithm presented here can measure the characteristics of this toy model rather well. A sequence of measurements converges fairly quickly to a distribution for λ that is well-peaked about the true value $\hat{\lambda}$. To further test the algorithm, I next apply it to a model of the coalescence that has much more interesting structure. Zhuge, Centrella, and McMillan (ZCM) modeled NS-NS coalescence using smooth-particle hydrodynamics with Newtonian gravity and a polytropic equation of state. The merger waveforms they produced exhibit several interesting features, corresponding to various hydrodynamical processes they observe in their simulations. I find that detector networks in this case cannot measure merger characteristics nearly as easily as in the toy case. Many iterations are required in order to discriminate among the various features of the waveform. Thus, I conclude that the effectiveness of networks for measuring NS-NS merger waves will depend quite strongly on the details of those waves. Robust theoretical modeling will have a strong influence on network design.

The remainder of this chapter is organized as follows. In Sec. 4.2, I present the formal details of the algorithm for designing the optimal detector network. Specifically, in Sec. 4.2.1, I calculate the probability distributions that are used, and then in Sec. 4.2.2 show how to use these distributions to design the optimal detector network. In Sec. 4.3, I briefly review and summarize the properties and sensitivities of the gravitational-wave detectors that are likely to constitute future detector networks. In Sec. 4.4, I apply the network design algorithm to the toy model described above; I apply the algorithm to the numerical waveforms of ZCM in Sec. 4.5. I present my conclusions and summarize the chapter Sec. 3.8.

4.2 Formalism

In this section, I present the formalism used to study measurement of NS-NS merger gravitational waves. My goal is to make the formalism as independent as possible of any assumptions about the details of the waveform. I assume only that there is some parameter λ that characterizes an important feature of the merger. Details of NS-NS merger waves (which at present are poorly understood) doubtless cannot be boiled down to a single parameter; on the other hand, it is probably realistic to assume that gravitational-wave measurements will only be able to determine simple, gross characteristics of the waveform. Sec. 4.2.1 develops the anticipated probability distribution for measuring a particular value of λ, assuming that a NS-NS inspiral has been measured. Among other factors, this probability distribution will depend on the noise characteristics of the detector network, and the prior probability distribution $p_0(\lambda)$.

As outlined in the Introduction, the probability distribution derived in Sec. 4.2.1 can be used to estimate the accuracy with which λ can be measured. By minimizing the anticipated errors in λ, one can design a detector network that measures λ as accurately as possible given what is known about λ's distribution prior to measurement. I outline how to perform such a minimization, and thus how to construct the optimal detector network in Sec. 4.2.2.

4.2.1 Anticipated probability distribution for λ

Consider a network of N gravitational wave detectors, split into $N_{\rm BB}$ broad-band instruments, such as LIGO and VIRGO, and $N_{\rm NB}$ narrow-band instruments. I use the notation of Appendix A of [26]. In particular, $\vec{g}(t)$ represents the (time-domain) output of the network; its component $g_j(t)$ is the output of the jth detector. I assume that $\vec{g}$ is known to contain some signal $\vec{h}_{\hat{\lambda}}(t)$, with unknown parameterization $\hat{\lambda}$ — a NS-NS inspiral has been detected in the data stream, so merger waves must be present in the data as well. The data stream can therefore be written $\vec{g}(t) = \vec{n}(t) + \vec{h}_{\hat{\lambda}}(t)$, where $\vec{n}(t)$ is the network's noise.

The goal now is to determine the probability that the waveform $\vec{h}_\lambda(t)$ is measured, given that the data stream is $\vec{g}(t)$. Using the terminology given in the Introduction, this is the posterior probability for $\vec{h}_\lambda(t)$ — the probability that $\vec{h}_\lambda(t)$ is present after measurement. The formalism for calculating such a probability in the case of one detector is given by Finn [24]. In a forthcoming series of papers [29], Finn will develop the multidetector Bayesian formalism in great detail. In this chapter, I rely on the less complete analysis of Ref. [26], which is adequate for my purposes.

Bayes' law states that

$$P(\vec{h}_\lambda|\vec{g}) = \frac{P(\vec{g}|\vec{h}_\lambda)P(\vec{h}_\lambda)}{P(\vec{g})}. \tag{4.5}$$

The probabilities written here have the same meaning as those used in Eq. (2.3) of [24]:

$$\begin{aligned}
P(\vec{h}_\lambda|\vec{g}) &\equiv \text{the conditional probability that the waveform } \vec{h}_\lambda \text{ is present given that} \\
&\quad \text{the data stream } \vec{g} \text{ is present;} \\
P(\vec{g}|\vec{h}_\lambda) &\equiv \text{the probability of measuring the data stream } \vec{g} \text{ given the waveform } \vec{h}_\lambda; \\
P(\vec{h}_\lambda) &\equiv \text{the } \textit{a priori} \text{ probability that the waveform } \vec{h}_\lambda \text{ is present} \\
&= p_0(\vec{h}_\lambda); \\
P(\vec{g}) &\equiv \text{the probability that the data stream } \vec{g} \text{ is observed.}
\end{aligned} \tag{4.6}$$

In this analysis, I will assume that, since $\vec{g}$ has already been measured and it is known that some signal is present, $\vec{g}$ is a fixed, determined quantity, and thus $P(\vec{g}) = 1$. This is rather different from the form that Finn uses in [24], stemming from the fact that the question addressed here is different from those Finn addresses. Finn does *not* assume that the data stream has already been measured — his $\vec{g}$ is *undetermined*, and has a non-trivial probability distribution.

However, the probability distribution $P(\vec{g}|\vec{h}_\lambda)$ used here is identical to that used by Finn. This is because $P(\vec{g}|\vec{h}_\lambda)$ answers the question "What is the probability that the data stream $\vec{g}$ is consistent with the gravitational wave $\vec{h}_\lambda$ being present?" Or, put another way, $P(\vec{g}|\vec{h}_\lambda)$ answers the question "What is the probability that, if the gravitational wave is assumed to be $\vec{h}_\lambda$, a noise $\vec{n}$ is present such that the sum $\vec{n} + \vec{h}_\lambda$ is consistent with the observed data stream $\vec{g}$?" From this second question, it is clear that $P(\vec{g}|\vec{h}_\lambda)$ is equivalent to $P(\vec{g} - \vec{h}_\lambda|0)$ — the probability that $\vec{g} - \vec{h}_\lambda$ is pure noise. This probability can be taken almost verbatim from Finn (with modifications as in [26, 29] to account for multiple detectors):

$$P(\vec{g}|\vec{h}_\lambda) = \mathcal{K} \exp\left[-\frac{1}{2}(\vec{g} - \vec{h}_\lambda|\vec{g} - \vec{h}_\lambda)\right]. \tag{4.7}$$

The inner product is given by

$$(\vec{a}|\vec{b}) \equiv 4\,\mathrm{Re} \int_0^\infty \tilde{a}_j(f)^* \left[\mathbf{S}_h(f)^{-1}\right]^{jk} \tilde{b}_k(f)\, df, \tag{4.8}$$

and $\mathcal{K}$ is a normalization constant. Here, $\tilde{a}_j(f)$ is the Fourier transform of $a_j(t)$:

$$\tilde{a}_j(f) = \int_{-\infty}^{\infty} a_j(t) e^{2\pi i f t}\, dt. \tag{4.9}$$

The asterisk denotes complex conjugation. The matrix $\mathbf{S}_h(f)$ is a generalization of the (one-sided) strain noise spectral density. Diagonal components $S_h(f)_{jj}$ represent the usual spectral density for detector j; off-diagonal elements $S_h(f)_{jk}$ represent correlations between detectors j and k. Repeated indices with one up, one down are to be summed. For more details, see Appendix A of [26]. Combining these distributions yields

$$P(\vec{h}_\lambda|\vec{g}) = \mathcal{K} p_0(\vec{h}_\lambda) \exp\left[-\frac{1}{2}(\delta\vec{h}|\delta\vec{h}) - (\vec{n}|\delta\vec{h}) - \frac{1}{2}(\vec{n}|\vec{n})\right]. \tag{4.10}$$

For notational simplicity, I have defined

$$\delta\vec{h} \equiv \vec{h}_{\hat{\lambda}} - \vec{h}_\lambda. \tag{4.11}$$

There is a difficulty with using (4.10) to compute a distribution for λ: it depends upon the specific noise instance $\vec{n}(t)$ present in the detector network. To circumvent this, I will take a "frequentist" viewpoint and ensemble average (4.10) with respect to the detector network noise. The resulting probability distribution is the final posterior distribution for λ, given $\hat{\lambda}$:

$$\begin{aligned} P_{\text{post}}(\lambda|\hat{\lambda}) &\equiv p_0(\vec{h}_\lambda) \mathrm{E}\left\{P(\vec{h}_\lambda|\vec{g})\right\}_{\vec{n}} \\ &= p_0(\vec{h}_\lambda) \int P(\vec{n})\, P(\vec{h}_\lambda|\vec{g})\, \mathcal{D}\vec{n} \\ &= \mathcal{K} p_0(\vec{h}_\lambda) \int \exp\left[-\frac{1}{2}(\vec{n}|\vec{n})\right] \exp\left[-\frac{1}{2}(\delta\vec{h}|\delta\vec{h}) - (\vec{n}|\delta\vec{h}) - \frac{1}{2}(\vec{n}|\vec{n})\right] \mathcal{D}\vec{n}. \end{aligned} \tag{4.12}$$

The integral is over all possible network noise functions $\vec{n}$, and so is a functional integral, rather similar to path integrals commonly encountered in quantum field theory. Since the argument of the exponential is a quadratic form, the integral is in fact rather elementary. Details of this calculation are given in Appendix A; the result is

$$P_{\text{post}}(\lambda|\hat{\lambda}) = \mathcal{K} p_0(\lambda) \exp\left[-\frac{1}{4}(\delta\vec{h}|\delta\vec{h})\right]. \tag{4.13}$$

For simplicity, I assume here that the waveform h_λ is parameterized only by λ; thus the distribution for the parameter λ entirely determines the distribution h_λ. As remarked in the beginning of this section, current uncertainties in our understanding of NS-NS merger waves cannot really be characterized by one parameter; but, since only gross features of the merger waveform are likely to be measurable, it is not unreasonable to characterize the measurement process in this way. As both detectors and theoretical understanding of the merger waves improve, this analysis could be extended to incorporate multiple parameter models of the merger waveform. (One effect that this analysis neglects, the cosmological redshift z, should be easy to incorporate — all masses and frequencies are simply redshifted according to $M \to (1+z)M$, $f \to f/(1+z)$; *cf.* [27, 28].)

The distribution $P_{\rm post}(\lambda|\hat{\lambda})$ is normalized such that $\int P_{\rm post}(\lambda|\hat{\lambda})d\lambda = 1$. The normalization constant is therefore constant only with respect to λ — it takes on different values if $\hat{\lambda}$ or the noise characteristics change. To indicate this, from now on I will write this constant $\mathcal{K}(\hat{\lambda}, \text{noise})$.

As was discussed in the Introduction, $P_{\rm post}(\lambda|\hat{\lambda})$ is not useful for choosing a detector network design because it is constructed after measurement; observers need to be able to configure their network before observations of the merger are made. This is reflected in the implicit dependence of the distribution upon $\hat{\lambda}$. A more useful quantity is obtained by calculating the value of $P_{\rm post}(\lambda|\hat{\lambda})$ that is expected modulo our ignorance regarding the distribution of $\hat{\lambda}$ — the *anticipated* distribution for λ:

$$P_{\rm ant}(\lambda) = \int P_{\rm post}(\lambda|\hat{\lambda}) p_0(\hat{\lambda})\, d\hat{\lambda}. \tag{4.14}$$

This probability distribution answers the question "What is the best-guess for the probability that a measurement of NS-NS merger will yield the value λ, given the information that is known about λ at this time?" This quantity forms the basis of this chapter's suggested algorithm for designing a network of detectors for measuring NS-NS merger.

4.2.2 Designing the optimal detector network

Turn, now, to choosing the detector configuration that measures λ as accurately as possible. Consider the mean and variance of the distribution (4.14),

$$\bar{\lambda}_{\rm ant} = \int \lambda\, P_{\rm ant}(\lambda)\, d\lambda, \tag{4.15}$$

$$\begin{aligned} \sigma^2_{\rm ant} &= \int (\lambda - \bar{\lambda}_{\rm ant})^2 P_{\rm ant}(\lambda)\, d\lambda, \\ &= \int \lambda^2 P_{\rm ant}(\lambda)\, d\lambda - \bar{\lambda}^2_{\rm ant}. \end{aligned} \tag{4.16}$$

The mean (4.15) represents the value of λ that we anticipate we would measure if it were possible to repeat the NS-NS merger measurement with many different detector networks [recall that an ensemble average over noise distributions is involved in calculating $P_{\rm ant}(\lambda)$]. It is indicative of the value of λ that a particular observation will measure. Likewise, (4.16) is an indicator of how accurately λ will be measured; we anticipate that a typical value of λ from the measurement ensemble will be within $\sigma_{\rm ant}$ of $\bar{\lambda}_{\rm ant}$.

Through the inner product (4.8), the variance (4.16) depends implicitly on the noise characteristics of the detector network. Suppose that there are $N_{\rm noise}$ noise parameters that can be adjusted; these represent quantities such as the central frequency of a narrow-band detector, or such a detector's bandwidth. Let the kth such parameter be ν_k. Then the optimal detector will be the detector characterized by the set of parameters ν_k such that, for all k,

$$\nabla_{\nu_k}\sigma^2_{\rm ant} = \int \left(\lambda^2 - 2\lambda\bar{\lambda}_{\rm ant}\right) \nabla_{\nu_k} P_{\rm ant}(\lambda)\, d\lambda = 0. \tag{4.17}$$

In practice, direct implementation of (4.17) is not a practical way to construct the optimal detector network, since Eq. (4.17) is the condition for local minima and maxima of $\sigma^2_{\rm ant}$ as well as global minima. The use of robust numerical global minimization algorithms on Eq. (4.16) is far more effective [30].

Finally, note that the prior probability distribution $p_0(\lambda)$ plays a crucial role, through Eqs. (4.13) and (4.14), in determining the optimal detector network. This gives a natural, Bayesian way to improve and update the detector network as knowledge of NS-NS mergers improves:

1. Before the first NS-NS merger measurement is made, our understanding of λ is likely to be rather crude. The best choice of prior information may be a uniform distribution between some upper and lower limits: $p_0(\lambda) = \text{const}$, $\lambda_{\rm MIN} \leq \lambda \leq \lambda_{\rm MAX}$.

2. Configure the detector network by minimizing (4.16) using this uniform prior distribution.

3. Measure a NS-NS merger. After this measurement, construct the posterior distribution for λ, $P_{\rm post}(\lambda|\hat{\lambda})$ [Eq. (4.13)].

4. This posterior distribution can now be used as a prior distribution for the next NS-NS merger measurement: set $p_0^{\rm new}(\lambda) = P_{\rm post}(\lambda|\hat{\lambda})$; then, reconfigure the network by minimizing (4.16) with this prior distribution.

In Secs. 4.4 and 4.5, I apply this algorithm to both a simple toy model of the NS-NS coalescence waveform (for which calculations are very simple) and to more realistic models, based on numerical calculations by Zhuge, Centrella, and McMillan [25]. As a foundation to these analyses, I first discuss and review the properties of the gravitational-wave detectors that will be used to make NS-NS merger measurements.

4.3 Detector properties

In this section, I briefly review the properties and sensitivities of the detectors that will comprise gravitational-wave detector networks. The sensitivities, and in particular the formulae I give below for the noise in these detectors, play an important role in optimizing a detector network to measure the merger of binary neutron stars.

4.3.1 Interferometric detectors

The noise in interferometers comes primarily from three fundamental sources: at $f \lesssim 10$ Hz, it is primarily due to seismic vibrations (the test masses' isolation is ineffective at these frequencies); at $10\,\mathrm{Hz} \lesssim f \lesssim 100\,\mathrm{Hz}$, it is primarily due to thermally induced vibrations of the test masses' suspensions; and at $f \gtrsim 100$ Hz it is due to photon shot noise (*i.e.*, Poisson fluctuations in the number of photons measured over an averaging time $\sim 1/f$). (These quoted numbers are for "advanced" LIGO interferometers, as in Ref. [8].) For the frequencies that are relevant to NS-NS merger, the dominant source of noise is therefore photon shot noise. Broad-band detectors will be run in the "standard" or "power" recycling configuration. In this configuration, a mirror is put into the interferometer topology at the input port, in order to boost the amount of circulating power in the interferometer arms; see Fig. 1 of [17]. A general formula for the spectral density of the standard recycling shot noise is

$$S_h^{\mathrm{SR}}(f) = \frac{S_0}{2}\frac{f_k}{f_0}\left(1 + \frac{f^2}{f_k^2}\right). \tag{4.18}$$

(See [15, 17] for derivations, and [18] for corrections.) In this formula, f_k is the "knee" frequency, a parameter that can be tuned by adjusting the reflectivity of the corner mirrors in each arm. Interferometers used in broad-band searches ($10\,\mathrm{Hz} \lesssim f \lesssim 1$ Khz) are expected typically to have $f_k \approx 100$ Hz, near the frequencies at which thermal noise becomes important. This puts the minimum of the noise curve near 100 Hz. It may be useful in other instances to tune f_k to a different frequency. In

contrast to f_k, the parameters S_0 and f_0 are not tunable, but are set by the technology available to the experimenter:

$$\begin{aligned} S_0 &\equiv \frac{\hbar c \lambda_{\rm laser}}{4\pi\eta I_0}\left(\frac{1-\mathcal{R}_{\rm end}}{L_{\rm arm}}\right)^2 \\ &\sim \frac{\text{laser wavelength}}{\text{laser power}}\left(\frac{1-\text{end mirror reflectivity}}{\text{arm length}}\right)^2; \\ f_0 &\equiv \frac{1-\mathcal{R}_{\rm end}}{4\pi}\frac{c}{L_{\rm arm}} \\ &\sim \frac{1-\text{end mirror reflectivity}}{\text{arm length}}. \end{aligned} \tag{4.19}$$

In these equations, $\lambda_{\rm laser}$ is the wavelength of laser light, I_0 is power of the laser, η is the efficiency of the interferometer's read-out photodiode (so that the product ηI_0 is the "effective power" of the laser), $\mathcal{R}_{\rm end}$ is the intensity reflectivity of the interferometer's end mirrors, and $L_{\rm arm}$ is the length of the interferometer's arms. Note that $1/f_0$ is roughly the amount of time it takes for light to leak out of the interferometer if the laser is suddenly shut off; $f_0 \sim 1$ Hz.

The advanced LIGO interferometers will typically be run with $f_k \simeq 70$ Hz; *cf.* the noise curves presented in [8]. The spectral density of noise for $f > 10$ Hz should be well approximated by Cutler and Flanagan's formula [33]:

$$S_h^{\rm CF}(f) = \frac{S_{\rm CF}}{5}\left[\left(\frac{f}{f_{\rm CF}}\right)^{-4} + 2\left(1+\frac{f^2}{f_{\rm CF}^2}\right)\right]. \tag{4.20}$$

Below 10 Hz, the noise is effectively infinite due to seismic vibrations. The values of $S_{\rm CF}$ and $f_{\rm CF}$ which best fit the advanced interferometers' projected noise curve are $S_{\rm CF} = 3.1 \times 10^{-48}{\rm Hz}^{-1}$, $f_{\rm CF} = 70$ Hz. The portion of the noise curve which scales as f^{-4} models thermal noise in the suspensions; the portion which scales as f^2 is the standard recycling shot noise. From this, it follows that Eqs. (4.18) and (4.20) must agree in the high frequency limit. Enforcing $S_h^{\rm CF}(f \to \infty) = S_h^{\rm SR}(f \to \infty)$ yields

$$\begin{aligned} f_k &= f_{\rm CF} = 70\,{\rm Hz} \\ S_0 &= \frac{4}{5}\frac{f_0}{f_{\rm CF}} S_{\rm CF} = 1.7 \times 10^{-50}\,{\rm Hz}^{-1}. \end{aligned} \tag{4.21}$$

Here, I used $f_0 = 0.48$ Hz as in [18]. The value of S_0 in Eq. (4.21) will be used in all of this chapter's analyses of broad-band detectors, and the value $f_k = 70$ Hz will be assumed for broad-band detec-

tors that measure the inspiral signal. However, f_k will be allowed to vary in some cases, in order to test how well the merger can be measured with broad-band, standard-recycling interferometers.

Turn now to narrow-banded interferometer configurations. The particular variant I will focus on in this chapter is "dual," or "signal" recycling; its noise curves are similar to those of other narrow-band interferometer configurations. In dual-recycling, mirrors are introduced at both the input and output ports of the interferometers. The mirror on the input port is simply a standard-recycling mirror, as described above. The mirror on the output port reflects the interferometer's output signal back into its arms; this causes the interferometer to resonate at some tunable frequency f_R, which is set by adjusting the position of this mirror. The interferometer thus has very low noise in a small band near the resonant frequency:

$$S_h^{\mathrm{DR}}(f) = 4S_0 \left(\frac{\Delta f}{2f_0}\right) \left[1 + 4\left(\frac{f - f_R}{\Delta f}\right)^2\right]. \tag{4.22}$$

(See [15, 16, 17] for derivations, and [18] for corrections.) The bandwidth Δf is also a tunable parameter; it is common, however, in theoretical analyses to set $\Delta f = 2f_0$ (the minimum bandwidth achievable) since the amplitude noise is thereby minimized on resonance. (This is the form presented in [31, 18].) In practice, it might not be desirable to make the bandwidth so small since thermally induced vibrational modes of the test masses may prevent one from achieving the minimum one would expect by setting $\Delta f = 2f_0$. For this reason, and also because it is interesting to see if anything can be gained by making the bandwidth large, I will leave Δf as a parameter.

4.3.2 Acoustic detectors

Acoustic detectors can be described with sensitivity curves that are similar in form to the curves of dual-recycled interferometers. The discussion here is based on the analysis of Merkowitz and Johnson [20]. As such, this analysis is strictly applicable only to the "TIGA" spherical acoustic antenna. However, the core physics and the characteristics of the noise curve are similar for all acoustic detectors; I focus on the analysis of [20] because it highlights the most important physical issues.

Eq. (40) of [20] gives a very general formula for the spectral density of strain noise in a single output channel of a TIGA. Of note is that their formula has multiple minima; this is because the resonant normal mode frequencies of the sphere are split when it is coupled to mechanical resonators (which are essential parts of the read-out system needed to actually measure the influence of a

gravitational wave on the TIGA). The splitting of the modes is not too severe however (*cf.* Fig. 14 of [20]), and it is sufficient for the purposes of this chapter to approximate the modes as unsplit. This is accomplished by setting Merkowitz and Johnson's parameter b to zero [*cf.* their Eqs. (31)–(33)]. The spectral density of strain noise in any given mode of the TIGA is then

$$\begin{aligned} S_h(f) &\simeq \frac{4\hbar N}{(2\pi f_0)^3 m_S m_R (\chi R)^2} r_n \mathcal{Y}_1 \left[1 + \left(\frac{f - f_R}{\Delta f}\right)^2\right], \\ \Delta f &= \mathcal{Y}_2 \frac{r_n}{2\pi m_s}, \end{aligned} \tag{4.23}$$

[22] where, defining $y \equiv \sqrt{3/2\pi}$,

$$\begin{aligned} \mathcal{Y}_1 &\equiv \frac{(1 + 6y^2 + y^4)^2}{16(y^2 + y^4)^2} = 2.10, \\ \mathcal{Y}_2 &\equiv \frac{(1 + 6y^2 + y^4)}{(1 - y^2)^4} = 54.9. \end{aligned} \tag{4.24}$$

In this equation, N is the so-called "noise number," equal to $k_B T / 2\pi\hbar f_0$, where T is the effective temperature of the detector. In a quantum limited detector, which I will assume from now on, $N = 1$. The masses m_S and m_R are the masses of the detector and the attached resonators, respectively. Typically, $m_R/m_S \sim 10^{-3} - 10^{-4}$ (*cf.* Table I of [20]). The physical radius of the sphere is R. The *effective* radius (meaning the radius which determines the cross section to gravitational waves) is χR; $\chi \simeq 0.6$ (Fig. 5 of [20]). The frequency f_R is the resonant frequency of the detector; it depends on the mass, radius, and material properties of the detector. For the aluminum spheres discussed in [20], $f_R \times R \simeq 1280$ meters/sec. Finally, r_n is the noise resistance, a parameter that measures the coupling of the resonator-sphere system. From [23], $r_n \sim 3 \times 10^3$ kg/sec.

In this unsplit-mode approximation, the bandwidth Δf of the detector is fixed by the noise resistance, r_n, and the detector's mass, m_S:

$$\Delta f = 2.6\,\mathrm{Hz} \left(\frac{r_n}{3 \times 10^3\,\mathrm{kg/sec}}\right) \left(\frac{10^4\,\mathrm{kg}}{m_S}\right). \tag{4.25}$$

In real detectors, the bandwidth will not be this narrow, because of mode splitting; instead, $\Delta f / f$ is likely to be of order 0.05 [23].

Finally, I rewrite Eq. (4.23) in the form

$$S_h(f) = S_{\mathrm{AD}} \left[1 + \left(\frac{f - f_0}{\Delta f}\right)^2\right], \tag{4.26}$$

and evaluate the acoustic detector's minimum strain noise spectrum, $S_{\rm AD}$:

$$S_{\rm AD} = 2.4 \times 10^{-46}\,{\rm Hz}^{-1} \times \left(\frac{r_n}{3\times 10^3\,{\rm kg/sec}}\right)\left(\frac{1250\,{\rm Hz}}{f_0}\right)^3\left(\frac{1.25\times 10^4\,{\rm kg}}{m_S}\right)\left(\frac{5\,{\rm kg}}{m_R}\right)\left(\frac{1\,{\rm m}}{R}\right)^2. \tag{4.27}$$

Although my goal is not to compare various detectors, it is worth noting that this strain noise is likely not competitive with the dual-recycled configuration of advanced interferometers; however, it should be competitive with the dual-recycled configuration of initial interferometers. It is also worth noting that the resonant antenna community has a great deal of experience studying and using their detectors in gravitational-wave searches, whereas dual-recycling and other narrow-banding techniques for interferometers are relatively untested.

4.4 Toy model

In this section, I describe a simple toy model of the coalescence waveform which approximately captures features that are seen in more realistic models of neutron star coalescence and makes calculations very simple. I assume that below the "merger frequency," $f_{\rm m} \equiv \lambda f_{\rm kHz} = \lambda \times 1000\,{\rm Hz}$, the waveform is described using the Newtonian, quadrupole wave formula, and above this frequency the waveform is zero. This toy model thus describes a merger in which the waves are suddenly shut off.

4.4.1 Evaluation of the probability distributions

The emitted waveform has two polarizations, h_+ and $h_\times$. Each detector in the network measures some linear combination of these polarizations:

$$h_j = F_{j,+}h_+ + F_{j,\times}h_\times. \tag{4.28}$$

The exact forms of the functions $F_{+,\times}$ depend on the nature of the detector. For interferometers, standard formulae for $F_{+,\times}$ are given in, *e.g.*, [31]; for spherical resonant mass antennae, $F_+ \simeq F_\times \simeq$ const — spherical antennae have very nearly equal sensitivity to both polarizations, independent of the location of the source on the sky.

The two polarizations of the Newtonian, quadrupole inspiral waveform are, in the frequency

domain [32],

$$\begin{aligned}
\tilde{h}_+(f) &= 2(1+\cos\iota^2)\tilde{h}_Q(f), \\
\tilde{h}_\times(f) &= 4\cos\iota\, e^{i\pi/2}\,\tilde{h}_Q(f); \\
\tilde{h}_Q(f) &\equiv \sqrt{\frac{5}{96}}\frac{\pi^{-2/3}\mathcal{M}^{5/6}}{r} f^{-7/6} e^{i\Phi(f)}.
\end{aligned} \tag{4.29}$$

Here, ι is the angle between the line of sight to the binary and its orbital angular momentum, r is the distance to the source, $\mathcal{M} \equiv (m_1 m_2)^{3/5}/(m_1+m_2)^{1/5}$ is the "chirp mass" of the system, and $\Phi(f)$ is a phase function whose value is not important in this analysis. The toy waveform I consider in this section is then given by multiplying $h_{+,\times}$ by $\Theta(\lambda f_{\rm kHz} - f)$, where Θ is the step function. The gravitational-wave signal measured in detector j of the network is therefore

$$\tilde{h}_j(f) = \left[2(1+\cos\iota^2)F_{j,+} + 4\cos\iota\, e^{i\pi/2}\, F_{j,\times}\right]\tilde{h}_Q(f)\Theta(\lambda f_{\rm kHz} - f). \tag{4.30}$$

Inserting this into Eq. (4.13) yields

$$\begin{aligned}
P_{\rm post}(\lambda|\hat{\lambda}) &= p_0(\lambda)\exp\left[-{\rm Re}\int_0^\infty [2(1+\cos\iota^2)F_{j,+} + 4\cos\iota\, e^{i\pi/2}\, F_{j,\times}][2(1+\cos\iota^2)F_{k,+} \right. \\
&+ \left. 4\cos\iota\, e^{i\pi/2}\, F_{k,\times}]\left[\Theta(\hat{\lambda}f_{\rm kHz} - f) - \Theta(\lambda f_{\rm kHz} - f)\right]^2 |\tilde{h}_Q(f)|^2 \left[\mathbf{S}_h(f)^{-1}\right]^{jk} df\right].
\end{aligned} \tag{4.31}$$

Define $\lambda_{\rm low} \equiv \min(\hat{\lambda}, \lambda)$, $\lambda_{\rm high} \equiv \max(\hat{\lambda}, \lambda)$. The domain of integration is now clearly restricted to the range $\lambda_{\rm low} f_{\rm kHz} \leq f \leq \lambda_{\rm high} f_{\rm kHz}$. For reasonable values of λ, this restricts the domain to $f \gtrsim 500$ Hz. I will assume that the noise of the various detectors in the network is uncorrelated for these frequencies. Correlations in the noise spectra of two detectors must arise because they jointly experience some physical effect. Acoustic detectors must be kept at cryogenic temperatures, and therefore will be very well isolated in their own special facilities. The noise in any given detector will arise from interactions with its local thermal bath, which cannot affect a different detector. We thus need only consider correlations between pairs of laser interferometers. The primary noise source in interferometers in this frequency band is photon shot noise. Since each interferometer uses its own laser, the shot noise in any interferometer should not correlate with any other interferometer. Thus, the noise of the detectors in the network should be uncorrelated in this frequency band[1]. It

[1]Noise due to fluctuations in the electric power grid could violate this assumption. Even widely separated detectors

should be noted, though, that interferometers housed in a common vacuum system will share a large number of noise sources — noise due to fluctuating electric and magnetic fields, outgassing of the beam tube, *etc.* These noise sources are likely less important than shot noise in broad-band interferometers, but may be important in narrow-band interferometers.

Assuming negligible correlations, (4.31) can be written

$$P_{\rm post}(\lambda|\hat{\lambda}) = p_0(\lambda) \exp\left[-\sum_{j=1}^{N} |\Psi|_j^2 \int_{\lambda_{\rm low} f_{\rm kHz}}^{\lambda_{\rm high} f_{\rm kHz}} \frac{|\tilde{h}_Q(f)|^2}{S_h(f)_j} df \right]. \tag{4.32}$$

Here, $|\Psi|_j^2 = 4[(1+\cos\iota^2)F_{j,+} + 4\cos\iota F_{j,\times}]^2$, and $S_h(f)_j$ is the spectral density of strain noise in detector j. Note that $|\Psi|_j^2$ is identical to the function Θ^2 defined by Finn and Chernoff [*cf.* [32], their Eq. (3.31)]; I use a different notation to avoid confusion with the step function.

To evaluate (4.32), a configuration of the detector network must be chosen. I will assume the following network: a single broad-band LIGO/VIRGO-type laser interferometer, and some number $N_{\rm DR}$ of dual-recycled narrow-band laser interferometers. The reason for this choice is that simple, analytic approximations exist for the noise spectral density of such detectors. For the broad-band detector, I use the approximate formula given in [33]; for dual-recycling, I use the formulae of [17], with corrections as in [18].

$$\begin{aligned} \text{broad band: } S_h(f) &= \frac{S_{\rm CF}}{5}\left[\left(\frac{f}{f_{\rm CF}}\right)^{-4} + 2\left(1+\frac{f^2}{f_{\rm CF}^2}\right)\right] \\ \text{narrow band: } S_h(f)_j &= \frac{8}{5} S_{\rm CF}\left(\frac{\Delta f_j}{f_{\rm CF}}\right)\left[1+4\left(\frac{f-f_j}{\Delta f_j}\right)^2\right]. \end{aligned} \tag{4.33}$$

Here, $S_{\rm CF}$ and $f_{\rm CF}$ are parameters chosen by Cutler and Flanagan to fit the projected advanced LIGO interferometer noise curve [8, 33]; their values are $S_{\rm CF} = 3.1\times10^{-48}\,{\rm Hz}^{-1}$, $f_{\rm CF} = 70\,{\rm Hz}$. Because the binary neutron star merger will take place at frequencies $\gtrsim 500$ Hz, we may ignore the f^{-4} and f^0 pieces of the broad-band noise curve, instead using

$$\text{broad band: } S_h(f) \simeq \frac{2S_{\rm CF}}{5}\frac{f^2}{f_{\rm CF}^2}. \tag{4.34}$$

The dual recycling frequency f_j and bandwidth Δf_j are tunable parameters. If $\Delta f_j \ll f_j$, the

could experience some correlated noise if they get their power from the same grid.

narrow-band noise curve may be approximated by

$$\text{narrow band: } \frac{1}{S_h(f)_j} \simeq \frac{5\pi}{16}\frac{f_{\rm CF}}{S_{\rm CF}}\delta(f-f_j). \tag{4.35}$$

As a final simplification, I assume that the binary is positioned such that $|\Psi|_j^2 = |\Psi|^2$ for all j. This is the case only if the response functions $F_{+,\times}$ are equal for all sites. In reality, this can only happen if all detectors are at the same site. If the detectors are at sites that are not too far apart on the Earth's surface, and they measure a binary that is directly above some point near the center of the sites, the response functions will differ by only a few percent. For example, this is a good approximation for a binary over the Rocky Mountains, measured by the Hanford, Washington and Livingston, Louisiana LIGO detectors. Using (4.34), it is now simple to integrate and obtain the following analytic form for the posterior distribution of λ:

$$\begin{aligned} P_{\rm post}(\lambda|\hat{\lambda}) &= p_0(\lambda)\exp\left[-\frac{3}{80}\frac{\rho^2_{\rm insp}}{I_7}\left(\frac{f_{\rm CF}}{f_{\rm kHz}}\right)^{10/3}\left(\frac{1}{\lambda_{\rm low}^{10/3}}-\frac{1}{\lambda_{\rm high}^{10/3}}\right)-\frac{1}{32}\frac{\rho^2_{\rm insp}}{I_7}\sum_{j=1}^{N_{\rm DR}}\frac{f_{\rm CF}^{7/3}}{\Delta f_j}\times\right. \\ &\left.\int_{\lambda_{\min f_{\rm kHz}}}^{\lambda_{\max f_{\rm kHz}}}\frac{f^{-7/3}df}{1+4(f-f_j)^2/\Delta f_j^2}\right] \\ &\simeq p_0(\lambda)\exp\left[-\frac{3}{80}\frac{\rho^2_{\rm insp}}{I_7}\left(\frac{f_{\rm CF}}{f_{\rm kHz}}\right)^{10/3}\left(\frac{1}{\lambda_{\rm low}^{10/3}}-\frac{1}{\lambda_{\rm high}^{10/3}}\right)-\right. \\ &\left.\frac{5\pi}{80}\frac{\rho^2_{\rm insp}}{I_7}\sum_{j=1}^{N_{\rm DR}}\left(\frac{f_{\rm CF}}{f_j}\right)^{7/3}\right]. \end{aligned} \tag{4.36}$$

The approximate equality holds when the narrow-band detectors are narrow enough that (4.35) holds. Note that I have used the SNR obtained for the inspiral part of the signal,

$$\rho^2_{\rm insp} = \frac{25}{24}\frac{|\Psi|^2\mathcal{M}^{5/3}I_7}{(\pi f_{\rm CF})^{4/3}S_{\rm CF}}\frac{1}{r^2}, \tag{4.37}$$

as a convenient means of parameterizing the waveform's amplitude. The number I_7 is a moment of the noise curve as defined in [9]:

$$I_7 \equiv \frac{S_{\rm CF}}{f_{\rm CF}^{4/3}}\int_0^\infty \frac{f^{-7/3}}{S_h(f)}df \simeq 0.284. \tag{4.38}$$

The anticipated probability distribution is then obtained by plugging (4.36) into (4.14).

4.4.2 Examples

In this subsection, I examine NS-NS merger measurement for some specific parameter sets, within the context of the toy model. First, consider measurements made only with broad-band instruments. Figure 4.1 shows the posterior distribution for measurements with inspiral SNRs of 20, 40, 80, and 160, under the assumption that $\hat{\lambda} = 0.8$, and with the prior distribution

$$\begin{aligned} p_0(\lambda) &= \frac{1}{\lambda_{\rm MAX} - \lambda_{\rm MIN}}, \qquad \lambda_{\rm MIN} \leq \lambda \leq \lambda_{\rm MAX}, \\ &= 0 \qquad\qquad\qquad\quad \text{elsewhere}, \end{aligned} \tag{4.39}$$

using $\lambda_{\rm MAX} = 1.5$, $\lambda_{\rm MIN} = 0.5$. This range of λ is chosen based on the results of Lai and Wiseman [34, 35]. Using equations of motion that incorporate terms from both the post-Newtonian expansion of general relativity and tidal coupling due to the finite size of the body, they find that the NS-NS inspiral is likely to end when the gravitational-wave frequency lies in the range $500\,{\rm Hz} \lesssim f_{\rm GW} \lesssim 1400\,{\rm Hz}$ (Table 1 of [34]). Note that these frequencies are rather lower than the frequencies which characterize NS-NS mergers under Newtonian gravity (*cf.* the energy spectra dE/df of [25]).

Several features of this posterior distribution are noteworthy. First, note that the mode of the distribution is in all cases $\hat{\lambda}$. This is not surprising — it is clear that with no narrow-band detectors, $P_{\rm post}(\lambda|\hat{\lambda})$ is peaked at $\lambda = \hat{\lambda}$ [*cf.* Eq. (4.36)]. Thus, the value of λ that is most likely to be measured in any given measurement is $\hat{\lambda}$. However, for all SNR levels the probability distribution has a large tail as $\lambda \to \lambda_{\rm MAX}$. This tail is due to the rapid growth of shot noise as one goes to higher frequencies — at these frequencies, it is hard to tell if the signal has shut-off, and thus difficult to measure the value of λ. Although the most likely value of λ that one would measure in these cases is $\hat{\lambda}$, there is an alarmingly high probability that one would measure a larger value of λ. Indeed, the values of $\bar{\lambda}_{\rm post}$ computed from the four distributions is in each case very close to 1. This is the same value one would get if the SNR were so low that $P_{\rm post} \simeq p_0$. The peaks in these distributions are rather broad, corresponding to large values of $\sigma_{\rm post}$. The peaked nature of the probability distribution is not strongly apparent until the inspiral SNR becomes rather large, $\gtrsim 100$. Such strong SNR values require that the source be $\lesssim 100$ Mpc from the Earth; events that close are expected to be rather rare [7]. This indicates that it is unlikely broad-band detectors, working alone, will be able to provide much interesting information about NS-NS mergers.

Figure 4.2 shows a similar analysis for $\hat{\lambda} = 1.2$ — *i.e.*, assuming that the frequency at which the

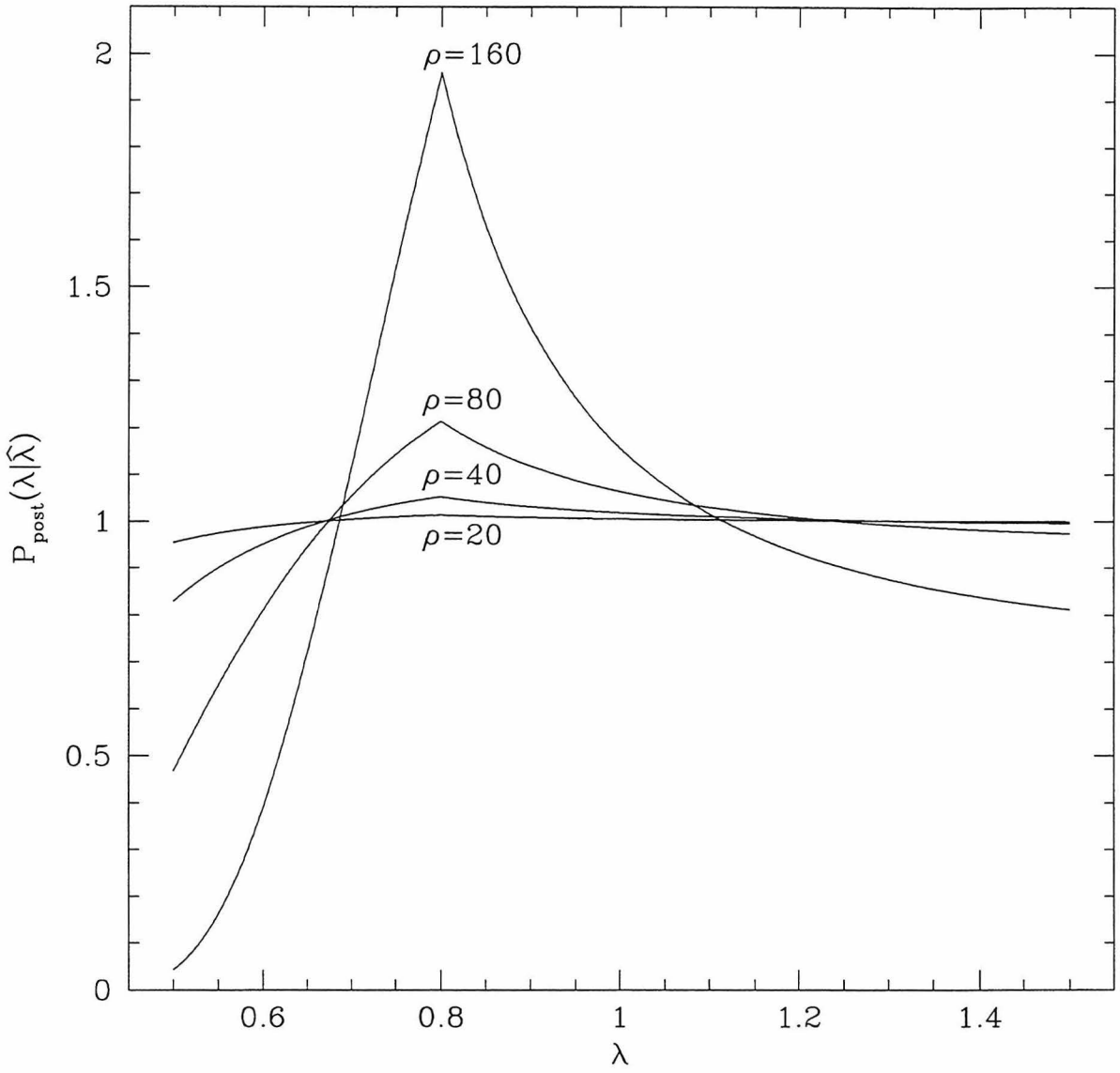

Figure 4.1: Posterior probability distribution for the toy model, $\hat{\lambda} = 0.8$ and using a single broad-band detector to measure the merger.

In this figure, ρ is the SNR for the inspiral. In all cases, the mode of the distribution is $\hat{\lambda}$; thus $\hat{\lambda}$ is the most likely value of λ to be measured. However, there is a very large tail for $\lambda > \hat{\lambda}$. This is due to shot noise; at these high frequencies, it becomes difficult to tell if a signal has shut off, and thus difficult to measure λ. Note that the distribution is not particularly well-peaked until the signal has gotten very strong.

signal goes from inspiral to merger is 1200 Hz rather than 800 Hz. The conclusions discussed with regard to Fig. 4.1 clearly hold even more strongly in this case: broad-band interferometers working alone can make at best rather crude measurements of characteristics of the final neutron star measurements. A trend that is apparent from these figures is that the quality with which characteristics of the merger can be measured deteriorates as $\hat{\lambda}$ increases. This is not surprising: as $\hat{\lambda}$ increases, interesting features of the merger are pushed to higher frequencies where shot noise grows more important.

One reason that the broad-band detectors discussed above do so poorly at measuring merger characteristics is that the knee frequency of their standard-recycled shot noise is chosen to be near 100 Hz. As discussed in Sec. 4.3, this puts the peak sensitivity of the detector near 100 Hz, a very good choice for measuring NS-NS inspiral, but a terrible choice for measuring the merger. In principle, one could do better at measuring the merger by using a larger value of the knee frequency. It turns out, however, one cannot do as well at measuring the merger using a standard-recycled broad-band interferometer with any choice of f_k as one can do with a narrow-band, dual-recycled interferometer. To see this, examine Fig. 4.3. In this figure, I consider an advanced LIGO broad-band instrument [with a noise curve given by Eq. (4.33)] operated in concert with several choices of dual and standard-recycled interferometers. In the upper plot, I combine the advanced LIGO interferometer with three different standard-recycled interferometers to measure a merger that has $\rho_{\rm insp} = 40$ and $\hat{\lambda} = 0.8$. The plot shown is the posterior distribution obtained versus λ, assuming a uniform prior distribution between $\lambda = 0.5$ and $\lambda = 1.5$. The distribution that is narrowest and most sharply peaked corresponds to a broad-band LIGO interferometer combined with a standard-recycled interferometer whose knee frequency is $f_k = 1000$ Hz. Thus, as stated, one can improve the effectiveness of the merger measurement by tuning the knee frequency of the standard-recycled interferometer. In the lower plot of Fig. 4.3, I compare the posterior distribution for the best case I found of advanced LIGO plus standard-recycled interferometer ($f_k = 1000$ Hz; dashed line) with the distribution obtained for advanced LIGO plus dual-recycling. I find that the distributions are comparable in width and height when the bandwidth Δf of the dual-recycled interferometer is about 225 Hz.

It turns out, however, that narrow-band instruments work best within this measurement scheme when their bandwidths are as narrow as possible. Consider Figure 4.4. This shows the posterior probability distribution that would be obtained in the case that $\rho_{\rm insp} = 20$, $\hat{\lambda} = 0.8$, the prior probability is uniform from $0.5 \leq \lambda \leq 1.5$, and two narrow-band detectors are used, with central

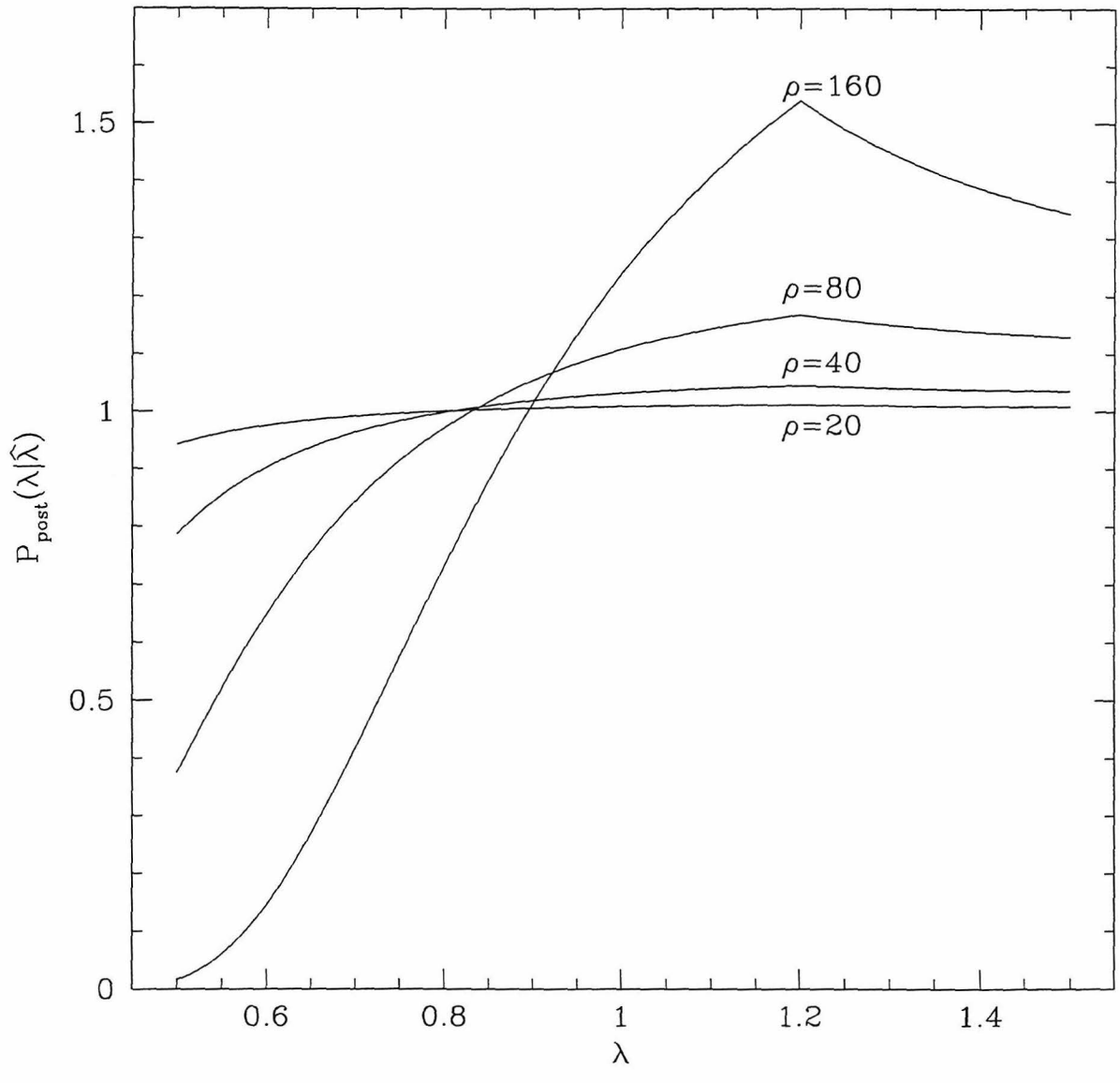

Figure 4.2: Posterior probability distribution for the toy model, $\hat{\lambda} = 1.2$ and using a single broad-band detector to measure the merger.

The characteristics apparent in Figure 4.1 are apparent here as well. The distributions are even less peaked in this case, as the interferometers' shot noise is stronger at 1200 Hz, the frequency that characterizes the merger.

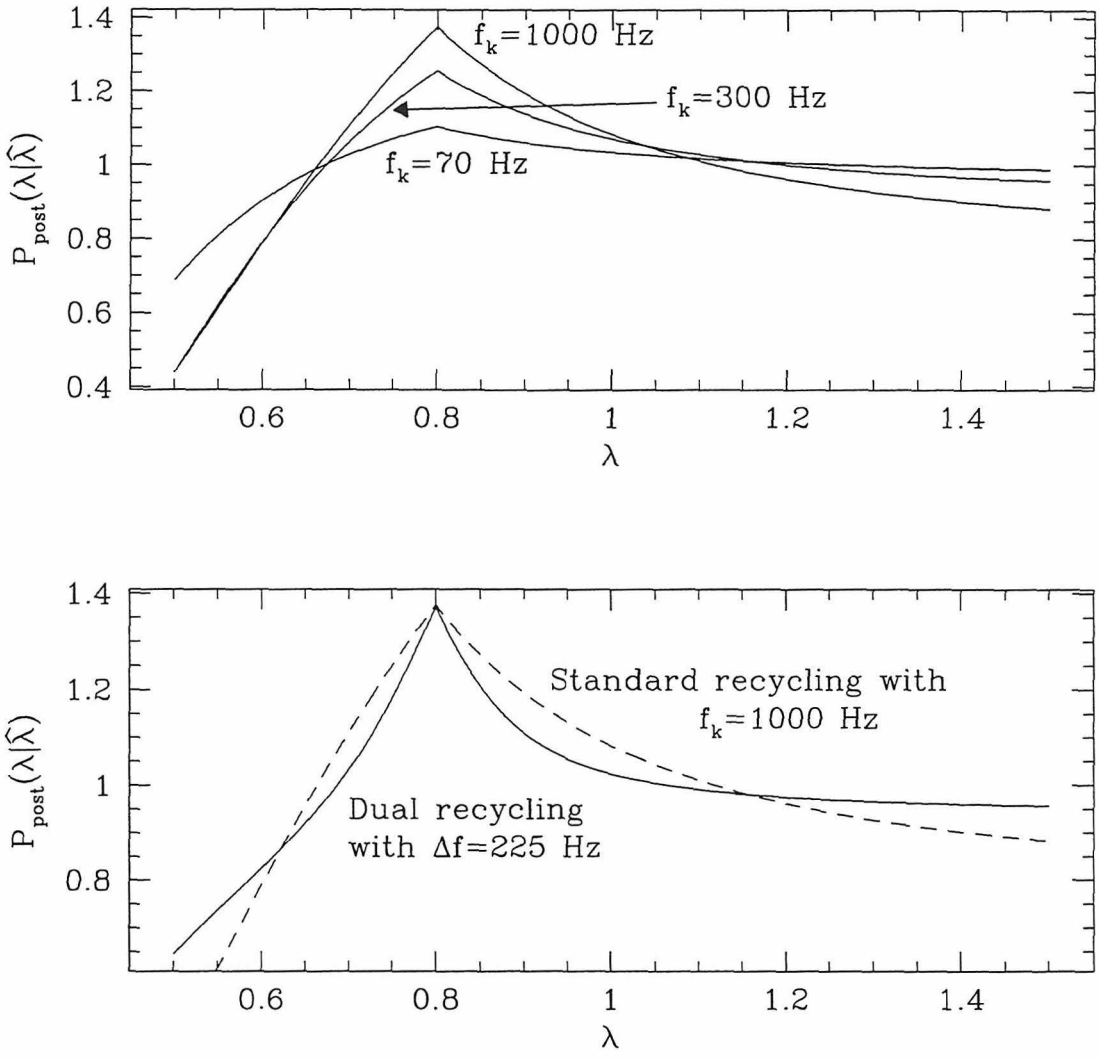

Figure 4.3: Posterior probability distribution for the toy model with $\hat{\lambda} = 0.8$, $\rho_{\rm insp} = 40$, and combining the outputs of a broad-band interferometer with various other dual and standard recycling interferometers.

In the upper plot, the advanced LIGO interferometer is combined with standard recycling interferometers that have knee frequencies $f_k = 70$ Hz, 300 Hz, and 1000 Hz. As the knee frequency is moved to higher frequencies, the posterior distribution becomes narrower and more strongly peaked about $\lambda = \hat{\lambda}$, indicating that the network measures λ more accurately. There is no further improvement beyond $f_k = 1000$ Hz. In the lower plot, I compare measurements using an advanced LIGO interferometer plus a standard recycling interferometer that has $f_k = 1000$ Hz with an advanced LIGO interferometer plus a dual-recycled interferometer that has $\Delta f = 225$ Hz. The distributions are roughly the same in this case, indicating that a standard recycling interferometer performs in a manner similar to a very wide bandwidth dual-recycled interferometer.

frequencies $f_1 = 780$ Hz, $f_2 = 820$ Hz. In both the upper and lower plots of the figure, the heavy black line is the posterior probability obtained using the delta function approximation (4.35) for the narrow-band noise. The lighter lines are the posterior probabilities obtained using Eq. (4.33) for various values of Δf. In the upper plot of Figure 4.4, the light line barely visible near the heavy line is the posterior probability when $\Delta f = 1$ Hz. It is practically indistinguishable from the line representing the delta function approximation; one may conclude that the delta function approximation is quite reasonable in this case. The other line in the upper plot of Figure 4.4 is the posterior probability when $\Delta f = 10$ Hz. Although the match is not as close as in the case $\Delta f = 1$ Hz, it is still fairly close to the delta function. The lower plot of Figure 4.4, on the other hand, shows the posterior distribution when $\Delta f = 100$ Hz and $\Delta f = 500$ Hz. In these two cases, the distributions are rather wide and poorly peaked, indicating that λ is not measured with very good accuracy. This indicates that it is preferable to measure the merger waveform with instruments that have as narrow bandwidth as is possible. This conclusion is intuitively obvious, given the way that narrow-band detectors work in this measurement scheme. Each detector is used to answer a single "yes/no" question: "Is there significant power in the gravitational waves at f?" The narrower the detector, the more accurately this question can be answered.

For the remainder of this chapter, I will assume that very narrow band dual-recycled interferometers are used to probe the merger waveform. I will assume that the delta function approximation, Eq. (4.35), is appropriate; the above analysis indicates that this is the case whenever $\Delta f / f \lesssim 0.01$.

Turn, now, to the design of detector networks. Designing the network means selecting the narrow detectors' central frequencies in the case of this simple network. Consider first using only a single narrow-band detector. This detector should be placed such that the anticipated variance (4.16) is minimized. Figure 4.5 shows this anticipated variance versus the central frequency f_1 of the narrow-band detector for several values of $\rho_{\rm insp}$. In general, there is one local minimum and one global minimum. One of these is typically near 700 Hz, the other near 1400 Hz. There is a simple, physical explanation for the existence of these two minima. Two competing phenomena drive the choice of f_1. First, the inspiral waveform drops off as $f^{-7/6}$. The signal therefore grows progressively weaker at higher frequencies. One is more likely to get a "false positive" (*i.e.*, an incorrect signal measurement due to noise) at higher frequencies. If the expected signal is weak, one therefore wants to place the narrow-band detector at some frequency close to $\lambda_{\rm MIN} f_{\rm kHz}$. On the other hand, the broad-band noise grows very strong at high frequencies. One wants to arrange narrow-band detectors in a way to fight excess high-frequency noise; thus, it is advantageous to

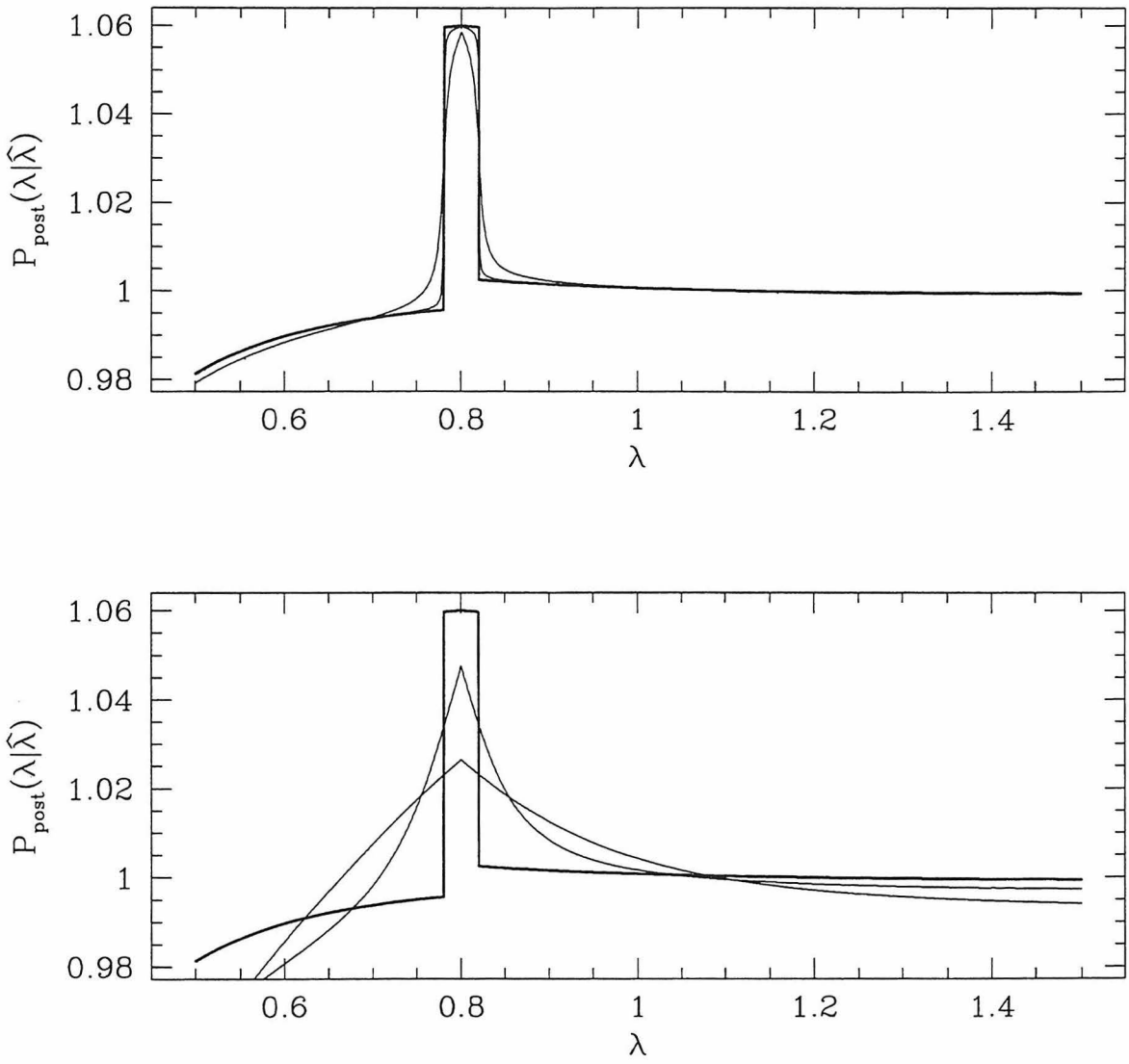

Figure 4.4: Posterior probability distribution for the toy model with $\hat{\lambda} = 0.8$, $\rho_{\rm insp} = 20$, and using two dual-recycled interferometers, centered at $f_1 = 780$ Hz, $f_2 = 820$ Hz.

In both plots, the heavy black line is the distribution obtained by using the delta function approximation Eq. (4.35). In the upper plot, the two lighter lines are the distributions resulting from use of the non-approximated noise curve (4.33) with $\Delta f = 1$ Hz and $\Delta f = 10$ Hz. The distribution for $\Delta f = 1$ Hz is practically indistinguishable from the delta function approximation; the distribution for $\Delta f = 10$ Hz is close also. In the lower plot, the two light lines are for $\Delta f = 100$ Hz and $\Delta f = 500$ Hz. These two distribution are drastically different from the delta function approximation, becoming wider and less peaked as Δf increases.

place the narrow-band detector near $\lambda_{\mathrm{MAX}} f_{\mathrm{kHz}}$.

Not surprisingly, for "weak" signals, the criterion that the narrow-band detector be placed near 700 Hz is more important; this can be seen in the $\rho_{\mathrm{insp}} = 50$ and $\rho_{\mathrm{insp}} = 100$ plots in Fig. 4.5. For strong signals, it is more advantageous to place the detector near 1400 Hz. The transition point occurs at $\rho_{\mathrm{insp}} \simeq 125$. This is a rather strong signal, corresponding to an optimally oriented binary at a distance $r \simeq 120$ Mpc (or even closer for non-optimally oriented binaries). Such sources are likely to be rather rare [7]. If it turns out that it is only practical to have one narrow-band detector, it should be arranged so that its peak sensitivity is near the lower end of the prior distribution.

Consider next using two narrow-band detectors. Figs. 4.6 and 4.7 are in essence identical to Fig. 4.5, but they plot the anticipated variance versus the central frequencies of two narrow-band detectors, f_1 and f_2. First, notice that $\sigma^2_{\mathrm{ant}}(f_1, f_2) = \sigma^2_{\mathrm{ant}}(f_2, f_1)$ — there is a reflection symmetry owing to the fact that the two narrow-band detectors are assumed to be identical in all respects except central frequency. Thus, the maxima and minima of $\sigma^2_{\mathrm{ant}}(f_1, f_2)$ come in pairs. Evident in Figs. 4.6 and 4.7 are four local minima, two global minima, and two maxima. The intuitive explanation for these minima is similar to that in the case of one narrow-band detector. Generally, minima occur near the lower end of the allowed frequency range, $f \sim \lambda_{\mathrm{MIN}} f_{\mathrm{kHz}}$ (avoidance of false positives due to weak signal at high frequencies), and near the upper end of the range, $f \sim \lambda_{\mathrm{MAX}} f_{\mathrm{kHz}}$ (compensation for high frequency shot-noise in broad-band detectors). This is why the six minima apparent in these two figures are at the corners of the (f_1, f_2) range. In the case $\rho_{\mathrm{insp}} = 60$, the global minimum is at $f_1 \simeq 620$ Hz, $f_2 \simeq 760$ Hz. The signal is weak enough that the optimal detector network has both narrow-band detectors near the lower end of the frequency range. In the case $\rho_{\mathrm{insp}} = 200$, the global minimum is at $f_1 \simeq 740$ Hz, $f_2 \simeq 1380$ Hz. With this stronger signal, the algorithm chooses to "split the difference," placing one detector near the lower end of the range and the other near the upper end.

These general features are also evident when more narrow-band detectors are used. Especially for $N_{\mathrm{DR}} \geq 3$, there are many more local minima and maxima than global minima. Because of this, looking for points where the gradient goes to zero [*i.e.*, implementing Eq. (4.17)] is not a good idea — such techniques will tend to find the local minima and the maxima. In Table 4.1, I present the detector networks found for this toy problem for the cases $N_{\mathrm{DR}} = 2, 3, 4, 5$, with inspiral SNRs $\rho_{\mathrm{insp}} = 40, 100, 200$. To find these networks, I looked for the global minima of Eq. (4.16) using Powell's multidimensional line minimization algorithm [30]. This technique, using Brent's method for the successive line minimizations, worked well at finding local minima. After finding a number

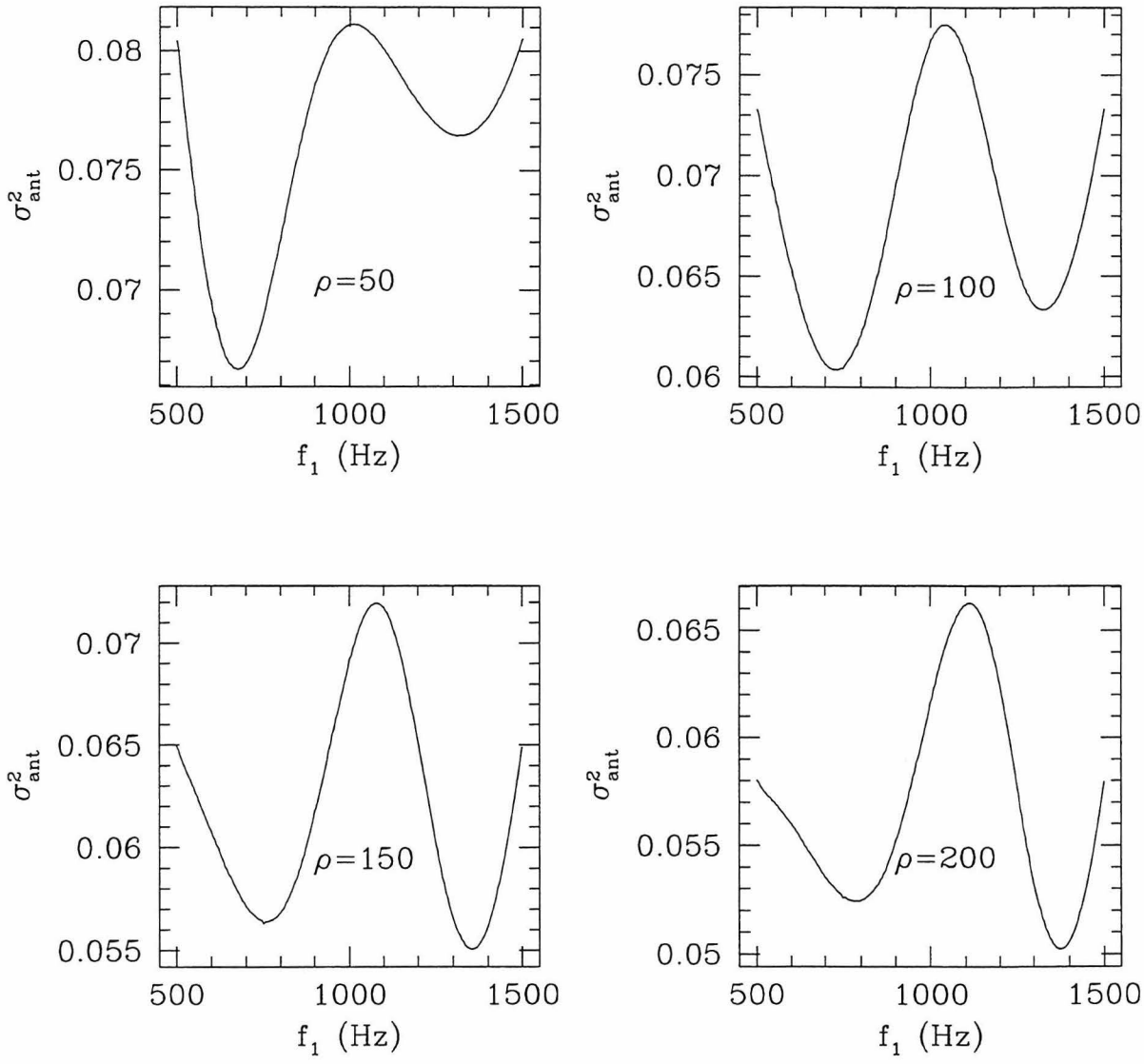

Figure 4.5: The anticipated variance (4.16) for the toy model, using one narrow-band detector, and for various levels of inspiral SNR ρ.

The optimal detector network is given by the choice of frequency f_1 that minimizes this variance. In each case, there is a local and a global minimum. One minimum is typically located near $f_1 \sim 700$ Hz. This is because the toy waveform signal grows weaker at high frequencies, so it is advantageous to place the detector near the lower end of the prior distribution in order to avoid "false positive" signal detections. The other is typically located near $f_1 \sim 1400$ Hz. This is because the broad-band shot noise grows rapidly with frequency in this band, so it is also advantageous to place the detector near the upper end of the prior distribution in order to combat the broad-band noise. The first effect is more important when the signal is weak; the second, when the signal is strong.

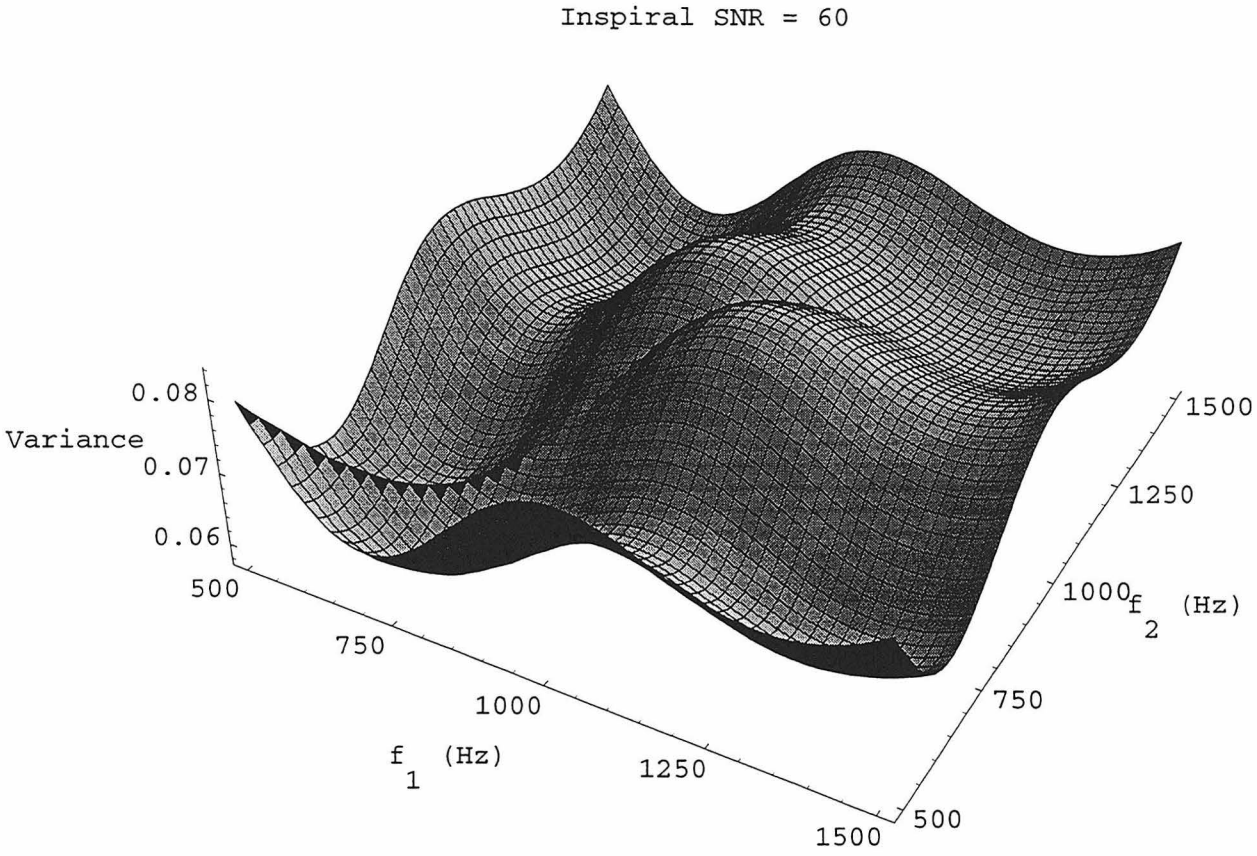

Figure 4.6: The anticipated variance for the toy model, using two narrow-band detectors, at $\rho_{\rm insp} = 60$.

The extrema of this function come in pairs, owing to the symmetry of $P_{\rm ant}(\lambda)$ under exchange of f_1, f_2. The minima are located at $f_1 \sim 700\,{\rm Hz}, 1400\,{\rm Hz}$, $f_2 \sim 700\,{\rm Hz}, 1400\,{\rm Hz}$, for the same reasons as given in the caption to Figure 4.5. In this case, the global minimum is located at $f_1 \simeq 620\,{\rm Hz}$, $f_2 \simeq 760\,{\rm Hz}$.

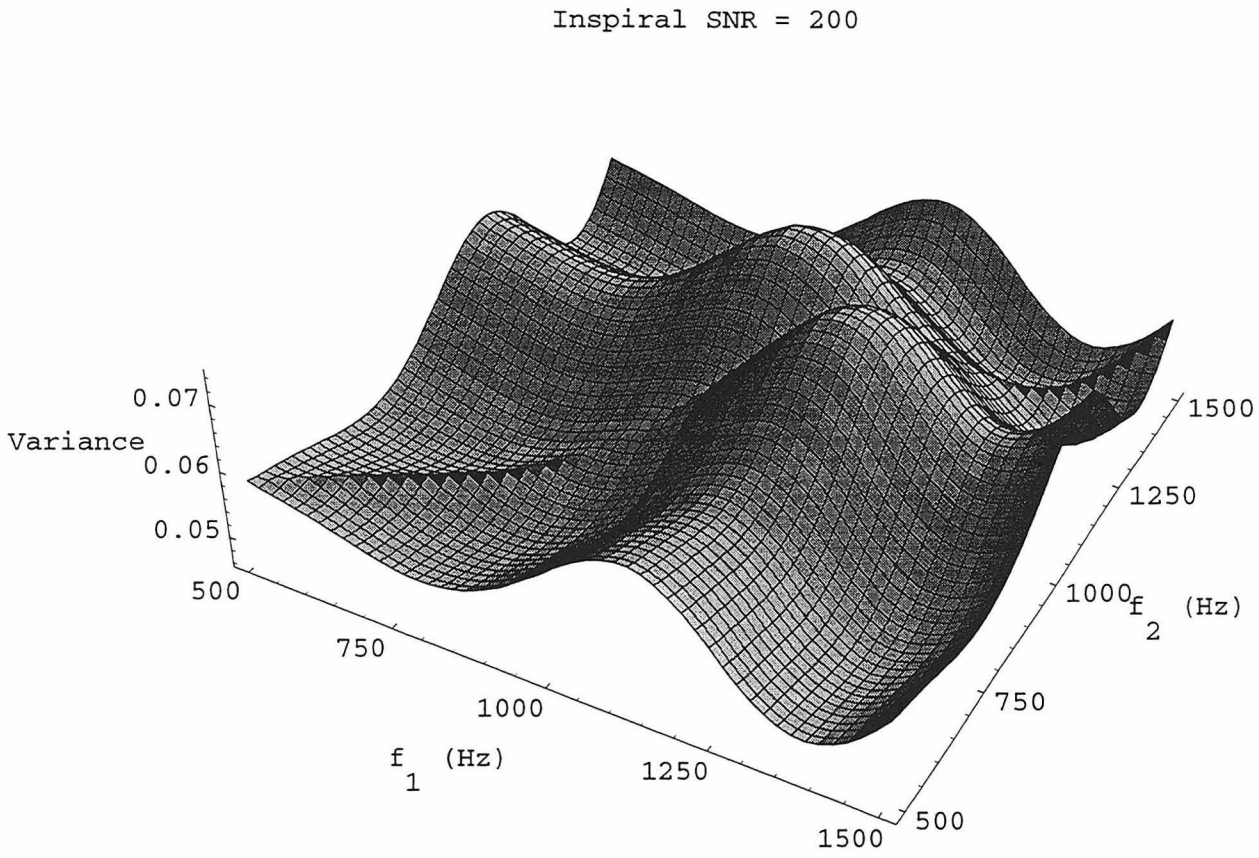

Figure 4.7: The anticipated variance for the toy model, using two narrow-band detectors, at $\rho_{\rm insp} = 200$.

In all respects except SNR, this figure is identical to Figure 4.6. The global minimum here is at $f_1 \simeq 740\,\mathrm{Hz}$, $f_2 \simeq 1380\,\mathrm{Hz}$.

Table 4.1: Optimal detector networks: one broad-band interferometer plus $N_{\rm DR}$ narrow-band interferometers.

The central frequencies of narrow-band interferometers for networks with one broad-band interferometer and $N_{\rm DR}$ narrow-band interferometers, for several values of inspiral SNR. These values are found using the toy waveform and a uniform prior probability distribution.

$N_{\rm DR}$	$\rho_{\rm insp} = 20$	$\rho_{\rm insp} = 100$	$\rho_{\rm insp} = 200$
2	$f_1 = 600$ Hz	$f_1 = 700$ Hz	$f_1 = 740$ Hz
	$f_2 = 650$ Hz	$f_2 = 1350$ Hz	$f_2 = 1380$ Hz
3	$f_1 = 600$ Hz	$f_1 = 600$ Hz	$f_1 = 700$ Hz
	$f_2 = 650$ Hz	$f_2 = 750$ Hz	$f_2 = 1300$ Hz
	$f_3 = 700$ Hz	$f_3 = 1350$ Hz	$f_3 = 1400$ Hz
4	$f_1 = 600$ Hz	$f_1 = 600$ Hz	$f_1 = 640$ Hz
	$f_2 = 640$ Hz	$f_2 = 730$ Hz	$f_2 = 760$ Hz
	$f_3 = 670$ Hz	$f_3 = 1300$ Hz	$f_3 = 1340$ Hz
	$f_4 = 700$ Hz	$f_4 = 1400$ Hz	$f_4 = 1430$ Hz
5	$f_1 = 600$ Hz	$f_1 = 570$ Hz	$f_1 = 640$ Hz
	$f_2 = 630$ Hz	$f_2 = 660$ Hz	$f_2 = 750$ Hz
	$f_3 = 660$ Hz	$f_3 = 770$ Hz	$f_3 = 1310$ Hz
	$f_4 = 690$ Hz	$f_4 = 1330$ Hz	$f_4 = 1400$ Hz
	$f_5 = 700$ Hz	$f_5 = 1400$ Hz	$f_5 = 1460$ Hz

of local minima, I took the global minimum to be the smallest local minimum. It may be possible to get better results using more robust global minimization methods, such as simulated annealing[2], especially when networks are designed with fewer symmetries than the (rather idealized) networks consider here.

Finally, Figures 4.8–4.11 demonstrate how repeated measurements of neutron star mergers with a given detector network will eventually converge, giving an accurate measurement of the true value $\hat{\lambda}$ present in the data. Figure 4.8 shows such a convergence when one narrow-band detector is used with an inspiral SNR $\rho_{\rm insp} = 50$, and when $\hat{\lambda} = 0.8$. The first plot, in the upper left, gives the posterior probability that would be obtained if no narrow-band detectors are used to measure the merger. It is practically flat — there is little information about λ in this distribution. For the first measurement, depicted in the upper right hand corner, minimization of the anticipated variance places the detector at $f_1 = 675$ Hz. Notice that the posterior distribution is near zero below $\lambda = 0.675$ and almost uniform above it. The reason for this is intuitively clear — there was significant power in gravitational waves at 675 Hz, so the probability distribution reflects the fact that $\lambda > 0.675$.

[2]Note, however, that (4.16) is a rather expensive function to evaluate; this is likely to make setting up an annealing schedule a rather painful process.

Now, use this posterior distribution as the prior distribution for the next measurement. Minimization of the anticipated variance places the detector at $f_1 = 770$ Hz. Qualitatively, the posterior distribution is similar to the distribution after the first measurement. Again, this is intuitively clear — there was significant gravitational-wave power at 770 Hz, so the distribution can only say that $\lambda > 0.770$. For the third measurement, minimization of the anticipated variance places the detector at $f_1 = 835$ Hz. Now, there is a drastic qualitative change in the shape of the posterior distribution: since there is no gravitational-wave power at $f_1 = 835$, the distribution shows it is very likely that $0.770 \leq \lambda \leq 0.835$. There is still, however, a large tail of the distribution at high λ. Further measurements would be necessary to reduce the size of this tail. Nonetheless, even with just one detector, it appears possible (in the context of this toy waveform) to get interesting merger information after just three measurements at moderate inspiral SNR.

Figure 4.9 presents the measurement convergence for a sequence of measurements identical to that used in Figure 4.8, except that now $\hat{\lambda} = 1.2$. The information about the merger is now buried in a region in which the broad-band noise is much higher (recall that the rms strain noise scales as $f^{3/2}$ in this regime — the noise amplitude in this case is about 1.8 times as large). Intuitively, we expect that it will take longer for the posterior distribution to become usefully peaked near the true value of λ present in the data. Figure 4.9 bears out this expectation: it takes about 10 measurements before the distribution shows peakedness. After 15 measurements, it is very well peaked.

Naturally, we expect that we can converge to an accurate value of λ more rapidly if multiple narrow-band detectors are used. Figure 4.10 is identical to Figure 4.8, except that two narrow-band detectors are used in the measurement sequence rather than one. Indeed, the posterior distribution is fairly well-peaked near $\lambda = \hat{\lambda}$ by the time that two measurements have been made, and is very well peaked after three. Likewise, Figure 4.11 is analogous to Figure 4.9. As in the case $\hat{\lambda} = 0.8$, the second detector effects a rather more rapid convergence to a peaked posterior probability distribution; however, as in the case of one detector, the convergence is still much slower than it is for smaller values of $\hat{\lambda}$.

4.5 Numerical waveforms

The results of the previous section indicate that the algorithm described here is effective at designing a detector network to measure characteristics of the NS-NS merger in the case of a simple toy model. Before claiming that is therefore an effective technique, it is salubrious to test the algorithm

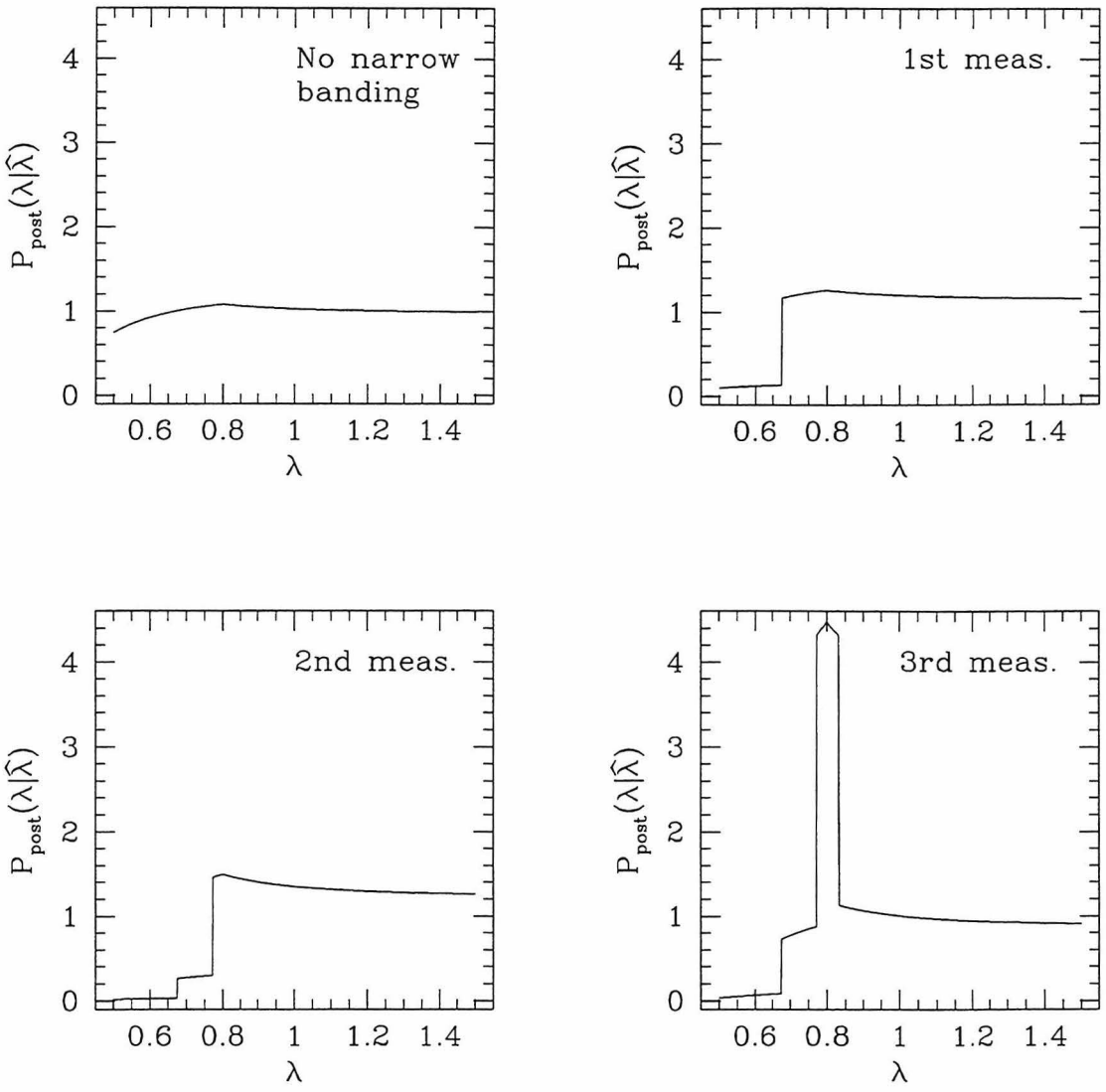

Figure 4.8: A sequence of measurements of the toy waveform model in which $\rho_{\rm insp} = 50$ and $\hat{\lambda} = 0.8$, using one narrow-band detector.

The upper left-most plot shows the posterior distribution when measuring with no narrow-band detectors. In the plot labeled "1st meas.," the location of the narrow-band detector has been chosen using a uniform prior probability distribution. The plot is the posterior probability distribution found after measurement. In the plot labeled "2nd meas.," the posterior probability from "1st meas." is used as the prior probability, both for selecting the new location of the narrow-band detector and in constructing the next posterior probability. The second posterior probability is rather similar to the first. Finally, the plot labeled "3rd meas." uses the second posterior probability as its prior. The third posterior probability is markedly peaked, indicating that the measurement sequence has begun to converge onto the "true" value, $\hat{\lambda}$.

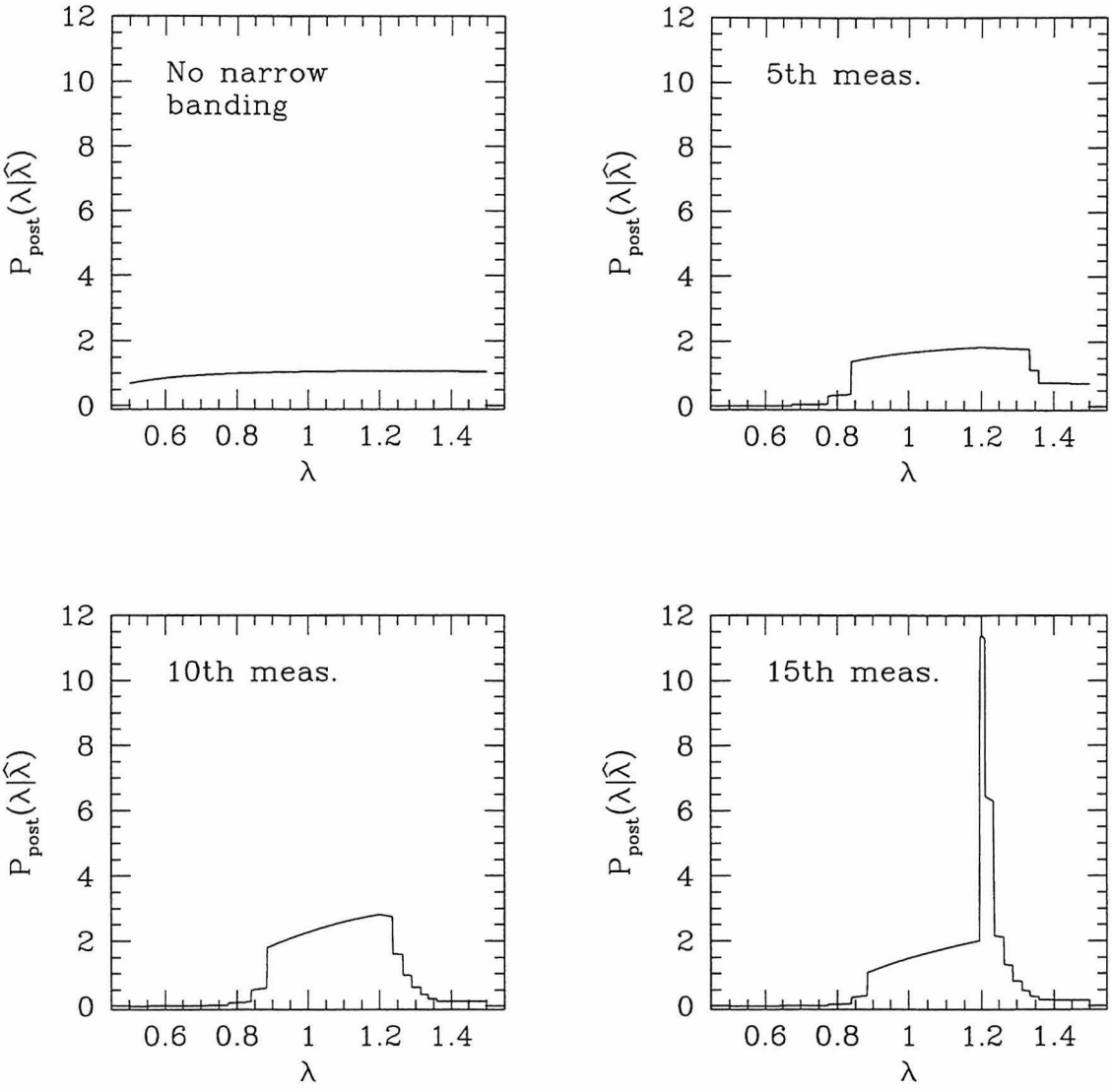

Figure 4.9: A sequence of measurements of the toy waveform model in which $\rho_{\text{insp}} = 50$ and $\hat{\lambda} = 1.2$, using one narrow-band detector.

This measurement sequence also convergence to a distribution that is peaked around $\lambda = \hat{\lambda}$; however, it takes many measurements. The reason is that the broad-band shot noise at 1200 Hz is rather larger than than at 800 Hz, and $\rho_{\text{insp}} = 50$ is not strong enough to compensate for the increased noise. Many measurements are therefore needed to get accurate information about λ.

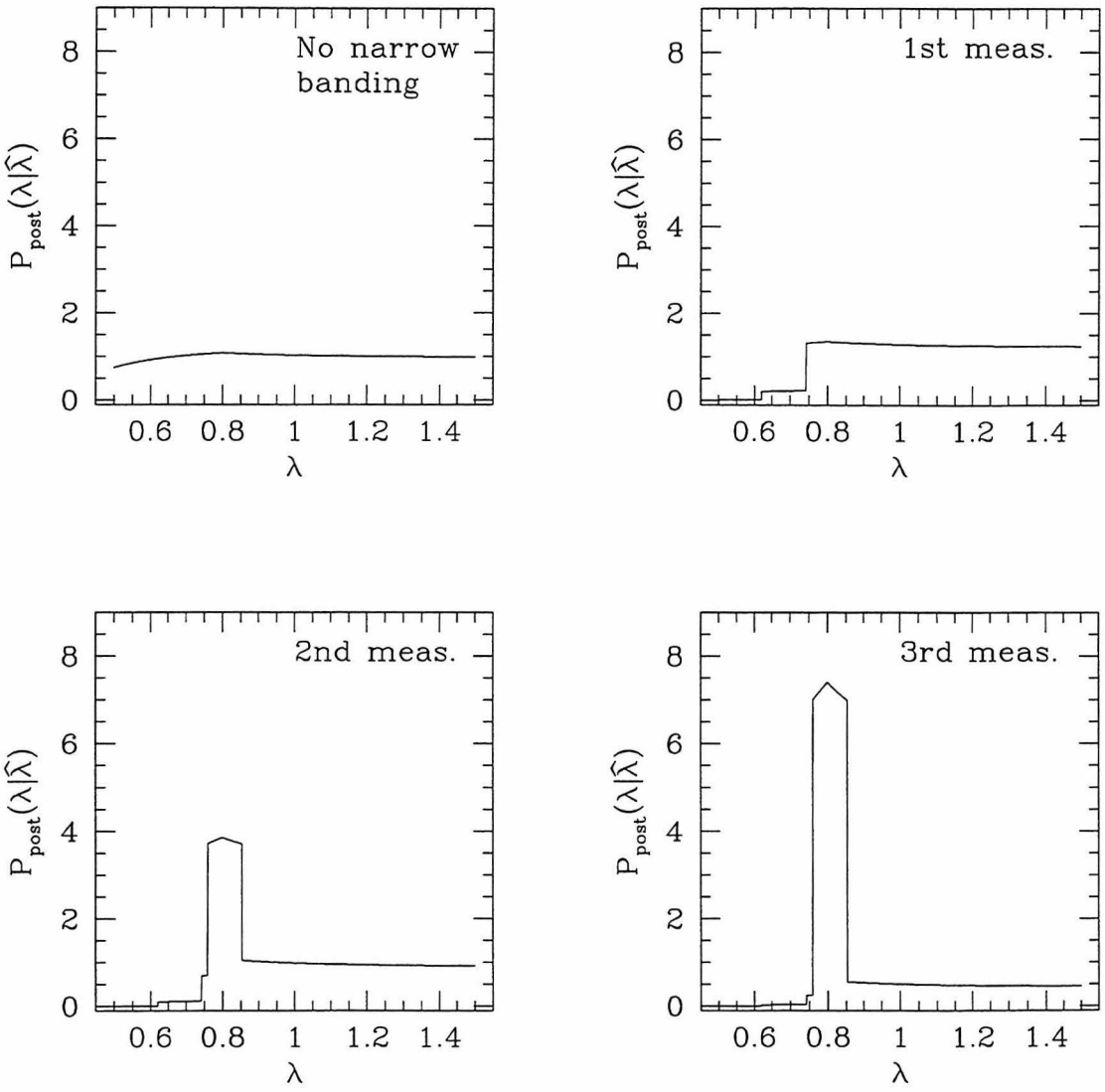

Figure 4.10: A sequence of measurements identical to that described in the caption to Figure 4.8, except that two narrow-band detectors are used.

Not surprisingly, the distribution converges to one peaked near $\hat{\lambda}$ more rapidly than when one narrow-band detector is used.

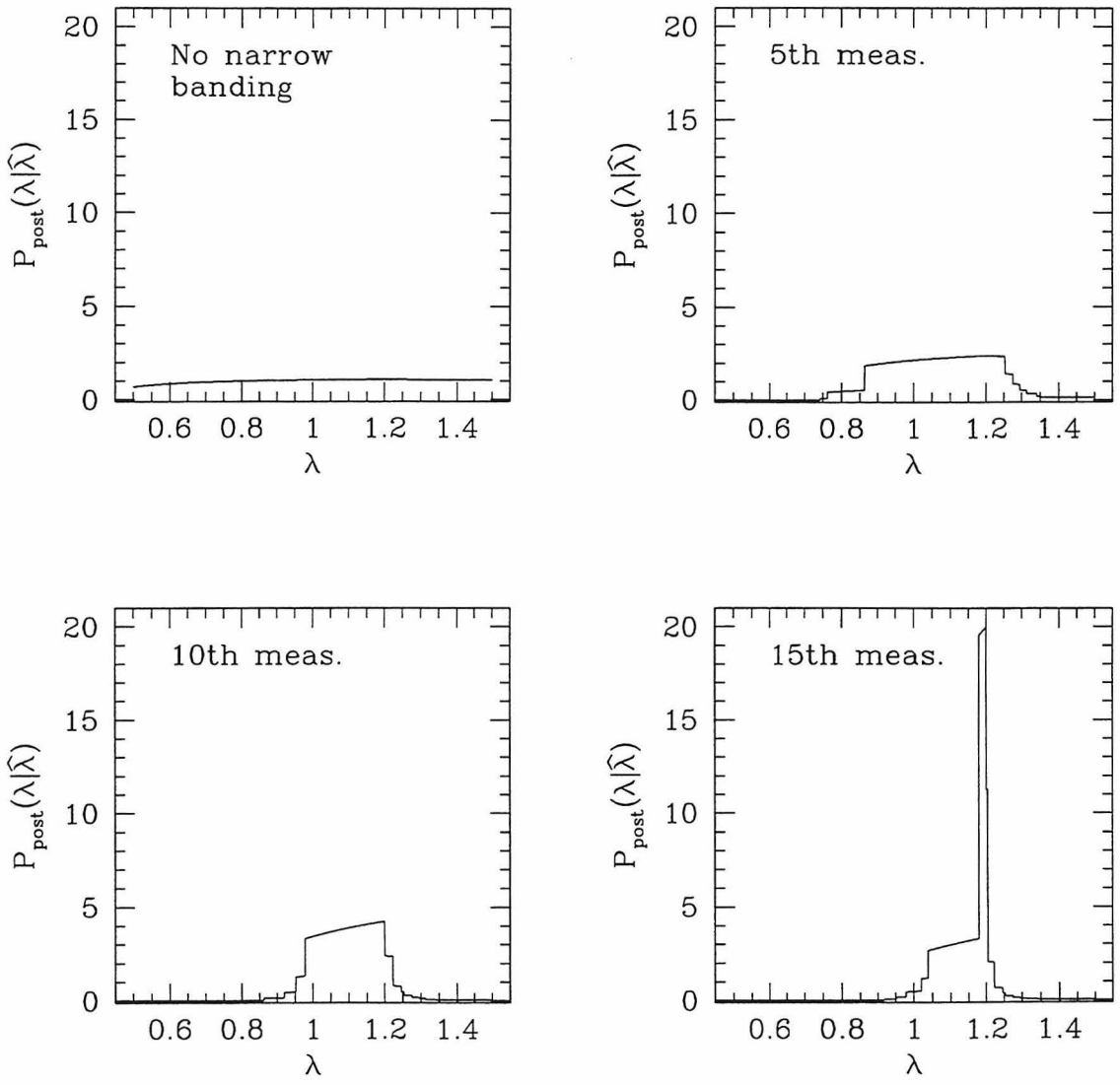

Figure 4.11: A sequence of measurements identical to that described in the caption to Figure 4.9, except that two narrow-band detectors are used.

The distribution again converges more slowly than when $\hat{\lambda} = 0.8$, but more quickly than when only one detector is used.

on merger waveforms with non-trivial structure. In this section, I test this algorithm on a model of the NS-NS merger that is based on the numerical waveforms of [25]. I describe exactly how I relate the model waveform h_λ to the waveforms of [25] in Sec. 4.5.1, and describe the results in Sec. 4.5.2. It is worth mentioning here that this analysis, of necessity, completely neglects the effects of neutron star mass ratio, and neutron star spins — there is, at present, simply no data available that incorporates such effects. These effects will have an influence, possibly quite important, on the merger waveform.

4.5.1 Technique

Using smooth-particle hydrodynamics (SPH) with Newtonian gravity and a polytropic equation of state, Zhuge, Centrella, and McMillan (hereafter ZCM) modeled the final merger of binary neutron stars [25]. I will focus on the waveforms produced by their run 1, which corresponds to a pair of $1.4\,M_\odot$ stars of radius 10 km, with polytropic index $n = 1$ (corresponding to adiabatic index $\Gamma = 2$). The plus polarization and energy spectrum of the gravitational radiation from this run are plotted in Figure 4.12. For concreteness, I will refer to this waveform as $h_{\rm ZCM}$.

Two important features are evident in Figure 4.12. First, the energy spectrum exhibits a peak at $f \sim 2500$ Hz, but swiftly drops after that. This corresponds roughly to the point at which the bodies come into contact, and is the behavior that is modeled by the sharp cut-off approximation used in Sec. 4.4. The second important feature, which is completely absent from the toy model, is the second peak at $f \sim 3200$ Hz. This peak appears to be due to the formation of a transient bar-like structure in the hydrodynamic detritus of the merged system.

The relevant frequencies of these structures are quite a bit higher than the frequencies that were analyzed in the toy model. This is typical of simulations that use Newtonian gravity; it seems likely that when the effects of general relativity on the NS-NS merger are fully accounted for, features such as these will crop up at lower frequencies. However, this is far from certain; only improved theoretical modeling — or observational evidence — will tell for certain.

The *ansatz* for the merger waveform which I will use in this section is that gross features of ZCM wave spectra are likely correct, but that the frequency band in which they appear may be shifted. More concretely, I assume

$$|\tilde{h}_\lambda(f)| = \lambda^{7/6}\,|\tilde{h}_{\rm ZCM}(\lambda f)|. \tag{4.40}$$

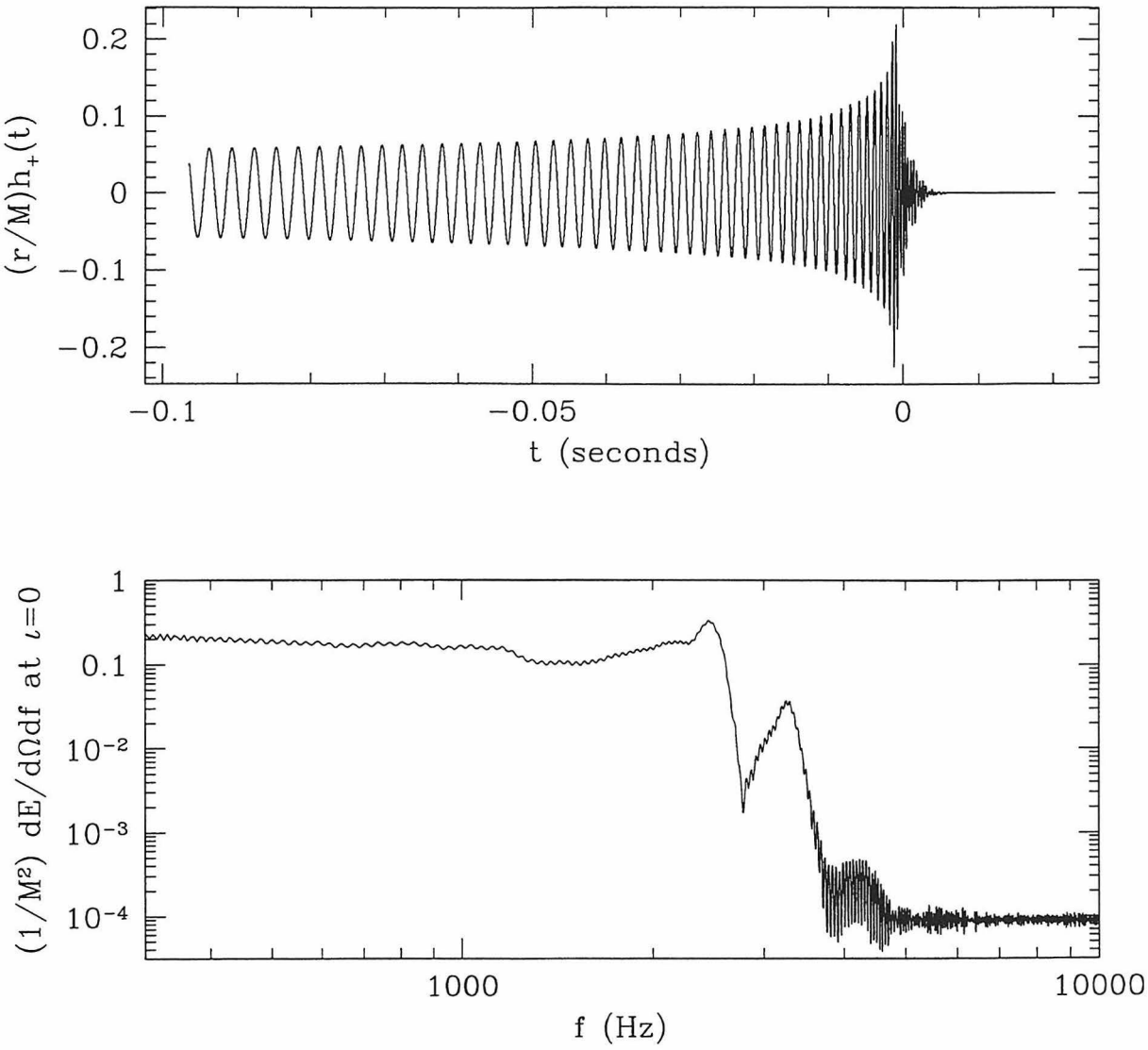

Figure 4.12: The + polarization and energy spectrum of the ZCM waveform.

The waveform is multiplied by r/M (where M is the total system mass, and r the distance to the source); the energy spectrum is per unit solid angle, evaluated at inclination angle $\iota = 0$, and multiplied by $1/M^2$. This waveform is taken from run 1 of ZCM; *cf.* their Fig. 6. Note that there is factor of two discrepancy between their figure and the figure here; this is because ZCM use the mass of a single neutron star for M, rather than the mass of the system. To calculate the energy spectrum, a point-mass inspiral was smoothly joined onto the numerical results; this is necessary to give accurate results at low frequencies.

Features at λf in the raw ZCM wave spectra are shifted to frequency f. The prefactor $\lambda^{7/6}$ is needed to insure that the "inspiral" portion of the waveform has the correct amplitude for all values of λ; recall that the inspiral waveform scales as $f^{-7/6}$.

The detector networks that I use in this analysis are identical to those used in Sec. 4.4 — a single broad-band interferometer and multiple dual-recycled narrow-band interferometers, with noise curves described as in Eq. (4.33). I assume in all calculations that the dual-recycled interferometers are narrow enough that Eq. (4.35) is an adequate description.

4.5.2 Results

To understand how well the ZCM waveform can be measured using broad and narrow-band detectors in concert, I again examine a sequence of measurements using some number of narrow-band detectors, fixing $\rho_{\rm insp} = 50$. The most striking result of this analysis is that it takes many more measurements to measure λ with reasonable accuracy when measuring the ZCM waveform than when measuring the toy waveform. Consider Figs. 4.13 and 4.14. These figures exhibit the convergence of repeated measurements to a peaked probability distribution in the cases $\hat{\lambda} = 2$ and $\hat{\lambda} = 1.2$, respectively. In both cases, $N_{\rm DR} = 2$. Notice that in both cases, the distribution is effectively not peaked at all until around 30 measurements have been made; after 50 measurements, the peak is reasonably well-developed, but is nonetheless rather broad.

Obviously, features of the ZCM waveform are quite a bit more difficult to measure in this measurement paradigm that are the features of the toy model. The reason for this is clear when one examines the ZCM waveform in the frequency domain (*cf.* the power spectrum in Fig. 4.12): with only a small number of narrow-band instruments, it is difficult for measurements to distinguish between gravitational-wave power in the primary peak at $f \lesssim 2500$ Hz and in the secondary peak at $f \lesssim 3200$ Hz. The energy spectrum is not sharp, as it is in the toy model, so many repeated measurements are needed in order to effectively measure λ.

The situation is not quite so grim if more narrow-band instruments are used to make measurements. In Fig. 4.15, I show a measurement sequence in which three dual-recycled interferometers are used to analyze the ZCM merger with $\hat{\lambda} = 2$, and in Fig. 4.16 I show a sequence with four dual-recycled interferometers. With more dual-recycled instruments, the observer has greater ability to probe the details of the merger spectrum, and is better able to distinguish between the waveform's various features. This is apparent in these figures: increasing the number of narrow-band instruments quickens the speed with which a measurement sequence converges to a well-peaked

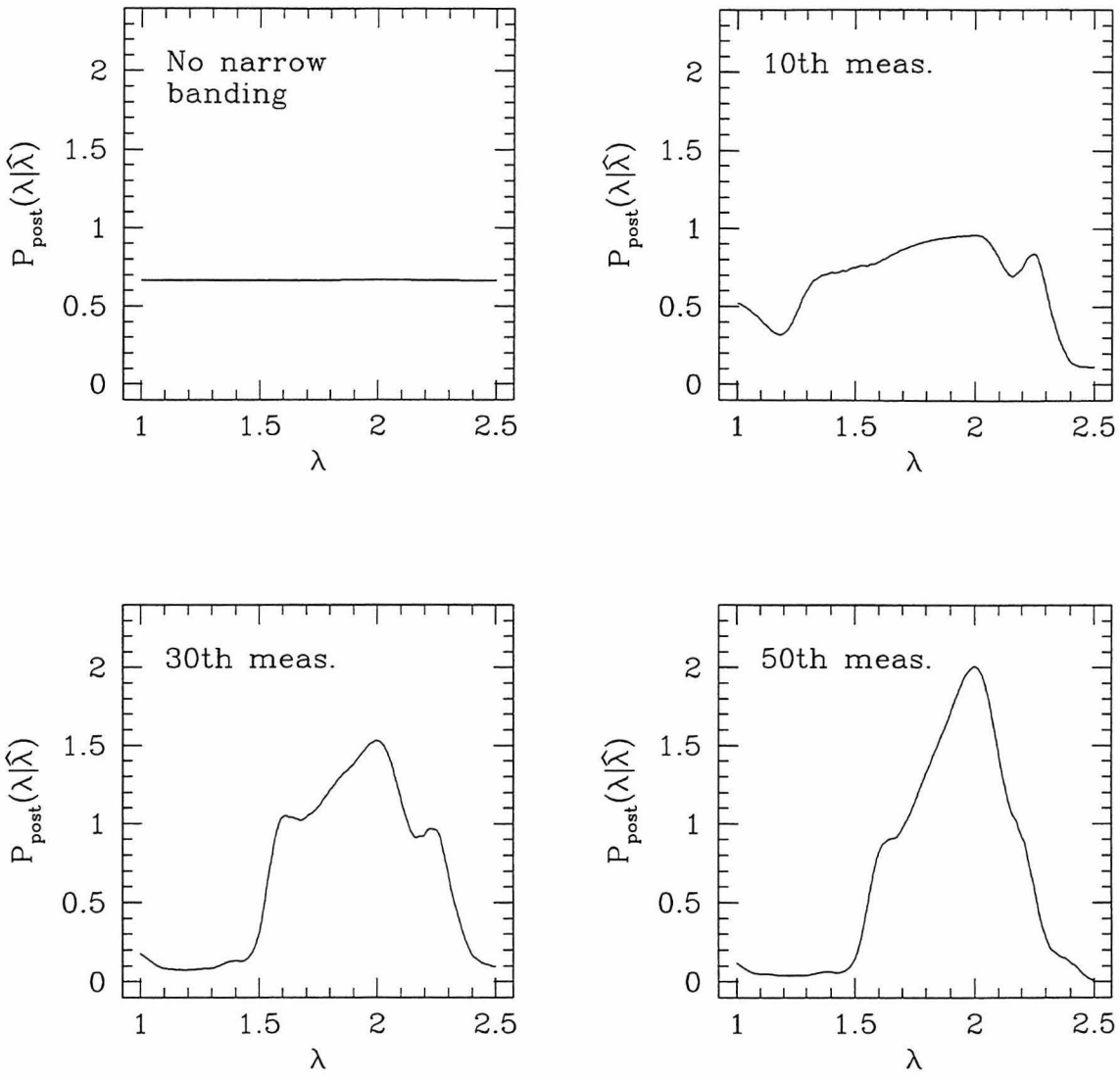

Figure 4.13: A sequence of measurements of the ZCM waveform, for which $\rho_{\rm insp} = 50$ and $\hat{\lambda} = 2$, using two narrow-band detectors.

The upper left-most plot shows the posterior distribution when measuring with no narrow-band detectors. The following plots are the posterior probability distributions for the 10th, 30th, and 50th measurements. Notice that the distribution is not particularly peaked until roughly the 30th measurement, and the peak is only strongly pronounced after 50 measurements. Even in that case, the distribution is still rather broad, especially compared to the toy distribution. The reason is that the measurement algorithm has difficulty discriminating between the many features at high frequencies that are apparent in Fig. 4.12. It can only discriminate among these features with certainty after very many measurements have been taken. If the true NS-NS merger waveform resembles the ZCM waveform, learning about the merger characteristics may take a very long time.

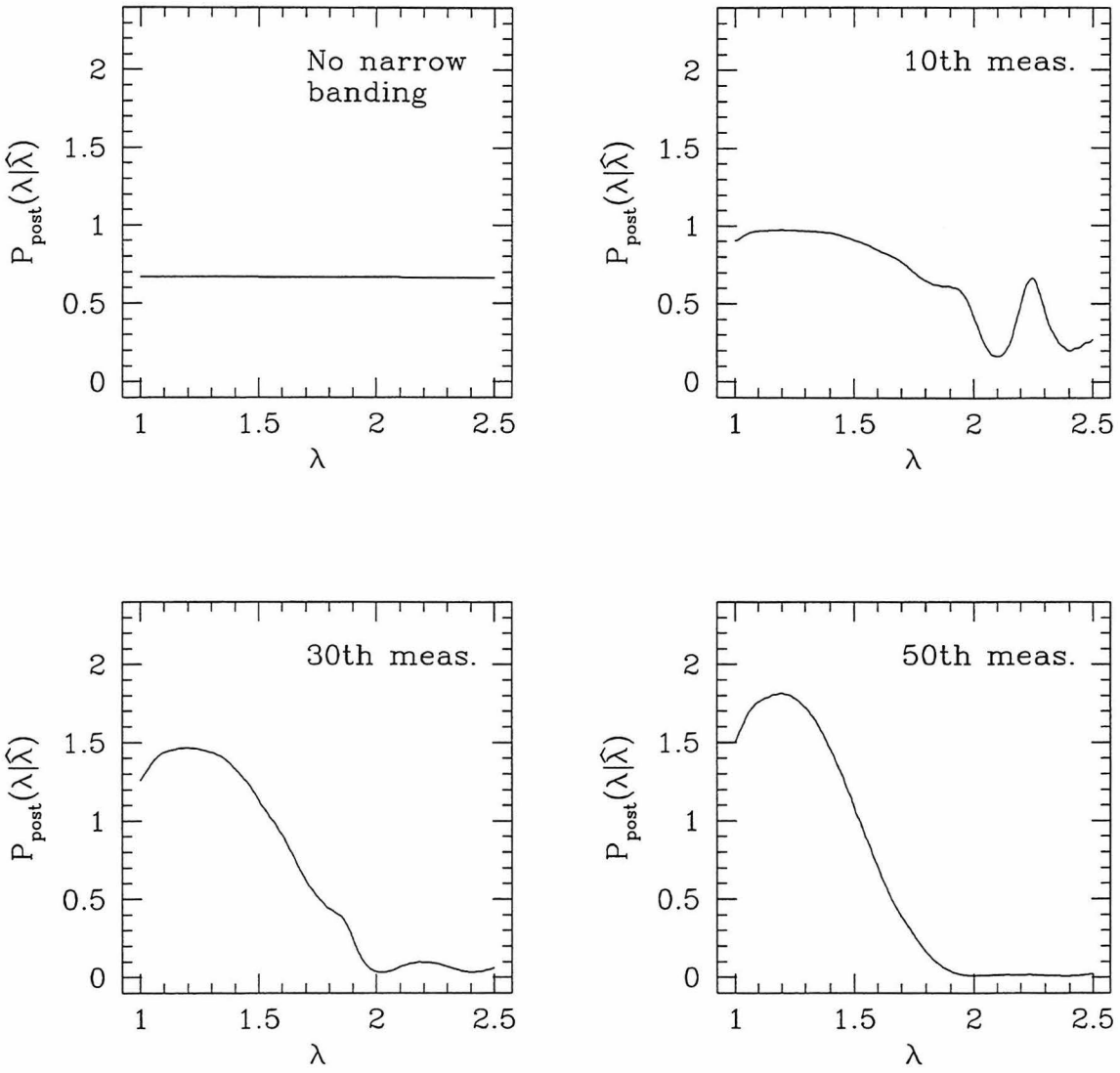

Figure 4.14: A sequence of measurements of the ZCM waveform, for which $\rho_{\text{insp}} = 50$ and $\hat{\lambda} = 1.2$, using two narrow-band detectors.

This scenario is much the same as in the case $\hat{\lambda} = 2$; in this waveform model, changing the value of $\hat{\lambda}$ does not have as striking an effect as it does with the toy model.

probability distribution for λ (although it remains rather slow compared to the toy model). This is not particularly surprising, but it is gratifying to see that this analysis performs as one intuitively expects. Further increasing the number of narrow-band detectors would be useful, but begins to become rather computationally intensive — as described above, finding the optimal configuration of $N_{\rm NB}$ narrow-band detectors involves locating the global minimum of a function in an $N_{\rm NB}$-dimensional parameter space in the presence of many local minima.

4.6 Conclusions and Summary

In this chapter, I have presented an algorithm for configuring a network of gravitational-wave detectors in order to most effectively measure information about the final merger of binary neutron stars. This algorithm is based on Bayesian probability distributions, and can be naturally updated to incorporate information about the final merger waves. As such information becomes available, the effectiveness of the algorithm improves.

In the context of a rather simple detector network (a single broad-band laser interferometer with advanced LIGO sensitivity, plus some number $N_{\rm DR}$ of narrow-band dual-recycled laser interferometers), I have demonstrated that iterating the algorithm on multiple binary neutron star coalescence measurements converges, in the sense that the information that one obtains about the NS-NS merger becomes accurate after repeated measurements. However, the number of measurements required to achieve such convergence depends quite strongly on details of the gravitational waveform. Convergence is very rapid in the case of a sharp-cutoff model of the merger, but is much slower when the merger has interesting features that might not be easily distinguished with a small number of narrow-band instruments.

Several conclusions may be drawn from this. First, it is clear that the design of future gravitational-wave detectors will need input from reliable, fully relativistic binary neutron star coalescence studies. The two waveforms considered here probably aren't reliable enough for this purpose, but probably are indicative of the extremes: the toy model has no interesting features beyond a certain frequency, and the ZCM model has several interesting features near one another in frequency space. The quality and distribution of features in accurate, relativistic waveforms will have a strong impact on how well observers will be able to study the characteristics of NS-NS mergers.

Second, future studies should examine detector networks that are more sophisticated than the

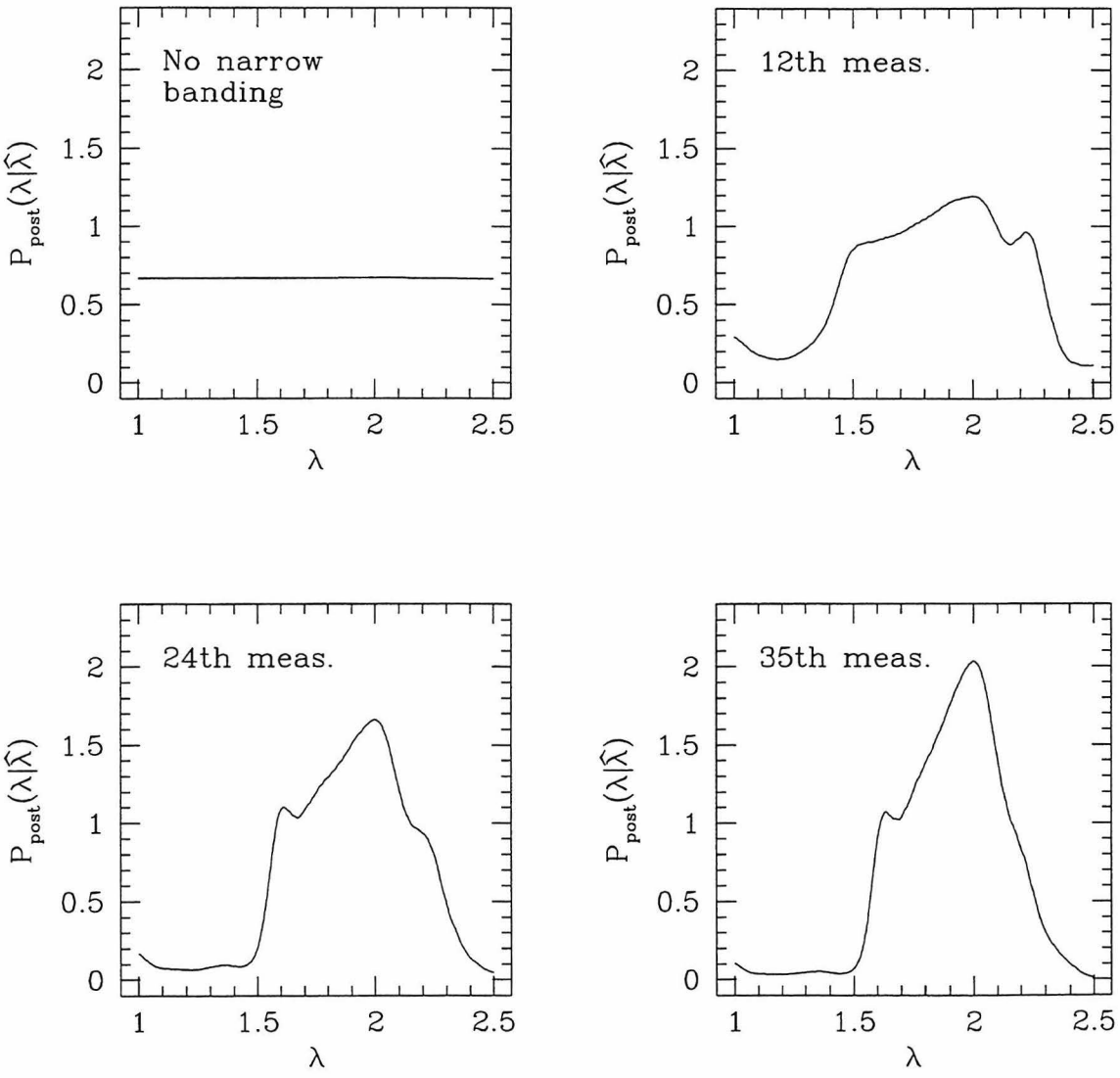

Figure 4.15: A sequence of measurements of the ZCM waveform, for which $\rho_{\text{insp}} = 50$ and $\hat{\lambda} = 2.0$, using three narrow-band detectors.

Notice that the convergence of the measurement sequence is somewhat accelerated, compared to when two detectors are used, although it is still rather lengthy.

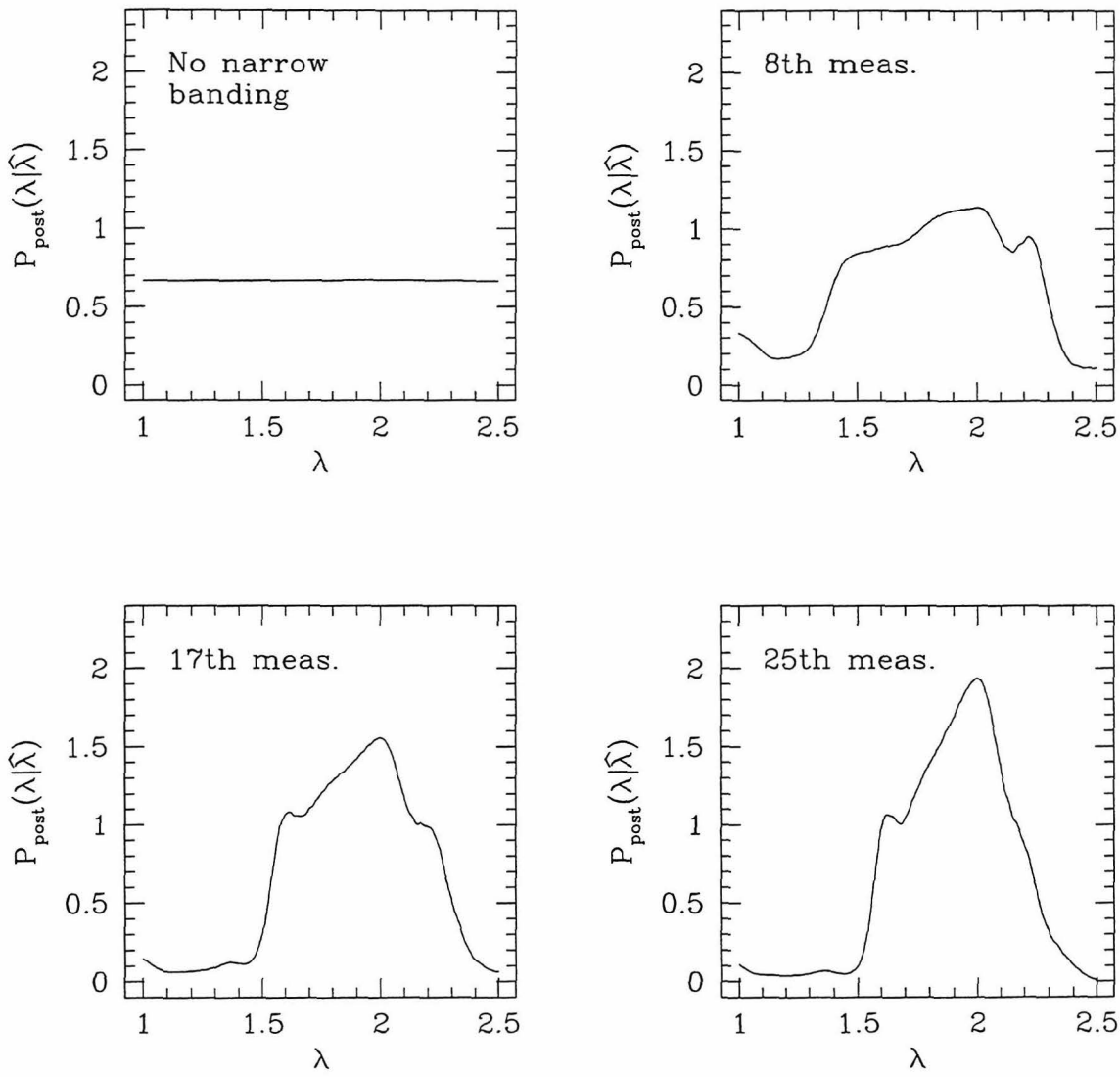

Figure 4.16: A sequence of measurements of the ZCM waveform, for which $\rho_{\text{insp}} = 50$ and $\hat{\lambda} = 2.0$, using four narrow-band detectors.

The sequence converges still more rapidly in this case.

simple networks considered here. I consider only a single broad-band detector coupled with a rather small ($N_{\rm DR} \leq 4$) number of dual-recycled interferometers; also, I ignore all correlations between instruments, and use an approximation to the dual-recycling sensitivity curve that is extremely simple. Relaxing these assumptions and approximations is likely to have some effect on how robustly the measurement sequence tends to converge. Future work should incorporate resonant mass detectors, multiple broad-band instruments, and should study measurement with more than 4 narrow-band detectors. The goal here was to present the network design algorithm and test it on simple, easy-to-handle cases; it is now time to seriously consider realistic, non-toy networks that will be used in the future.

Finally, thought should be given to ways in which the algorithm presented here could be improved. In the case of the ZCM model waveform, the measurement sequence converges slowly because the algorithm has difficulty discriminating between power at $f \lesssim 2500$ Hz (*i.e.*, the inspiral and early phase of merger) and power in the secondary peak at $f \lesssim 3200$ Hz. It may be possible to improve the algorithm's discriminating ability, perhaps by comparing the amplitude of waves at different frequencies and then deciding whether it is more consistent to ascribe that amplitude to the inspiral phase or to the merger phase. Such an extension is likely to depend strongly on models of the NS-NS coalescence; and, it is also likely to be very sensitive to noise. More work is needed to develop such algorithms if binary neutron star merger measurements are to be effective.

Acknowledgments

I thank Kip Thorne, who played an instrumental role in helping develop the major ideas that lie at the core of this paper, and offered helpful comments and criticisms. I also thank Joan Centrella for permission to use the numerical waveforms generated by Zhuge, Centrella, and McMillan; Andrzej Królak for discussions regarding laser shot noise; Jim Mason for discussions regarding dual-recycling and resonant sideband extraction; and Yuri Levin for suggesting that the integral for the posterior probability distribution might be regarded as a path integral. This research was supported by NSF Grant PHY–9424337. I gratefully acknowledge the support of a National Science Foundation Graduate Fellowship.

Appendix A Evaluation of the integral (4.12)

In this appendix, I evaluate the integral (4.12) and thereby calculate the posterior probability distribution $P_{\rm post}(\lambda|\hat{\lambda})$. First, consider only one detector. In this case, the integral may be written

$$P_{\rm post}(\lambda|\hat{\lambda}) = p_0(\lambda)\int \exp\left[-\frac{1}{2}(n|n)\right]\exp\left[-\frac{1}{2}(\delta h|\delta h) - (n|\delta h) - \frac{1}{2}(n|n)\right]\mathcal{D}n, \qquad (4.41)$$

where the "one-detector" inner product is given by

$$(a|b) = 4\,\mathrm{Re}\int_0^\infty \frac{\tilde{a}(f)^*\tilde{b}(f)}{S_h(f)}\,df. \qquad (4.42)$$

Consider now discretely sampled data of finite duration T. Let the sampling time be Δt, and make the following definitions:

$$\begin{aligned} t_i &= i\Delta t, \qquad i = 1,\ldots,\mathcal{N}, \\ a_i &= a(t_i), \\ C_{n,ij} &= C_n(t_i - t_j). \end{aligned} \qquad (4.43)$$

Here, $C_n(t)$ is the noise autocorrelation, defined by

$$C_n(\tau) = \mathrm{E}\{n(t)n(t+\tau)\}_n, \qquad (4.44)$$

and related to the spectral density of noise by

$$S_h(f) = 2\int_{-\infty}^{\infty} e^{2\pi i f\tau} C_n(\tau)\,d\tau. \qquad (4.45)$$

For notational simplicity, let $\mathbf{a}$ be the vector whose components are a_i, and let $\mathbf{C}_n$ be the matrix whose components are $C_{n,ij}$. Note that $\mathbf{C}_n$ is a real, symmetric matrix.

Using these definitions, the inner product (4.42) may be written [*cf.* [24], Eq. (2.20)]

$$(a|b) = \lim_{\substack{\Delta t\to 0\\ T\to\infty}} \mathbf{a}\cdot\mathbf{C}_n^{-1}\cdot\mathbf{b}. \qquad (4.46)$$

The probability distribution (4.41) can therefore be written

$$P_{\rm post}(\lambda|\hat{\lambda}) = \lim_{\substack{\Delta t \to 0 \\ T \to \infty}} p_0(\lambda) \int \exp\left[-\mathbf{n}\cdot\mathbf{C}_n^{-1}\cdot\mathbf{n} - \mathbf{n}\cdot\mathbf{C}_n^{-1}\cdot\delta\mathbf{h} - \frac{1}{2}\delta\mathbf{h}\cdot\mathbf{C}_n^{-1}\cdot\delta\mathbf{h}\right] d\mathbf{n}. \tag{4.47}$$

This integral is of a form commonly encountered in path integral quantization (see, for example, [39]). It evaluates to

$$\begin{aligned} P_{\rm post}(\lambda|\hat{\lambda}) &= \lim_{\substack{\Delta t \to 0 \\ T \to \infty}} p_0(\lambda) \exp\left[-\frac{1}{4}\delta\mathbf{h}\cdot\mathbf{C}_n^{-1}\cdot\delta\mathbf{h}\right] \\ &= p_0(\lambda)\exp\left[-\frac{1}{4}(\delta h|\delta h)\right]. \end{aligned} \tag{4.48}$$

[I have absorbed a constant factor which is proportional to $1/\sqrt{\det \mathbf{C_n}}$ into the prior probability $p_0(\lambda)$.]

Now consider the entire detector network:

$$P_{\rm post}(\lambda|\hat{\lambda}) = P(\vec{h}_\lambda)\int \exp\left[-\frac{1}{2}(\vec{n}|\vec{n})\right]\exp\left[-\frac{1}{2}(\delta\vec{h}|\delta\vec{h}) - (\vec{n}|\delta\vec{h}) - \frac{1}{2}(\vec{n}|\vec{n})\right]\mathcal{D}\vec{n}. \tag{4.49}$$

Recall that the "network" inner product is

$$(\vec{a}|\vec{b}) \equiv 4\,\mathrm{Re}\int_0^\infty df\ \tilde{a}_i(f)^*\left[\mathbf{S}_h(f)^{-1}\right]^{ij}\tilde{b}_j(f). \tag{4.50}$$

Because the matrix $\mathbf{S}_h(f)^{-1}$ is real and symmetric, its eigenvectors are orthonormal. If the matrix of eigenvectors is $\mathbf{A}$ then $\mathbf{A}^{-1} = \mathbf{A}^T$, so the matrix

$$\mathbf{Z}_h(f)^{-1} = \mathbf{A}\cdot\mathbf{S}_h(f)^{-1}\cdot\mathbf{A}^T \tag{4.51}$$

is diagonal. Let us further define

$$\begin{aligned} \tilde{a}'_j(f)^* &= \tilde{a}_i(f)^* A^i_j, \\ \tilde{b}'_j(f) &= A^i_j\tilde{b}_i(f). \end{aligned} \tag{4.52}$$

Using (4.51) and (4.52), (4.50) can be written

$$\begin{aligned}(\vec{a}|\vec{b}) &= 4\,\mathrm{Re}\int_0^\infty \tilde{a}_n(f)^* A_k^n A_i^k \left[\mathbf{S}_h(f)^{-1}\right]^{ij} A_j^l A_j^m \tilde{b}_m(f)\,df \\ &= 4\,\mathrm{Re}\int_0^\infty \tilde{a}'_k(f)^* \left[\mathbf{Z}_h^{-1}(f)\right]^{kl} \tilde{b}'_l(f)\,df \\ &= \sum_k 4\,\mathrm{Re}\int_0^\infty \tilde{a}'_k(f)^* \left[\mathbf{Z}_h^{-1}(f)\right]^{kk} \tilde{b}'_k(f)\,df \\ &\equiv \sum_k \langle a'_k|b'_k\rangle_k. \end{aligned} \tag{4.53}$$

The third equality follows from the fact that the matrix $\mathbf{Z}_h^{-1}(f)$ is diagonal. The inner product $\langle a'_k|b'_k\rangle_k$ is identical to the inner product (4.42) except that $[\mathbf{Z}_h^{-1}]^{kk}$ is used as the weighting function instead of $1/S_h(f)$. Eq. (4.49) can now be written

$$\begin{aligned}P_{\mathrm{post}}(\lambda|\hat{\lambda}) &= P(\vec{h}_\lambda)\int \exp\left[-\sum_k\left(\frac{1}{2}\langle\delta h'_k|\delta h'_k\rangle_k + \langle n'_k|\delta h'_k\rangle_k + \langle n'_k|n'_k\rangle_k\right)\right]\mathcal{D}\vec{n}' \\ &= P(\vec{h}_\lambda)\prod_k\int \exp\left[-\frac{1}{2}\langle\delta h'_k|\delta h'_k\rangle_k - \langle n'_k|\delta h'_k\rangle_k - \langle n'_k|n'_k\rangle_k\right]\mathcal{D}n'_k. \end{aligned} \tag{4.54}$$

(Since the matrix $\mathbf{A}$ is unitary, the functional differential element $\mathcal{D}\vec{n}' = \mathcal{D}\vec{n}$.) The integral on the last line of (4.54) is identical to (4.41), except for the slightly different inner product. The result is therefore

$$\begin{aligned}P_{\mathrm{post}}(\lambda|\hat{\lambda}) &= P(\vec{h}_\lambda)\prod_k \exp\left[-\frac{1}{4}\langle\delta h'_k|\delta h'_k\rangle_k\right], \\ &= P(\vec{h}_\lambda)\exp\left[-\frac{1}{4}\sum_k\langle\delta h'_k|\delta h'_k\rangle_k\right], \\ &= P(\vec{h}_\lambda)\exp\left[-\frac{1}{4}(\delta\vec{h}|\delta\vec{h})\right]. \end{aligned} \tag{4.55}$$

This is the result claimed in Eq. (4.13).

Bibliography

[1] Information about LIGO's early planned operations can be found at the URL

http://www.ligo.caltech.edu/LIGO_web/Collaboration/lsc_interm.html .

[2] C. Bradaschia *et al.*, Nucl. Instrum. & Methods **A289**, 518 (1990); also in *Gravitation: A Banff Summer Institute*, ed. R. Mann and P. Wesson (World Scientific, Singapore, 1991).

[3] J. Hough *et al*, *GEO600, Proposal for a 600 m Laser-Interferometric Gravitational-wave Antenna*, unpublished, 1994.

[4] Information regarding, and a description of the TAMA (Tokyo Advanced Medium-scale Antenna) project can be found at the URL

http://tamago.mtk.nao.ac.jp .

[5] Information regarding ACIGA (the Australian Consortium for Interferometric Gravitational Astronomy) can be found at the URL

http://www.anu.edu.au/Physics/ACIGA/ .

[6] K. S. Thorne, in *Proceedings of the Snowmass 95 Summer Study on Particle and Nuclear Astrophysics*, eds. E. W. Kolb and R. Peccei (World Scientific, Singapore, 1995); gr-qc/9506086.

[7] E. S. Phinney, Astrophys. J. **380**, L17 (1991); R. Narayan, T. Piran, and A. Shemi, Astrophys. J. **379**, L17 (1991); E. P. J. Van den Heuvel and D. R. Lorimer, Mon. Not. R. Astron. Soc. **283**, L37 (1996); A. V. Tutukov and L. R. Yungelson, Mon. Not. R. Astron. Soc. **260**, 675 (1993); S. F. P. Zwart and L. R. Yungelson, "Formation and evolution of binary neutron stars", Astron. Astrophys. (to be published), astro-ph/9710347.

[8] A. Abramovici *et al.*, *LIGO: The Laser Interferometer Gravitational-wave Observatory*, Science **256**, 325 (1992).

[9] E. Poisson and C. M. Will, Phys. Rev. D **52**, 848 (1995).

[10] L. Lindblom, Ap. J **398**, 569 (1992).

[11] C. Cutler *et al*, Phys. Rev. Lett. **70**, 2984 (1993). Xylophones of narrow-band detectors are discussed in the text surrounding Eq. (3). Note also that the right hand side Eq. (3) is a factor of $\sqrt{2}$ large, coming from an error in the integral of the inverse noise spectral density given in their endnote [23]. The correct integral is

$$\int_0^\infty \frac{df}{S_h^{\rm DR}(f)} = \frac{\pi\eta I_0}{4\hbar}\frac{L_{\rm arm}}{\lambda_{\rm laser}}\frac{1}{A^2},$$

as can be easily verified using Eq. (4.22) above.

[12] D. Kennefick, D. Laurence, and K. S. Thorne, in *Proceedings of the 7th Marcel Grossman Meeting*, edited by R. T. Jantzen and G. MacKeiser (World Scientific, Singapore, 1997), pp. 1090–1092.

[13] The ALLEGRO experiment, at Louisiana State University, is described in the URL

http://phwave.phys.lsu.edu/www/allegro/index.html ;

The Rome group's Explorer, Nautilus, and Altair antennae are described in

http://www.roma1.infn.it/rog/rogmain.html ;

and the Italian AURIGA experiment is described in

http://axln01.lnl.infn.it .

[14] The American TIGA project is described in the URL

http://phwave.phys.lsu.edu/www/tiga/index.html ;

the Dutch GRAIL project is described in

http://www.nikhef.nl/pub/projects/grail/grail.html ;

the Brazilian spherical bar project is described in

http://crux.das.inpe.br/~graviton/home.html ;

and the Italian SFERA project is described in

http://www.roma1.infn.it/rog/sphere .

All of these groups are brought together under the aegis of the OMEGA collaboration, described at

http://phwave.phys.lsu.edu/omega/ .

[15] B. J. Meers, Phys. Rev. D **38**, 2317 (1988).

[16] J. Y. Vinet, B. Meers, C. N. Man, and A. Brillet, Phys. Rev. D **38**, 433 (1988).

[17] A. Królak, J. A. Lobo, and B. J. Meers, Phys. Rev. D **43**, 2470 (1991).

[18] A. Królak, *Acta Cosmologica*, Fasciculus XXII-1, 1996.

[19] J. Mizuno *et al*, Phys. Lett. A, **175**, 273 (1993); J. Mizuno, Max-Planck-Institut für Quantenoptik report 203, "Comparison of optical configurations for laser-interferometric gravitational-wave detectors", unpublished Ph.D thesis, 1996.

[20] S. M. Merkowitz and W. W. Johnson, Phys. Rev. D **51**, 2546 (1995).

[21] G. M. Harry, T. R. Stevenson, and H. J. Paik, Phys. Rev. D **54**, 2409 (1996).

[22] Note that I approximated the factor $\sum |B_{mj}|^2$ [from Eq. (40) of [20]] to be 1; the validity of this approximation can easily be verified using the definition of B_{mj} [*cf.* Eq. (23) of [20]] and the resonator angular distribution shown in Fig. 7 of [20].

[23] N. S. Magalhães *et al*, Gen. Rel. Grav. **29**, 1511 (1997).

[24] L. S. Finn, Phys. Rev. D **46**, 5236 (1992).

[25] X. Zhuge, J. M. Centrella, and S. L. W. McMillan, Phys. Rev. D **50**, 6247 (1994).

[26] É. É. Flanagan and S. A. Hughes, Phys. Rev. D **57**, 4566 (1998); also Chapter 3.

[27] É. É. Flanagan and S. A. Hughes, Phys. Rev. D **57**, 4535 (1998); also Chapter 2.

[28] D. Marković, Phys. Rev. D **48**, 4738 (1993).

[29] L. S. Finn, in preparation; L. S. Finn, private communication.

[30] W. H. Press, S. A. Teukolsky, W. T. Vetterling, and B. P. Flannery, *Numerical Recipes*, Second edition (Cambridge University Press, Cambridge, 1992).

[31] K. S. Thorne, in *300 Years of Gravitation*, ed. S. W. Hawking and W. Israel (Cambridge University Press, Cambridge, 1987), pp. 380–458.

[32] L. S. Finn and D. F. Chernoff, Phys. Rev. D **47**, 2198 (1993).

[33] É. É. Flanagan and C. Cutler, Phys. Rev. D **49**, 2658 (1994).

[34] D. Lai and A. G. Wiseman, Phys. Rev. D **54**, 3958 (1996).

[35] The results of Lai and Wiseman are found by combining the hybrid equations of motion of [36] with the extended body potentials of [37]. This method gives a "best-guess" of the location of the innermost stable circular orbit (ISCO) when post-Newtonian corrections due to general relativity are combined with finite size effects. However, it is worth noting that recent work [38] indicates the hybrid equations of motion may not reliably predict the location of the ISCO. Using Padé approximants to construct from the (non-convergent) post-Newtonian series a rational expression for the orbital energy, Ref. [38] puts the ISCO at roughly 2000 Hz, compared to roughly 1400 Hz in [36]. However, finite size effects are not taken into account in [38]; as noted by Lai and Wiseman, such effects will decrease the frequency of the ISCO. The frequency range used here for the toy waveform (500 Hz $\leq f \leq$ 1500 Hz) should be accurate enough for test the network design algorithm.

[36] L. E. Kidder, C. M. Will, and A. G. Wiseman, Phys. Rev. D, **47**, 3281 (1993).

[37] D. Lai, F. A. Rasio, and S. L. Shapiro, Astrophys. J **420**, 811 (1994).

[38] T. Damour, B. R. Iyer, and B. S. Sathyaprakash, Phys. Rev. D **57**, 885 (1998).

[39] L. H. Ryder, *Quantum Field Theory* (Cambridge University Press, Cambridge, 1985), Chapter 5.

Chapter 5

Central density of a neutron star is unaffected by a binary companion at linear order in μ/R

Coauthored with Patrick R. Brady; published in *Physical Review Letters* [Phys. Rev. Lett. **79**, 1186 (1997)].

Abstract

Recent numerical work by Wilson et al. on binary neutron star coalescence shows a striking instability as the stars come close together: Each star's central density increases by an amount proportional to 1/(orbital radius). This overwhelms tidal stabilization effects [which scale as 1/(orbital radius)^6] and causes the stars to collapse before they merge. By considering the perturbation limit, where a point particle of mass μ orbits a neutron star, we prove analytically that the neutron star's central density is unaffected *by the companion's presence to linear order in μ/R.*

Wilson, Mathews, and Marronetti (WMM) [1] have proposed a method of approximating the fully General Relativistic analysis of binary neutron star coalescence. The essence of their scheme is to choose a simple form of the spacetime metric (one in which the spatial three slices are conformally flat), and solve the constraint equations of General Relativity (GR) for some initial matter configuration. They evolve only the fluid equations forward in time until the fluid reaches a quasi-equilibrium configuration, then solve the constraint equations again for the new matter configuration and iterate until a quasi-equilibrium solution to the combined Einstein-fluid equations is found. Their method makes 3-dimensional simulations of such systems more tractable by reducing the computational requirements.

These simulations yield an extremely surprising result: neutron stars that are close to the maximum allowed mass are "crushed" into black holes long before the neutron stars coalesce. WMM claim that the origin of this effect is a non-linear gravitational interaction due to the companion's presence that strengthens the gravitational potential of each star. Consider a binary star system — star-A has mass M_A, and star-B has mass M_B. WMM claim that non-linear interactions cause the potential at star-A to be increased by a term that scales as M_B/R (where R is the orbital sepa-

ration[1]). This, in turn, increases the internal energy and density of star-A by terms that scale as M_B/R. If star-A happens to be marginally stable in isolation, the effect is sufficient to push it over the edge, causing a catastrophic collapse to a black hole. Moreover, the stabilizing effects of tidal coupling [2, 3], which scale as M_B^2/R^6, would be overwhelmed by this effect.

The scaling law claimed by WMM is precisely what one would expect if this effect were due to a post-1-Newtonian enhancement of the gravitational interaction. Motivated by this observation, Wiseman has recently done a careful analysis of the effect that a binary companion has on a fluid star, using the first post-Newtonian approximation to GR [4]; he finds no change to either the central energy density or the angle averaged proper radius of the star at this order. Wiseman's calculation does not rule out completely a star-crushing effect, but does show that it is not evident at post-1-Newtonian order in GR.

Suppose for a moment that the WMM effect is a property of neutron star binaries in GR, and that it scales as M_B/R at star-A. Clearly, it should also be apparent in the limit that we shrink star-B down to a point particle of mass $\mu \ll M_A \equiv M$. In this limit, the exact solution of the Einstein field equations describing a binary neutron star system can be approximated by a perturbative expansion in μ/R about the solution for an isolated star. We write the metric as $g_{\alpha\beta} = g^0_{\alpha\beta} + \epsilon h_{\alpha\beta} + O(\epsilon^2)$, where the superscript 0 indicates the background metric, and we have introduced an order counting parameter ϵ with the formal value unity. Quantities multiplied by ϵ scale linearly with μ/R, quantities multiplied by ϵ^2 scale with $(\mu/R)^2$, *etc.* In what follows, we ruthlessly discard all terms of order ϵ^2, constructing an argument that is valid only to linear order in μ/R.

The neutron star material is considered to be perfect fluid with stress-tensor

$$T_{\alpha\beta} = P\, g_{\alpha\beta} + (P + \rho) u_\alpha u_\beta \,. \tag{5.1}$$

This must be supplemented with an equation of state relating the energy density ρ and the pressure P. The energy density ρ is directly related to the fluid's baryon density n by the first law of thermodynamics; see Eqs. (3.2.6-7) of Ref. [6].

We take the background spacetime to be that of an isolated, spherical star with the line element

$$ds^2 = -e^{2\Phi(r)} dt^2 + \frac{dr^2}{[1 - 2m(r)/r]} + r^2 d\Omega^2 \,. \tag{5.2}$$

[1] We use units where $G = c = 1$.

Here $m(r)$ is the gravitational mass inside a sphere of radius r, and $d\Omega^2 = d\theta^2 + \sin^2\theta\, d\phi^2$. The combined Einstein-perfect fluid equations, generally referred to as the Oppenheimer-Volkoff (OV) equations (see for example Chapter 23 of Ref. [5]) are solved by demanding regularity of the origin $[m(0) = 0]$ and by fixing the value of the central baryon density n_c. The radius of the star R_S^0 is the coordinate radius at which the baryon density n^0 becomes zero. The central density n_c uniquely determines R_S^0, the total mass $M = m(R_S^0)$, and baryon mass M_b; this statement is equivalent to Theorem 7 of Ref. [7].

For physically reasonable matter, $dP^0/d\rho^0$ must be bounded. Therefore, using the relation between the baryon density $n(r)$ and energy density $\rho(r)$, plus the OV equation for the pressure,

$$\frac{dP^0}{dr} = -\frac{(\rho^0 + P^0)[m(r) + 4\pi r^3 P^0]}{r[r - 2m(r)]}\,, \tag{5.3}$$

one can show that

$$\left.\frac{dn^0}{dr}\right|_{r\to 0} \to 0\,. \tag{5.4}$$

Finally, the background geometry outside the star is described by the Schwarzschild solution with $m = M$ and $\exp(2\Phi) = 1 - 2M/r$ in Eq. (5.2).

The perturbing source is a single point particle of proper mass μ in a circular orbit at radius R. It is described by the stress-energy tensor [8]

$$T^{\alpha\beta} = \frac{\epsilon\mu}{R^2}\frac{v^\alpha v^\beta}{v^t}\delta(r - R)\delta(\cos\theta)\delta(\phi - \Omega t), \tag{5.5}$$

where $v^\alpha = (1 - 3M/R)^{-1/2}(1, 0, 0, \Omega)$ and $\Omega = \sqrt{M/R^3}$. The presence of this point "star" will alter the geometry and disturb the material in the central star, modifying the description of the spacetime and matter by terms of order ϵ. Linearizing $G_{\alpha\beta} = 8\pi T_{\alpha\beta}$ and $T^{\alpha\beta}{}_{;\beta} = 0$ in ϵ, we find that the first-order perturbation equations separate by expanding the angular dependence in spherical harmonics, and the time dependence in Fourier modes. This is enough to address the issue of how central quantities scale.

Consider the expansion of the baryon mass density. It may be written

$$n(r, \theta, \phi, t) = n^0(r) + \epsilon \sum_{l,m,\omega} \delta n_{lm\omega}(r) Y_{lm}(\theta, \phi) e^{i\omega t}\,. \tag{5.6}$$

An immediate consequence of Eq. (5.6) is that $\delta n_{lm\omega}(0) = 0$ for $l \geq 1$: if it were non-zero, the

density would be multi-valued at $r = 0$. Thus, only the monopole could affect the central density if the center of the perturbed star were to remain at the origin. In reality, the star's center will not be at the coordinate origin: the orbiting body will move it to some point in the orbital plane. However, the magnitude of this shift must be of the same order as the perturbation itself: $r_{\rm cent} = \epsilon\xi(t)$ for some function $\xi(t)$. Now evaluate the density at the star's center with a Taylor expansion:

$$n_{\rm cent} = n^0(0) + \epsilon\xi \left.\frac{dn^0}{dr}\right|_{r=0} + \epsilon \sum_{l,m,\omega} \left[\delta n_{lm\omega}(0) + \epsilon\xi \left.\frac{d\delta n_{lm\omega}}{dr}\right|_{r=0}\right] Y_{lm}(\theta,\phi)e^{i\omega t} . \qquad (5.7)$$

As we have already shown, $\delta n_{lm\omega}(0) = 0$, except possibly for $l = 0$, while $dn^0/dr \to 0$ as $r \to 0$ by Eq. (5.4). Thus, the baryon density at the center of mass is given by

$$n_{\rm cent} = n^0(0) + \epsilon\delta n_{000}(0) + O(\epsilon^2) . \qquad (5.8)$$

Only the monopole can produce changes in the central density which scale linearly in μ/R.

It is straightforward to solve for the $l = m = 0$ corrections to the metric outside the fluid. Define the function

$$H(r) = \begin{cases} 0 & r < R \\ \dfrac{2\mu}{r}\dfrac{(1-2M/R)}{(1-3M/R)^{1/2}} & r > R \end{cases} ; \qquad (5.9)$$

then $h_{tt} = H(r)$, $h_{rr} = H(r)/(1-2M/r)^2$. We have set $h_{\theta\theta} = h_{\phi\phi} = 0$ using the first order gauge freedom available for the monopole. As the point particle spirals into the star, some of its total mass-energy (its contribution to the total mass as measured at infinity) is radiated away, though its locally measured mass (rest mass) is conserved. The multiplicative factor in the above expression correctly accounts for that radiation loss. Notice that there is no monopole contribution to the metric inside the orbital radius of the particle — Keplerian orbits inside the orbital radius measure *only* the mass of the unperturbed neutron star at monopole order.

Is it possible for the monopole part of the perturbation to rearrange the fluid in the star, but leave its total gravitational mass unchanged? The answer is unequivocally no. A monopole perturbation is spherically symmetric and can only take one spherical solution into another. However, when the equation of state is fixed, all spherical solutions are parameterized by the gravitational mass — for each value of the gravitational mass M there exists a unique spherical configuration of the star. Spherical solutions therefore exhibit a one-to-one correspondence between the gravitational mass and the central density of the star. Since the gravitational mass M is unchanged at monopole order,

the central density cannot be affected either. Indeed, all physically relevant quantities, evaluated at the center of the star, are unaffected by the presence of a binary companion at order μ/R. *There is no crushing effect which scales linearly with* μ/R.

Interestingly, it is easily shown that incorrectly imposing boundary conditions can lead to an increase in central density at order μ/R. If the total gravitational mass of the star *and particle* is held fixed in a sequence of quasi-equilibrium solutions (ignoring the gravitational radiation that causes the orbital radius to shrink), *and* the particle's locally measured mass (rest mass) is held fixed, then the star's total mass and baryon mass must go up by an amount of order $\mu M/R$, contrary to how a real binary would behave. This mass increase will drive the central density up by a fractional amount of order μ/R, which is what the WMM simulations show. We have no evidence that this is what actually happens in the WMM simulations; it merely illustrates one way in which the observed density increase could arise.

It is a pleasure to thank Alan Wiseman for valuable conversations and many helpful insights. We are also grateful to Kip Thorne for suggesting improvements in the presentation, and to Eric Poisson for a suggestion that strengthened part of the argument. This work was supported in part by NSF grants AST–9417371 and PHY–9424337. SAH gratefully acknowledges the support of a National Science Foundation Graduate Fellowship. PRB is supported by a PMA Division Prize Fellowship at Caltech.

Bibliography

[1] J. R. Wilson and G. J. Mathews, Phys. Rev. Lett. **75**, 4161 (1995); J. R. Wilson, G. J. Mathews and P. Marronetti, Phys. Rev. D **54**, 1317 (1996); G. J. Mathews and J. R. Wilson, astro-ph/9701142.

[2] D. Lai, Phys. Rev. Lett. Phys. Rev. Lett. **76**, 4878 (1996).

[3] K. S. Thorne, "Tidal Stabilization of Rigidly Rotating, Fully Relativistic Neutron Stars", Phys. Rev. D, in press; gr-qc/9706057.

[4] A. G. Wiseman, Phys. Rev. Lett. **79**, 1189 (1997).

[5] C. W. Misner, K. S. Thorne, and J. A. Wheeler, *Gravitation* (Freeman, San Francisco, 1973).

[6] S. L. Shapiro and S. A. Teukolsky, *Black Holes, White Dwarfs, and Neutron Stars: The Physics of Compact Objects* (Wiley, New York, 1983).

[7] B. K. Harrison, K. S. Thorne, M. Wakano, and J. A. Wheeler, *Gravitation Theory and Gravitational Collapse* (University of Chicago Press, Chicago, 1965).

[8] E. Poisson, Phys. Rev. D **47**, 1497 (1993).

Chapter 6

Seismic gravity gradient noise in interferometric gravitational-wave detectors

Coauthored with Kip S. Thorne; to be submitted to *Physical Review D*.

Abstract

When ambient seismic waves pass near and under an interferometric gravitational-wave detector, they induce density perturbations in the earth, which in turn produce fluctuating gravitational forces on the interferometer's test masses. These forces mimic a stochastic background of gravitational waves and thus constitute a noise source. This seismic gravity-gradient noise has been estimated and discussed previously by Saulson using a simple model of the earth's ambient seismic motions. In this paper, we develop a more sophisticated model of these motions, based on the theory of multimode Rayleigh and Love waves propagating in a multilayer medium that approximates the geological strata at the LIGO sites (Tables 6.2–6.4), and we use this model to revisit seismic gravity gradients. We characterize the seismic gravity-gradient noise by a transfer function, $T(f) \equiv \tilde{x}(f)/\tilde{W}(f)$, *from the spectrum of rms seismic displacements averaged over vertical and horizontal directions,* $\tilde{W}(f)$, *to the spectrum of interferometric test-mass motions,* $\tilde{x}(f) \equiv L\tilde{h}(f)$; *here* L *is the interferometer arm length,* $\tilde{h}(f)$ *is the gravitational-wave noise spectrum, and* f *is frequency. Our model predicts a transfer function with essentially the same functional form as that derived by Saulson,* $T \simeq 4\pi G\rho(2\pi f)^{-2}\beta(f)$, *where* ρ *is the density of the earth near the test masses,* G *is Newton's constant, and* $\beta(f) \equiv \gamma(f)\Gamma(f)\beta'(f)$ *is a dimensionless reduced transfer function whose components* $\gamma \simeq 1$ *and* $\Gamma \simeq 1$ *account for a weak correlation between the interferometer's two test masses (Fig. 6.1) and a slight reduction of the noise due to the height of the test masses above the earth's surface. This paper's primary foci are (i) a study of how* $\beta'(f) \simeq \beta(f)$ *depends on the various Rayleigh and Love modes that are present in the seismic spectrum (Figs. 6.4–6.11 and Table 6.1), (ii) an attempt to estimate which modes are actually present at the two LIGO sites at quiet times and at noisy times, and (iii) a corresponding estimate of the magnitude of* $\beta'(f)$ *at quiet and noisy times. We conclude that at quiet times* $\beta' \simeq 0.35 - 0.6$ *at the LIGO sites, and at noisy times* β' *might get as large as* ~ 1.4. *(For comparison, Saulson's simple model*

gave $\beta = \beta' = 1/\sqrt{3} = 0.58$.) By folding our resulting transfer function into the "standard LIGO seismic spectrum" [Eq. (6.30)], which approximates $\tilde{W}(f)$ at typical times, we obtain the gravity-gradient noise spectra shown in Fig. 6.2. At quiet times this noise is below the benchmark noise level of "advanced LIGO interferometers" at all frequencies (though not by much at $\sim$ 10 Hz); at noisy times it may significantly exceed the advanced noise level near 10 Hz. The lower edge of our quiet-time noise constitutes a limit, beyond which there would be little gain from further improvements in vibration isolation and thermal noise — unless one can also reduce the seismic gravity gradient noise. Two methods of such reduction are briefly discussed: monitoring the earth's density perturbations near each test mass, computing the gravitational forces they produce, and correcting the data for those forces; and constructing narrow moats around the interferometers' corner and end stations to shield out the fundamental Rayleigh waves, which we suspect dominate at quiet times.

6.1 Introduction and Summary

Now that the LIGO/VIRGO international network of gravitational-wave detectors [1, 2, 3, 4] is under construction, it is important to revisit the various noise sources that will constrain the network's ultimate performance. Improved estimates of the ultimate noise spectra are a foundation for long-term planning on a number of aspects of gravitational-wave research, including facilities design, interferometer R&D, data analysis algorithm development, and astrophysical source studies.

In this paper and a subsequent one [5] we revisit *gravity-gradient noise* — noise due to fluctuating Newtonian gravitational forces that induce motions in the test masses of an interferometric gravitational-wave detector. Gravity gradients are potentially important at the low end of the interferometers' frequency range, $f \lesssim 20$ Hz. Another noise source that is important at these frequencies is *vibrational seismic noise*, in which the ground's ambient motions, filtered through the detector's vibration isolation system, produce motions of the test masses. It should be possible and practical to isolate the test masses from these seismic vibrations down to frequencies as low as $f \sim 3$ Hz [6], but it does not look practical to achieve large amounts of isolation from the fluctuating gravity gradients. Thus, gravity gradients constitute an ultimate low-frequency noise source; seismic vibrations do not.

Gravity gradients were first identified as a potential noise source in interferometric gravitational-wave detectors by Rai Weiss in 1972 [7]. The first quantitative analyses of such gravity-gradient

noise were performed by Peter Saulson [8] and Robert Spero [9] in the early 1980s. There has been little further study of gravity-gradient noise since then, except for some updating in Saulson's recent monograph [10].

In his updating, Saulson concluded that the most serious source of gravity-gradient noise will be the fluctuating density of the earth beneath and near each of the interferometer's test masses. These density fluctuations are induced by ambient seismic waves that are always present; their resulting gravitational forces are called *seismic gravity-gradient noise*. Saulson [8, 10] also estimated the gravity gradient noise from atmospheric fluctuations, concluding that it is probably weaker than that from earth motions. Spero [9] showed that gravity-gradient noise due to jerky human activity (and that of dogs, cattle, and other moving bodies) can be more serious than seismic gravity-gradient noise if such bodies are not kept at an adequate distance from the test masses. We shall revisit seismic gravity-gradient noise in this paper, and gravity gradients due to human activity in a subsequent one [5]; Teviet Creighton at Caltech has recently initiated a careful revisit of gravity gradient noise due to atmospheric fluctuations.

Our detailed analysis in this paper reveals a level of seismic gravity-gradient noise that agrees remarkably well with Saulson's much cruder estimates. Our analysis reveals the uncertainties in the gravity gradient noise, the range in which the noise may vary from seismically quiet times to noisy times, and the dependence of the noise on the various seismic modes that are excited. This dependence on modes is a potential foundation for methods of mitigating the seismic gravity gradient noise, discussed in our concluding section.

A preliminary version of this paper [11] was circulated to the gravitational-wave-detection community in 1996. That version considered only fundamental-mode Rayleigh waves (which we suspect are responsible for the dominant seismic gravity-gradient noise at quiet times), and (as Ken Libbrecht pointed out to us) it contained a serious error: the omission of the "surface-source" term [denoted ξ_V in Eq. (6.24) below] for the gravity-gradient force. It also contained errors in its two-geological-layer analysis for the LIGO Hanford site. All these errors are corrected in this final version of the manuscript, and the analysis has been extended to include more realistic models of the geological strata at the two LIGO sites and higher-order seismic modes.

As we were completing this manuscript, we learned of a paper in press [12] by Giancarlo Cella, Elena Cuoco and their VIRGO Project collaborators, which also analyzes seismic gravity-gradient noise in interferometric gravitational wave detectors. That paper is complementary to ours. Both papers analyze the RF mode (which we suspect is the dominant contributor to the seismic gravity-

gradient noise at quiet times), obtaining the same results in the 3–30 Hz band. But, whereas our paper carries out an extensive study of other modes, the Cella-Cuoco paper extends the RF-mode analysis to frequencies below 3 Hz and above 30 Hz, and computes (and finds to be small) the gravity gradient noise caused by seismically-induced motions of the experimental apparatus and its massive physical infrastructure in the vicinity of the VIRGO test masses.

This paper is organized as follows: In Sec. 6.1.1, we describe the phenomenology of the seismic-wave modes that can contribute to ambient earth motions at horizontally stratified sites like LIGO-Hanford and LIGO-Livingston. In Sec. 6.1.2, we introduce the transfer function $T(f)$ used to characterize seismic gravity-gradient noise, break it down into its components [most especially the reduced transfer function $\beta'(f)$], and we express it as an incoherent sum over contributions from the various seismic modes. In Sec. 6.1.3, we briefly describe Saulson's computation of the reduced transfer function, and then in Sec. 6.1.4 we describe our own computation and results. More specifically, in 6.1.4 we gather together and summarize the body of the paper our principal conclusions about β' for the various modes at the two LIGO sites, we discuss the evidence as to which modes actually contribute to the noise at quiet times and at noisy times, and we therefrom estimate the net values of β' at quiet and noisy times. We then fold those estimates into the standard LIGO seismic spectrum to get spectral estimates of the seismic gravity-gradient noise (Fig. 6.2).

The remainder of the paper (summarized just before the beginning of Sec. 6.2) presents our detailed models for the geological strata at the two LIGO sites, and our analyses of the various seismic modes that those strata can support and of the seismic gravity-gradient noise produced by each of those modes.

6.1.1 Phenomenology of ambient seismic motions in the LIGO frequency band

Seismic motions are conventionally decomposed into two components [31, 32, 33, 34]: *P-waves* and *S-waves*. P-waves have material displacements along the propagation direction, a restoring force due to longitudinal stress (pressure — hence the name P-waves), and a propagation speed determined by the material's density ρ and bulk and shear moduli K and μ:

$$c_P = \sqrt{\frac{K + 4\mu/3}{\rho}} \,. \tag{6.1}$$

S-waves have transverse displacements, restoring force due to shear stress, and propagation speed

$$c_S = \sqrt{\frac{\mu}{\rho}} = \sqrt{\frac{1-2\nu}{2-2\nu}}\, c_P \sim \frac{c_P}{2} \,. \tag{6.2}$$

Here ν is the material's Poisson ratio

$$\nu = \frac{3K - 2\mu}{2(3K+\mu)} \,. \tag{6.3}$$

Near the earth's surface, where seismic gravity-gradient noise is generated, these speeds are in the range $c_P \sim$ 500–2000 m/s and $c_S \sim$ 250–700 m/s. However, some of the modes that may contribute to the noise extend down to much greater depths, even into the bedrock where $c_P \sim$ 5000–6000 m/s and $c_S \sim$ 3200 m/s.

The ambient seismic motions are a mixture of P-waves and S-waves that propagate horizontally ("surface waves"), confined near the earth's surface by horizontal geological strata. Depending on the mode type and frequency, the horizontal propagation speed c_H can range from the surface layers' lowest S-speed to the bedrock's highest P-speed: $250\,\mathrm{m/s} \lesssim c_H \lesssim 6000\,\mathrm{m/s}$.

P- and S-waves are coupled by geological inhomogeneities (typically discontinuities at geological strata) and by a boundary condition at the earth's surface. At both LIGO sites the strata are alluvial deposits above bedrock, with discontinuities that are horizontal to within 2 degrees (more typically to within less than 1 degree). Throughout this paper we shall approximate the material as precisely horizontally stratified.

Seismic gravity-gradient noise is a potentially serious issue in the frequency band from $f \sim 3$ Hz (the lowest frequency at which mechanical seismic isolation looks practical) to $f \sim 30$ Hz; *cf.* Fig. 6.2 below. In this frequency band, the wavelengths of P- and S-waves are

$$\lambda_P = 100\,\mathrm{m}\frac{(c_P/1000\,\mathrm{ms}^{-1})}{(f/10\,\mathrm{Hz})},\ \lambda_S = 50\,\mathrm{m}\frac{(c_S/500\,\mathrm{ms}^{-1})}{(f/10\,\mathrm{Hz})}. \tag{6.4}$$

Neglecting coupling, the amplitudes of these waves attenuate as $\exp(-\pi r/Q\lambda)$, where r is the distance the waves have propagated and Q is the waves' quality factor. The dominant dissipation is produced by the waves' shear motions and can be thought of as arising from an imaginary part of the shear modulus in expressions (6.1) and (6.2) for the propagation speeds c_S and c_P (and thence also from an imaginary part of the propagation speeds themselves). Since the restoring force for S-waves is entirely due to shear, and for P-waves only about half due to shear, the S-waves attenuate

about twice as strongly as the P-waves. The measured Q-factors for near-surface materials are $Q_S \sim 10$–25, $Q_P \sim 20$–50 [25, 26], corresponding to amplitude attenuation lengths

$$\begin{aligned} \mathcal{L}_P &= \frac{Q_P \lambda_P}{\pi} = 1000\,\mathrm{m} \frac{(Q_P/30)(c_P/1000\,\mathrm{ms}^{-1})}{f/10\,\mathrm{Hz}} \,, \\ \mathcal{L}_S &= \frac{Q_S \lambda_S}{\pi} = 250\,\mathrm{m} \frac{(Q_S/15)(c_S/500\,\mathrm{ms}^{-1})}{f/10\,\mathrm{Hz}} \,. \end{aligned} \tag{6.5}$$

For bedrock (and basalt that overlies it at Hanford), the Q's and attenuation lengths can be higher than this — Q_P as high as a few hundred [27].

Shallowly seated wave modes which cause ambient seismic motions in our band, *i.e.*, modes that are confined to the alluvia so $c_H \lesssim 2500$ m/s (and more typically $\lesssim 1000$ m/s), must be generated in the vicinity of the interferometers' corner and end stations by surface sources such as wind, rain, and human activities (automobile traffic, sound waves from airplanes, *etc.*); their attenuation lengths are too short to be generated from further than a kilometer or so. Deep seated modes that reach into the bedrock could originate from rather further away — at 10 Hz and in a layer that has $Q \sim 100$, $c_P \sim 5500$ m/s, modes can propagate as far as ~ 20 km.

In horizontally stratified material, the wave components that make up each mode all propagate with the same angular frequency $\omega = 2\pi f$, horizontal wave vector $\vec{k} = k\hat{k}$ (where $\hat{k}$ is their horizontal direction, and $k = 2\pi/\lambda$ their horizontal wavenumber), and horizontal phase speed $c_H = \omega/k$. Their vertical motions differ from one horizontal layer to another and from P-component to S-component. The horizontal dispersion relation $\omega(k)$ [or equivalently $c_H(f)$] depends on the mode (Figs. 6.5, 6.6, 6.9, and 6.11 below).

Geophysicists divide these surface normal modes into two types [33, 34]:

- *Love modes,* which we shall denote by L. These are shear waves with horizontal motions ("SH-waves") that resonate in the near-surface strata. They involve no P-motions and thus have no compression and no density variations; thus, they produce no fluctuating gravitational fields and no seismic gravity-gradient noise.

- *Rayleigh modes,* which we shall denote by R. These are combinations of P-waves and S-waves with vertical motions ("SV-waves") that are coupled by the horizontal discontinuities at strata interfaces, including the earth's surface. Rayleigh modes are the producers of seismic gravity-gradient noise.

We shall divide the Rayleigh modes into two groups: the *fundamental* Rayleigh mode, denoted

RF, and Rayleigh *overtones* (all the other modes). Rayleigh overtones require stratification of the geological structure in order to be present; they essentially consist of coupled SV- and P-waves which bounce and resonate between the earth's surface and the interfaces between strata. We shall further divide the Rayleigh overtones into two broad classes: those that are composed predominantly of SV-waves, denoted RS, and those composed predominantly of P-waves, denoted RP. In the geophysics literature, the modes we identify as RP are sometimes referred to simply as P-modes, and our RS modes are referred to as the Rayleigh overtones. However, when RP modes are intermixed with RS modes in the (c_H, f) space of dispersion relations (as turns out to be the case at Hanford; *cf.* Fig. 6.6 below), a given Rayleigh overtone will continuously change character from RS to RP. Because this will be quite important for the details of the seismic gravity-gradient noise, we prefer to emphasize the similarities of the two mode types by designating them both as Rayleigh overtones and denoting them RS and RP.

We shall append to each Rayleigh overtone an integer that identifies its order in increasing horizontal speed c_H at fixed frequency f. Each successive Rayleigh mode, RF, RS1, RS2, ... (and, as a separate series, RF, RP1, RP2, ...) penetrates more deeply into the earth than the previous one. In our frequency band, the fundamental RF is typically confined to within $\sim \lambda_S/\pi \sim 10$ m of the earth's surface.

The RF mode is evanescent in all layers (except, at low frequencies, in the top layer). The overtones RS1, RS2, ... are composed primarily of SV-waves that propagate downward from the earth's surface, reflect off some interface, return to the surface and reflect back downward in phase with the original downward propagating waves, thereby guaranteeing resonance. On each reflection and at each interface between layers, these modes generate a non-negligible admixture of P-waves. The RP overtones are similar to RS, but with the propagating and reflecting waves being largely P with some non-negligible accompanying SV.

Dissipation will cause an overtone's waves to damp out with depth. If that damping is substantial in traveling from the surface to the reflection point, the overtone will not resonate and will be hard to excite. Roughly speaking, the amount of amplitude decay in traveling from the surface to the reflection point and back to the surface is $n\pi/Q$ where n is the mode number (or equivalently the number of round-trip wavelengths); *cf.* Eqs. (6.5). The round-trip damping therefore exceeds $1/e$ for mode numbers $n \gtrsim Q_S/\pi \sim 5$ for RS modes and $n \gtrsim Q_P/\pi \sim 10$ for RP modes. Correspondingly, in this paper we shall confine attention to modes with mode numbers $n \lesssim 10$.

The RP modes are harder to analyze with our formalism than RS modes — typically, when RP

modes turn on, there are many modes very closely spaced together and it is difficult to distinguish them. For this reason, we shall study only the lowest one at each site, RP1, plus RP modes that travel nearly horizontally in the several-km thick basalt layer at Hanford. We expect RP1 to be typical of other low-order RP modes, and the basalt-layer RP waves to be typical also of such waves propagating nearly horizontally in the bedrock.

6.1.2 Transfer functions and anisotropy ratio

Following Saulson [10], we shall embody the results of our gravity-gradient analysis in a *transfer function*

$$T(f) \equiv \frac{\tilde{x}(f)}{\tilde{W}(f)} \tag{6.6}$$

from seismic-induced earth motions $\tilde{W}(f)$ to differential test-mass motion $\tilde{x}(f)$. The precise definitions of $\tilde{W}(f)$ and $\tilde{x}(f)$ are as follows:

We shall denote the square root of the spectral density (the "spectrum") of the earth's horizontal surface displacements along some arbitrary horizontal direction by $\tilde{X}(f)$ (units $\mathrm{m}/\sqrt{\mathrm{Hz}}$), where f is frequency. We assume that $\tilde{X}(f)$ is independent of the chosen direction, *i.e.* the seismic motions are horizontally isotropic. This is justified by seismometer measurements at the LIGO sites before construction began [13, 14] and by rough estimates of the diffractive influence of the constructed facilities (Sec. 6.5). We shall denote the spectrum of vertical displacements at the earth's surface by $\tilde{Z}(f)$. The quantity $\tilde{W}(f)$ that appears in the transfer function is the displacement rms-averaged over 3-dimensional directions:

$$\tilde{W}(f) = \sqrt{\frac{2\tilde{X}^2(f) + \tilde{Z}^2(f)}{3}} \,. \tag{6.7}$$

The other quantity $\tilde{x}(f)$ that appears in the transfer function (6.6) is related to the interferometer's gravitational-wave strain noise spectrum $\tilde{h}(f)$ by $\tilde{x}(f) \equiv \tilde{h}(f)L$, where L is the interferometer arm length (4 km for LIGO). Physically, $\tilde{x}(f)$ is the spectrum of the interferometer's arm-length difference and is called the interferometer's "displacement noise spectrum". Since $\tilde{x}(f)$ and $\tilde{W}(f)$ both have units of $\mathrm{m}/\sqrt{\mathrm{Hz}}$, the transfer function $T(f)$ is dimensionless.

In this paper we shall express $T(f)$ in terms of a dimensionless correction $\beta(f)$ to a simple and

elegant formula that Saulson [8] derived:

$$T(f) \equiv \frac{\tilde{x}(f)}{\tilde{W}(f)} = \frac{4\pi G\rho}{\sqrt{(\omega^2-\omega_0^2)^2+\omega^2/\tau^2}}\beta(f) \simeq \frac{4\pi G\rho}{(2\pi f)^2}\beta(f) \quad \text{at } f \gtrsim 3\,\text{Hz}\,. \tag{6.8}$$

Here $\rho \simeq 1.8\,\mathrm{g/cm^3}$ is the mass density of the earth in the vicinity of the interferometer, G is Newton's gravitational constant, $\omega = 2\pi f$ is the angular frequency of the seismic waves and their fluctuating gravitational forces, and $\omega_0 \sim 2\pi$ rad/s and $\tau \sim 10^8\,\mathrm{s}$ are the angular frequency and damping time of the test mass's pendular swing. We shall call $\beta(f)$ the *reduced transfer function.* Saulson's estimate for $\beta(f)$ was

$$\beta_{\text{Saulson}} = 1/\sqrt{3} = 0.58\,; \tag{6.9}$$

cf. Eq. (21) of Ref. [8]. Our analyses (below) suggest that at quiet times β may be ~ 4 times smaller than β_{Saulson}, but at noisy times it may be as much as twice β_{Saulson}. Thus, Saulson's rough estimate was remarkably good.

Each mode of the earth's motion will contribute to the transfer function, and since the relative phases of the modes should be uncorrelated, they will contribute to $\beta(f)$ in quadrature:

$$\beta = \sqrt{\sum_J w_J {\beta_J}^2}\,. \tag{6.10}$$

The sum runs over all Rayleigh and Love modes, $J \in (\mathrm{RF}, \mathrm{RS}n, \mathrm{RP}n, \mathrm{L}n)$; $\beta_J(f)$ is the reduced transfer function for mode J, with

$$\beta_{Ln} = 0 \tag{6.11}$$

because the Love modes produce no gravity-gradient noise. The weighting factor w_J is the fractional contribution of mode J to the mean square seismic displacement $\tilde{W}^2$, and correspondingly the w_J's are normalized by

$$\sum_J w_J = 1\,. \tag{6.12}$$

Besides this normalization condition, there is another constraint on the weighting factors w_J: each mode (at each frequency) has its own ratio $\mathcal{A}_J$ of vertical to horizontal displacement at the

earth's surface:

$$\mathcal{A}_J(f) = \frac{\tilde{Z}_J(f)}{\tilde{X}_J(f)} \,. \tag{6.13}$$

We shall call this ratio the mode's *anisotropy ratio*[1]. Since the Love modes have purely horizontal motions, their anisotropy ratios vanish:

$$\mathcal{A}_{Ln} = 0 \,. \tag{6.14}$$

It is straightforward to show that the anisotropy ratios for the various modes combine to produce the following net anisotropy in the earth's surface displacement:

$$\mathcal{A} \equiv \frac{\tilde{Z}}{\tilde{X}} = \frac{\sqrt{\sum_J w_J \mathcal{A}_J^2/(2+\mathcal{A}_J^2)}}{\sqrt{\sum_J w_J/(2+\mathcal{A}_J^2)}} \,. \tag{6.15}$$

At quiet times, measurements show this to be near unity at Hanford [14], and ~ 0.6 at Livingston [13], while at noisy times it can fluctuate from ~ 0.2 to ~ 5. The measured value of this ratio is an important constraint on the mixture of modes that produces the observed seismic noise and thence on the net reduced transfer function. For example, if the observed noise is due to one specific Rayleigh mode J with large anisotropy ratio $\mathcal{A}_J$, accompanied by enough Love waves to reduce the net anisotropy ratio to $\mathcal{A}_{\rm net} = 1.0$ (Hanford) or 0.6 (Livingston), then Eqs. (6.10)–(6.15) imply that the net reduced transfer function for the seismic gravity gradient noise is

$$\beta_{JL} = \beta_J \sqrt{\frac{1+2/\mathcal{A}_J^2}{1+2/\mathcal{A}_{\rm net}^2}} \,. \tag{6.16}$$

In Appendix A it is shown that for each mode J, the reduced transfer function β_J can be split into the product of three terms:

$$\beta_J = \gamma_J \Gamma_J \beta'_J \,. \tag{6.17}$$

The first term, γ_J, accounts for the correlation between the gravity-gradient noise at the interferometer's two corner test masses. It is a universal, mode-independent function of the waves' horizontal phase shift in traveling from one test mass to the other:

$$\gamma_J = \gamma(\omega l/c_{HJ}) \,. \tag{6.18}$$

Here $\omega = 2\pi f$ is the waves' angular frequency, $l \sim 5$ m is the distance between the two corner test

[1] Geophysicists use the name *spectral ratio* for $1/\mathcal{A} = 1/(\text{anisotropy ratio})$.

masses, c_{HJ} is the horizontal phase speed c_H for mode J, and $\omega/c_H \equiv k$ is the mode's horizontal wave number. For frequencies and modes of interest to us, the argument $y = \omega l/c_{HJ}$ of γ is of order unity. The function $\gamma(y)$, given by

$$\gamma(y) \equiv \sqrt{1 + \frac{1}{2\pi}\int_0^{2\pi} \cos\phi \sin\phi \cos\left(y\frac{\cos\phi + \sin\phi}{\sqrt{2}}\right) d\phi}\ , \tag{6.19}$$

is plotted in Fig. 6.1. As Fig. 6.1 shows, $\gamma(y)$ is within about 10 per cent of unity for all frequencies, so we shall regard it as unity througout the rest of this manuscript, except in Appendix A.

The second term, Γ_J, in Eq. (6.17) for β_J describes the attenuation of the gravity gradient noise due to the height $\mathcal{H}$ of the test masses above the earth's surface. We show in Appendix A that

$$\Gamma_J = \exp(-\omega\mathcal{H}/c_{HJ})\ . \tag{6.20}$$

For LIGO interferometers $\mathcal{H}$ is about 1.5 m, the frequency of greatest concern is $f = \omega/2\pi \simeq 10$ Hz (*cf.* Fig. 6.2 below), and at quiet times the dominant contribution to the noise probably comes from the RF mode (*cf.* Sec. 6.1.4) for which, near 10 Hz, $c_H \simeq 330$ m/s (*cf.* Figs. 6.6 and 6.9); correspondingly, $\Gamma_{RF} \simeq 0.75$. For other modes, c_H will be larger so Γ_J will be even closer to unity than this. For this reason, throughout the rest of this paper, except in Appendix A, we shall approximate Γ_J by unity. With γ_J and Γ_J both approximated as unity, we henceforth shall blur the distinction between β_J and β'_J, treating them as equal [*cf.* Eq. (6.17)].

In Appendix A we derive expressions for the reduced transfer function $\beta'_J(f)$ and the anisotropy ratio $\mathcal{A}_J$ in terms of properties of the eigenfunctions for mode J: denote by ξ_{HJ} and ξ_{VJ} the mode's complex amplitudes at the earth's surface ($z = 0$) for horizontal displacement and *upward* vertical displacement, so the mode's surface displacement eigenfunction is

$$\vec{\xi}_J = (\xi_{HJ}\hat{k} - \xi_{VJ}\vec{e}_z)e^{i(\vec{k}\cdot\vec{x}-\omega t)}\ , \tag{6.21}$$

where $\vec{e}_z$ is the unit vector pointing *downward* and $\hat{k} = \vec{k}/k$ is the unit vector along the propagation direction. Also, denote by $\mathcal{R}_J(z)$ the mode's amplitude for the fractional perturbation of density $\delta\rho/\rho$ at depth z below the surface, so

$$\frac{\delta\rho_J}{\rho} = [\xi_{VJ}\delta(z) + \mathcal{R}_J(z)]\, e^{i(\vec{k}\cdot\vec{x}-\omega t)}\ . \tag{6.22}$$

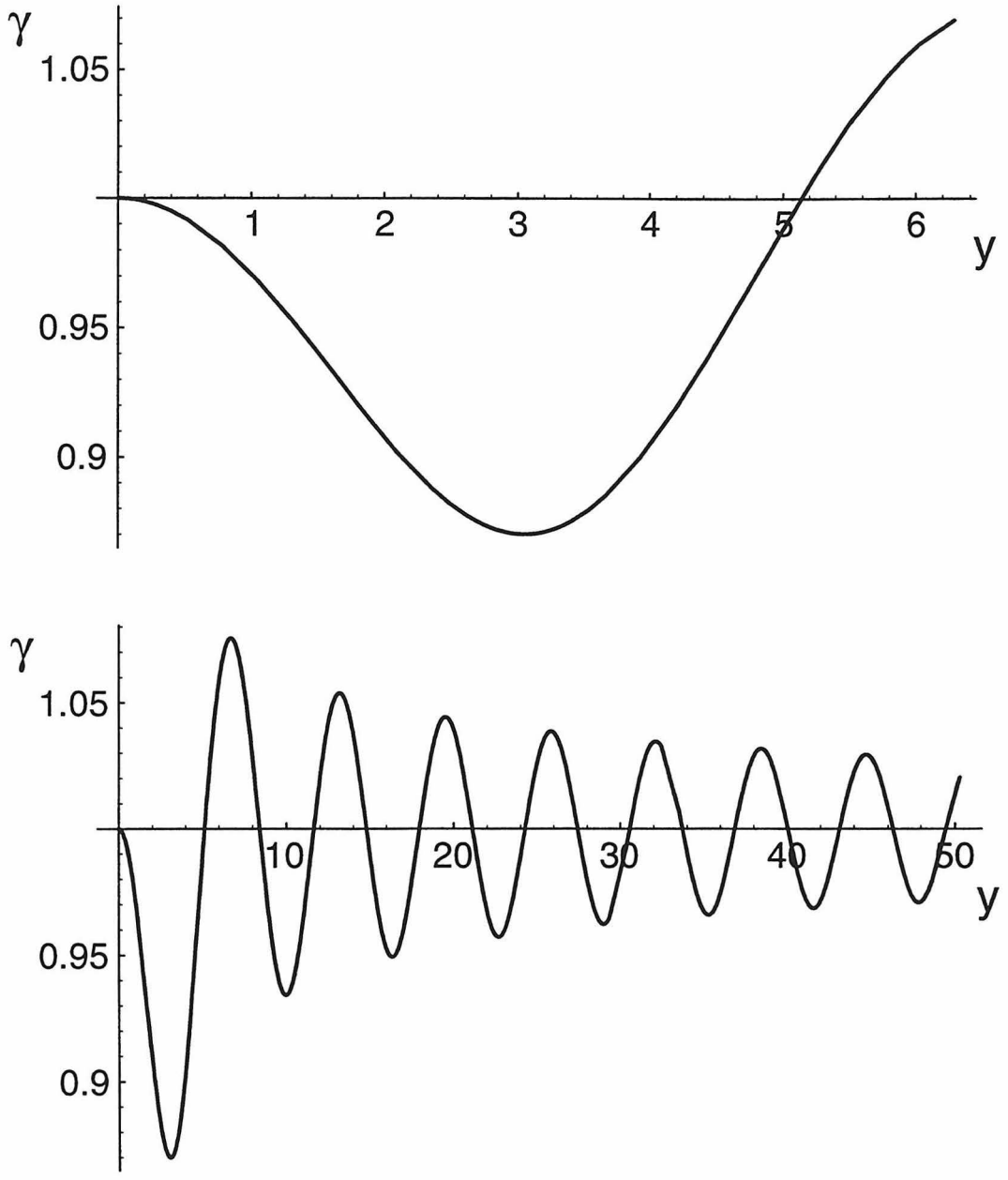

Figure 6.1: The function $\gamma(y)$.

This function accounts for correlations of seismic gravity-gradient noise in the two corner test masses. This function is given analytically by Eq. (6.19), and it appears in all of the reduced transfer functions: $\beta(f) = \beta'(f)\gamma(2\pi f l/c_H)\Gamma(f)$.

Here the term $\xi_{VJ}\delta(z)$ accounts for the mass moved above $z = 0$ by the upward vertical displacement ξ_V. Then, we show in Appendix A [Eq. (6.52)] that

$$\mathcal{A}_J = \sqrt{2}\frac{|\xi_{VJ}|}{|\xi_{HJ}|} , \tag{6.23}$$

where the $\sqrt{2}$ comes from the fact that when this mode is incoherently excited over all horizontal directions $\hat{k}$, its rms horizontal amplitude along any chosen direction is $|\xi_{HJ}|/\sqrt{2}$. Similarly, we show in Appendix A [Eq. (6.66)] that

$$\beta'_J(f) = \sqrt{\frac{3/2}{|\xi_{HJ}|^2 + |\xi_{VJ}|^2}} \left| \xi_{VJ} + \int_0^\infty \mathcal{R}_J(z) e^{-kz} dz \right| . \tag{6.24}$$

We shall refer to the ξ_{VJ} term in Eq. (6.24) as the *surface source* of gravity gradients, and the $\int \mathcal{R}_J e^{-kz} dz$ term as the *subsurface source.*

Note that the influence of a given density perturbation dies out as e^{-kz}, where $k = 2\pi f/c_H$ is the horizontal wave number; so unless $\mathcal{R}_J(z)$ increases significantly with depth, the seismic gravity gradients arise largely from depths shallower than the *gravity-gradient e-folding length*

$$\mathcal{Z}_{\rm sgg} = \frac{1}{k} = \frac{c_H}{2\pi f} = 16{\rm m}\frac{(c_H/1000{\rm ms}^{-1})}{(f/10{\rm Hz})} . \tag{6.25}$$

This has a simple explanation: (i) to produce much gravitational force on a test mass, a compressed bit of matter must reside at an angle $\alpha \gtrsim \pi/4$ to the vertical as seen by the test mass, and (ii) bits of matter all at the same $\alpha \gtrsim \pi/4$ and at fixed time have fractional compressions $\delta\rho/\rho$ that oscillate with depth z as $e^{ikx} = e^{ikz\tan\alpha}$, and that therefore tend to cancel each other out below a depth $1/(k\tan\alpha) \sim 1/k$.

From Eq. (6.24) we can estimate the magnitude of the reduced transfer function. The mode's fractional density perturbation $\mathcal{R}_J$ is equal to the divergence of its displacement eigenfuction (aside from sign), which is roughly $k\xi_{HJ}$ and often does not vary substantially over the shallow depths $z \lesssim \mathcal{Z}_{\rm sgg}$ where the gravity gradients originate. Correspondingly, the integral in Eq. (6.24) is $\sim \xi_{HJ}$, so $\beta'_J \sim \sqrt{1.5|\xi_{HJ} + \xi_{VJ}|^2/(|\xi_{HJ}|^2 + |\xi_{VJ}|^2)} \sim 1$, since the horizontal and vertical displacements are comparable.

As we shall see in Secs. 6.2 and 6.3.2 below, for RP modes the gravity gradients produced by the surface and subsurface sources tend to cancel, so β' actually tends to be somewhat smaller than

unity,

$$\beta'_{\rm RP} \lesssim 0.2 \,, \tag{6.26}$$

while for RF and RS modes, the surface source tends to dominate, so

$$\beta'_{\rm RF} \sim \beta'_{\rm RS} \sim \frac{1}{\sqrt{2}}\sqrt{\frac{3}{1+2\mathcal{A}_J^2}} \sim \frac{1}{\sqrt{2}} = 0.7 \,. \tag{6.27}$$

If we had normalized our transfer function to the vertical displacement spectrum $|\tilde{Z}(f)|$ instead of the direction-averaged spectrum $|\tilde{W}(f)|$ [Eq. (6.6)], then for modes in which the surface source strongly dominates, β'_J would be $1/\sqrt{2}$ independently of the mode's anisotropy ratio.

In Secs. 6.3 and 6.4 and associated Appendices, we shall derive, for each low-order Rayleigh mode at Hanford and Livingston, the reduced transfer function β'_J and the anisotropy ratio $\mathcal{A}_J$. In Sec. 6.1.4, we shall discuss the likely and the allowed weightings w_J of the various modes [subject to the constraints (6.12) and (6.15)], and shall estimate the resulting net reduced transfer functions $\beta(f)$ for the two sites and for quiet and noisy times.

Henceforth we typically shall omit the subscript J that denotes the mode name, except where it is needed for clarity.

6.1.3 Saulson's analysis and transfer function

In his original 1983 analysis of seismic gravity-gradient noise [8], Saulson was only seeking a first rough estimate, so he used a fairly crude model. He divided the earth near a test mass into regions with size $\lambda_P/2$ (where λ_P is the wavelength of a seismic P-wave), and he idealized the masses of these regions as fluctuating randomly and independently of each other due to an isotropic distribution of passing P-waves. Saulson's final analytic result [his Eq. (21)] was the transfer function (6.6) with $\beta = 1/\sqrt{3}$.

Saulson's 1983 numerical estimates[8] of the seismic gravity-gradient noise were based on seismic noise levels $\tilde{W}(f) = 0.5 \times 10^{-8}(10\,{\rm Hz}/f)^2{\rm cm}/\sqrt{\rm Hz}$ for "average sites" and a factor 10 lower than this for "quiet sites". The resulting gravity-gradient noise $\tilde{x}(f) = T(f)\tilde{W}(f)$ was substantially below the projected vibrational seismic noise in (seismically well isolated) "advanced" LIGO interferometers [1].

In updating these estimates for his recent monograph [10], Saulson noted that his original "average" and "quiet" sites were based on measurements at underground seismological stations. Surface

sites, such as those chosen for LIGO and VIRGO, are far noisier than underground sites in the relevant frequency band, $3\,\mathrm{Hz} \lesssim f \lesssim 30\,\mathrm{Hz}$, because of surface seismic waves. More specifically, even though the chosen LIGO sites (at Hanford, Washington and Livingston, Louisiana) are among the more quiet locations that were studied in the LIGO site survey, their noise at typical times is approximately isotropic [$\tilde{Z}(f) \sim \tilde{X}(f) \sim \tilde{W}(f)$] and has approximately the following form and magnitude [13, 14]

$$\begin{aligned} \tilde{W}(f) &= 1\times 10^{-7}\frac{\mathrm{cm}}{\sqrt{\mathrm{Hz}}} \quad \text{at } 1 < f < 10\,\mathrm{Hz}\,, \\ &= 1\times 10^{-7}\frac{\mathrm{cm}}{\sqrt{\mathrm{Hz}}}\left(\frac{10\mathrm{Hz}}{f}\right)^2 \quad \text{at } f > 10\,\mathrm{Hz}\,. \end{aligned} \tag{6.28}$$

This so-called *standard LIGO seismic spectrum* is 20 times larger than at Saulson's original "average" sites for $f \geq 10$ Hz. Correspondingly, Saulson pointed out in his update, the seismic gravity-gradient noise may stick up above the vibrational seismic noise in "advanced" LIGO interferometers[2]. On the other hand, at very quiet times — at night and with winds below 5 mph — the LIGO seismic ground noise $\tilde{W}(f)$ can be as low as $\sim 1/10$ the level (6.28), thereby pushing Saulson's seismic gravity-gradient noise below the vibrational seismic noise of an "advanced" LIGO interferometer.

6.1.4 Our analysis and transfer function

Saulson's new, more pessimistic estimates of the seismic gravity gradient noise triggered us to revisit his derivation of the transfer function $T(f)$ from seismic ground motions to detector noise. Our analysis consists of:

(i) splitting the ambient seismic motions into Love and Rayleigh modes (body of this paper and appendices);

(ii) computing the reduced transfer function for each mode and for models of the geological strata at each LIGO site (body and appendices);

(iii) using seismic measurements at the LIGO sites and geophysical lore based on other sites to estimate the mode mixture present at the two sites under both quiet and noisy conditions (this section); and

(iv) evaluating for these mode mixtures the expected reduced transfer function and resulting

[2]Saulson informs us that in evaluating the noise at the LIGO sites, he made an error of $\sqrt{3}$; his transfer function and the standard LIGO seismic spectrum actually predict a noise level $\sqrt{3}$ smaller than he shows in Fig. 8.7 of his book [10].

Table 6.1: Reduced transfer functions predicted for Hanford and Livingston by our 4-layer models. Notation: "RS shallow" — RSn modes with $n \leq 4$ and no evidence of RP admixture, "RS deep" — RSn modes with$n \geq 4$ and no evidence of RP admixture, "RP shallow" — RP modes confined to the alluvial layers, "RP deep" — RP modes that propagate nearly horizontally in the deep basalt or bedrock, β' — the reduced transfer function with the test-mass correlation $\gamma \simeq 1$ factored out, β'_L — the value of β' when enough Love waves are added to bring the anisotropy ratio down to the values appropriate at the two sites ($\mathcal{A} \simeq 1$ for Hanford, $\mathcal{A} \simeq 0.6$ for Livingston).

Modes	Hanford β'	Hanford β'_L	Livingston β'	Livingston β'_L
RF $f < 10$Hz	0.4–0.85	0.35–0.6	0.65–0.9	0.35–0.45
RF $f > 10$Hz	0.85	0.6	0.65–0.9	0.35–0.45
RS shallow	0.4–1.4	0.4–1.05	0–1.2	0–0.9
RS deep			0.05–0.8	0.05–0.8
RP shallow	0–0.15	0–0.15	0.02–0.08	0.005–0.04
RP deep	0–1.3	0–0.7		

noise (this section).

Our reduced transfer functions

Table 6.1 summarizes the results of our model computations for each LIGO site. Shown there are the range of computed reduced transfer functions β' for specific types of Rayleigh modes, and the range of net reduced transfer functions β'_L that would result if each Rayleigh mode were mixed with enough Love waves to bring its (often rather high) anisotropy ratio $\mathcal{A}$ down to the level typical of quiet times at the LIGO sites ($\mathcal{A} \simeq 1.0$ at Hanford [14], $\mathcal{A} \simeq 0.6$ at Livingston [13]).

The modes shown in Table 6.1 are the RF mode, the RS modes with no sign of RP admixture, and the RP modes. The RS and RP modes are split into two groups: "shallow" and "deep". The "deep" modes are those that (i) extend down to sufficient depth to produce, in our frequency band, resonant excitations of subsurface geophysical layers (layer 2 and/or layer 3), and (ii) have sufficiently large gravity-gradient e-folding lengths $\mathcal{Z}_{\rm sgg}$ for such a resonating layer to contribute to the gravity-gradient noise. The "shallow" modes are those that do not have these properties. In our models (Secs. 6.3 and 6.4), the only deep RS modes are those at Livingston with order $n \geq 4$, and the only deep RP modes are those at Hanford that reach into the basalt (depth > 220 m).

Notice in Table 6.1 that the RF and shallow RS modes have β' in the range 0.4 to 1.2, while the shallow RP modes have far smaller β': 0 to 0.15. This marked difference arises from the fact that for RF and RS the surface source tends to dominate over the subsurface source, while for RP the two sources tend to cancel each other. (If the surface source were absent, the pattern would be reversed:

the subsurface source $\int \mathcal{R}$, which arises from compressional density perturbations, is quite weak for RS modes because they consist primarily of non-compressional S-waves, but is strong for RP modes since they consist primarily of compressional P-waves.)

At those frequencies where a subsurface, resonating layer contributes significantly to the deep-mode gravity gradients, that contribution makes the RP β' large (up to 1.3), and can make the RS β' small (as low as 0.05). The reduction of the RS β' results from a cancellation of the S-wave, surface-sourced gravity gradients by the P-wave, subsurface-sourced gravity gradients that accompany the subsurface S-wave resonance.

Modes actually present and resulting seismic noise

There is little direct evidence regarding which modes contribute to the ambient surface motions and thence to the gravity-gradient noise at the LIGO sites during quiet times. Past seismic measurements do not shed much light on this issue. In the concluding section of this paper (Sec. 6.5), we shall propose measurements that could do so.

Fortunately, the nature of the ambiently excited modes has been studied at other, geophysically similar sites (horizontally stratified alluvia over bedrock). The preponderance of evidence suggests that at quiet times the surface motions at such sites and in our frequency band are due to a mixture of Love waves and the fundamental Rayleigh mode RF plus perhaps a few low order RS modes [15, 16, 17, 18, 19]. In at least one case, some amount of RP excitation is also seen [20]; these RP excitations are ascribed to "cultural noise" (noise generated by human activity of some sort) near the measurement site. Deep borehole measurements indicate that RP dominates at very great depths ($\lesssim$ 5 km) [21]; this is probably not relevant to our analysis, however. It merely indicates that very deep down, the majority of the surface waves have damped away, leaving only some residual RP modes. The deep motions due to these modes are typically an order of magnitude or two smaller than the motions at the surface.

On this basis, we presume that at quiet times the net reduced transfer function is about that for the RF mode, with enough admixed Love waves to bring the net $\mathcal{A}$ down to the typical quiet-time values of 1.0 for Hanford and 0.6 for Livingston. In other words, $\beta'_{\rm net}$ is about equal to β'_L for the RF mode:

$$\begin{aligned} \beta'_{\text{net, quiet times}} &\simeq \text{0.35–0.45 at Livingston,} \\ &\simeq \text{0.35–0.6 at Hanford.} \end{aligned} \tag{6.29}$$

We have folded these quiet-time estimates for β' into the standard LIGO seismic spectrum (6.28) to obtain the gravity-gradient noise estimates shown as the dark gray band in Fig. 6.2. The thickness of the band indicates the range of our β' [Eq. (6.29)]: 0.35 to 0.6. To produce this plot, we took expression (6.8) for the transfer function $T(f)$ with γ and Γ set to unity, so $\beta = \beta'$ [*cf.* Eq. (6.17)]. Then, we multiplied this by the standard LIGO seismic spectrum (6.28) for the ground displacement with an assumed density $\rho = 1.8$ g/cm^3. This yields

$$\begin{aligned} \tilde{h}_{\rm SGG}(f) &= \frac{\beta'}{0.6}\frac{6\times 10^{-23}}{\sqrt{\rm Hz}}\left(\frac{10{\rm Hz}}{f}\right)^2 , \ 3\,{\rm Hz} \lesssim f < 10\,{\rm Hz} , \\ &= \frac{\beta'}{0.6}\frac{6\times 10^{-23}}{\sqrt{\rm Hz}}\left(\frac{10{\rm Hz}}{f}\right)^4 , \ 10\,{\rm Hz} < f \lesssim 30\,{\rm Hz} , \end{aligned} \tag{6.30}$$

which we plotted for the indicated values of β.

At very quiet times, the ambient seismic spectrum near 10 Hz can be as much as a factor ~ 10 lower than the standard LIGO spectrum assumed in Eq. (6.30) and Fig. 6.2, and correspondingly the quiet-time gravity gradient noise can be a factor ~ 10 lower.

At noisier times, there appear to be excitations of a variety of RF, RS and RP modes. For example, at the LIGO sites, time delays in correlations between surface motions at the corner and the end stations reveal horizontal propagation speeds $c_H \sim 5000$ m/s, corresponding to deeply seated RP-modes (although for the most part these modes are seen at frequencies too low to be of interest in this analysis — $f \lesssim 0.2$ Hz [23, 24]). Moreover, the measured anisotropy ratios can fluctuate wildly from about 0.2 to 5 at noisy times, suggesting a wildly fluctuating mixture of RF, RS and RP modes. Thus, at noisy times it is conceivable that β' can get as high as the largest value shown if Table 6.1

$$\beta'_{\rm net,\ noisy\ times} \lesssim 1.4 , \tag{6.31}$$

We have folded this estimated upper limit on $\beta'_{\rm net}$ into the standard LIGO seismic spectrum to obtain the upper edge of the light gray band in Fig. 6.2. This light gray band is our best estimate of the range of seismic gravity-gradient noise at noisy times, assuming the standard LIGO seismic spectrum. Since, at noisy times, the seismic spectrum can be somewhat higher than the standard one, the gravity-gradient noise will be correspondingly higher.

For the next few years, the most important application of these estimates is as a guide for the development of seismic isolation systems and suspension systems for LIGO. There is not much point

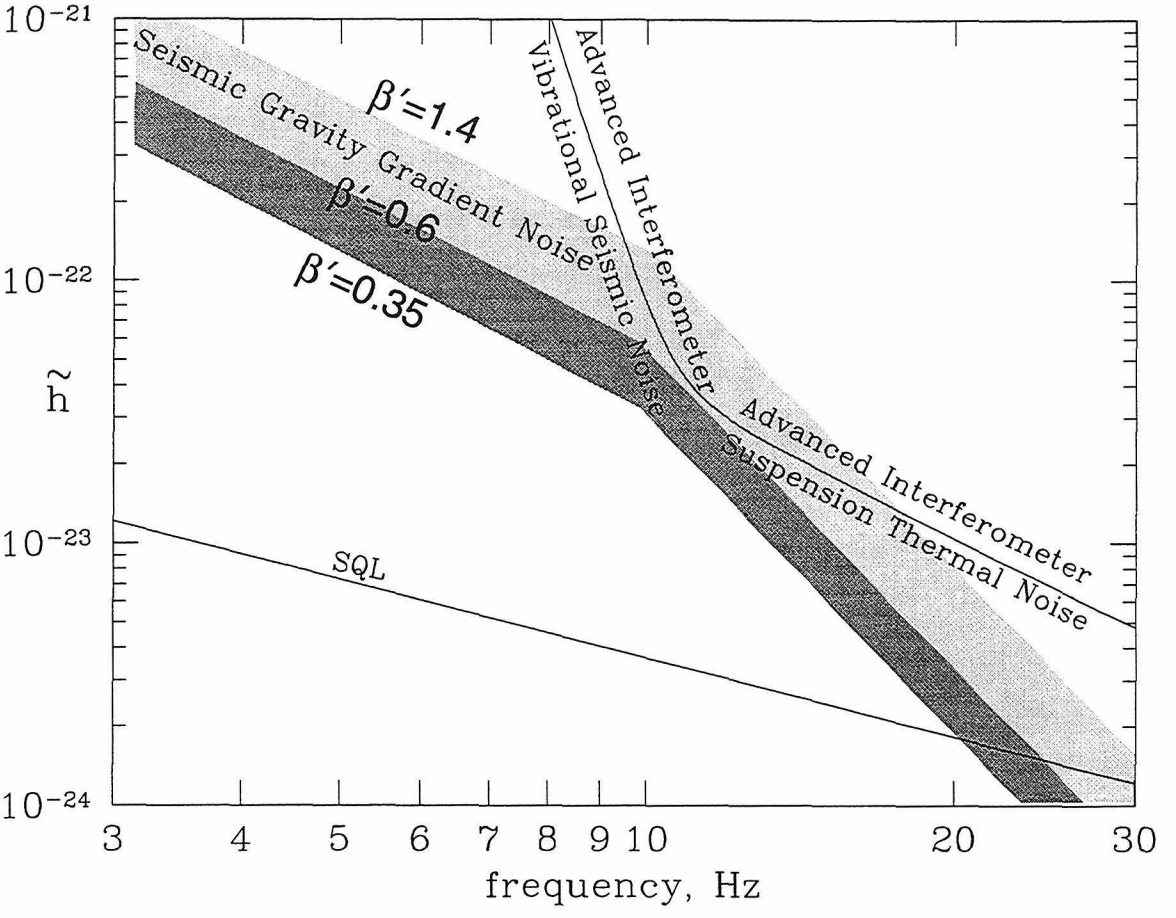

Figure 6.2: Seismic gravity-gradient noise in a LIGO interferometer.

In this Figure, we assume that the direction-averaged spectrum of earth displacements has the form of the standard LIGO seismic spectrum, Eq. (6.28). The edges of the gray bands are for the indicated values of the reduced transfer function β' (assumed equal to β; *i.e.*, for γ and Γ approximated as unity). The dark gray band is our estimate of the range of noise for quiet times, when we expect β' to lie between 0.35 and 0.60. The light gray band is for noisy times, when we expect β' to be as large as 1.4. At very quiet times, the ground spectrum can be a factor ~ 10 smaller than (6.28), which will lower these bands accordingly. Conversely, at noisy times the ground spectrum can be larger, raising these bands. Also shown for comparison is the projected noise in an "advanced" LIGO interferometer, and the standard quantum limit (SQL) for an interferometer with one tonne test masses. The SQL is the square root of Eq. (122) of Ref. [39]. The "advanced" interferometer noise is taken from Fig. 7 of Ref. [1], with correction of a factor 3 error in the suspension thermal segment (Fig. 7 of Ref. [1] is a factor 3 too small, but Fig. 10 of that reference is correct, for the parameters listed at the end of the section "LIGO Interferometers and Their Noise").

in pushing such systems so hard that the vibrational seismic or the suspension thermal noise is driven far below our lowest estimates of the seismic gravity-gradient noise [bottom of the black line in Fig. 6.2, lowered by the amount that the actual very quiet time spectrum falls below the standard LIGO spectrum (6.28)]—unless corresponding steps are taken to mitigate the seismic gravity gradient noise; see Sec. 6.5.

In Fig. 6.2 we compare our predicted seismic gravity gradient noise to the projected noise in "advanced" LIGO interferometers and to the standard quantum limit for an interferometer with one tonne test masses ("SQL"). Notice that our lower bound on the seismic gravity-gradient noise is everywhere smaller than the "advanced" interferometer noise, but it is larger than the SQL at frequencies below ~ 20 Hz. Our lower bound rises large enough below ~ 10 Hz to place limits on seismic-isolation and suspension-noise R&D that one might contemplate doing at such frequencies.

The remainder of this paper is organized as follows: we begin in Sec. 6.2 by discussing Rayleigh waves and seismic gravity-gradient noise in the idealized case of a homogeneous half-space (not a bad idealization for some regions of some modes at Hanford and Livingston). Then we develop multilayer geophysical models for Hanford and Livingston and use them to derive the reduced transfer functions for the various Rayleigh modes (Secs. 6.3 and 6.4). We conclude in Sec. 6.5 with a discussion of the uncertainties in our analysis and research that could be undertaken to reduce the uncertainties, and also a brief discussion of the physical interaction of the seismic waves with the foundations of the LIGO facilities, and of the possibility to modify the facilities in such a way as to reduce the strength of the seismic gravity-gradient noise. Mathematical details of our analysis are confined to Appendices. Those Appendices may form a useful foundation for analyses of seismic gravity-gradient noise at other sites.

6.2 Homogeneous half space

6.2.1 Fundamental Rayleigh mode

As a first rough guide to seismic gravity-gradient noise, we idealize the LIGO sites as a homogeneous half space with density ρ, Poisson ratio ν, S-wave speed c_S and P-wave speed c_P given by

$$\rho = 1.8\,\mathrm{g/cm^3}, \quad \nu = 0.33, \quad c_P = 440\,\mathrm{m/s}, \quad c_S = 220\,\mathrm{m/s}. \tag{6.32}$$

(These are the measured parameters of the surface material at Livingston; for Hanford, the parameters are only a little different; *cf.* Sec. 6.3.1 below.)

This homogeneous half space can only support the RF mode, as mentioned in the Introduction. The theory of the RF mode and the seismic gravity-gradient noise that it produces is sketched in Appendix B. Here we summarize the results.

The RF mode propagates with a horizontal speed c_H that depends solely on the Poisson ratio. It is a bit slower than the speed of S-waves, and is much slower than P-waves. For the above parameters,

$$c_H = 0.93 c_S = 205\,\mathrm{m/s}\ ; \tag{6.33}$$

cf. Eq. (6.67). Correspondingly, the waves' horizontal wave number k and horizontal reduced wavelength are

$$\frac{\lambda}{2\pi} = \frac{1}{k} = 3.3\,\mathrm{m}\left(\frac{10\,\mathrm{Hz}}{f}\right)\ . \tag{6.34}$$

Because $c_H < c_S < c_P$, RF waves are evanescent vertically: the P-waves die out with depth z as e^{-qkz}, and the SV-waves as e^{-skz}, where

$$\begin{aligned} q &= \sqrt{1-(c_H/c_P)^2} = 0.88\ , \\ s &= \sqrt{1-(c_H/c_S)^2} = 0.36\ . \end{aligned} \tag{6.35}$$

Thus, the vertical e-folding lengths for compression (which produces seismic gravity gradients) and shear (which does not) are

$$\mathcal{Z}_P = \frac{1}{qk} = 3.7\,\mathrm{m}\left(\frac{10\,\mathrm{Hz}}{f}\right)\ , \quad \mathcal{Z}_S = \frac{1}{sk} = 9.2\,\mathrm{m}\left(\frac{10\,\mathrm{Hz}}{f}\right)\ . \tag{6.36}$$

These RF waves produce substantially larger vertical motions than horizontal at the earth's surface. For waves that are horizontally isotropic, the anisotropy ratio is

$$\mathcal{A} = \sqrt{2}\frac{q(1-s^2)}{1+s^2-2qs} = 2.2\ . \tag{6.37}$$

This large ratio is indicative of the fact that RF waves contain a large component of P-waves. As mentioned in the Introduction, this is substantially larger than the values typically observed at the LIGO sites in the band $3\,\mathrm{Hz} \lesssim f \lesssim 30\,\mathrm{Hz}$ — seismic measurements taken at those sites [13, 14] show that, at quiet times, $\mathcal{A} \simeq 1.0$ at Hanford, $\mathcal{A} \simeq 0.6$ at Livingston. Thus, RF waves cannot

alone be responsible for the seismic motions. To the extent that our homogeneous-half-space model is realistic, RF waves must be augmented by a large amount of horizontally-polarized S-waves ("SH-waves"), which have $\mathcal{A} = 0$.

RF waves produce a reduced transfer function

$$\beta' = \sqrt{\frac{3(1+s^2-2q)^2}{2(1+s^2)[(1+s^2)(1+q^2)-4qs]}} = 0.85\ . \tag{6.38}$$

This β' is produced primarily by the surface source ξ_V in Eq. (6.24); if there were no surface source, the subsurface term $\int \mathcal{R}$ (arising solely from the P-wave compressions) would produce the far smaller value $\beta' = 0.17$. When the RF waves are augmented by enough Love waves to reduce the net $\mathcal{A}$ to 1.0 (Hanford) or 0.6 (Livingston), they produce a net reduced transfer function [Eq. (6.16) with primes added to the β's]

$$\beta'_L = 0.58 \text{ (Hanford), } 0.39 \text{ (Livingston).} \tag{6.39}$$

As we shall see in the next two sections, the earth is strongly stratified over the relevant vertical length scales at both Hanford and Livingston, and this gives rise to significant differences from the homogeneous-half-space model. Nevertheless, as discussed in the Introduction (Sec. 6.1.4), it is likely that at quiet times the RF mode produces the dominant gravity-gradient noise. It is worth noting that this RF mode is modified somewhat from the description given here due to stratification; however, as we shall see (Figs. 6.7 and 6.10), these modifications typically alter its anisotropy ratio and reduced transfer function by only a few tens of percent. Thus, the homogeneous-half-space model may be a reasonable indicator of seismic gravity-gradient noise in LIGO at quiet times.

6.2.2 P-up and SV-up waves

The principal effect of stratification is to produce a rich variety of normal-mode oscillations, in which mixtures of SV- and P-waves resonate in leaky cavities formed by the strata. These oscillations are Rayleigh-mode overtones, whose (rather complex) theory is sketched in Appendices C and D and discussed in Secs. 6.3 and 6.4. In this subsection we will momentarily ignore that fact, and will seek insight from a much simpler analysis that gives gives results which agree approximately, and in some cases quite well, with those of the Rayleigh-overtone theory.

If the top layer (labeled by a subscript 1) has a thickness D_1 somewhat larger than half a verti-

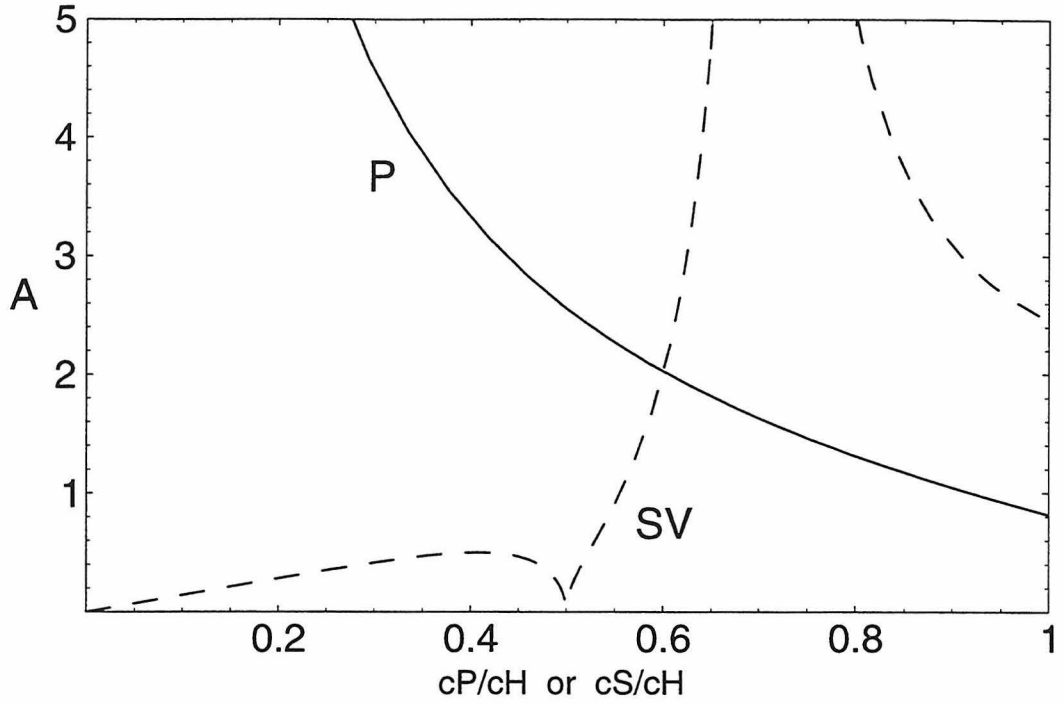

Figure 6.3: Anisotropy ratio for P-up and SV-up waves.

These waves propagate upward in a homogeneous half space, reflect off the Earth's surface, and propagate back downward. The curve "P" is for the case when the upward propagating waves are pure P (P-up waves), in which case the abscissa is $c_P/c_H \equiv \sin\alpha_P$; "SV" is for SV-up waves, with abscissa $c_S/c_H \equiv \sin\alpha_S$. It is assumed that $c_P = 2c_S$; this is approximately the case for the surface layers at Hanford and Livingston.

cal wavelength of the waves' oscillations, $D_1 > (c_{P1}/2f)/\sqrt{1-(c_{P1}/c_H)^2}$ [*cf.* Eq. (6.41) below and associated discussion], then the trapped modes can be thought of (more or less) as propagating upward through the top layer, reflecting at the earth's surface, and then propagating back downward. By ignoring the effects of the interfaces below, these waves can be idealized as traveling in a homogeneous half space.

The behavior of these waves depends on the mixture of P- and SV-waves that composes them as they propagate upward. Because these two components will superpose linearly, we can decompose the mixture and treat the P-wave parts and SV-wave parts separately. We will call these components P-up and SV-up waves. In Appendix E, we derive simple analytic formulae for the anisotropy ratio $\mathcal{A}$ and reduced transfer function β' for P-up and SV-up waves, and in Figs. 6.3 and 6.4 we graph those formulae. In these plots, for concreteness, we have chosen $c_S = c_P/2$.

Consider, first, the P-up waves (solid curves in Figs. 6.3 and 6.4). Due to Snell's law [*cf.* Eq. (6.40) below], these waves propagate at an angle $\alpha_P = \arcsin(c_P/c_H)$ to the vertical. Such

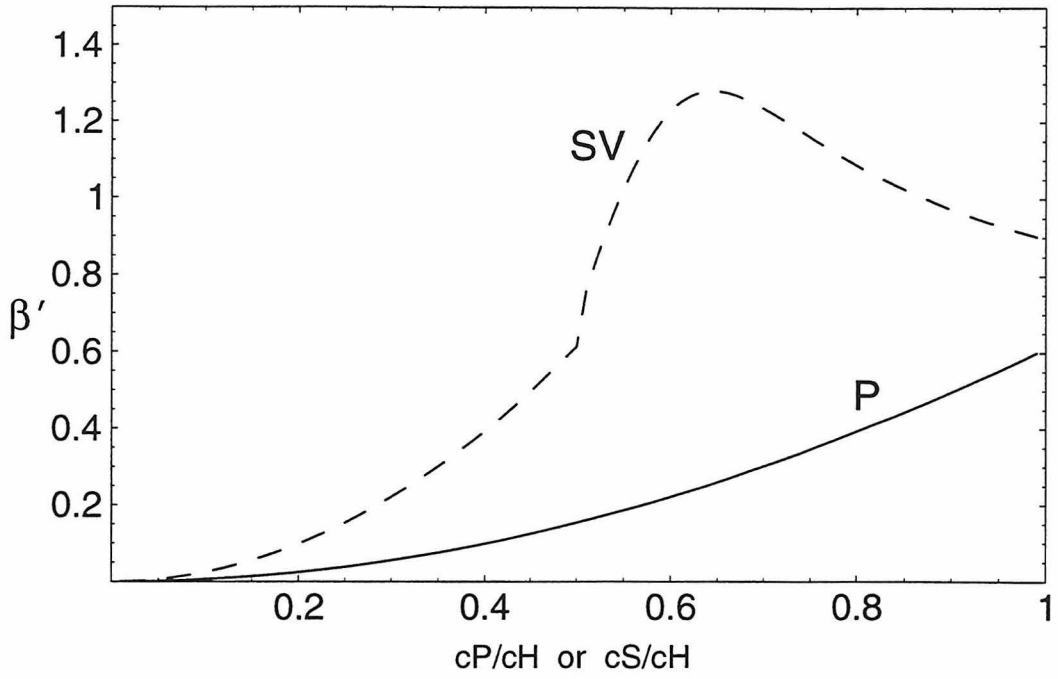

Figure 6.4: Reduced transfer function P-up and SV-up waves.
Notation and description of these waves is exactly as for Fig. 6.3.

propagating waves can therefore exist only for $c_H > c_P$; when $c_H < c_P$, P-waves are evanescent. For this reason, in the Figures we plot on the abscissa the ratio c_P/c_H running from 0 to 1. When P-up waves hit the surface, some of their energy is converted into SV-waves propagating downward at an angle $\alpha_S = \arcsin(c_P/c_H)$; the rest of the energy goes into reflected P-waves. The resulting combination of upgoing P- and downgoing P- and SV-waves gives rise to the anisotropy and reduced transfer functions shown in the Figures.

For $c_H \gg c_P$ the waves travel nearly vertically. Their P-components produce vertical motions, while the much weaker SV-waves created on reflection produce horizontal motions. As a result, $\mathcal{A}$ is large, diverging in the limit $c_H \to \infty$, and decreasing gradually to unity as $c_H \to c_P$. As we shall see below, this is typical: when P-waves predominate in a wave mixture, $\mathcal{A}$ is typically somewhat larger than unity.

For these P-up waves, the gravity gradients produced by the surface source cancel those from the subsurface source in the limit $c_H \gg c_P$, causing β' to vanish. As c_H is reduced (moving rightward in Fig. 6.4), the cancellation becomes imperfect and β' grows, though never to as large a value as β' would have in the absence of the surface term ($\sim 1.3 - 2.4$). The surface-subsurface cancellation is easily understood. In the limit $c_H \gg c_P$, the P-waves propagate nearly vertically, with vertical

reduced wavelength for their density oscillations, $1/k_V = c_P/\omega$, that is small compared to the gravity-gradient e-folding length $\mathcal{Z}_{\rm sgg} = 1/k = c_H/\omega$ over which the waves' sources are integrated in Eq. (6.24) to produce the gravitational force. The surface source plus the top quarter wavelength of subsurface source (multiplied by ρ) constitute the mass per unit area that has been raised above a node of the mode's displacement eigenfunction; and correspondingly their sum vanishes. Below that node, alternate half wavelengths of the subsurface source cancel each other in a manner that gets weighted exponentially with depth, e^{-kz}; their cancellation is excellent in the limit $1/k_V \ll 1/k$.

Turn now to the SV-up waves. Upon reflection from the surface, these produce a mixture of downgoing SV- and P-waves. This combination gives rise to the anisotropy and reduced transfer functions shown dashed in Figs. 6.3 and 6.4. Again by Snell's law, SV-up waves propagate at an angle $\alpha_S = \arcsin(c_S/c_H)$ to the vertical; thus, propagation is possible only for $c_H > c_S$, and so we plot on the abscissa c_S/c_H running from 0 to 1. When $c_H > 2c_S = c_P$ (left half of graphs), the downgoing P-waves generated at the surface can propagate; when $c_H < 2c_S = c_P$ (right half of graphs), the downgoing P-waves have imaginary propagation angle α_P and thus are evanescent (decay exponentially with depth). This is analogous to the phenomenon of total internal reflection which one encounters in elementary optics. The downgoing P-waves are the sole subsurface source of gravity-gradient noise, and since they are only a modest component of the SV-Up mode, the subsurface source is small. The SV-waves produce no subsurface source (no compressions), but they produce a large surface source (large surface vertical motions). This surface source is the dominant cause of the gravity-gradient noise and predominantly responsible for the rather large reduced transfer function shown in Fig. 6.4. Note that the maximum value, $\beta' \simeq 1.4$, is the same as the largest β' for RS modes in our 4-layer models of the LIGO sites (Table 6.1).

When propagating more or less vertically ($c_H > 2c_S$), these SV-up waves produce small anisotropies ($\mathcal{A} < 0.4$ — large horizontal motions and small vertical motions). When they propagate more or less horizontally, $\mathcal{A}$ is large. The divergence of $\mathcal{A}$ at $c_S/c_H = 1/\sqrt{2} = 0.707$ ($\alpha_S = \pi/4$) occurs because the SV-up waves at this angle generate no P-waves upon reflection; they only generate downgoing SV-waves, and the combination of the equal-amplitude up and down SV-waves produces purely vertical motions at the earth's surface.

6.3 Hanford

6.3.1 Hanford geophysical structure

At the LIGO site near Hanford, Washington, the top 220 m consists of a variety of alluvial layers (fluvial and glacio-fluvial deposits of the Pliocene, Pleistocene, and Holocene eras; coarse sands and gravels, fine sands, silts, and clays, in a variety of orders). The upper 40 m are dry; below about 40 m the alluvium is water-saturated. From the base of the alluvium (220 m) to a depth of $\sim$ 4 km lies a sequence of Columbia River basalts, and below that, bedrock [35, 36].

The density of the alluvial material is $\rho \simeq 1.8$ g/cm^3, independent of layer. Velocity profiles (c_P and c_S as functions of depth z) have been measured at the site by contractors in connection with two projects: LIGO [35] and the Skagit nuclear power plant [36] (which was never constructed). We have relied primarily on the Skagit report because it contains more detailed information over the range of depths of concern to us, and because there is a moderately serious discrepancy between the two reports in a key depth range, 5–25 m. The Skagit velocities there are more plausible than the LIGO ones[3].

Table 6.2 shows velocity profiles as extracted from the Skagit report. Notice the overall gradual increase in both wave speeds. This is due to compression of the alluvia by the weight of overlying material, with a consequent increase in the areas of the contact surfaces between adjacent particles (silt, sand, or gravel) [26]. Notice also the sudden increase of c_P and ν at 40 m depth, due to a transition from dry alluvia to water-saturation; the water contributes to the bulk modulus but not the shear modulus, and thence to c_P but not c_S. Notice, finally, the large jump in both c_P and c_S at the 220 m deep transition from alluvial deposits to basalt.

For ease of analysis, we have approximated the measured Hanford velocity profiles (Table 6.2) with their twelve distinct layers by the simpler four-layer model shown in Table 6.3. Layers 1 and 2 are dry alluvia, layer 3 is water-saturated alluvium, and layer 4 is basalt.

[3]The report prepared for LIGO [35] claims $c_P = 1400$ m/s, $c_S = 370$ m/s, corresponding to a Poisson ratio of $\nu = 0.46$. This might be appropriate for water-saturated materials at this depth, but is not appropriate for the dry materials that actually lie there. The Skagit report [36] shows two layers in this range of depths: one with $c_P = 520$ m/s, $c_S = 275$ m/s, for which $\nu = 0.31$; the other with $c_P = 820$ m/s, $c_S = 460$ m/s, for which $\nu = 0.28$. For dry alluvia, these values are much more reasonable than $\nu = 0.46$. We thank Alan Rohay for bring this point to our attention.

Table 6.2: Velocity profiles at the Hanford LIGO site.

These velocities were extracted from from Table 2.5–3, Fig. 2.5–10, and Sec. 2.5.2.5 of the Skagit Report [36]. They are based on (i) cross-hole measurements (waves excited in one borehole and measured in another) down to 60 m depth; (ii) downhole measurements (waves excited at surface and arrivals measured in boreholes) from $z = 60$ m to $z = 175$ m; (iii) extrapolations of downhole measurements at other nearby locations, and surface refraction measurements (waves excited at surface and measured at surface) at the LIGO site, from $z = 175$ m down into the basalt at $z > 220$ m. The downhole measurements at one well (Rattlesnake Hills No. 1) have gone into the basalt to a depth of 3230 m. Depths are in meters, velocities are in m/s.

Depths	c_P	c_S	ν
0–12	520	270	0.31
12–24	820	460	0.28
24–32	1000	520	0.32
32–40	1260	530	0.39
40–50	1980	560	0.46
50–80	2700	760	0.46
80–110	2700	910	0.44
110–160	1800	610	0.44
160–210	2400	910	0.42
210–220	2900	1200	0.39
220–250	4900	2700	0.27
250–3230	5000–5700 competent basalt flows 4000–5500 interbeds		

Table 6.3: Four-layer model for the velocity profiles at the Hanford LIGO site.

Notation: n — layer number, D_n — layer thickness, c_{Pn} — P-wave speed in this layer, c_{Sn} — S-wave speed in this layer, ν_n — Poisson ratio in this layer. Depths and thicknesses are in meters, speeds are in m/s.

n	Depths	D_n	c_{Pn}	c_{Sn}	ν_n
1	0–12	12	520	270	0.32
2	12–40	28	900	500	0.28
3	40–220	180	2400	700	0.45
4	220–4000	3780	4900	2700	0.28

6.3.2 Hanford model results

The horizontally stratified geologies at Hanford and Livingston support a variety of Love and Rayleigh modes, as described in the Introduction and in, *e.g.*, Refs. [33, 34]. We shall focus on Rayleigh modes in this section, since they are the sole producers of seismic gravity-gradient noise.

In each geological layer, consider a specific Rayleigh mode. It consists of a superposition of plane-fronted P- and SV-waves. Because each layer is idealized as homogeneous, the mode's SV- and P-waves are decoupled within the layer. However, they are coupled at layer interfaces and the earth's surface by the requirement that material displacement and normal stress be continuous across the interface (or with the atmosphere in the case of the earth's surface). The details of this coupling and its consequences are worked out in Appendix C.

In each layer, the mode's P- and SV-components propagate at different angles to the vertical: α_{Pn} for the P-waves in layer n and α_{Sn} for the SV-waves. However, the components must all move with the same horizontal speed

$$c_H = \frac{c_{Pn}}{\sin\alpha_{Pn}} = \frac{c_{Sn}}{\sin\alpha_{Sn}} \tag{6.40}$$

(Snell's law), and they must all have the same horizontal wave number k and frequency $\omega = 2\pi f$.

Each mode can be characterized by its dispersion relation for horizontal motion $\omega(k)$, or equivalently $c_H(f)$. It will be helpful, in sorting out the properties of the modes, to understand first what their dispersion relations $c_H(f)$ would be if their SV-wave components were decoupled from their P-wave components. We shall do so in the next subsection, and then examine the effects of coupling in the following subsection. Note that we shall ignore the effects of damping in these two subsections, since the lengthscales involved are less than (or at most of the same order as) the dissipation lengthscales of both P- and SV-waves [*cf.* Eq. 6.5].

P-SV decoupling approximation

Recall that we denote by RPn the nth Rayleigh mode of P-type and by RSn the nth Rayleigh mode of SV-type. In the approximation of P-SV decoupling, Mode RPn with horizontal speed c_H propagates from the earth's surface through sequences of strata (generating no SV-waves) until it reaches a depth D_P where c_P first exceeds c_H. At that location, it reflects and returns to the surface, and then is reflected back downward. The mode's dispersion relation $c_H(f)$ is determined by the resonance condition that the reflected waves arrive at the surface in phase with the original downgoing waves.

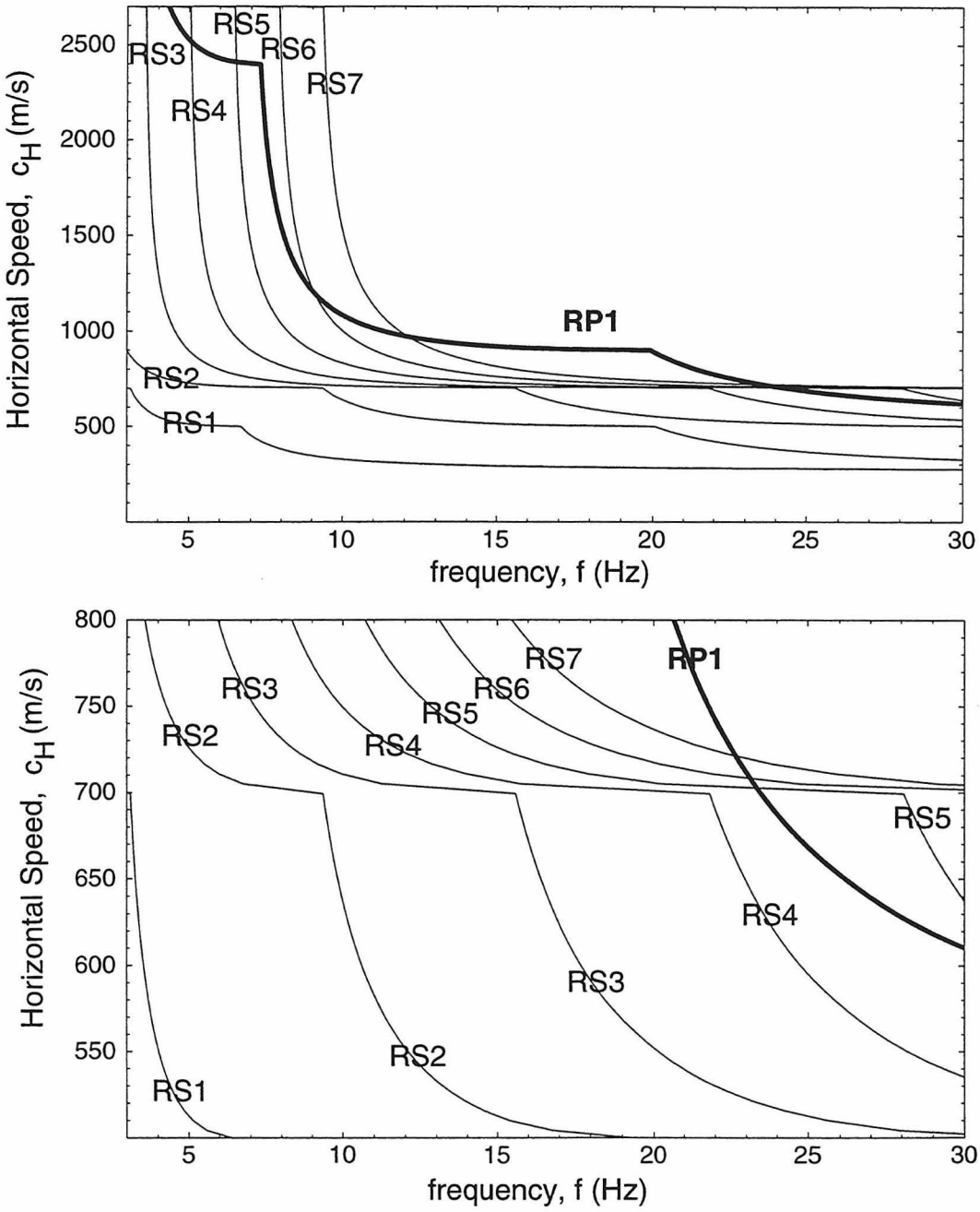

Figure 6.5: Dispersion relations for the 4-layer Hanford model, neglecting P-SV coupling.

These dispersion relations were computed using the P-SV decoupling approximation, Eqs. (6.42) and (6.43).

This resonance condition is evaluated most easily by following the (locally) planar waves vertically downward and then back up, thereby returning precisely to the starting point. On this path, the vertical component of the wave vector is $(\omega/c_P)\cos\alpha_P$. Correspondingly, the waves' total roundtrip phase shift is

$$\Delta\Phi = 2\int_0^{D_P} (\omega/c_P)\cos\alpha_P\, dz + \delta\Phi_{\text{interfaces}} \,. \tag{6.41}$$

Here $\delta\Phi_{\text{interfaces}}$ is the total phase shift acquired at the interfaces and upon reflecting at the earth's surface. Setting $\omega = 2\pi f$ and $\cos\alpha_P = \sqrt{1-(c_P/c_H)^2}$ [Snell's law (6.40)], and imposing the resonance condition $\Delta\Phi = 2n\pi$, we obtain the following dispersion relation for mode RPn:

$$f = \frac{n - (\delta\Phi_{\text{interfaces}}/2\pi)}{2\int_0^{D_P}\sqrt{c_P^{-2}-c_H^{-2}}\,dz} \,. \tag{6.42}$$

Similarly, for mode RSn the dispersion relation is

$$f = \frac{n - (\delta\Phi_{\text{interfaces}}/2\pi)}{2\int_0^{D_S}\sqrt{c_S^{-2}-c_H^{-2}}\,dz} \,, \tag{6.43}$$

where D_S is the depth at which c_S first reaches c_H.

Figure 6.5 shows these decoupling-approximation dispersion relations for our 4-layer model of $c_P(z)$ and $c_S(z)$ (Table 6.3). For the RS-waves, the total interface phase shift has been set to $\delta\Phi_{\text{interfaces}} = \pi$, which would be the value for a single layer with a huge rise of c_S at its base. For the sole RP mode shown, RP1, it has been set to $\delta\Phi_{\text{interfaces}} = \pi/2$, which is a fit to the dispersion relation with P-SV coupling (Fig. 6.6, to be discussed below).

Notice that for fixed horizontal speed c_H, the lowest RP mode, RP1, occurs at a much higher frequency f than the lowest RS mode, RS1. This is because of the disparity in propagation speeds, c_P = several $\times$ c_S. Notice also the long, flat plateaus in $c_H(f)$ near $c_H = c_{S2} = 500$ m/s and especially $c_{S3} = 700$ m/s for the RSn modes, and near $c_H = c_{P2} = 900$ m/s and $c_H = c_{P3} = 2400$ m/s for RP1. Mathematically these are caused by the vanishing square roots in the denominators of the dispersion relations (6.42) and (6.43). Physically they arise because the mode's waves "like" to propagate horizontally in their deepest layer. At high frequencies (*e.g.*, $f \gtrsim 10$ Hz for $c_H \simeq c_{S3} =$ 700 m/s), several modes propagate together nearly horizontally in that deepest layer.

Effects of P-SV coupling on dispersion relations

Figure 6.6 shows the dispersion relations $c_H(f)$ for the lowest 8 modes of our 4-layer model at Hanford, with P-SV coupling included. These dispersion relations were computed using the multilayer equations of Appendix C. We shall now discuss these various dispersion relations, beginning with that for the fundamental mode, which is labeled RF in the Figure.

Mode RF was studied in Sec. 6.2.1 for an idealized homogeneous half space. It is vertically evanescent in both its P- and SV-components (except at low frequencies in the top layer); for this reason, it did not show up in our idealized decoupling-approximation dispersion relation (Fig. 6.5). At frequencies $f \gtrsim 10$ Hz, its vertical e-folding lengths $\mathcal{Z}_P$ and $\mathcal{Z}_S$ are both short enough that it hardly feels the interface between layers 1 and 2, and the homogeneous-half-space description is rather good. Below 10 Hz, interaction with the interface and with layer 2 pushes c_H up.

By contrast with the P-SV-decoupled Fig. 6.5, every Rayleigh overtone mode RPn or RSn in Fig. 6.6 now contains a mixture of SV- and P-waves. This mixture varies with depth in the strata and is generated by the same kind of interface reflection and refraction as we met in Sec. 6.2.2 for SV-up and P-up waves. Most regions of the (c_H, f) plane are dominated either by SV- or P-waves — the ratio of energy in one mode to that in the other is > 2.

In the vicinity of the wide gray band marked RP1, the modes are predominately of RP type; away from that vicinity they are predominately RS. The location of the RP1 band has been inferred from the computed S- and P-wave amplitudes. Notice how well it agrees with the decoupling approximation's RP1 dispersion relation (Fig. 6.5). Away from the RP1 band, the dispersion relation for each RSn mode is reasonably close to its decoupling-approximation form (compare Figs. 6.6 and 6.5). As each mode nears and crosses the RP1 band, its dispersion relation is distorted to approximately coincide, for awhile, with the RP1 shape. Correspondingly, all its other properties become, for awhile, those of an RP mode.

Anisotropy ratios and reduced transfer functions

Figure 6.7 shows the anisotropy ratio $\mathcal{A}$ and reduced transfer function β' for the lowest eight modes of our 4-layer model of Hanford. These were computed using the multilayer equations of Appendix C. On the Figure, the mode names "RSn" have been shortened to "n", and "RF" to "F". The bottom set of graphs is the value β'_L that the net reduced transfer function would have if the mode of interest were mixed with enough Love waves to reduce the net anisotropy ratio to the value $\mathcal{A}_{\text{net}} \simeq 1.0$

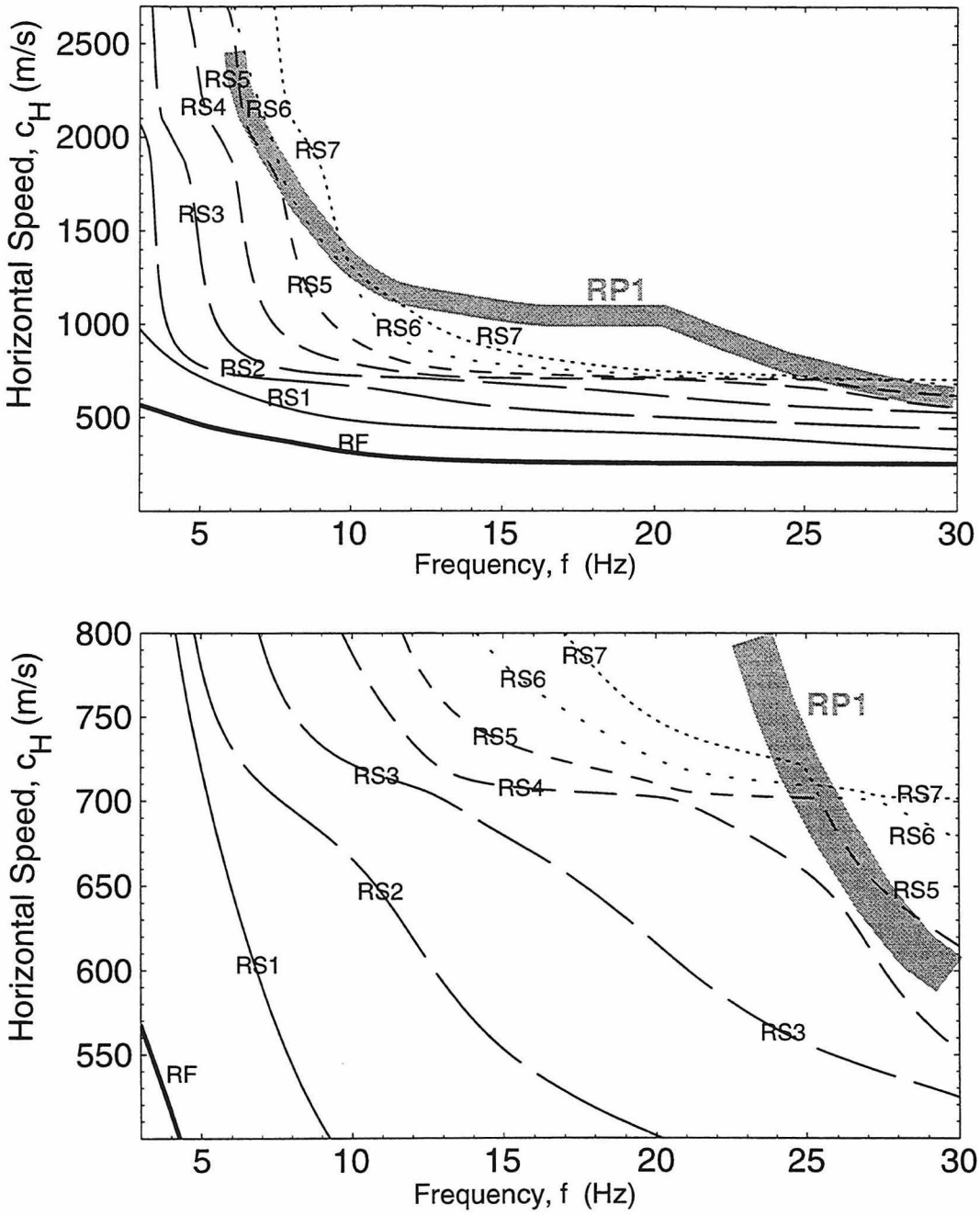

Figure 6.6: Dispersion relations for the 4-layer Hanford model, including P-SV coupling.

These dispersion relations were computed by including coupling between P- and SV-waves produced at boundaries between layers and at the earth's surface. We show the RF mode, lowest 7 RS modes, and mode RP1.

typical of measured seismic spectra at Hanford during quiet times [14].

Fundamental Mode RF. Above 10 Hz, mode RF has $\mathcal{A} \simeq 2.2$, $\beta' \simeq 0.84$, and $\beta'_L \simeq 0.58$, in accord with our homogeneous half-space model (Sec. 6.2). Below 10 Hz, coupling of the RF mode to layer 2 produces a growth of the subsurface source to partially cancel the surface source, and a resulting fall of β' to 0.4 and β'_L to 0.35.

RS Overtones. In RS regions (away from the RP1 band) the overtone modes RSn generally have $\mathcal{A} \lesssim 1$ so $\beta'_L \simeq \beta'$ — little or no admixed Love waves are needed to bring the anisotropy down to 1.0. The value of β' ranges from ~ 0.4 to 1.4 in the RS regions; but when the RP1 mode is nearby in the c_H–f plane, its admixture drives β' down to $\lesssim 0.2$.

Mode RS1 shows characteristic "SV-up" behavior near 25 Hz (compare Fig. 6.7 with Figs. 6.3 and 6.4). Its $\mathcal{A}$ has a very large resonance and its subsurface source (not shown in the Figures) has a sharp dip to nearly zero, resulting from 45° upward propagation of its SV-component in the top layer and no production of P-waves upon reflection. At frequencies above our range of interest, this same SV-Up behavior will occur in successively higher RSn modes.

RP1 Mode. The region of RP1 behavior is shown as thick gray bands in Fig. 6.7 (*cf.* the bands in Fig. 6.6). The RP1 reduced transfer function is small, $\lesssim 0.2$, due to the same near-cancellation of its surface and subsurface sources as we met for P-Up waves in Sec. 6.2.2 and Fig. 6.4. As each RS mode crosses the core of the RP1 region, its β' shows a dip and its anisotropy shows a peak, revealing the temporary transition to RP behavior.

Higher-order RP Modes. The higher-order RP modes ($n = 2, 3, ...$) in our frequency band will lie in the vicinity of RSn overtones with $n > 8$. We expect these RPn modes to show similarly small reduced transfer functions to those for RP1, but we have not attempted to compute them, with one important exception: high-order RP modes that travel horizontally in Hanford's ~ 4 km thick basalt layer. We consider these modes in the next subsection and find an (explainable) surprise: β' can be as large as for RS modes due to a resonance.

RP modes that travel horizontally in the basalt

As discussed in the Introduction (Sec. 6.1.4), the ground motions at the Hanford corner and end stations sometimes show time delays in correlated motion, corresponding to wave propagation speeds of $\sim$ 5000–6000 m/s [14, 23]. These motions must be due to wave modes that travel horizontally in the ~ 4 km thick basalt layer at the base of the alluvium, or in the bedrock beneath the basalt. We have computed the properties of such wave modes for the case of horizontal propagation in the

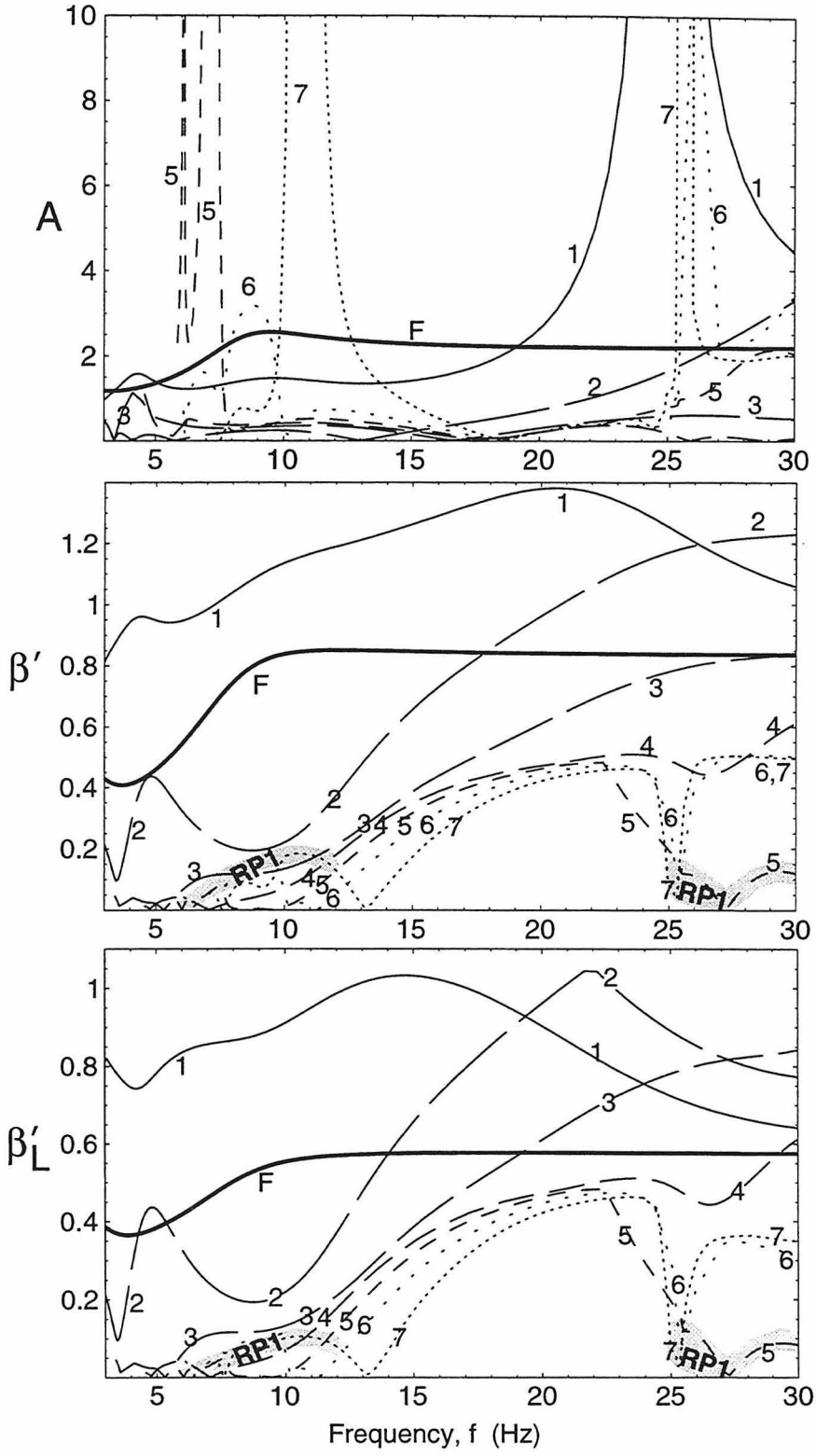

Figure 6.7: Properties of the RF, RS1-7, and RP1 modes of the 4-layer Hanford model, including P-SV coupling.

basalt layer — layer 4 of our 4-layer Hanford model.

Because of the many closely spaced modes in the relevant (c_H, f) region (c_H a little larger than $c_{P4} = 4900$m/s, $3\,\text{Hz} \leq f \leq 30\,\text{Hz}$), it is not reasonable, or even of interest, to compute their dispersion relations explicitly. Instead, we have assumed an idealized dispersion relation $c_H = 4910$ m/s independent of frequency.

The basalt layer is so thick that nearly horizontally propagating waves will be substantially damped in traveling from its lower face to its upper face and back; and, the S-waves will be much more strongly damped than the P-waves. For this reason, we idealize these waves as purely P-up as they impinge from the basalt layer 4 onto the layer 3–4 interface. These P-up waves at interface 3–4 are treated as a source for other wave components in all 4 layers.

For these waves, dissipation [Eqs. (6.5) and associated discussion] may be much more important than for the RF, RS and RP1 modes treated above. We therefore include it in our analysis. We do so in the 4-layer equations of Appendix C by giving the sound speeds appropriate imaginary parts,

$$\begin{aligned} \frac{\Im(c_{Pn})}{\Re(c_{Pn})} &= -\frac{1}{2Q_P} = -0.015\,, \\ \frac{\Im(c_{Sn})}{\Re(c_{Sn})} &= -\frac{1}{2Q_S} = -0.03\,, \end{aligned} \tag{6.44}$$

while keeping their real parts equal to the values shown in Table 6.3. We have solved the resulting multilayer equations numerically, obtaining the anisotropy ratios and reduced transfer functions shown in Fig. 6.8.

The oscillations in $\mathcal{A}$ with frequency $\Delta f = c_{P3}/\left(2D_3\sqrt{1 - c_{P3}^2/c_H^2}\right) = 7$ Hz are associated with resonant excitations of layer 3 and their influence on layer 2 and thence on layer 1; *cf.* the decoupling-approximation dispersion relation (6.42). The oscillations in both $\mathcal{A}$ and β' with frequency $\Delta f = c_{P2}/\left(2D_2\sqrt{1 - c_{P2}^2/c_H^2}\right) = 16$ Hz are associated with resonant excitations of layer 2. The large values of $\mathcal{A}$ are what we have learned to expect for RP modes.

The two broad peaks in β' are far higher ($\beta'_{\text{max}} \sim 0.6$ and 1.3) than the maximum β' that we have previously seen for RP modes (~ 0.2) or P-Up waves (~ 0.4). One key to this large β' is the strong resonant excitations of layer 2, with their accompanying large compressions and large contributions to the subsurface source of gravity gradients. A second key is the waves' large horizontal speed $c_H = 4910$ m/s, which produces a long horizontal reduced wavelength $1/k = c_H/(2\pi f) \simeq 30$ m and a correspondingly long vertical e-folding length $\mathcal{Z}_{\text{sgg}} = 1/k \sim 30$–$60$ m for the contributions to β' [Eq. (6.25)]. This e-folding length is longer than the depth $D_1 = 12$ m of the top layer and

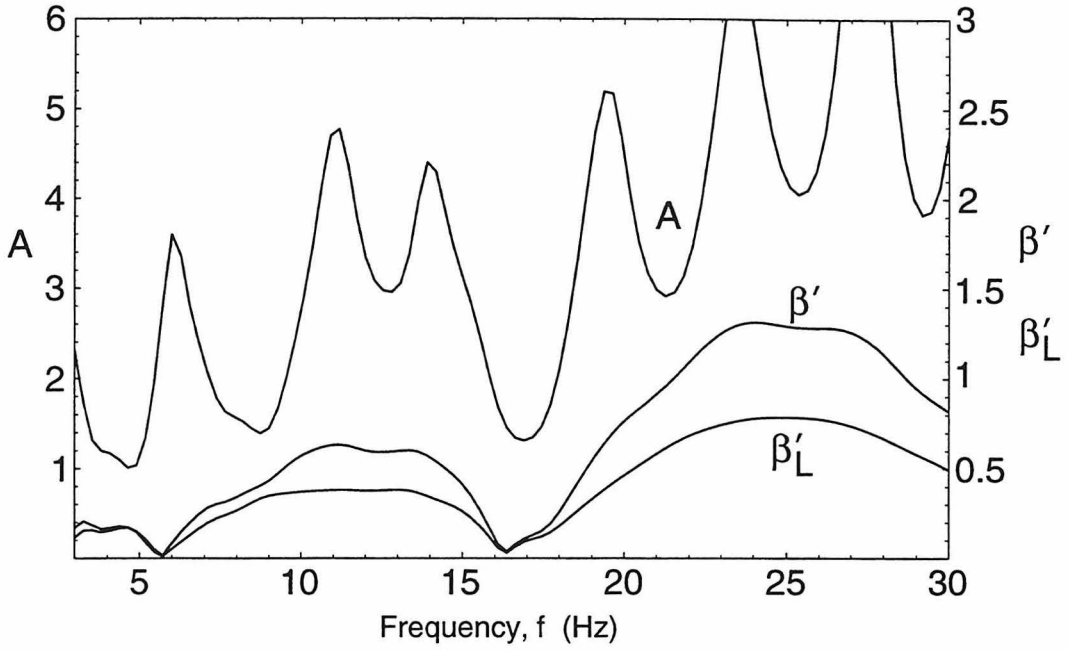

Figure 6.8: Properties of RP modes propagating in the deep basalt at Hanford

These RP modes propagate nearly horizontally in layer 4 ($\sim$ 4 km thick basalt layer) at Hanford (c_H slightly larger than c_{P4} = 4900 m/s); we include here the effects of volumetric damping in the alluvium above the basalt. We show the anisotropy $\mathcal{A}$ and reduced transfer function β' for the pure RP modes, as well as the reduced transfer function β'_L for RP modes mixed with enough Love waves to lower the net anisotropy to 1.0.

is comparable to the depths of the top two layers, $D_1 + D_2 = 40$ m at Hanford. As a result, layer 2 and the upper parts of layer 3 are significant contributors to the seismic gravity-gradient noise, along with layer 1.

Summary of Hanford model results

The most important of the above results are those for the reduced transfer functions of the various modes at Hanford. They are summarized in Table 6.1 and their implications are discussed in the Introduction, Sec. 6.1.4.

6.4 Livingston

6.4.1 Livingston geophysical structure

At the LIGO site near Livingston, Louisiana, the geological strata consist of alluvial deposits laid down by water flowing into the Gulf of Mexico. As the ocean level has risen and fallen, alluvial terraces of varying thickness have been formed. This alluvium (layers of clay, silt, sand, and gravel in various orders) is of the Holocene, Pleistocene, and Pliocene eras going down to a depth of about 700 m, and compacted alluvium of the upper Miocene and earlier eras below that. These sedimentary deposits extend down to a depth of about 3 km [27] before reaching bedrock.

For our analysis the principal issue is the vertical velocity profiles $c_P(z)$ and $c_S(z)$. The primary difference between Livingston and Hanford is the depth of the water table: it is only about 2 m down at Livingston, versus about 40 m at Hanford. This difference should cause c_P to soar to about 1600 m/s at depths of a few meters at Livingston; it only does so roughly 40 m down at Hanford.

The only measurements of the Livingston velocity profiles that we have been able to find are those performed in a site survey for LIGO [37]. Those measurements only include c_S, not c_P, and only go down to a depth of 15 m. Accordingly, we have had to estimate the velocity profiles from these sparse data and from the lore accumulated by the geophysics and seismic engineering communities.

That lore suggests that c_S should increase as about the $1/4$ power of depth [26]. (This increase is due to the fact that the shear restoring force must be carried by the small-area interfaces between the grains of gravel, sand, silt, or clay; the weight of overlying material compacts the grains, increasing the areas of their interfaces.) We have fit the measured $c_S(z)$ in the top 15 m ({7 ft, 700 ft/s}, {21 ft,

810 ft/s}, {50 ft, 960 ft/s}) to a 1/4 power law, adjusting the fit somewhat to give speeds at greater depths in rough accord with measurements at a similar sedimentary site in Tennessee [38]. Our resulting fit is

$$c_S = 185\,\mathrm{m/s}(1 + z/2.9\,\mathrm{m})^{1/4}\ . \tag{6.45}$$

A combination of theory and phenomenology [Eqs. (6.24), (6.26) of [26] and associated discussion] tells us that in these water-saturated alluvia, the material's Poisson ratio should be about

$$\nu = \frac{1}{2}\left[1 - 0.39\left(\frac{c_S}{1000\,\mathrm{m}}\right)^2\right]\ . \tag{6.46}$$

(The Poisson ratio goes down gradually with increasing compaction and increasing c_S because water is playing a decreasing role compared to the grains.) The standard relation

$$c_P = c_S\sqrt{\frac{2-2\nu}{1-2\nu}}\ , \tag{6.47}$$

combined with Eqs. (6.45) and (6.46), then gives us the vertical profile for c_P.

These profiles are valid only in the water-saturated region. Although the water table is at $\sim$ 2 m, measurements elsewhere [38] suggest that one must go downward an additional several meters before the effects of the water on c_P will be fully felt. Accordingly, we expect $c_P \sim 2c_S$ in the top $\sim$ 5 m at Livingston, followed by a sharp rise to the values dictated by Eqs. (6.45)–(6.47).

6.4.2 Livingston 4-layer model

We have fit a four-layer model to these estimated Livingston velocity profiles. Our fit is shown in Table 6.4. This model is the primary foundation for our exploration of seismic gravity gradients at Livingston. As discussed above, it principally differs from the 4-layer Hanford model by the rapid increase of c_P at 5 m depth at Livingston, due to the higher water table. All other differences have a much more minor influence on the seismic gravity-gradient noise.

6.4.3 Livingston model results

Mode overview

Because the top, unsaturated layer is so thin, RP modes cannot resonate in it in our frequency band; and because water makes c_P so large just below the top layer, the RP modes in our band can only

Table 6.4: Four-layer model for the velocity profiles at the Livingston LIGO site. Notation and units are as in Table 6.3.

n	Depths	D_n	c_{Pn}	c_{Sn}	ν_n
1	0–5	5	440	220	0.33
2	5–105	100	1660	400	0.47
3	105–905	800	1700	700	0.40
4	905–3005	2100	1900	1000	0.31

propagate at a correspondingly high speed, $c_H \geq 1660$ m/s. The lowest 10 RS modes, by contrast, are confined to speeds $c_H \lesssim 1000$ m/s. As a result — in contrast to Hanford — there is no mixing between these lowest RS modes and the RP modes. The RS modes have purely RS character, with no significant RP admixture.

In the next section we shall study the lowest 10 RS modes along with the fundamental mode. In the following section, we shall examine the lowest RP mode.

RF and RS modes

We have computed the dispersion relations, anisotropy ratios, and reduced transfer functions for modes RF and RS1–10 in our 4-layer Livingston model, using the multilayer equations of Appendix C. The dispersion relations are shown in Fig. 6.9. Because of the separation in the (c_H, f) plane of these modes from the RP mode, we expect the P-SV decoupling approximation to work quite well here. Indeed, the RS modes have just the form one would expect from the decoupling approximation [Eqs. (6.43)] and from their forms at Hanford (Fig. 6.6). The anisotropy ratios and reduced transfer functions are shown in Fig. 6.10.

RF Mode. Because the top layer is 2.5 times thinner in our Livingston model than at Hanford, the frequency at which the RF mode becomes like that of a homogeneous half space is 2.5 times higher: 25 Hz compared to 10 Hz. Only above 25 Hz do the mode's properties asymptote toward their homogeneous-half-space values of $c_H = 205$ m/s, $\mathcal{A} = 2.2$, $\beta' = 0.85$ and $\beta'_L = 0.39$. At lower frequencies, interaction with layer 2 pushes β' into the range 0.65–0.9, and β'_L into the range 0.35–0.45.

It is possible that the effects of water saturation will cause c_P to shoot up at depths shallower than the 5 m assumed in our model; a transition anywhere in the range $2\,\mathrm{m} \lesssim z \lesssim 5\,\mathrm{m}$ must be considered reasonable. If the transition in fact occurs at depths shallower than 5 m, the peaks of β'

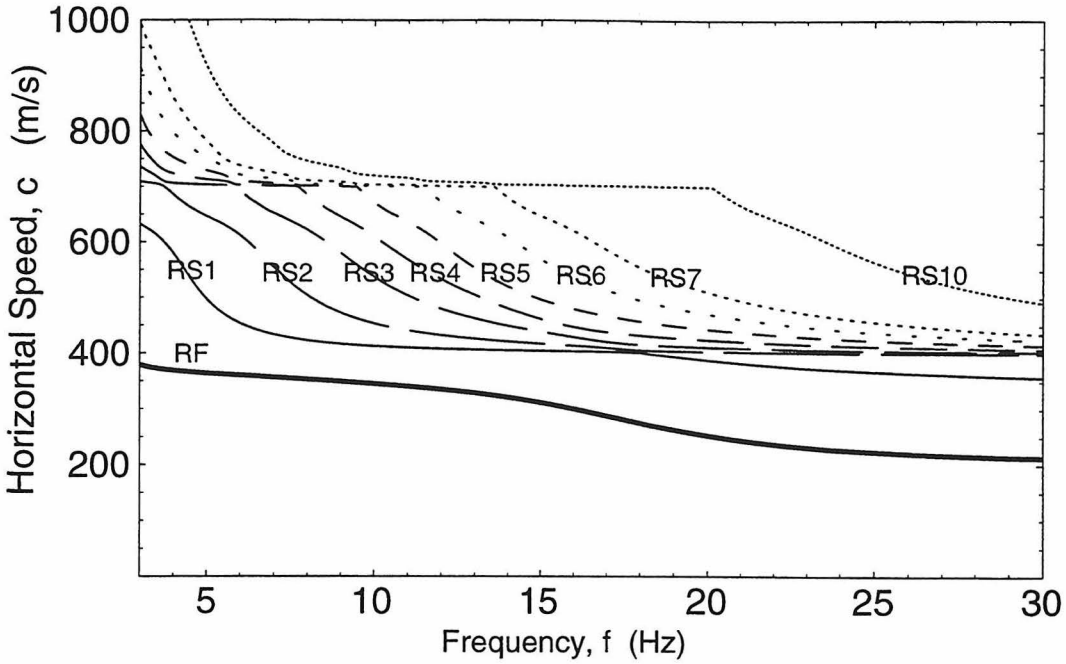

Figure 6.9: Dispersion relations for the 4-layer Livingston model, including P-SV coupling. These dispersion relations were computed by including coupling between P- and SV-waves produced at boundaries between layers and at the earth's surface. We show the fundamental mode and the lowest 10 RS modes.

and β'_L will be pushed to correspondingly higher frequencies. Thus, we must be prepared for the RF mode to have β' anywhere in the range 0.65–0.9, and β'_L in the range 0.35–0.45 at just about any frequency in our band of interest.

RS Modes. In our frequency band, the RS modes have negligible excitation in layers 3 and 4, and their P-waves are evanescent in layers 2, 3 and 4. As a result, these modes can be well approximated by SV-up waves in layer 2, impinging on the layer 1–2 interface. We have verified this by computing their anisotropies and reduced transfer functions in this 2-layer SV-up approximation by the method outlined at the beginning of Appendix E. The results for $\mathcal{A}$ and β', which relied on the 4-layer dispersion relations of Fig. 6.9, agree to within a few per cent with those of our 4-layer model (Fig. 6.10) except at frequencies below 5 Hz where the differences become somewhat larger.

Throughout our frequency band these RS modes have vertical seismic-gravity-gradient e-folding lengths $\mathcal{Z}_{\rm sgg} = 1/k \gtrsim D_1 = 5$ m. Thus, the upper parts of layer 2 contribute significantly to the reduced transfer function β', along with all of layer 1.

For modes RS1–RS5, the reduced transfer functions have the familiar range $\beta' \simeq 0.6$–1.2 that we encountered for RS modes at Hanford (Sec. 6.3.2) and for SV-Up modes in a homogeneous half

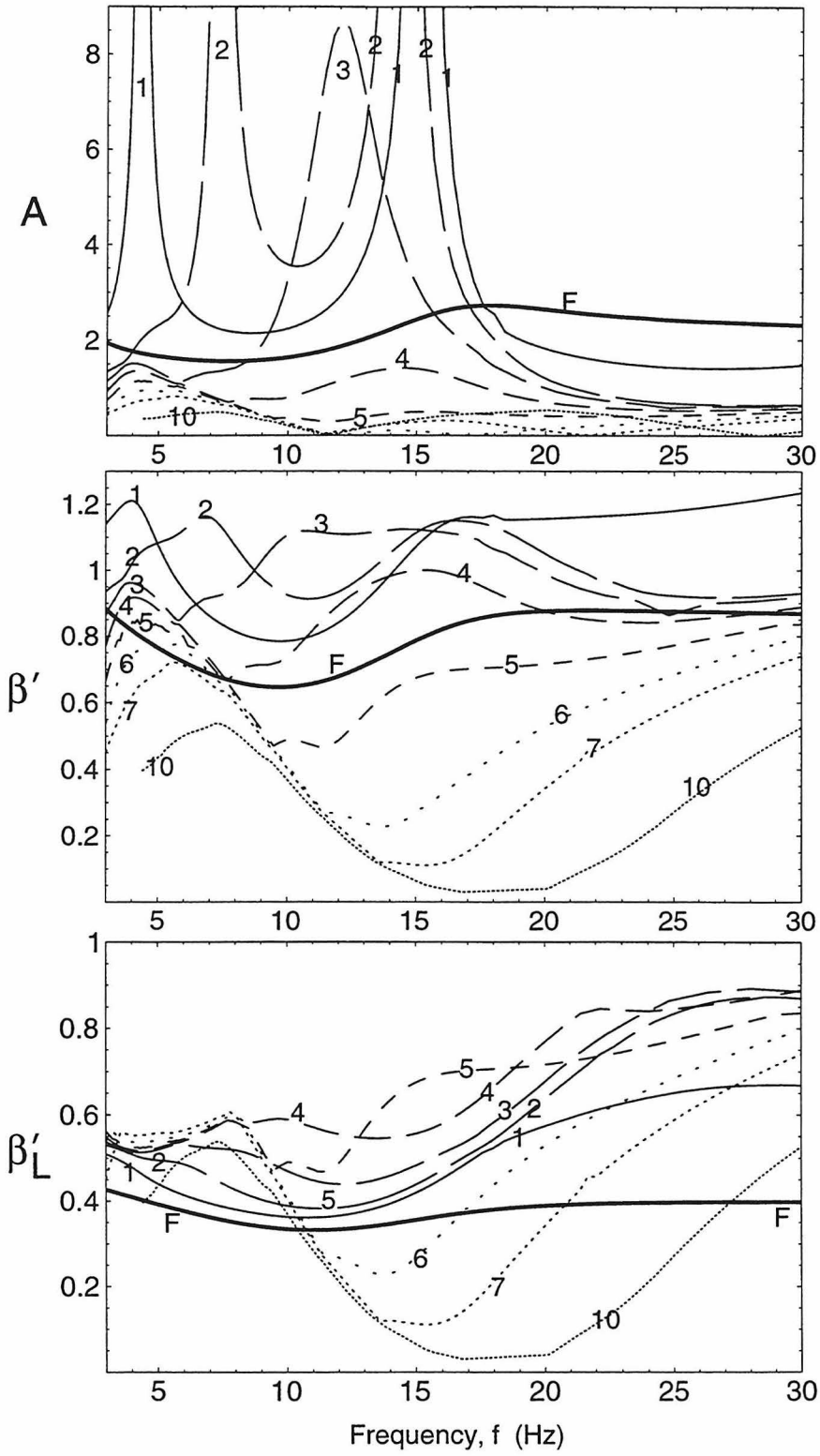

Figure 6.10: Properties of the RF and RS1-10 modes of the 4-layer Livingston model, including P-SV coupling.

Modes RS8 and RS9 are not shown; their curves are sandwiched between 7 and 10.

space (Fig. 6.4), and the gravity gradients are largely due to the S-waves' vertical surface motion.

For modes RS6–RS10, by contrast, β' shows a significant, broad dip at frequencies $f \sim 15-20$ Hz. In this frequency band, these modes contain a significant amount of P-waves in the upper layer, and so β' is rather small.

Mode RP1

Figure 6.11 shows the dispersion relation for the lowest RP mode, RP1, at Livingston, along with the RF and lowest 10 RS modes. As noted earlier, RP1 does not overlap the other modes [by contrast with Hanford (Figs. 6.5 and 6.6)].

At frequencies $f < 22.8$ Hz, the RP1 mode has horizontal speed $c_H > c_{P2} = 1660$ m/s and thus its P-waves can propagate in layers 1 and 2 (and also in layer 3 below 11.3 Hz). In this region we have evaluated $c_H(f)$ using the P-SV decoupling approximation [Eq. (6.42)].

At frequencies $f > 22.8$ Hz, the horizontal speed is $c_H < c_{P2}$, so the mode's P-waves are evanescent in layers 2, 3, and 4. In this regime we have adopted an approximation that is much more accurate than the decoupling one. We have idealized the material as two-layered: a 5 m thick upper layer with the properties of layer 1 of Table 6.4, and below that a homogeneous half space with the properties of layer 2. For this layer-plus-half-space model we have used an analytic dispersion relation due to Lee [40] (Appendix D). Because the mode's SV-waves can leak out of layer 1 into layer 2 (and then propagate away to "infinity" — or, more realistically, dissipate), Lee's dispersion relation predicts a complex frequency f if c_H is chosen real, and a complex c_H if f is chosen real. The predicted losses are small (quality factors Q decreasing from $\simeq 50$ at $f \simeq 24$ Hz to $\simeq 15$ at 30 Hz). The real part of the dispersion relation is shown in the upper panel of Fig. 6.11.

The lower panel of Fig. 6.11 shows the anisotropies and reduced transfer functions for this RP1 mode. At $f < 22.8$ Hz, where the P-waves are propagating nearly horizontally in layer 2, these properties were computed using the P-up approximation in the above two-layer (layer-plus-half-space) model; *cf.* the introduction to Appendix E. More specifically, the dispersion relation (with both c_H and f real) was taken from the P-SV decoupling approximation, the P-waves with this c_H and f were regarded as impinging from layer 2 onto the top of layer 1 at a glancing angle, and the reflected P- and SV-waves were regarded as propagating off to "infinity" (or, more realistically, dissipating before any return to the interface). This is the approximation that was so successful for the RS modes when combined with the correct 4-layer dispersion relation, but we don't have a good handle on its accuracy here, with the less reliable P-SV-decoupling dispersion relation. We

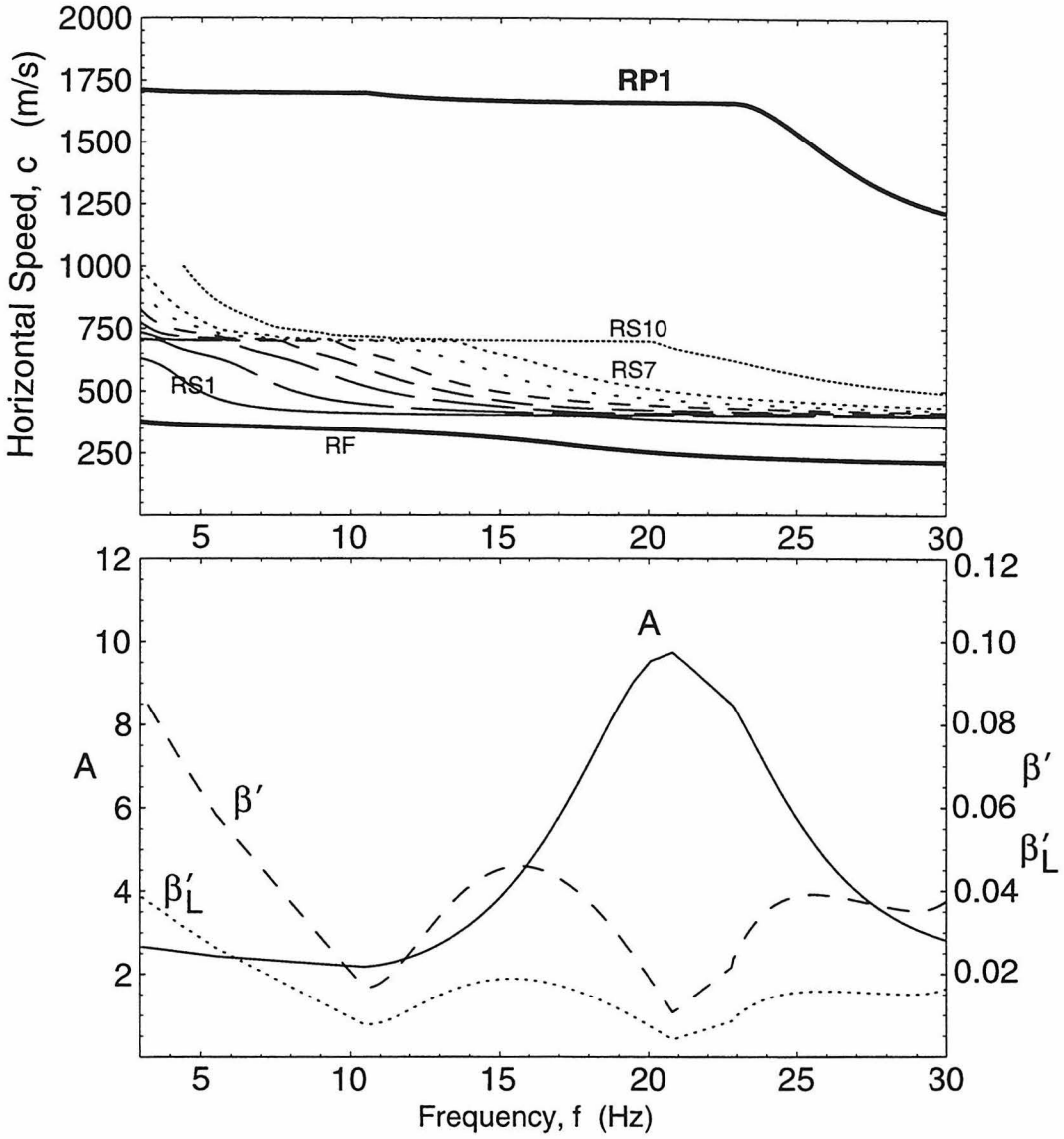

Figure 6.11: Dispersion relation and properties of mode RP1 in the 4-layer Livingston model.

Upper panel: dispersion relation for mode RP1. Also shown for comparison are the dispersion relations for the fundamental Rayleigh mode RF and the lowest few RS modes (*cf.* Fig. 6.9). Lower panel: properties of mode RP1. We show the anisotropy $\mathcal{A}$ (scaled down by factor 10 — its actual maximum is $\mathcal{A}_{\max} \simeq 9$, not 0.9), the reduced transfer function β', and the reduced transfer function β'_L when enough Love waves are mixed in to lower the net $\mathcal{A}$ to 0.6.

are much more confident of our approximation for $f > 22.8$ Hz. There we used the exact two-layer equations (Appendix C), together with Lee's exact, complex dispersion relation $c_H(f)$.

These computations produced an anisotropy that peaks at $f = 22.8$ Hz where $c_H = c_{P2}$, with a peak value of $\mathcal{A} \sim 8$ (Fig. 6.11). This is smaller than the peak anisotropies for mode RP1 at Hanford (Fig. 6.7), but comparable to those for the higher-order RP modes that propagate nearly horizontally in the Hanford basalt (Fig. 6.8). The reduced transfer function β' is everywhere small (< 0.1 and usually $\lesssim 0.04$), as a result of the by-now-familiar cancellation between contributions of the surface source and the subsurface source.

Summary of Livingston model results

The most important of the above results are those for the reduced transfer functions β' of the various modes at Livingston. They are summarized in Table 6.1 and their implications are discussed in the Introduction, Sec. 6.1.4.

6.5 Concluding Remarks

6.5.1 Summary

In this paper, we have used the theory of seismic surface waves to calculate the seismic gravity-gradient noise spectra that are to be expected at the Hanford, Washington and Livingston, Louisiana LIGO sites. Our final noise strengths, as shown in Fig. 6.2, are close to Saulson's previous rough estimate. At noisy times and near 10 Hz, the seismic gravity-gradient noise is likely to be more serious than vibrational and thermal seismic noise in advanced interferometers. Unless means are found to combat gravity-gradient noise (see below for possible methods), the hard-won gains in sensitivity due to R&D on vibration isolation and thermal noise may be compromised by seismic gravity gradients, at least at noisy times.

6.5.2 Effects of topography and of LIGO construction

In our analysis we have idealized the earth's surface near the LIGO test masses as perfectly planar and as undisturbed by LIGO construction. Irregularities in topography will significantly disturb the waves' propagation and their vertical structure only if the surface height varies by amounts as large as $\sim 2\,\mathrm{m}/(f/10\mathrm{Hz}) = (\sim 1/2$ the shortest vertical e-folding length for RF waves), on horizontal

lengthscales as short as $\sim 8\,\mathrm{m}/(f/10\mathrm{Hz}) = (\sim 2$ times the horizontal reduced wavelength $1/k$ of those RF waves), within distances of the test masses $\sim 25\,\mathrm{m}/(f/10\mathrm{Hz}) =$ (the horizontal wavelength of those RF waves), for frequencies $\sim 3 - 30$ Hz. (Of all the modes we have studied, the RF modes hug the surface most tightly and thus will be most influenced by the topography.)

Variations on these scales were rare at the two LIGO sites before construction. However, the grading that made the arms flat produced topographic variations in the vicinity of some of the test masses that are marginally large enough to disturb the propagation. Examples are the long pits dug alongside the arms at Livingston to get material for building up the arms' heights, and excavation to lower the arms below the level of the surrounding land near the southwest arm's midstation and the northwest arm's endstation at Hanford.

We speculate that these topographic modifications will alter the seismic gravity gradient noise by a few tens of percent, but probably not by as much as a factor 2. Future studies should examine this issue.

The 1 m deep concrete foundations of the buildings that house the test masses will likely also influence the noise by a few tens of percent, particularly at $\sim 20 - 30$ Hz where the RF waves' vertical penetration is short. The foundation extends approximately 10 meters by 25 meters at the interferometer's end stations (and also, in the case of Hanford, at the mid station). The foundation is approximately "X" shaped for the corner stations, with each arm of the "X" extending roughly 100 meters by 20 meters [41]. The sound speeds in the concrete will be a factor of several higher than the surrounding ground, so the foundations will form very sharp "geophysical" interfaces in the ground, causing diffraction of impinging waves and altering their vertical structure. Because the foundations are so shallow, we doubt that their net effect on the seismic gravity gradient noise can be as large as a factor 2, but future studies should examine it.

6.5.3 Measurements that could firm up our understanding of seismic gravity gradients

Our analysis is plagued by a large number of uncertainties regarding the true make-up of the ambient seismic background at the LIGO sites. We made extensive use of measurements of ground motion which functioned as constraints on what modes could be present. These measurements were helpful, but certain other measurements would be considerably more helpful. We suggest that, to the extent that resources permit, these measurements be included in future seismic surveys for gravitational-wave interferometer sites, including future surveys at the LIGO sites. [42].

First, we recommend careful measurements of the sound speeds and dynamical Poisson ratios of the ground as a function of depth, especially in the top few tens of meters and if possible down to the bedrock. At Hanford, we had reasonably complete data [36], thanks to earlier plans to build a nuclear power plant in the vicinity. As discussed in this paper, we encountered serious discrepancies between those old data and data from the LIGO geotechnical survey. At Livingston, we had no P-wave speed or Poisson ratio profiles, and the S-wave speed profiles available only went down to a depth of 15 meters. As a result, we had to use a mixture of theory, profiles from other sites, and phenomenological fitting to obtain a plausible velocity profile. Velocity profiles are of crucial importance in determining how the various modes behave in the ground.

Second, we recommend measurements that more nearly directly determine the modes that characterize the seismic motion. In this paper, as discussed above, we were able to put together very rough estimates of the modes that characterize the seismic background by using surface motion data as constraints, particularly anisotropy ratios measured at the sites. However, other techniques could provide much more useful and restrictive constraints, thereby more sharply differentiating among the various modes. In particular:

- Surface seismic arrays [21, 22] allow one to measure the phase relationships of ground motion at appropriately separated points, from which one can infer the excited modes' wave numbers $k(f)$ and horizontal propagation speeds $c_H(f)$.

- Borehole measurements [21] allow one to measure the phase correlation of motion at the surface and at some depth z underground, and the variation of amplitudes with depth, thereby introducing additional constraints on the background.

- Specialty seismic instruments called "dilatometers" [28, 29] measure directly the fractional density perturbation $\delta\rho/\rho$ that are the subsurface source of seismic gravity gradients. Measurements down a borehole with such devices could place further constraints on the mode mixtures present, and could show how $\delta\rho/\rho$ varies with depth, at fixed frequency. When correlated with vertical surface seismic measurements, they could give information about the cancellation of gravity gradients from the surface and subsurface sources.

6.5.4 Mitigation of seismic gravity gradient noise

Seismic gravity gradients are unlikely to be a major concern to LIGO detectors in the near future, since these detectors are only sensitive to frequencies $f \gtrsim 35$ Hz. Eventually, however, LIGO ex-

perimenters may succeed in achieving extremely good vibration isolation and thermal noise control at frequencies $f \lesssim 10$ Hz. At this time, the detectors may well be plagued by seismic gravity-gradient noise, at least at noisy times; and there may be a strong need to try to mitigate it.

We see two possibilities for modest amounts of mitigation: (i) monitoring the noise and removing it from the LIGO data, and (ii) building moats to impede the propagation of RF-mode seismic waves into the vicinities of the test masses.

Monitoring and correction: By using dedicated 3-dimensional arrays of vertical surface seismometers and borehole-mounted dilatometers in the vicinities of all test masses, one might be able to determine both the surface and subsurface components of $\delta\rho/\rho$ with sufficient resolution spatial and temporal resolution for computing the seismic gravity gradient noise and then removing it from the data.

Moats: By constructing a narrow, evacuated moat around each test mass, one might succeed in shielding out a large portion of the RF waves that we suspect are the dominant source of quiet-time seismic gravity gradients. The portion of $\delta\rho/\rho$ that is due to the RF mode has an attenuation length $z_{\rm atten} = q/k \simeq (3-5)\,\text{meters} \times (10\,\text{Hz}/f)$; each moat should be at least this deep. If the moat's radius is $\gtrsim \lambda/2 \sim 15$ meters, the resulting reduction in seismic gravity-gradient noise could be $\sim 1/e$.[4]

Although such a moat may be well-suited to reduce gravity gradients generated by the RF mode, it is probably not so well-suited to reduce gravity gradients generated by Rayleigh overtones. The overtones can be visualized as seismic waves that propagate by bouncing between layer interfaces and the earth's surface; they could propagate right under the moat and into the region under the test mass. Conceivably, they could even resonantly "ring" the earth under the mass, *worsening* the seismic gravity-gradient noise.

If seismic gravity-gradients are found to be a problem in the future, ideas such as moats and arrays of seismometers and dilatometers will have to be carefully considered and studied.

Acknowledgments

We thank Peter Saulson for triggering this research, and Kenneth Libbrecht, Rai Weiss and Stan Whitcomb for helpful comments. We thank Hiroo Kanamori and Susan Hough for helpful con-

[4]Such moats probably would not be effective at Livingston, where the ground is saturated, unless it is somehow possible to keep the water out of them. Water does not support shear modes, but *does* support pressure modes; the P-components of the RF-waves would propagate right through a flooded moat, invalidating its insulating properties.

versations, and Alan Rohay for helpful conversations and for providing his measurements of the seismic ground motion at Hanford and Livingston. We also thank Albert Lazzarini for facilitating access to Rohay's data sets and to blueprints of the LIGO site facilities, Fred Asiri for helping us to track down information about the geological structures at the sites (including the Skagit report), and Ronald Scott for pointing us to very useful literature as well as helpful conversations. Finally, we thank Giancarlo Cella for providing us, shortly before this paper was submitted, a copy of the VIRGO-Project manuscript on seismic gravity gradient noise [12] and for a helpful discussion. This research was supported by NSF Grant PHY–9424337. S. A. H. gratefully acknowledges the support of the National Science Foundation Graduate Fellowship Program. K. S. T. thanks the Albert Einstein Institute, Potsdam, Germany for hospitality during the final weeks of writing this manuscript.

Appendix A General Expression for Reduced Transfer Function

In this Appendix we derive Eqs. (6.17)–(6.24) for the reduced transfer function and anisotropy ratio of an arbitrary Rayleigh mode. In the text the mode is labeled J; in this Appendix we shall omit the subscript J.

The mode has frequency f, angular frequency $\omega = 2\pi f$, horizontal wave number k, horizontal phase speed $c_H = \omega/k$, and propagation direction $\hat{k}$. At the earth's surface its displacement vector is $(\xi_H \hat{k} + \xi_V \vec{e}_z) e^{i(\vec{k}\cdot\vec{x}-\omega t)}$, and beneath the earth's surface it produces a fractional density perturbation $\delta\rho/\rho = \mathcal{R}(z) e^{i(\vec{k}\cdot\vec{x}-\omega t)}$; here $\vec{k} = k\hat{k}$ is the horizontal wave vector.

Since the ambient seismic motions are horizontally isotropic, this mode is excited equally strongly for all horizontal directions $\hat{k}$, and also for all wave numbers in some (arbitrarily chosen) small band Δk around k—*i.e.*, in the annulus $C_{\Delta k}$ of width Δk in wave-vector space. Correspondingly (with an arbitrary choice for the strength of excitation), the net displacement along some horizontal direction $\hat{n}$, in the frequency band $\Delta f = c_H \Delta k/2\pi$, is

$$X(t) = \sum_{\vec{k}} \xi_H (\hat{k}\cdot\hat{n}) e^{i(\vec{k}\cdot\vec{x}-\omega t)} , \tag{6.48}$$

and the power of this random process $X(t)$ in the frequency band Δf is

$$\tilde{X}^2(f)\Delta f = \sum_{\vec{k}} |\xi_H|^2 (\hat{k}\cdot\hat{n})^2 = |\xi_H|^2 \frac{N_{\Delta \mathrm{k}}}{2} , \tag{6.49}$$

where $N_{\Delta \mathrm{k}}$ is the (normalization-dependent) total number of allowed $\vec{k}$ values in the annulus $C_{\Delta k}$. Similarly the net displacement and power along the vertical $\vec{e}_z$ direction are

$$Z(t) = \sum_{\vec{k}} \xi_V e^{i(\vec{k}\cdot\vec{x}-\omega t)} , \tag{6.50}$$

and

$$\tilde{Z}^2(f)\Delta f = \sum_{\vec{k}} |\xi_V|^2 = |\xi_V|^2 N_{\Delta \mathrm{k}} . \tag{6.51}$$

The mode's anisotropy ratio, $\mathcal{A} = \tilde{Z}/\tilde{X}$ is therefore

$$\mathcal{A}_J = \sqrt{2}|\xi_V|/|\xi_H| , \tag{6.52}$$

cf. Eq. (6.23); and the direction-averaged power $\tilde{W}^2\Delta f = (2\tilde{X}^2\Delta f + \tilde{Z}^2\Delta f)/3$ is

$$\tilde{W}^2\Delta f = \frac{|\xi_H|^2 + |\xi_V|^2}{3} N_{\Delta k} \ . \tag{6.53}$$

By analogy with Eq. (6.48), the isotropically excited mode produces a fractional perturbation in density on and beneath the earth's surface given by

$$\frac{\delta\rho}{\rho} = \left[\xi_V \delta(z) + \sum_{\vec{k}} \mathcal{R}\right] e^{i(\vec{k}\cdot\vec{x} - \omega t)} \ , \tag{6.54}$$

where $\delta(z)$ is the Dirac delta function. As an aid in computing the gravitational acceleration produced on one of the interferometer's test masses by these density perturbations, we place the origin of coordinates (temporarily) on the earth's surface, immediately beneath the test mass. Then the location of the test mass is $-\mathcal{H}\vec{e}_z$, where $\mathcal{H}$ is its height above the surface. We denote by $\hat{m}$ the unit vector along the laser beam that is monitoring the test mass's position. Then the gravitational acceleration along the $\hat{m}$ direction is

$$a_{\hat{m}}(t) = -\int d^3x' \frac{(\vec{x}'\cdot\hat{m}) G\delta\rho(\vec{x}', t)}{|\vec{x}' + \mathcal{H}\vec{e}_z|^3} \ . \tag{6.55}$$

Invoking Eq. (6.54) and introducing Cartesian coordinates (x', y', z') inside the sum with $\vec{k}$ along the x'-direction, we bring Eq. (6.55) into the form

$$a_{\hat{m}} = -\sum_{\vec{k}} e^{-i\omega t} G\rho \int\int\int \frac{(x'm_x + y'm_y) e^{ikx'} [\xi_V \delta(z') + \mathcal{R}(z')]}{[x'^2 + y'^2 + (z' + \mathcal{H})^2]^{3/2}} dz'dx'dy' . \tag{6.56}$$

Integrating out the horizontal directions x' and y', we obtain our final expression for the gravitational acceleration on the test mass

$$a_{\hat{m}} = -\sum_{\vec{k}} 2\pi i G\rho(\hat{m}\cdot\hat{k}) e^{-i\omega t} e^{-k\mathcal{H}} \left(\xi_V + \int_0^\infty \mathcal{R}(z') e^{-kz'} dz'\right) \ . \tag{6.57}$$

We next solve the pendular equation of motion for the displacement $\delta\vec{x}_j \cdot \hat{m}_j$ of the test mass in response to this gravitational acceleration (where the label $j = 1$, 2, 3, or 4 indicates which of the

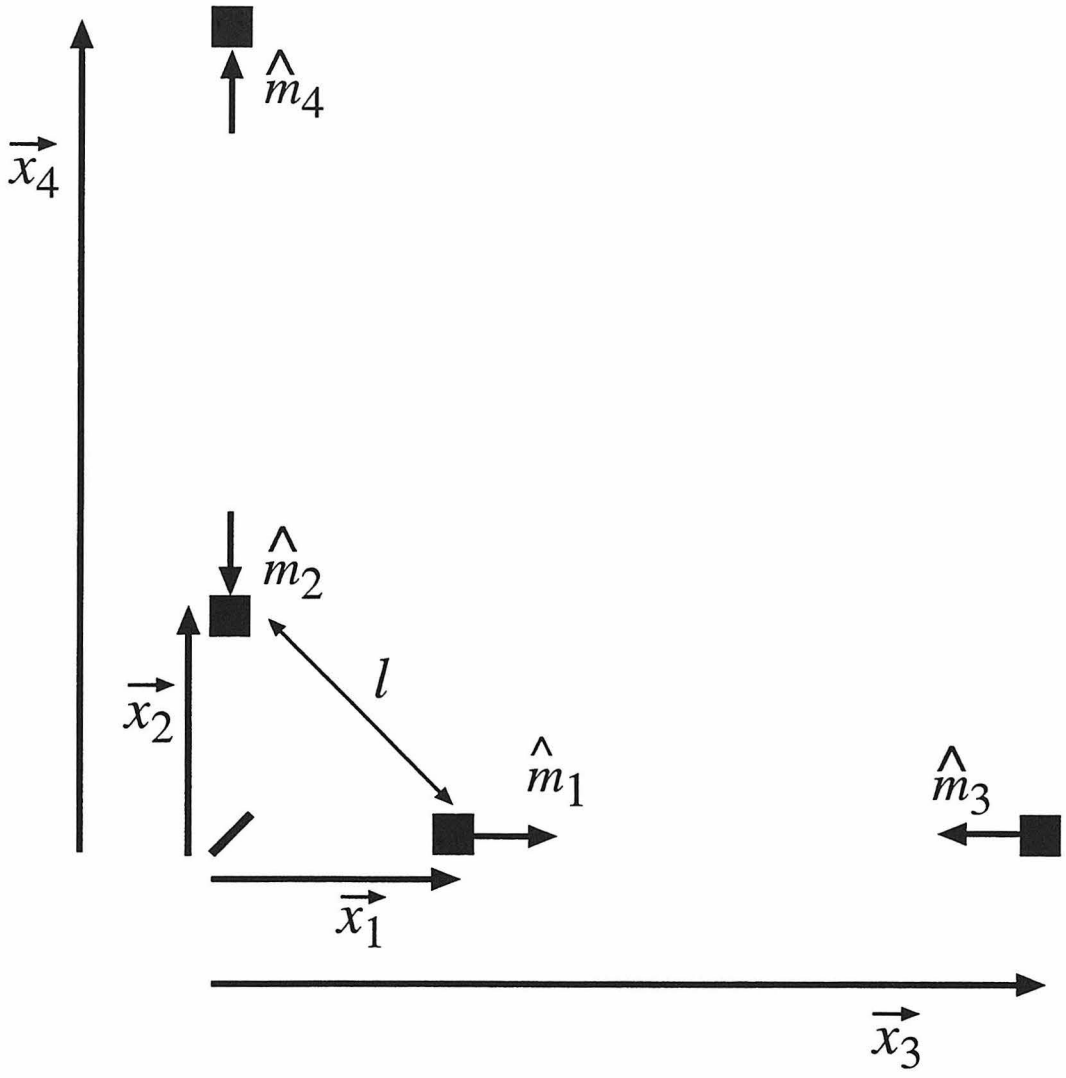

Figure 6.12: The geometry of the interferometer.

interferometer's four test masses we are discussing); the result is

$$\delta\vec{x}_j \cdot \hat{m}_j = -\sum_{\vec{k}} \frac{2\pi i G\rho(\hat{k}\cdot\hat{m}_j)e^{i(\vec{k}\cdot\vec{x}_j-\omega t)}e^{-k\mathcal{H}}}{\omega_0^2-\omega^2+i\omega/\tau}\left(\xi_V+\int_0^\infty \mathcal{R}(z')e^{-kz'}dz'\right) . \qquad (6.58)$$

Here ω_0 and τ are the angular eigenfrequency and damping time of the test mass's pendular motion. After completing the calculation we have moved the origin of coordinates to the interferometer's beam splitter, thereby producing the term $i\vec{k}\cdot\vec{x}_j$ in the exponential, where $\vec{x}_j$ is the test mass's location; *cf.* Fig. 6.12.

The interferometer's displacement signal $x(t) = Lh(t)$ is its difference in arm lengths,

$$x(t) = \sum_{j=1}^{4} \delta\vec{x}_j \cdot \hat{m}_j \ . \tag{6.59}$$

We have chosen $\hat{m}_j$ to point away from the test mass's mirror on the first arm and toward the mirror on the second arm as shown in Fig. 6.12. The seismic gravity-gradient noise is obtained by inserting expression (6.58) into (6.59) for each of the four test masses.

The contributions to this noise coming from the two end masses, $j = 3$ and 4, are not correlated with those coming from any other test mass in our 3–30 Hz frequency band, since 3 and 4 are each so far from the corner and each other ($4\,\mathrm{km} \gg \lambda = 2\pi/k$). However, there is a significant correlation between the two corner test masses, 1 and 2. Taking account of this correlation, the interferometer's displacement signal $x(t)$ [Eqs. (6.58) and (6.59)] exhibits the following noise power in the frequency band Δf:

$$\tilde{x}^2(f)\Delta f = \frac{(2\pi G\rho)^2}{(\omega^2 - \omega_0^2)^2 + \omega^2/\tau^2} e^{-k\mathcal{H}} \sum_{\Delta k} \left| \xi_V + \int_0^\infty \mathcal{R}(z') e^{-kz'} dz' \right|^2 J_k \ , \tag{6.60}$$

where

$$J_k = \sum_{\hat{k}} \left[|\hat{k} \cdot \hat{m}_1 e^{i\vec{k}\cdot\vec{x}_1} + \hat{k} \cdot \hat{m}_2 e^{i\vec{k}\cdot\vec{x}_2}|^2 + (\hat{k} \cdot \hat{m}_3)^2 + (\hat{k} \cdot \hat{m}_4)^2 \right] \ . \tag{6.61}$$

Here we have broken up the sum over $\vec{k}$ into one over all directions $\hat{k}$ and one over its length k in the range Δk. Each of the last two terms in J_k (the uncorrelated contributions of masses 3 and 4) average to 1/2. The first term can be rewritten in terms of $\vec{x}_1 - \vec{x}_2$:

$$J_k = \sum_{\hat{k}} \left[|\hat{k} \cdot \hat{m}_1 e^{i\vec{k}\cdot(\vec{x}_1 - \vec{x}_2)} + \hat{k} \cdot \hat{m}_2|^2 + 1 \right] \tag{6.62}$$

By virtue of the geometry of the interferometer's corner test masses (Fig. 6.12), $\vec{x}_1 - \vec{x}_2 = l(\hat{m}_1 + \hat{m}_2)/\sqrt{2}$, where l is the separation between those masses. Inserting this into Eq. (6.62), setting $\hat{k}\cdot\hat{m}_1 = \cos\phi$ and $\hat{k}\cdot\hat{m}_2 = \sin\phi$, and replacing the summand in (6.62) by its average over $\hat{k}$ (*i.e.*, over ϕ), we obtain

$$J_k = 2 \sum_{\hat{k}} \gamma^2(kl) \ , \tag{6.63}$$

where

$$\gamma(y) = \sqrt{1 + \frac{1}{2\pi} \int_0^{2\pi} \cos\phi \sin\phi \cos\left(y \frac{\cos\phi + \sin\phi}{\sqrt{2}} \right) d\phi} \tag{6.64}$$

[Eq. (6.19)]. This function is graphed in Fig. 6.1. Inserting Eq. (6.63) into Eq. (6.60) and noting that $\sum_{\Delta k} \sum_{\hat{k}} = \sum_{\vec{k}} = N_{\Delta k}$ is the number of allowed wave vectors in the annulus $\mathcal{C}_{\Delta k}$, we obtain our final expression for the interferometer's displacement noise power:

$$\tilde{x}^2(f)\Delta f = \frac{(4\pi)^2(G\rho)^2}{(\omega^2-\omega_0^2)^2+\omega^2/\tau^2}\,\gamma\left(\frac{\omega l}{c_H}\right)e^{-k\mathcal{H}}\left|\xi_V+\int_0^\infty \mathcal{R}(z')e^{-kz'}dz'\right|^2\frac{N_{\Delta k}}{2}\,. \qquad (6.65)$$

The transfer function $T(f)$ for the seismic gravity-gradient noise is obtained by dividing the direction-averaged ground displacement noise power (6.53) into the interferometer displacement noise power (6.65) and taking the square root. The result is expression (6.8) with the reduced transfer function β given by $\beta = \gamma\Gamma\beta'$ [Eq. (6.17)], where $\Gamma = e^{-k\mathcal{H}}$ [Eq. (6.20)] and

$$\beta'(f) = \sqrt{\frac{3/2}{|\xi_H|^2+|\xi_V|^2}}\left|\xi_V+\int_0^\infty \mathcal{R}(z')e^{-kz'}dz'\right|\,; \qquad (6.66)$$

[Eq. (6.24)].

Appendix B Fundamental Rayleigh mode in homogeneous half space

In this Appendix we briefly review the theory of Rayleigh waves propagating in a homogeneous half space (*i.e.*, a homogeneous, planar model of the earth), and then we derive the anisotropy ratio $\mathcal{A}$ and reduced transfer function β' for such waves.

A homogeneous half space can support only the fundamental Rayleigh mode, since the overtones all require inhomogeneities to confine them in the vicinity of the earth's surface. The theory of this mode is developed in a variety of standard texts [31, 32, 33, 34]. According to that theory, the waves propagate with a horizontal speed c_H which is slightly slower than the S-wave speed c_S (which in turn is slower than c_P). The ratio c_H/c_S is a function of the material's Poisson ratio ν, varying from $c_H/c_S = 0.904$ for $\nu = 0.16$ (fused quartz) to $c_H/c_S = 0.955$ for $\nu = 0.5$ (fluids and other easily sheared materials). More generically, it is given by $c_H/c_S = \sqrt{\zeta}$, where ζ is the real root, in the range $0 < \zeta < 1$, of the equation

$$\zeta^3 - 8\zeta^2 + 8\left(\frac{2-\nu}{1-\nu}\right)\zeta - \frac{8}{(1-\nu)} = 0\,. \tag{6.67}$$

The Rayleigh waves' horizontal wave number is $k = \omega/c_H$, and their wavelength is $\lambda = 2\pi/k$. The P-wave of the fundamental Rayleigh mode decays with depth z as e^{-qkz}, where the dimensionless ratio q of vertical e-folding rate to horizontal wave number is

$$q = \sqrt{1 - (c_H/c_P)^2}\,. \tag{6.68}$$

Similarly, the SV-wave part decays with depth as e^{-skz}, where the dimensionless ratio s of vertical e-folding rate to horizontal wave number is

$$s = \sqrt{1 - (c_H/c_S)^2} = \sqrt{1-\zeta}\,. \tag{6.69}$$

More specifically, the mode's displacement eigenvector $\vec{\xi}$ can be decomposed into a P-wave which is the gradient of a scalar potential plus an SV-wave which is the curl of a vector potential. We shall denote by ψ the complex amplitude of the scalar potential. The normal components of elastodynamic stress produced by this wave must vanish[5] at the earth's surface. Upon imposing these boundary conditions, a standard calculation [31, 32] gives the following expression for the

[5]More accurately, they must be continuous with the stress produced by the earth's atmosphere, which we approximate as vacuum.

displacement vector:

$$\vec{\xi} = ik\psi \left(e^{-qkz} - \frac{2qs}{1+s^2} e^{-skz} \right) e^{i(\vec{k}\cdot\vec{x}-\omega t)} \hat{k} - qk\psi \left(e^{-qkz} - \frac{2}{1+s^2} e^{-skz} \right) e^{i(\vec{k}\cdot\vec{x}-\omega t)} \vec{e}_z \ . \tag{6.70}$$

Here, $\vec{e}_z$ is the unit vector pointing in the z-direction, which we take to be down, t is time, $\vec{x}$ denotes horizontal location, and $\vec{k} = k\hat{k}$ is the mode's horizontal wave vector. From this displacement vector we read off the following expressions for the horizontal and vertical displacement amplitudes at the earth's surface, $z = 0$:

$$\xi_H = ik\psi \left(\frac{1+s^2-2qs}{1+s^2} \right) \ , \quad \xi_V = -qk\psi \left(\frac{1-s^2}{1+s^2} \right) \ . \tag{6.71}$$

The wave displacement (6.70) produces a fractional perturbation $\delta\rho/\rho$ of the earth's density given by

$$\frac{\delta\rho}{\rho} = -\vec{\nabla}\cdot\vec{\xi} = \mathcal{R} e^{i(\vec{k}\cdot\vec{x}-\omega t)} \ , \tag{6.72}$$

where

$$\mathcal{R}(z) = (1-q^2)k^2\psi e^{-qkz} \ . \tag{6.73}$$

Inserting Eqs. (6.71) into Eq. (6.23), we obtain the anisotropy ratio for the RF mode of a homogeneous half space,

$$\mathcal{A} = \sqrt{2} \frac{q(1-s^2)}{1+s^2-2qs} \ , \tag{6.74}$$

and inserting (6.71) and (6.73) into (6.24) and integrating, we obtain the mode's reduced transfer function

$$\beta' = \sqrt{\frac{3(1+s^2-2q)^2}{2(1+s^2)[(1+s^2)(1+q^2)-4qs]}} \ . \tag{6.75}$$

Appendix C Multilayer model

In this Appendix we derive the equations governing Rayleigh overtones and the reduced transfer function in a multilayer model of geophysical strata.

Model and notation

Our model consists of N homogeneous layers labeled by the index $n = 1, 2, 3, \ldots, N$. Layer 1 is at the surface, layer N is a homogeneous half-space at the bottom, and the interfaces between layers are horizontal. The Rayleigh modes propagate as decoupled planar SV- and P-waves in each layer; they are coupled at the interfaces by continuous-displacement and continuous-normal-stress boundary conditions.

We have already introduced much of our notation in the body of the paper; to make this Appendix self-contained, we reiterate some of it here:

$\omega = 2\pi f$: Angular frequency of waves.

$\vec{k} = k\hat{k}$: Horizontal wave vector, with k its magnitude and $\hat{k}$ the unit vector in its direction.

$c_H = \omega/k$: Horizontal phase velocity of waves.

D_n: Thickness of layer n.

z_n: Depth below the top of layer n.

ξ_n: Displacement vector for waves in layer n.

K_n: Bulk modulus in layer n

μ_n: Shear modulus in layer n

c_{Pn}: Speed of propagation of P-waves in layer n.

c_{Sn}: Speed of propagation of S-waves in layer n.

α_{Pn}: Angle to vertical of P-wave propagation direction (between 0 and $\pi/2$ if real, by convention). If P-waves are evanescent in the layer, α_{Pn} will be imaginary.

α_{Sn}: Angle to vertical of SV-wave propagation vector (between 0 and $\pi/2$ if real, by convention). If SV-waves are evanescent in the layer, α_{Sn} will be imaginary.

$\mathcal{P}_n$: Complex amplitude of upgoing P-waves at the top of layer n.

$\mathcal{P}'_n$: Complex amplitude of downgoing P-waves at the top of layer n.

$\mathcal{S}_n$: Complex amplitude of upgoing SV-waves at the top of layer n.

$\mathcal{S}'_n$: Complex amplitude of downgoing SV-waves at the top of layer n.

In accord with this notation, the displacement vector in layer n has the following form:

$$\begin{aligned}\vec{\xi}_n &= e^{i(\vec{k}\cdot\vec{x}-\omega t)} \times \left[\left(\mathcal{P}'_n e^{ikz_n \cot\alpha_{Pn}} + \mathcal{P}_n e^{-ikz_n \cot\alpha_{Pn}}\right) \sin\alpha_{Pn}\, \hat{k}\right. \\ &+ \left(\mathcal{P}'_n e^{ikz_n \cot\alpha_{Pn}} - \mathcal{P}_n e^{-ikz_n \cot\alpha_{Pn}}\right) \cos\alpha_{Pn}\, \vec{e}_z \\ &+ \left(\mathcal{S}'_n e^{ikz_n \cot\alpha_{Sn}} - \mathcal{S}_n e^{-ikz_n \cot\alpha_{Sn}}\right) \cos\alpha_{Sn}\, \hat{k} \\ &- \left.\left(\mathcal{S}'_n e^{ikz_n \cot\alpha_{Sn}} + \mathcal{S}_n e^{-ikz_n \cot\alpha_{Sn}}\right) \sin\alpha_{Sn}\, \vec{e}_z\right] .\end{aligned} \tag{6.76}$$

Since the waves are generated at the Earth's surface, the upward propagating waves are absent in the lowermost layer:

$$\mathcal{P}_N = 0\,, \quad \mathcal{S}_N = 0\,. \tag{6.77}$$

Consequently, the waves have $4N - 2$ complex amplitudes.

Equations for the dispersion relation, the propagation angles, and the amplitudes

Once one has specified the Rayleigh mode of interest, its horizontal propagation direction $\hat{k}$, and one of its amplitudes, say $\mathcal{P}_1$, then all its other properties are uniquely determined as a function of frequency. To evaluate its properties one first computes its horizontal dispersion relation $\omega(k)$ [or equivalently $c_H(f)$] by a procedure to be outlined below. Then one computes all the waves' propagation angles by imposing Snell's law (*i.e.*, by demanding that all components of the wave propagate with the same horizontal speed c_H):

$$\frac{c_{Pn}}{\sin\alpha_{Pn}} = \frac{c_{Sn}}{\sin\alpha_{Sn}} = c_H\,. \tag{6.78}$$

At the Earth's surface, the (primed) amplitudes of the reflected waves are related to the (unprimed) amplitudes of the incident waves by the following two standard equations [31, 32, 33, 34]:

$$\begin{aligned} 2\sin\alpha_{S1}\cos\alpha_{P1}(\mathcal{P}'_1 - \mathcal{P}_1) + \cos 2\alpha_{S1}(\mathcal{S}'_1 + \mathcal{S}_1) &= 0 \\ \sin\alpha_{P1}\cos 2\alpha_{S1}(\mathcal{P}'_1 + \mathcal{P}_1) - \sin\alpha_{S1}\sin 2\alpha_{S1}(\mathcal{S}'_1 - \mathcal{S}_1) &= 0\,. \end{aligned} \tag{6.79}$$

These equations can be derived by setting the vertical-vertical and vertical-horizontal components

of the stress to zero at the Earth's surface, and by expressing the ratio of bulk to shear modulus in terms of the propagation angles:

$$\frac{K_n}{\mu_n} = \frac{{c_{Pn}}^2}{{c_{Sn}}^2} - \frac{4}{3} = \frac{\sin^2 \alpha_{Pn}}{\sin^2 \alpha_{Sn}} - \frac{4}{3} \, . \tag{6.80}$$

The junction conditions at the interface between layer n and layer $n+1$ take the following form [33, 34]:

$$\begin{aligned} &\left(\mathcal{P}'_{n\vec{k}} e^{ik \cot \alpha_{Pn} D_n} + \mathcal{P}_{n\vec{k}} e^{-ik \cot \alpha_{Pn} D_n}\right) \sin \alpha_{Pn} \; + \\ &\qquad \left(\mathcal{S}'_{n\vec{k}} e^{ik \cot \alpha_{Sn} D_n} - \mathcal{S}_{n\vec{k}} e^{-ik \cot \alpha_{Sn} D_n}\right) \cos \alpha_{Sn} \; = \\ &\left(\mathcal{P}'_{n+1\vec{k}} e^{ik \cot \alpha_{Pn+1}} + \mathcal{P}_{n+1\vec{k}} e^{-ik \cot \alpha_{Pn+1}}\right) \sin \alpha_{Pn+1} \; + \\ &\qquad \left(\mathcal{S}'_{n+1\vec{k}} e^{ik \cot \alpha_{Sn+1}} - \mathcal{S}_{n+1\vec{k}} e^{-ik \cot \alpha_{Sn+1}}\right) \cos \alpha_{Sn+1} \, , \end{aligned} \tag{6.81}$$

$$\begin{aligned} &\left(\mathcal{P}'_{n\vec{k}} e^{ik \cot \alpha_{Pn} D_n} - \mathcal{P}_{n\vec{k}} e^{-ik \cot \alpha_{Pn} D_n}\right) \cos \alpha_{Pn} \; - \\ &\qquad \left(\mathcal{S}'_{n\vec{k}} e^{ik \cot \alpha_{Sn} D_n} + \mathcal{S}_{n\vec{k}} e^{-ik \cot \alpha_{Sn} D_n}\right) \sin \alpha_{Sn} \; = \\ &\left(\mathcal{P}'_{n+1\vec{k}} e^{ik \cot \alpha_{Pn+1}} - \mathcal{P}_{n+1\vec{k}} e^{-ik \cot \alpha_{Pn+1}}\right) \cos \alpha_{Pn+1} \; - \\ &\qquad \left(\mathcal{S}'_{n+1\vec{k}} e^{ik \cot \alpha_{Sn+1}} + \mathcal{S}_{n+1\vec{k}} e^{-ik \cot \alpha_{Sn+1}}\right) \sin \alpha_{Sn+1} \, , \end{aligned} \tag{6.82}$$

$$\begin{aligned} &\mu_n \left[(1 - \cot^2 \alpha_{Sn}) \left(\mathcal{P}'_{n\vec{k}} e^{ik \cot \alpha_{Pn} D_n} + \mathcal{P}_{n\vec{k}} e^{-ik \cot \alpha_{Pn} D_n}\right) \sin \alpha_{Pn} \; + \right. \\ &\qquad \left. 2 \left(\mathcal{S}'_{n\vec{k}} e^{ik \cot \alpha_{Sn} D_n} - \mathcal{S}_{n\vec{k}} e^{-ik \cot \alpha_{Sn} D_n}\right) \cos \alpha_{Sn}\right] \; = \\ &\mu_{n+1} \left[(1 - \cot^2 \alpha_{Sn+1}) \left(\mathcal{P}'_{n+1\vec{k}} e^{ik \cot \alpha_{Pn+1}} \mathcal{P}_{n+1\vec{k}} e^{-ik \cot \alpha_{Pn+1}}\right) \sin \alpha_{Pn+1} \; + \right. \\ &\qquad \left. + 2 \left(\mathcal{S}'_{n+1\vec{k}} e^{ik \cot \alpha_{Sn+1}} - \mathcal{S}_{n+1\vec{k}} e^{-ik \cot \alpha_{Sn+1}}\right) \cos \alpha_{Sn+1}\right] \, , \end{aligned} \tag{6.83}$$

$$\mu_n \left[2 \left(\mathcal{P}'_{n\vec{k}} e^{ik \cot \alpha_{Pn} D_n} \mathcal{P}_{n\vec{k}} e^{-ik \cot \alpha_{Pn} D_n}\right) \cos \alpha_{Pn} \; -$$

$$(1-\cot^2\alpha_{Sn})\left(\mathcal{S}'_{n\vec{k}}e^{ik\cot\alpha_{Sn}D_n}+\mathcal{S}_{n\vec{k}}e^{-ik\cot\alpha_{Sn}D_n}\right)\sin\alpha_{Sn}\Big] =$$
$$\mu_{n+1}\left[2\left(\mathcal{P}'_{n+1\vec{k}}e^{ik\cot\alpha_{Pn+1}}-\mathcal{P}_{n+1\vec{k}}e^{-ik\cot\alpha_{Pn+1}}\right)\cos\alpha_{Pn+1}\ -\right.$$
$$\left.(1-\cot^2\alpha_{Sn+1})\left(\mathcal{S}'_{n+1\vec{k}}e^{ik\cot\alpha_{Sn+1}}+\mathcal{S}_{n+1\vec{k}}e^{-ik\cot\alpha_{Sn+1}}\right)\sin\alpha_{Sn+1}\right]\ . \tag{6.84}$$

Equation (6.81) is continuity of the horizontal displacement, (6.82) is continuity of the vertical displacement, (6.83) is continuity of the vertical-vertical component of the stress, and (6.84) is continuity of the vertical-horizontal component of the stress.

Equations (6.79) and (6.81)–(6.84) are $4N-2$ homogeneous linear equations for $4N-3$ independent ratios of amplitudes, and for the horizontal dispersion relation $\omega(k)$ [or equivalently $c_H(f)$]. It is convenient to evaluate the dispersion relation by setting to zero the determinant of the coefficients of the amplitudes in Eqs. (6.79) and (6.81)–(6.84). The remaining $4N-3$ amplitudes can then be computed in terms of $\mathcal{P}_1$ using any $4N-3$ of these equations. This was the procedure used to derive the 4-layer results quoted in the text. Once the dispersion relation and the amplitudes have been evaluated as functions of frequency, the anisotropy ratio and reduced transfer function can be computed using the equations derived in the following subsection.

Anisotropy ratio, and reduced transfer function

From the displacement eigenfunction (6.76) for layer $n=1$, we read off the horizontal and vertical displacement amplitudes at the earth's surface:

$$\xi_H = (\mathcal{P}'_1+\mathcal{P}_1)\sin\alpha_{P1}+(\mathcal{S}'_1-\mathcal{S}_1)\cos\alpha_{S1}\ , \tag{6.85}$$
$$\xi_V = -(\mathcal{P}'_1-\mathcal{P}_1)\cos\alpha_{P1}+(\mathcal{S}'_1+\mathcal{S}_1)\sin\alpha_{S1}\ . \tag{6.86}$$

The wave displacement (6.76) produces a fractional density perturbation $\delta\rho_n/\rho_n=-\vec{\nabla}\cdot\vec{\xi}_n=\mathcal{R}_n(z_n)e^{i(\vec{k}\cdot\vec{x}-\omega t)}$ in layer n, with amplitude given by given by

$$\mathcal{R}_n(z_n)=\frac{-ik}{\sin\alpha_{Pn}}\left(\mathcal{P}'_n e^{ikz_n\cot\alpha_{Pn}}+\mathcal{P}_n e^{-ikz_n\cot\alpha_{Pn}}\right)\ , \tag{6.87}$$

By inserting Eqs. (6.85) and (6.86) into Eq. (6.23), we obtain the anisotropy ratio

$$\mathcal{A} = \frac{1}{2}\left|\frac{(\mathcal{P}_1' + \mathcal{P}_1)\sin\alpha_{P1} + (\mathcal{S}_1' - \mathcal{S}_1)\cos\alpha_{S1}}{(\mathcal{P}_1' - \mathcal{P}_1)\cos\alpha_{P1} - (\mathcal{S}_1' + \mathcal{S}_1)\sin\alpha_{S1}}\right| . \tag{6.88}$$

By inserting Eqs. (6.85), (6.86), (6.87), and the relation

$$z = z_n + \sum_{n'=1}^{n-1} D_{n'} \tag{6.89}$$

into Eq. (6.24), integrating, and summing over all four layers, we obtain the reduced transfer function

$$\beta'(f) = \frac{\mathcal{N}(f)}{\mathcal{D}(f)} , \tag{6.90}$$

where

$$\begin{aligned}\mathcal{N}(f) &= \sqrt{\frac{3}{2}}\Bigg|(\mathcal{P}_1 - \mathcal{P}_1')\cos\alpha_P + (\mathcal{S}_1 + \mathcal{S}_1')\sin\alpha_S \\ &\quad + \sum_{n=1}^{N}\frac{\rho_n}{\rho_1}\Big[-\mathcal{P}_n e^{i\alpha_{Pn}} e^{-[k(\sum_{n'=1}^{n-1} D_{n'})(1+i\cot\alpha_{Pn})]}\left(1 - e^{-[kD_n(1+i\cot\alpha_{Pn})]}\right) \\ &\quad + \mathcal{P}_n' e^{-i\alpha_{Pn}} e^{-[k(\sum_{n'=1}^{n-1} D_{n'})(1-i\cot\alpha_{Pn})]}\left(1 - e^{-[kD_n(1-i\cot\alpha_{Pn})]}\right)\Big]\Bigg| ,\end{aligned} \tag{6.91}$$

$$\begin{aligned}\mathcal{D}^2(f) &= \left|(\mathcal{P}_1' + \mathcal{P}_1)\sin\alpha_{P1} + (\mathcal{S}_1' - \mathcal{S}_1)\cos\alpha_{S1}\right|^2 \\ &+ \left|(\mathcal{P}_1' - \mathcal{P}_1)\cos\alpha_{P1} - (\mathcal{S}_1' + \mathcal{S}_1)\sin\alpha_{S1}\right|^2 .\end{aligned} \tag{6.92}$$

Appendix D Lee's dispersion relation for 2-layer model

When there are only two layers, the dispersion relation $\omega(k)$ [or equivalently $c_H(f)$] of the multi-layer model (Appendix C) can be brought into an explicit form that permits rapid numerical solutions. This form was derived by Lee [40] by manipulating the 6×6 determinant of the coefficients of the amplitudes in Eqs. (6.79) and (6.81)–(6.84). The standard textbook by Eringen and Şuhubi [34] presents and discusses Lee's dispersion relation [pages 547–550; note that on the first line of their Eq. (7.7.44) $\bar{\nu}_2$ should be $\bar{\nu}_1$]. The dispersion relation consists of the following prescription:

The unknown to be solved for is

$$\zeta = (c_H/c_{S2})^2 \ . \tag{6.93}$$

At low propagation speeds c_H (high frequencies) the SV-waves in layer 1 will typically propagate rather than decay, with vertical wave number divided by horizontal wave number given by

$$\sigma_1 = \sqrt{(c_H/c_{S1})^2 - 1} = \cot \alpha_{S1} \ , \tag{6.94}$$

while the other waves will typically be evanescent with ratios of e-folding rate to horizontal wave number given by

$$q_1 = \sqrt{1 - (c_H/c_{P1})^2}, \tag{6.95}$$

$$q_2 = \sqrt{1 - (c_H/c_{P2})^2}, \tag{6.96}$$

$$s_2 = \sqrt{1 - (c_H/c_{S2})^2}, \tag{6.97}$$

Regardless of the magnitude of c_H and thence regardless of whether these quantities are real or imaginary, we regard them all as functions of c_H given by the above expressions.

We define two quantities

$$Q = \mu_2/\mu_1 \ , \quad R = \rho_1/\rho_2 \tag{6.98}$$

that appear in what follows. In terms of ζ, Q, and R, we define

$$X = Q\zeta - 2(Q-1) \ , \tag{6.99}$$

$$Y = QR\zeta + 2(Q-1) \ , \tag{6.100}$$

$$Z = Q(1-R)\zeta - 2(Q-1) \ , \tag{6.101}$$

$$W = 2(Q-1)\,. \tag{6.102}$$

In this dispersion relation and only here X, Y, Z, W represent these functions instead of representing earth displacements. In terms of the above quantities we define

$$\begin{aligned}
\xi_1 &= (1-{\sigma_1}^2)\left[X\cosh(kq_1D) + \frac{q_2}{q_1}Y\sinh(kq_1D)\right] \\
&+ 2\sigma_1\left[q_2W\sin(k\sigma_1D) - \frac{1}{\sigma_1}Z\cos(k\sigma_1D)\right]\,, \qquad (6.103)\\
\xi_2 &= (1-{\sigma_1}^2)\left[s_2W\cosh(kq_1D) + \frac{1}{q_1}Z\sinh(kq_1D)\right] \\
&+ 2\sigma_1\left[X\sin(k\sigma_1D) - \frac{s_2}{\sigma_1}Y\cos(k\sigma_1D)\right]\,, \qquad (6.104)\\
\eta_1 &= (1-{\sigma_1}^2)\left[q_2W\cos(k\sigma_1D) + \frac{1}{\sigma_1}Z\sin(k\sigma_1D)\right] \\
&+ 2q_1\left[-X\sinh(kq_1D) - \frac{q_2}{q_1}Y\cosh(kq_1D)\right]\,, \qquad (6.105)\\
\eta_2 &= (1-{\sigma_1}^2)\left[X\cos(k\sigma_1D) + \frac{s_2}{\sigma_1}Y\sin(k\sigma_1D)\right] \\
&+ 2q_1\left[-s_2W\sinh(kq_1D) - \frac{1}{q_1}Z\cosh(kq_1D)\right]\,. \qquad (6.106)
\end{aligned}$$

In terms of these four quantities, Lee's dispersion relation takes the form

$$\xi_1\eta_2 - \xi_2\eta_1 = 0\,. \tag{6.107}$$

In the language of Lee's dispersion relation, finding multiple Rayleigh modes is a matter of finding multiple values of ζ that satisfy (6.107). Overtone modes undergo a transition in layer 2 from propagating and lossy (so that seismic wave energy is lost from layer 1 into layer 2), to evanescent and confined (so the waves are restricted to the vicinity of the top layer)] at speed $c_H(f) = c_{S2}$, which is equivalent to $\zeta = 1$. Thus, to produce dispersion relations for overtone modes, one can look for solutions to (6.107) in the vicinity of $\zeta = 1$, and then, depending on whether one wants confined modes or lossy modes, trace them from $\zeta = 1$ to higher frequencies and lower horizontal speeds, or to lower frequencies and higher horizontal speeds.

In Sec. 6.4.3 we use Lee's dispersion relation to study the RP1 mode at Livingston in the lossy regime.

Appendix E P-up and SV-up modes

In the text we encounter situations in which one can approximate an overtone mode as P- or SV-waves that propagate upward through a homogeneous half space until they encounter the Earth's surface or one or more layers near the surface, and then (exciting the layers) reflect back downward with accompanying production of the other type of wave. Such "P-up" and "SV-up" modes can be described by the multilayer equations of Appendix C, with the up (unprimed) amplitudes in the bottom layer (homogeneous half space), b, set to $\{\mathcal{P}_b \neq 0, \mathcal{S}_b = 0\}$ for P-up modes, and $\{\mathcal{P}_b = 0, \mathcal{S}_b \neq 0\}$ for SV-up modes.

We can derive simple formulas for the anisotropy ratio $\mathcal{A}$ and reduced transfer function β' of such modes for the case of no surface layers (a pure homogeneous half space):

P-up modes in a homogeneous half space

The displacement function is given by Eq. (6.76) with the subscript n's deleted since there is only one layer. The primed (down) amplitudes are given in terms of the unprimed (up) amplitude $\mathcal{P}$ by the surface junction conditions (6.79); in particular

$$\mathcal{P}' = \frac{4\cos\alpha_P \sin^3\alpha_S \cos\alpha_S - \sin\alpha_P \cos^2 2\alpha_S}{4\cos\alpha_P \sin^3\alpha_S \cos\alpha_S + \sin\alpha_P \cos^2 2\alpha_S}\mathcal{P} , \tag{6.108}$$

$$\mathcal{S}' = \frac{4\sin\alpha_P \cos\alpha_P \sin\alpha_S \cos 2\alpha_S}{4\cos\alpha_P \sin^3\alpha_S \cos\alpha_S + \sin\alpha_P \cos^2 2\alpha_S}\mathcal{P} . \tag{6.109}$$

Inserting these into Eq. (6.88) we obtain the following anisotropy ratio:

$$\mathcal{A} = \sqrt{2}\cot 2\alpha_S , \tag{6.110}$$

where, by Snell's law [Eq. (6.40)],

$$\alpha_S = \arcsin(c_S/c_H) . \tag{6.111}$$

Inserting expressions (6.108) into the one-layer version of equations (6.90), we obtain the following reduced transfer function:

$$\beta' = \sqrt{6}\sin^2\alpha_S . \tag{6.112}$$

The anisotropies and reduced transfer functions of Eqs. (6.110) and (6.112) are shown graphically, for $c_P/c_S = 2$ (approximately appropriate to the surface materials at Livingston and Hanford) in Figs. 6.3 and 6.4.

SV-up modes in a homogeneous half space

For SV-up modes, as for P-up modes, the displacement function is given by Eq. (6.76) with the subscript n's deleted. The primed (down) amplitudes are given in terms of the unprimed (up) amplitude $\mathcal{S}$ by the surface junction conditions (6.79); in particular

$$\mathcal{P}' = -\frac{\sin\alpha_S \sin 4\alpha_S}{4\cos\alpha_P \sin^3\alpha_S \cos\alpha_S + \sin\alpha_P \cos^2 2\alpha_S}\mathcal{S} , \tag{6.113}$$

$$\mathcal{S}' = \frac{4\cos\alpha_P \sin^3\alpha_S \cos\alpha_S - \sin\alpha_P \cos^2 2\alpha_S}{4\cos\alpha_P \sin^3\alpha_S \cos\alpha_S + \sin\alpha_P \cos^2 2\alpha_S}\mathcal{S} . \tag{6.114}$$

Inserting these into Eq. (6.88), we obtain the following anisotropy ratio

$$\mathcal{A} = 2\sqrt{2}\left|\frac{\cot\alpha_P}{\cot^2\alpha_S - 1}\right| , \tag{6.115}$$

where, by Snell's law,

$$\alpha_S = \arcsin(c_S/c_H) , \quad \alpha_P = \arcsin(c_P/c_H) . \tag{6.116}$$

Inserting expressions (6.113) into the one-layer version of equations (6.90), we obtain the following reduced transfer function:

$$\beta' = \frac{\sqrt{6}\sin^2\alpha_S \, |1 - 2i\cot\alpha_P \sin^2\alpha_S \sec 2\alpha_S|}{\sqrt{1 + (2\,|\cot\alpha_P|\,\sin^2\alpha_S \sec 2\alpha_S)^2}} . \tag{6.117}$$

The anisotropies and reduced transfer functions of Eqs. (6.115) and (6.117) are shown in Figs. 6.3 and 6.4, for $c_P/c_S = 2$.

Bibliography

[1] A. Abramovici *et al.*, Science **256**, 325 (1992).

[2] C. Bradaschia *et al.*, Nucl. Instrum. & Methods **A289**, 518 (1990).

[3] J. W. Cronin *et al.*, in *Proceedings of the Snowmass 95 Summer Study on Particle and Nuclear Astrophysics*, edited by E. W. Kolb and R. Peccei (World Scientific, Singapore, 1995).

[4] K. S. Thorne, in *Proceedings of the Snowmass 95 Summer Study on Particle and Nuclear Astrophysics*, edited by E. W. Kolb and R. Peccei (World Scientific, Singapore, 1995) (gr-qc/9506086).

[5] K. S. Thorne and C. J. Winstein, Phys. Rev. D, in preparation.

[6] S. Braccini *et al.*, Rev. Sci. Ins. **64**, 310 (1993); M. Beccaria *et al.*, Nucl. Inst. A **394**, 397 (1997).

[7] R. Weiss, "Quarterly Progress Report of the Research Laboratory of Electronics of the Massachusetts Institute of Technology", Volume 105, p. 54 (1972).

[8] P. R. Saulson, Phys. Rev. D **30**, 732 (1984).

[9] R. Spero, in *Science Underground*, Proceedings of the Los Alamos Conference, 1982, edited by M. M. Nieto *et al.* (AIP, New York, 1983)

[10] P. R. Saulson, *Fundamentals of Interferometric Gravitational Wave Detectors* (World Scientific, Singapore, 1994).

[11] S. A. Hughes and K. S. Thorne, unpublished manuscript (1996).

[12] S. Bracini *et al.*, *Class. Quant. Grav.*, in press. The Corresponding Authors for this 42-author paper are G. Cella and E. Cuoco.

[13] A. Rohay, "Ambient Ground Vibration Measurements at the Livingston, Louisiana LIGO Site", LIGO Document LIGO–C961022–A–O1.

[14] A. Rohay, "Ambient Ground Vibration Measurements at the Hanford, Washington LIGO Site", LIGO Document LIGO–C950572–02–O1.

[15] M. W. Asten, Bull. Seis. Soc. Am. **68**, 1623 (1978).

[16] E. J. Douze and S. J. Laster, Geophys. **44**, 1570 (1979).

[17] A. C. Liaw and T. V. McEvilly, Geophys. **44**, 1097 (1979).

[18] C. A. Powell, Bull. Seis. Soc. Am. **82**, 1889 (1992).

[19] S. E. Hough *et al.*, Bull. Seis. Soc. Am. **82**, 1186 (1992).

[20] G. Milana *et al.*, Bull. Seis. Soc. Am. **86**, 320 (1996).

[21] E. J. Douze, Bull. Seis. Soc. Am. **57**, 55 (1967).

[22] L. Malagnini, A. Rovelli, S. E. Hough, and L. Seeber, Bull. Seis. Soc. Am. **83**, 1744 (1993).

[23] A. Rohay, "Analysis of Differential Motions at the Hanford, Washington and Livingston, Louisiana LIGO Sites," LIGO Document LIGO–C962289-B-01.

[24] A. Rohay, private communication.

[25] R. E. Abercrombie, Bull Seis. Soc. Am. **87**, 731 (1997); also, for a review of measurements: R. E. Abercrombie, Pure Appl. Geophys., special volume, edited by B. J. Mitchell and B. A. Romanovicz, in press.

[26] K. Ishihara, *Soil Behavior in Earthquake Geotechnics* (Oxford Science Publications, Oxford, 1996).

[27] *CRC Practical Handbook of Physical Properties of Rocks and Minerals*, edited by R. S. Carmichael (CRC Press, Boca Raton, Florida, 1989).

[28] Hiroo Kanamori, private communication.

[29] Dilatometers are described in Sacks, I. S. *et al.*, Papers in Meteorology and Geophysics **23**, 195 (1971).

[30] E. Field and K. Jacob, Geophys. Res. Lett. **20**, 2925 (1993).

[31] L. D. Landau and E. M. Lifshitz, *Theory of Elasticity* (Pergamon Press, Oxford, 1986), Chapter 24.

[32] A. E. H. Love, *A Treatise on the Mathematical Theory of Elasticity*, 4th Edition (Dover, New York, 1944).

[33] W. L. Pilant, *Elastic Waves in the Earth* (Elsevier Scientific Publishing Company, New York, 1979), Chapter 8.

[34] A. C. Eringen and E. S. Şuhubi, *Elastodynamics, Volume II, Linear Theory* (Academic Press, New York, 1975), Chapter 7.

[35] "Report of Geotechnical Survey", LIGO Project, Hanford, Washington, Dames and Moore, February 1993.

[36] "Safety Evaluation Report Related to the Operation of WPPS Nuclear Project No. 2", Report NUREG-0892 (Nuclear Regulatory Commission, Washington DC, 1982), Section 2.5, dated 12/21/81.

[37] "Geotechnical Investigation of the LIGO site", Livingston, Louisiana, Woodward-Clyde Consultants, January 1995.

[38] H. Liu *et al.*, Engineering Geology **46**, 313 (1997).

[39] K. S. Thorne, in *300 Years of Gravitation*, edited by S. W. Hawking and W. Israel (Cambridge University Press, Cambridge, 1987).

[40] A. W. Lee, Mon. Not. Roy. Astron. Soc. Geophys. Suppl., **3**, 83 (1932).

[41] LIGO site blueprints, Document Numbers LIGO-D960052-O0-□, LIGO–D960055-O0-□, LIGO-D960917-O0-□, LIGO–D960242-A-□.

[42] R. Weiss, private communication.